Studies of the emittance growth due to noise in the Crab Cavity RF systems

UNIVERSITY OF LIVERPOOL

Thesis submitted in accordance with the requirements of the University of Liverpool for the degree of Doctor in Philosophy

by

Natalia Triantafyllou

January 2023

Declaration

This thesis is primarily my own work. The work done by other people is clearly identified and referenced as appropriate in the main body of the thesis.

Acknowledgments

With the following lines, I would like to thank all the people who have helped me undertake this challenging but exciting journey.

In particular, this work would not have been possible without the guidance of my supervisor at CERN, Dr. Hannes Bartosik. I would like to thank him for sharing his immense knowledge in the field with me, and for the numerous hours of valuable and interesting discussions.

I am sincerely thankful to my university supervisor, Prof. Andrzej Wolski, for being an excellent teacher, for the numerous fruitful discussions, and his valuable feedback. His interest in the work and his inputs on the topic were always beneficial. I would furthermore like to thank him for his careful guidance through every step of this PhD project.

I would like to express my appreciation to my viva examiners, Prof. Andrew Mehta and Prof. Robert Appleby, for their valuable feedback and comments.

I would also like to thank Dr. Yannis Papaphilippou and Dr. Fanouria Antoniou for welcoming me into the field of accelerator physics and for their valuable suggestions for the project.

Special thanks to Dr. Xavier Buffat for his amazing ideas, help, and contribution to understanding the mechanism of the emittance growth suppression by the impedance. I am grateful for all the discussions and our collaboration over the past two years.

I would also like to thank Rama Calaga and Philippe Baudrenghien for the realisation of the SPS experiments with Crab Cavities and for an excellent collaboration with the SY-RF team. I am also grateful to Lee Carver for transferring his knowledge from the first experimental campaign with Crab Cavities in 2018.

Acknowledgments

Abstract

"Studies of the emittance growth due to noise in the Crab Cavity RF systems" by Natalia Triantafyllou.

The High-Luminosity LHC (HL-LHC) is the upgrade of the Large Hadron Collider (LHC) machine which aims to increase significantly the luminosity at the experiments in order to extend the potential for physics discoveries. Crab Cavities are a key component of the HL-LHC upgrade, as they will be deployed to mitigate the luminosity reduction induced by the crossing angle at the main LHC experiments (ATLAS and CMS). An important point to consider is the undesired transverse emittance growth due to noise in the Crab Cavities RF system, which can result in considerable loss of luminosity.

This thesis explored the mechanisms for emittance growth from Crab Cavity RF noise through numerical simulations and experimental measurements. The studies focused on the Super Proton Synchrotron (SPS) machine, in which two prototype Crab Cavities were installed in 2018, prior to their installation in the LHC, to be tested for the first time with proton beams. It was found that the beam transverse impedance plays an important role in the emittance growth driven by Crab Cavity RF noise. The measured emittance growth rates are much smaller than predicted from simulations and available theoretical models without including impedance effects. When impedance effects are included in the simulations, the results are in much better agreement with the experiment. The simulations including the machine impedance also demonstrate the dependence of the emittance growth suppression on the tune shift with amplitude, which is another feature consistent with experimental observations. The significance of these results and the implications for the HL-LHC are also discussed.

Contents

Contents

Contents

Contents

List of Figures

List of Tables

List of Symbols

L Instantaneous luminosity of a collider.

L_{int} Integrated luminosity of a collider.

n_b Number of colliding bunch pairs.

f_{rev}, ω_{rev} Revolution frequency and angular revolution frequency of the beam.

N_1, N_2 Number of particles per colliding bunch.

σ_{xing} Transverse beam size in the crossing plane.

σ_{xing} Crossing angle between the colliding beams.

σ_x, σ_y Horizontal and vertical rms beam size.

σ_z Rms bunch length in meters.

σ_t Rms bunch length in seconds.

σ_{xing} Transverse beam size in the crossing plane.

t Time parameter.

s Parameter of the position along the accelerator ring.

(x, x') Horizontal co-ordinates: position and angle.

(y, y') Vertical co-ordinates: position and angle.

List of Symbols

(z, δ)	Longitudinal co-ordinates: position and relative momentum offset.
(p_x, p_y, p_z)	Particle's momentum in the horizontal, vertical and longitudinal plane respectively.
E_0, p_0, v_0	Energy, momentum, and velocity of the reference particle.
β_0, γ_0	Relativistic beta and gamma (Lorentz factor).
e, m_p	Charge and rest mass of a proton.
ρ	Local bending radius.
i	Imaginary unit
b_n, α_n	Strength of a normal and skew multiple components of nth order.
k_n	Normalised normal multipole coefficient.
$\mathbf{F_L}$	Lorentz force vector.
$\mathbf{E}, \mathbf{B}$	Electric and magnetic field vector.
$\mathbf{v}$	Velocity vector.
B_x, B_y	Horizontal and vertical components of the magnetic field.
c	Speed of light.
C_0	Circumference of the circular accelerator.
J_x, J_y	Horizontal and vertical actions.
ψ_x, ψ_y	Horizontal and vertical phase advances from $s = 0$ to s.

$\Delta\psi_u$	Phase advance between two locations along the ring, with $u = (x, y)$ for the horizontal and vertical plane respectively.
$\alpha_u(s), \beta_u(s), \gamma_u(s)$	Alpha, beta and gamma functions respectively or Twiss or Courant-Snyder parameters, with $u = (x, y)$.
Q_x, Q_y	Horizontal and vertical betatron tunes.
Q_{x0}, Q_{y0}	Horizontal and vertical working points of an accelerator.
$\epsilon_x^{\text{geom}}, \epsilon_y^{\text{geom}}$	Horizontal and vertical geometric emittance.
ϵ_x, ϵ_y	Horizontal and vertical normalised emittance.
$D_x(s), D_y(s)$	Horizontal and vertical dispersion functions.
σ_δ	Momentum spread or rms momentum deviation.
$Q_x^{(n)}, Q_y^{(n)}$	Horizontal and vertical chromaticity of nth order.
Q_x', Q_y'	Horizontal cand vertical chromaticity of first order.
L_3	Length of an octupole magnet.
$\alpha_{xx}, \alpha_{yy}, \alpha_{xy}$	Horizontal, vertical, and cross-term detuning coefficients, respectively.
T_{rev}	Revolution period.
$f_{\text{RF}}, \omega_{\text{RF}}$	Frequency and angular frequency of the main RF system of the accelerator.
V_{RF}	Voltage of the main RF system of the accelerator.
h	Harmonic number.

List of Symbols

ϕ_s The phase of the synchronous particle.

η_p Phase slip factor.

Q_s, ω_s Synchrotron tune and angular synchrotron frequency, respectively.

$W_x(z), W_y(z)$ Horizontal and vertical wakefunctions.

$W_x^{\mathrm{const}}(z), W_y^{\mathrm{const}}(z)$ Horizontal and vertical constant wakefunctions.

$W_x^{\mathrm{dip}}(z), W_y^{\mathrm{dip}}(z)$ Horizontal and vertical dipolar wakefunctions.

$W_x^{\mathrm{quad}}(z), W_y^{\mathrm{quad}}(z)$ Horizontal and vertical quadrupolar wakefunctions.

$Z_x(\omega), Z_y(\omega)$ Horizontal and vertical impedance.

(m, l) Transverse and azimuthal head, respectively.

$\Omega_{u0}^{(l)}$ Complex coherent frequency of head-tail mode l, with $u = (x, y)$ denoting the horizontal and vertical plane, respectively.

$\Delta\Omega_u^{(l)}$ Complex frequency shift of head-tail mode l, with $u = (x, y)$ denoting the horizontal and vertical plane respectively.

$\Delta\Omega_{u,\mathrm{re}}^{(l)}, \Delta\Omega_{u,\mathrm{im}}^{(l)}$ Real and imaginary part of the complex frequency shift of head-tail mode l, with $u = (x, y)$ denoting the horizontal and vertical plane respectively.

ω_x, ω_y Horizontal and vertical angular betatron frequencies

Γ Gamma function.

Z_{eff} Effective impedance.

$1/\tau_u$	Growth (+ sign) or damping (- sign) rate of the head-tail mode l, where $u = (x, y)$ denotes the horizontal and vertical planes, respectively.
N_{mp}	Number of macroparticles used in the tracking simulations.
N_{turns}	Number of turns used in the tracking simulations.
$\Delta Q_u^{(l)}$	Coherent frequency shifts in tune units of head-tail mode l, with $u = (x, y)$ denoting the horizontal and vertical plane respectively.
$\Delta Q_x^{\mathrm{rms}}, \Delta Q_y^{\mathrm{rms}}$	Horizontal and vertical rms betatron tune spread.
q_x, q_y	Fractional part of the horizontal and vertical betatron tunes.
S_θ	Power spectral density of dipole noise.
$S_{\Delta A}, S_{\Delta \phi}$	Power spectral density of amplitude and phase noise signal.
$V_{\mathrm{CC}}(t)$	Crab Cavity voltage.
$V_{0,\mathrm{CC}}$	Peak amplitude of Crab Cavity voltage.
f_{CC}	Crab Cavity frequency.
ϕ_{CC}	Crab Cavity phase.
$\Delta A, \Delta \phi$	Relative deviation from the nominal amplitude and deviation from the nominal phase of the Crab Cavity.
$\sigma_{\Delta A}^2, \sigma_{\Delta \phi}^2$	Total noise power of amplitude and phase noise.
$I_n(x)$	Modified Bessel function of the first kind.

$C_{\Delta A}, C_{\Delta \phi}$ Correction terms to account for the dependence of the amplitude and phase noise induced emittance growth predicted from the Mastoridis–Baudrenghien model on the bunch length.

σ_ϕ Rms bunch length in radians.

f Frequency parameter.

$\mathscr{L}(f)$ Script-ell of f: the standard measure for characterising instabilities in the frequency domain.

(A, θ, d) Amplitude, phase, and vertical offset parameter of the sinusoidal fitting function used in this thesis.

(P, k, μ, σ) Amplitude, offset, mean, and standard deviation of the Gaussian fitting function used in this thesis.

(c_0, c_1) Initial value of the emittance and emittance growth rate for the polynomial fitting function used in this thesis.

τ_{decoh} Decoherence time of the betatron oscillations.

f_b Frequency of the first betatron sideband.

E_b Beam energy.

$k_{\mathrm{LOF}}, k_{\mathrm{LOD}}$ Normalised strength of the focusing and defocusing Landau octupole families in the Super Proton Synchrotron (SPS).

N_b Bunch intensity i.e. number of particles in the bunch.

List of Acronyms

ABWLM	A: RF, B: Beam , W: Wideband, L: Longitudinal, M: Measurement
AD	Anti-proton Decelerator
ADT	LHC Transverse Damper
AWAKE	Wakefield Acceleration Experiment
ALICE	A Large Ion Collider Experiment
ATLAS	A Toroidal LHC Apparatus
BBQ	Base-band tune measurement system
BCT	Beam Current Transformer
BPM	Beam Position Monitor
CERN	European Organisation of Nuclear Research
CC	Crab Cavity
CMS	Compact Muon Solenoid
DC	Direct Current
DQW	Double-Quarter Wave
FBCT	Fast Beam Current Transformer
FFT	Fast Fourier Transform
GPU	Graphics Processing Unit
HL-LHC	High-Luminosity Large Hadron Collider
HT monitor	Head-Tail monitor
IEEE	Institute of Electrical and Electronics Engineers
ISOLDE	Online Isotope Mass Separator
LEP	Large Electron Positron collider
Linac4	Linear accelerator 4

LIU	LHC Injectors Upgrade
LHC	Large Hadron Collider
LOF	SPS Landau Octupole for Focusing
LOD	SPS Landau Octupole for Defocusing
LSA	LHC Software Architecture
NAFF	Algorithm of Numerical Analysis of Fundamental Frequencies
RF	Radio-Frequency
RFD	RF dipole
rms	Root mean square
PM	Photomultiplier
PS	Proton Synchrotron
PSD	Power Spectral Density
PSB	Proton Synchrotron Booster
SI	International System of Units
SPS	Super Proton Synchrotron
WCM	Wall Current Monitor
WS	Wire Scanners

1 | Introduction

Particle accelerators were first developed in the early 20th century as a tool for high-energy physics research. By accelerating the particles to high energy, they allow us to investigate the subatomic structure of the world and to study the properties of the elementary particles and the fundamental forces. Through the years significant technological progress has been achieved resulting in higher energies and greatly enhanced performance of the machines. Additionally, various types of accelerators have been developed (cyclotrons, linacs, synchrotrons, etc) using different types of particles (hadrons or leptons), and their use was also expanded in other fields such as medicine and industrial research.

1.1 The CERN accelerator complex

CERN (European Organisation of Nuclear Research), located on the Franco-Swiss border near Geneva, is at the forefront of the accelerator physics research as it operates an extensive network of accelerators, illustrated in Fig. 1.1, including the well-known Large Hadron Collider (LHC) [1].

The LHC is a circular machine, 27 km long, built about 100 m underground and is currently the largest and most powerful accelerator in the world. It accelerates and collides two counter-rotating beams of protons or ions (circulating in two different rings) at the four main experiments, which are located around the LHC ring, namely ATLAS, CMS, ALICE, and LHCb [2, 3, 4, 5]. The highlight of CERN and of the LHC operation up to now was the discovery of the Higgs boson in 2012 from ATLAS [6] and CMS [7], from proton collisions at 3.5 TeV (center-of-mass energy of 7 TeV), which was a milestone for the validation of the standard model.

The beams used by the LHC are produced and gradually accelerated by the injector chain, which is a sequence of smaller machines boosting the energy of the beam. In

particular, through the chain of Linac4, Proton Synchrotron Booster (PSB), Proton Synchrotron (PS), and the Super Proton Synchrotron (SPS) the beam is accelerated up to 450 GeV before injecting into the LHC. In the LHC they are accelerated up to the collision energy of 6.8 TeV (center-of-mass energy of 13.6 TeV). It should be noted, that LHC delivered collisions with center-of-mass energy of 7 TeV during Run 1 (2010-2013) which was increased to 13 TeV for the Run 2 (2015-2018), and reached 13.6 TeV in Run 3 (2022-present).
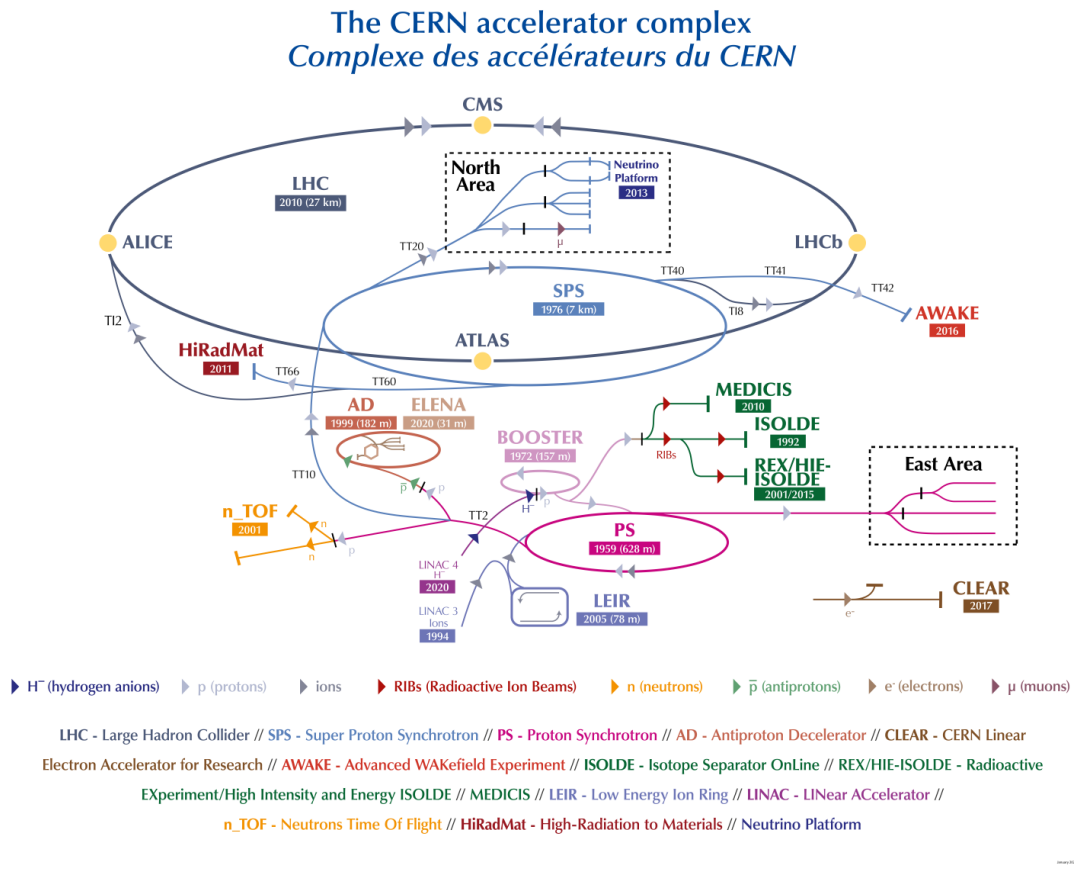
Figure 1.1: Schematic view of the CERN accelerator complex. The different colors correspond to the different machines. The year of commissioning and the type of particles used in each one of them are also indicated along with the circumference for the circular machines. The image is courtesy of CERN [8].

It is worth mentioning that not only protons but also lead ions are accelerated in the LHC, starting their journey from Linac3 and Low Energy Ion Ring (LEIR) and then in PS and SPS as proton beams. Oxygen atoms are also proposed to be used in 2024.

Finally, the accelerators in the injector chain not only prepare the beam for the LHC but also provide beams to various other facilities and experiments at lower

energies. Examples are the Anti-proton Decelerator (AD) which studies antimatter, the Online Isotope Mass Separator (ISOLDE) which studies the properties of the atomic nuclei using radioactive beams, and the Advanced Proton Driven Plasma Wakefield Acceleration Experiment (AWAKE) which investigates particle acceleration by proton-driven plasma wakefields.

1.1.1 The CERN Super Proton Synchrotron

The research described in this thesis was conducted at the Super Proton Synchrotron (SPS) and some additional information about this machine is provided here. The SPS (shown with light blue color in Fig. 1.1) was first commissioned in 1967 and has a circumference of 6.9 km. The SPS was originally built to provide beams for the fixed target experiments. It also used to operate as a proton-antiproton collider (Sp$\bar{\mathrm{p}}$S) and later on as an injector for the Large Electron Positron collider (LEP). Even though the SPS can accelerate various particle types (protons, antiprotons, electrons, and heavy ions) the following information will concern its operation with proton beams which is the topic of the research presented in this thesis.

Currently, the SPS is the second biggest accelerator at CERN and it can accelerate protons up to 450 GeV. Due to its past use as a collider, it can also operate as a storage ring. This operational mode is called "coast" and was used for the majority of the experimental studies presented in this thesis. During coast, the bunches circulate in the machine for long periods at constant energy. The highest energy at which SPS can operate in coast is 270 GeV due to limited cooling of the magnets to transfer away the heat when operating at high energy and consequently at large currents for long periods.

1.2 The High-Luminosity LHC project and Crab Cavities

The High-Luminosity LHC project (HL-LHC) [9, 10] is the upgrade of the LHC machine, which will extend its potential for discoveries. In particular, it aims to

increase the instantaneous luminosity by a factor of 5 beyond the current operational values and the integrated luminosity by a factor of 10.

The luminosity, along with the energy, is a key parameter defining the performance of a collider as it is a measure of the collision rate. The instantaneous luminosity is obtained as [11]:

$$L = \frac{n_b f_{\text{rev}} N_1 N_2}{4\pi \sigma_x^* \sigma_y^*} \frac{1}{\sqrt{1 + \left(\frac{\sigma_z}{\sigma_{\text{xing}}} \frac{\theta_c}{2}\right)^2}}, \tag{1.1}$$

where f_{rev} is the revolution frequency (the number of times per second a particle performs a turn in the accelerator), n_b is the number of colliding bunch pairs, $N_{1,2}$ is the number of particles per bunch, $\sigma_{x,y}^*$ is the transverse beam size at the interaction point, σ_z the rms bunch length of the colliding bunches, σ_{xing} the transverse beam size in the crossing plane and θ_c is the full crossing angle between the colliding beams. The crossing angle is often introduced between the bunches in a collider to reduce parasitic collisions and get rid of the remnants after the collision. For reference, in the LHC, the crossing angle is on the order of magnitude 10^{-4} radians.

The integrated luminosity is the one that ultimately defines the performance of the machine as it provides the total number of recorderd events. It depends both on the instantaneous luminosity and on the machine availability. The integrated luminosity, is expressed as [9]:

$$L_{\text{int}} \equiv \int_{\Delta t} L \, dt, \tag{1.2}$$

where L is the instantaneous luminosity as defined in Eq. (1.1).

HL-LHC aims to achieve instantaneous luminosity of $L \sim 5 \cdot 10^{34}$ cm^{-2}s^{-1} and an increase on the integrated luminosity from 300 fb^{-1} to 3000 fb^{-1} over its lifetime of 10-12 years and considering 160 days of operation per year [12].

1.2.1 Crab cavities

To achieve its luminosity goals, the HL-LHC will employ numerous innovative technologies. The Crab Cavity technology (will be denoted as CC in this thesis) [13] is one of the key components of the project as it will be employed to mitigate the luminosity reduction caused by the crossing angle, θ_c (see Eq. (1.1)).

A crab cavity is an RF cavity which provides a transverse, sinusoidal like, kick to the particles depending on their longitudinal position within the bunch. A graphical visualisation of the kick is shown in Fig. 1.2. It can be seen that the head (leading part) and the tail (trailing part) of the bunch receive opposite deflection while the particles at the center remain unaffected.
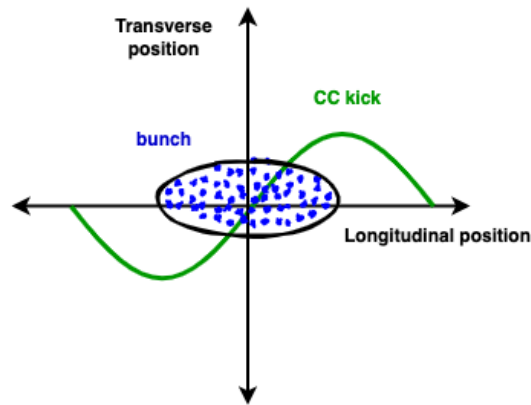
Figure 1.2: Visualisation of the CC kick (green line) on the bunch particles (blue dots).

The CCs will be installed in the two main interaction points of LHC, ATLAS and CMS. According to the plan, CCs will be installed on each ring and on each side of the interaction points (eight in total). This is displayed in Fig. 1.3 with the red (ATLAS) and orange (CMS) markers. The reason why CCs are needed on each side of the IP is discussed in the following paragraphs (local vs global scheme).

In this configuration, the bunches receive the transverse deflection from the first pair of CCs just before reaching the interaction point. This results in a rotation of the bunch, which mitigates the crossing angle and restores the head-on collisions. The deflection is cancelled once the bunches reach the second pair of CCs which are symmetrically placed at the opposite side of the interaction point. The collision

1. Introduction
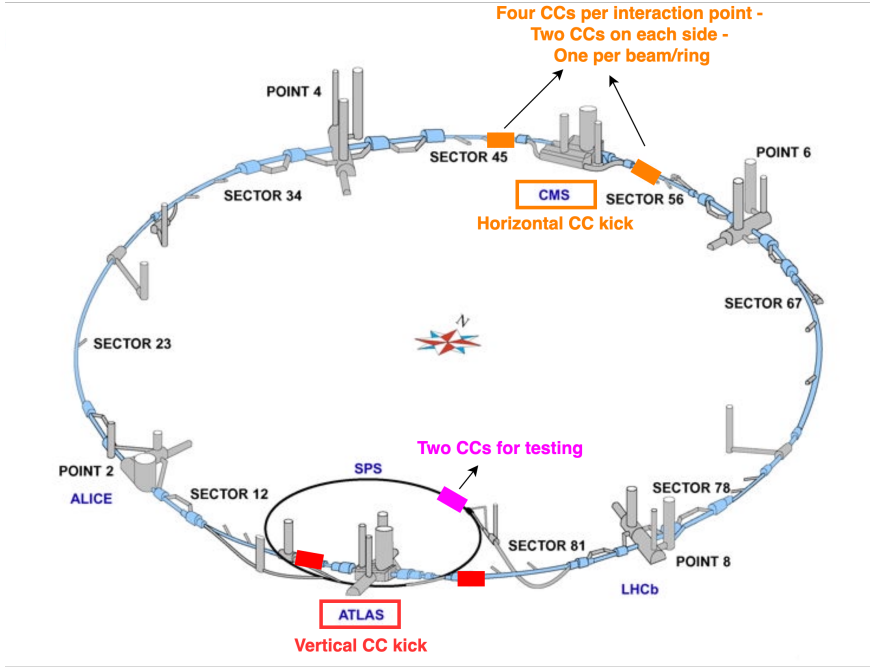
Figure 1.3: Layout of the LHC and the SPS. The CC location for the HL-LHC configuration is marked. Two CCs (one per ring) will be installed on each side of ATLAS (red) and CMS (orange). Two prototype CCs were also installed in the SPS (magenta) in 2018, to be tested before their installation in LHC. The layout can be found in [14].

of the bunches in the presence of the CCs is illustrated in Fig. 1.4.

(a) Crossing without CCs

(b) Crossing with CCs
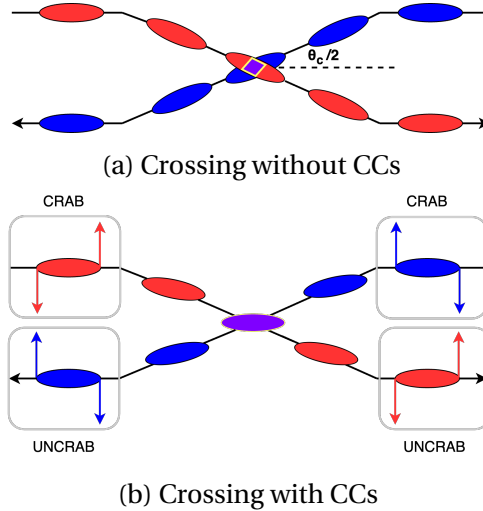
Figure 1.4: Collision with and without the use of CCs. The CCs restore the overlap between the bunches recovering the luminosity reduction caused by the crossing angle, θ_c. The blue and red colors indicate two bunches in the different rings.

The above scheme, with CCs before and after the interaction point, is called the local crabbing scheme. An alternative scheme, named the global crabbing scheme,

was also under discussion in the first stages of the project. In such as scheme, the closed orbit distortion that is caused by the fact that the head and the tail of the bunch are kicked in opposite directions propagates around the ring [10].This scheme is cost-efficient compared to the local scheme as it only requires two CCs. However, it introduces significant constraints on the betatron phase advance between the interaction points and the CCs. The constraints are enhanced by the fact that the bunch crossing in ATLAS takes place in the vertical plane while in CMS in the horizontal. To this end, the local CC scheme was chosen for the HL-LHC project.

In order to accommodate the crossing in both transverse planes two CC designs have been developed: the Double-Quarter Wave (DQW) and the RF dipole (RFD), which provide vertical and horizontal deflection respectively. Information on their design can be found in [15, 16, 17, 18].

Crab cavities have already been successfully used in the KEKB collider [19] in Japan, during 2007-2010, with lepton beams ($e^+ - e^-$) [20, 21, 22]. However, there are significant differences in the beam dynamics between leptons and hadrons (HL-LHC case). One of the most crucial points is that noise-induced emittance growth is not an issue of concern for lepton beams as they experience emittance damping due to synchrotron radiation. For proton beams, the synchrotron radiation damping is much weaker so that the beam degradation due to emittance growth eventually can result in loss of luminosity.

As the CCs have never been used with protons before, two prototype superconducting CCs were installed in the SPS (Fig. 1.3, magenta markers) to test the technical systems, to validate their operation with proton beams and to identify and address potential issues before their installation in LHC. The SPS provides an ideal test bed for these studies as it allows testing under conditions that are closer to those in HL-LHC than any other machine. In particular, the SPS operates with proton beams, can run in storage-ring mode, and in terms of the energy reach is second only to LHC. The two CCs that were installed in SPS [23] were both fabricated at CERN and of the DQW type (like the ones that will be used in ATLAS interaction point in HL-LHC).

1.3   Motivation, objectives and thesis outline

As mentioned above, one of the main concerns regarding the CC operation with protons is the emittance growth due to noise in their RF system leading to luminosity loss. For the HL-LHC, the target values regarding the luminosity loss and emittance growth are very tight. In particular, the maximum allowed luminosity loss due to CC RF noise induced emittance growth is targeted at just 1% during a physics fill, which corresponds to an CC RF noise-induced emittance growth of 2 %/h [24, 25, 26]. To this end, a good understanding and characterization of the emittance growth mechanism is crucial for the HL-LHC project.

For reference, a physics fill is the time period during which the beams are successfully injected in the LHC at the desired conditions, they are accelerated at the desired energy and they are kept in the machine for consecutive collisions. After some hours, due to beam degradation the beams are dumped and a new fill is prepared. A fill in the HL-LHC will last a couple of hours.

The main objective of this thesis is to understand, characterise and evaluate the mechanism of CC RF noise-induced emittance growth including numerical and experimental studies. The studies presented in this thesis were conducted for the SPS machine where the two prototype CCs have been installed to allow for some tests with a proton beam in a running machine prior to their installation in the LHC. Hence direct comparison of predictions from models and experimental data is possible. It should be emphasised that the CC tests in SPS constitute the first experimental beam dynamics studies with CCs and proton beams. The results and the understanding obtained from this research are essential for the HL-LHC, in order to predict the long-term emittance and to define limits on the acceptable noise levels for the CCs.

This thesis reports research that was carried out between 2018 and 2022, based at CERN and is structured as follows:

Chapter 2 presents the basics of accelerator beam dynamics focusing on the

concepts that are relevant for understanding the studies presented in this thesis. In particular, definitions are given for single-particle beam dynamics, addressing both transverse and longitudinal motion. Furthermore, the collective effects are introduced focusing on the effect of wakefields. A brief discussion on optics models for accelerators is also provided. Finally, the two simulation codes used in this thesis for macroparticle tracking, PYHEADTAIL, and Sixtracklib, are described.

The available theoretical model for predicting the emittance growth driven by Crab Cavity RF noise, developed by T. Mastoridis and P. Baudrenghien [27], is described in Chapter 3. This model will be referred to as Mastoridis–Baudrenghien model or theory throughout the thesis. The modeling of the noise effects in the simulations is also discussed. Last, a short reference to the experiment with crab cavities at KEKB in Japan is also made.

Chapter 4 is devoted to the results of the first experimental studies of the emittance growth from CC RF noise in the SPS. The experimental configuration and procedure are reported and the artificial noise injected in the CC RF system for the measurements is discussed in detail. Subsequently, the emittance growth measurements are presented along with the measured bunch length and intensity evolution. Last the measured emittance growth rates are compared with the predictions from the Mastoridis–Baudrenghien theory. It was found that the measured growth rates were systematically a factor of 4 on average lower than the predictions.

Various possible factors were investigated as a possible explanation for this discrepancy. These studies are described in Chapter 5. Initially, parametric studies based on the theoretical model studied the sensitivity of the CC RF noise-induced emittance growth to possible uncertainties in the CC voltage amplitude and bunch length. The theory was also benchmarked with different simulation codes: PyHEADTAIL and Sixtracklib. The sensitivity of the emittance evolution on the non-linearities of the SPS machine (which is not included in the Mastoridis–Baudrenghien theory) was also tested. Finally, studies were performed to exclude the possibility that the discrepancy is not a result of the z-dependent orbit shift induced by the CC kick or the actual noise spectra applied on the CCs.

However, none of these factors could explain the discrepancy.

Finally, simulations including the SPS transverse impedance model (not included in the Mastoridis–Baudrenghien theory) showed a significant impact on the emittance growth. Chapter 6 discusses the investigation and characterisation of the phenomenon of the emittance growth suppression from the beam coupling impedance as observed in simulations with PyHEADTAIL. It was shown that the suppression is related to the dipole motion which is excited by the CC RF phase noise.

Chapter 7, presents the results from the experimental studies that took place in the SPS in 2022. The objective of this experimental campaign was to validate the mechanism of the suppression of the CC RF noise-induced emittance growth from the beam coupling impedance as observed in simulations (described in Chapter 6). This would also confirm that this impedance-induced effect is the reason for the discrepancy observed in the 2018 experiment between the measurements and the Mastoridis–Baudrenghien theoretical predictions. Despite the challenging conditions of the studies, the experiments of 2022 successfully confirmed the emittance growth suppression mechanism.

Last, Chapter 8 summarises the conclusions of the thesis. The project is viewed from a broad perspective highlighting its importance for the HL-LHC project.

2 | Basics of accelerator beam dynamics

In this chapter, the basic concepts of accelerator beam physics that are essential for understanding the studies presented in this thesis are introduced. A more complete description can be found in References: [28, 29, 30]. Additionally, in the last section, the tracking simulation codes used in this work are described.

Synchrotrons are circular accelerators in which electric fields accelerate the particles while magnetic fields steer and focus them. The magnetic fields are not constant but they vary according to the particles' energy, allowing acceleration and operation at very high (relativistic) energies. The LHC and SPS machines at CERN are synchrotrons like many of the machines used for High Energy Physics experiments. Usually, in synchrotrons, the beams consist of multiple bunches, longitudinally spaced around the machine. Although the bunches interact with each other, these interactions are not relevant to the studies presented later in this thesis, and will not be considered further

2.1 Electromagnetic fields in circular accelerators

The motion of a particle with charge q and velocity $\mathbf{v} = (v_x, v_y, v_z)$ moving in an electric field $\mathbf{E}$ and a magnetic field $\mathbf{B}$ is influenced by the Lorentz force [29]:

$$\mathbf{F}_L = q(\mathbf{E} + \mathbf{v} \times \mathbf{B}). \tag{2.1}$$

Note that in this thesis the vectors are denoted in bold font (e.g. $\mathbf{E}$).

From Eq. (2.1) it can be seen that the change of the kinetic energy is achieved only through the interaction with the electric field (due to the cross product of the

velocity and the magnetic field). The steering and the focusing of the charged particles can be achieved with both electric and magnetic fields. However, in the relativistic regime (which is the regime of interest for this thesis) the magnetic fields are typically used for guiding the particles since they become more efficient with increasing velocity of the particles [29].

The electric fields which are used for accelerating the beams are generated by radiofrequency (RF) cavities. The magnetic fields are used to steer (dipoles) and focus (quadrupoles) and apply corrections (sextupoles, octupoles, and higher-order multipoles) to the motion of the beam.

2.1.1 Co-ordinate system for the motion of charged particles in electromagnetic fields

The co-ordinate system used to describe the individual trajectories of the beam particles around the accelerator is illustrated in Fig. 2.1 and it is known as Frenet-Serret co-ordinate system. It consists of the orthogonal co-ordinate system $\Sigma(s) = (\mathbf{e_x}, \mathbf{e_y}, \mathbf{e_z})$ the origin of which moves along the reference trajectory (red line), which is the ideal path of a charged particle according to the design of the accelerator without imperfections.

In this co-ordinate system, the variable s denotes the distance along the reference trajectory. In accelerator physics, s is usually chosen as the independent variable instead of time, t. Therefore, at any given location s around the ring, the coordinates $(x(s), y(s), z(s))$ give the horizontal, vertical, and longitudinal position of the particle with respect to the origin of the orthogonal moving system Σ. In the following paragraphs, the dependence of the co-ordinates on the position s along the ring is omitted when possible to facilitate the notation (e.g. $x(s)$ will be denoted as x).

At any point s along the reference trajectory each particle is represented by the six-dimensional phase space vector $(x, x', y, y', z, \delta)$ where:
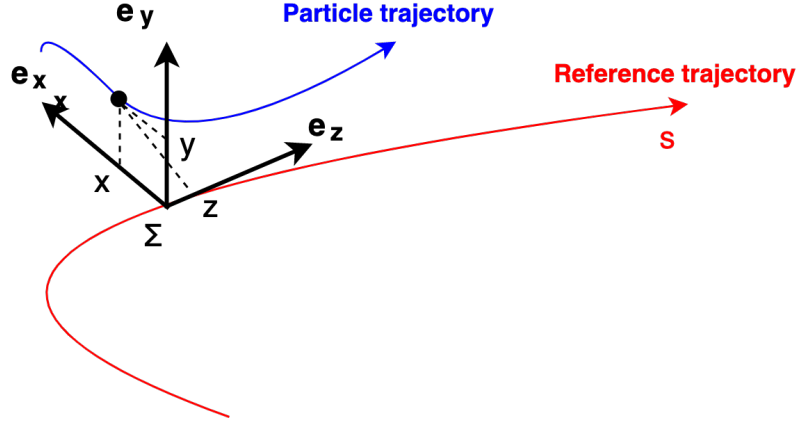
Figure 2.1: Co-ordinate system to describe particles' motion in a synchrotron. This is a local co-ordinate system, with the origin following the reference trajectory around the accelerator. The unit vector $\mathbf{e_z}$ is tangential to the reference trajectory at each point, $\mathbf{e_y}$ is vertical, and $\mathbf{e_x}$ is horizontal, and perpendicular to $\mathbf{e_z}$ and $\mathbf{e_y}$.

$$x' = \frac{dx}{ds} = \frac{dx}{dt}\frac{dt}{ds} = \frac{v_x}{v_z} = \frac{p_x}{p_z} \approx \frac{p_x}{p_0}, \tag{2.2a}$$

$$y' = \frac{dy}{ds} = \frac{dy}{dt}\frac{dt}{ds} = \frac{v_y}{v_z} = \frac{p_y}{p_z} \approx \frac{p_y}{p_0}, \tag{2.2b}$$

$$\delta = \frac{\Delta p}{p_0} = \frac{p - p_0}{p_0}, \tag{2.2c}$$

$$z = \beta_0 c(t_0 - t), \tag{2.2d}$$

where p_0 and β_0 are the momentum and relativistic (scaled) velocity, respectively, of the reference particle, t_0 is the time at which the reference particle arrives at the location s and t is the time at which the individual particle arrives at the same location. The parameter δ is the relative momentum offset from the reference particle. The longitudinal parameter z indicates the longitudinal offset from the reference particle at the centre of the bunch. If $z > 0$ ($z < 0$) the corresponding particle arrives earlier (later) than the centre of the bunch at an arbitrary reference point. In the ultra-relativistic regime the momentum of the particles in the $\mathbf{e_z}$ direction is much larger than the transvserse ones and almost equals the reference momentum: $p_x, p_y \ll p_z \approx p_0$. This is why the values of x' and y' are close to p_x/p_0 and p_y/p_0, respectively.

2. Basics of accelerator beam dynamics

Reference particle

The particle that follows the reference trajectory is called the reference particle and has momentum, p_0, energy E_0, and velocity v_0. This particle is often called the synchronous particle as it always passes from the centre of the RF cavities (assuming constant energy and no energy losses). For a proton, the reference momentum is defined by: $p_0 = \gamma_0 m_p v_0$, where m_p is the proton rest mass.

Beam rigidity

Assuming that a reference particle moves only under the influence of a uniform vertical dipole field $\mathbf{B}_{\text{dip}} = (0, B_1, 0)$, it would follow a circular path of local bending radius ρ which is defined by the Lorentz force (Eq. (2.1)) being equal to the centrifugal force, as follows [28]:

$$ev_0 B_1 = \frac{\gamma_0 m_p v_0^2}{\rho} \Rightarrow B_1 \rho = \frac{\gamma_0 m_p v_0}{e} \Rightarrow B_1 \rho = \frac{p_0}{e}, \tag{2.3}$$

where e and m_p are the charge and rest mass of a particle respectively, p_0 is the reference momentum, and γ_0, β_0 are the relativistic gamma and beta. The quantity, v_0, is the velocity of the reference particle.

The quantity $B_1 \rho$, is known as the beam rigidity and is often used in accelerators as a normalisation factor and is a measure of how the charged particles resist bending by a dipolar magnetic field.

Mulitpole fields

In high-energy synchrotrons, the magnetic field generated by the synchrotron magnets can usually be considered in "hard edge" approximation. In this case, the magnetic fields of various magnet types have purely transverse components and can be expressed through the following multipole expansion:

$$B_y(x, y) + i B_x(x, y) = \sum_{n=1}^{\infty} C_n (x + i y)^{n-1}, \tag{2.4}$$

where n indicates the order of the field component: n=1 for a dipole (steering), n=2 for quadrupole (focusing), n=3 for sextupoles (chromaticity correction), n=4 for octupole (error or field correction) etc, $C_n = (b_n + i a_n)$ is a complex constant which

denotes the strength and orientation of the multipole field. The coefficients $b_n = \frac{1}{(n-1)!} \frac{\partial^{n-1} B_y}{\partial x^{n-1}}$ and $a_n = \frac{1}{(n-1)!} \frac{\partial^{n-1} B_x}{\partial x^{n-1}}$ denote the strength of a normal and skew (normal multipole rotated by $\pi/2(n)$) multipole respectively.

In accelerator physics, the values of the multipole strengths are often quoted normalised to the magnetic rigidity as defined in Eq. (2.3) and are denoted by:

$$k_n = \frac{b_n}{B_1 \rho},$$
(2.5)

This is the convention that will be used in this thesis. By definition for a pure dipole vertical field $b_1 = B_1$.

2.2   Single-particle beam dynamics

In this section, the interactions between the particles within a bunch are neglected, hence the term single-particle beam dynamics.

2.2.1   Transvserse motion

In the transverse plane the motion is orthogonal to the reference trajectory (see Fig. 2.1) and its co-ordinates are (x, x', y, y'). For the discussion on the transverse beam dynamics, (u, u') will be used to notate either (x, x') or (y, y').

Here the transverse motion of a particle moving through the two-dimensional magnetic fields described in Eq. (2.4) is discussed. For now, the discussion is limited only to dipolar and quadrupolar components ($n = 1$ and $n = 2$) of the multipole expansion which are the basic magnetic elements of a synchrotron, providing bending and focusing of the particle beam.

As mentioned above, the particles transversely oscillate around the reference trajectory. This motion through a sequence of dipoles and quadrupoles, is called betatron motion and is described by the following equations of motion [30]:

$$x'' - \frac{\rho + x}{\rho^2} = -\frac{B_y}{B_1 \rho} \frac{p_0}{p} \left(1 + \frac{x}{\rho}\right)^2,$$
(2.6)

$$y'' = \frac{B_x}{B_1\rho}\frac{p_0}{p}\left(1+\frac{x}{\rho}\right)^2, \tag{2.7}$$

where $B_1\rho$ and ρ the magnetic rigidity and local bending radius as defined in Eq. (2.3), B_y, B_x the transverse magnetic fields of Eq. (2.4), and p_0 the reference momentum.

Since the amplitudes of the betatron oscillations are usually small, linear approximations in the above equations of motion provide good representations of the beam dynamics. Expanding Eqs. (2.6) and (2.7) up to the first order in x and y and taking into account the possible momentum deviation, δ, of particle we write [30]:

$$x'' + \left(\frac{1-\delta}{\rho^2(1+\delta)} + \frac{K_2(s)}{1+\delta}\right)x = \frac{\delta}{\rho(1+\delta)}, \tag{2.8}$$

$$y'' - \left(\frac{K_2(s)}{1+\delta}\right)y = 0, \tag{2.9}$$

where $\delta = (p - p_0)/p_0$ is the relative momentum offset from the reference particle, and $K_2 = B_2/(B_1\rho)$ is the focusing function. The sign-convention here is $K_2(s) > 0$ for focusing (defocusing) in the horizontal (vertical) and vertical plane.

Solutions for on-momentum particles

For on-momentum particles (with $\delta = 0$) these linear equations of motion can be simplified even more to the equation of motion for an harmonic oscillator (but with an s dependent strength $K_u(s)$), named Hill's equation [30]:

$$u''(s) + K_u(s)u(s) = 0, \tag{2.10}$$

where $u = (x, y)$ and:

$$K_u(s) = \begin{cases} \dfrac{1}{\rho^2(s)} + K_2(s), & u = x \\[2mm] -K_2(s), & u = y \end{cases} \tag{2.11}$$

It should be noted that for Eq. (2.10) it is assumed that the motion of the particle in the horizontal and vertical planes are independent, i.e. there is no transverse coupling.

For a circular accelerator K_u is periodic: $K_u(s + C_0) = K_u(s)$, where C_0 is the circumference of the accelerator. In this case, the solution of Eq. (2.10) resembles the one of a harmonic oscillator and can be written as [30]:

$$u(s) = \sqrt{2\beta_u(s)J_u}\cos(\psi_u(s) + \psi_{u,0}), \tag{2.12}$$

$$u'(s) = -\sqrt{\frac{2J_u}{\beta_u(s)}}(\sin(\psi_u(s) + \psi_{u,0}) + \alpha_u(s)\cos(\psi_u(s) + \psi_{u,0})), \tag{2.13}$$

where J_u and $\psi_{u,0}$ are the constants of integration and are determined by the chosen initial conditions, $\alpha_u(s) = -\frac{1}{2}\beta'_u(s)$ and $\beta_u(s)$ are periodic function determined by the sequence of the quadrupole magnets in the accelerator and follow the periodicity of the machine. Equation (2.12) shows that a stable particle[1]undergoes transverse oscillations around the reference trajectory, which are referred to as betatron oscillations. Since the J_u is constant, the beta function determines the maximum amplitude of the single particle trajectory at any given position s in the ring. The function $\psi_u(s)$ is the betatron phase advance from the position $s = 0$ to s and equals:

$$\psi_u(s) = \int_0^s \frac{ds}{\beta_u(s)}. \tag{2.14}$$

Betatron tune

The phase advance for one complete revolution around the machine divided by 2π defines the betatron tune, Q_u:

$$Q_u = \frac{\psi_u(s + C_0) - \psi_u(s)}{2\pi} = \frac{1}{2\pi}\oint_{C_0} \frac{ds}{\beta_u(s)}, \tag{2.15}$$

where C_0 is the circumference of the machine. The betatron tune represents the number of betatron oscillations that a particle performs during one full revolution around the machine.

The tune of the individual particles may vary due to effects such as the chromaticity,

---

[1]The condition for a particle motion to be stable is expressed quantitatively in terms of the transfer matrix as: $|\mathrm{Tr}M_u| \leq 2$, where M_u is the transfer matrix as defined in Eq. (2.29) for one periodic section of the machine lattice, assuming zero coupling [28].

the detuning with their transverse amplitude, and collective forces (e.g. impedance) that will be discussed in the following paragraphs. The horizontal and vertical tune of the reference particle will be referred to as the bare tunes and define what is called the working point of the machine, (Q_{x0}, Q_{y0}).

Courant-Snyder ellipse

Inserting $\cos(\psi_u(s) + \psi_{u,0}) = u(s)/(\sqrt{\beta_u(s) J_u})$ from Eq. (2.12) to Eq. (2.13) it is found that:

$$J_u = \frac{1}{2}(\gamma_u(s) u^2(s) + 2\alpha_u(s) u(s) u'(s) + \beta_u(s) u'^2(s)), \qquad (2.16)$$

where $\gamma_u(s) = \frac{1 + \alpha_u(s)^2}{\beta_u(s)}$. Equation (2.16) describes an ellipse in phase space (u, u') at any given position s in the ring. This ellipse is known as phase space or Courant-Snyder ellipse and is illustrated in Fig. 2.2. The parameter J_u is also known as action or the Courant-Snyder invariant. The parameters $\alpha_u(s), \beta_u(s)$, and $\gamma_u(s)$ are the Courant-Snyder or the Twiss parameters and they define the shape and the orientation of the ellipse. The centre of the ellipse is the closed orbit which, in the absence of steering errors in a synchrotron, can be identified with the reference trajectory and is also shown in the plot. The area of the phase space ellipse as defined here equals: $2\pi J_u$ and remains the same at any given location s.

The trajectory of each individual particle turn after turn follows the phase space ellipse described by Eq. (2.16) at any given position s. It is worth mentioning, that the ellipse's size is different for each particle as it depends on their individual actions, J_u.

Transvserse emittance

Up to now, the Twiss parameters were used to describe the dynamics of single particles. However, they can also describe the distribution of the particles within a bunch. The statistical average of u^2 over all particles at a given point s along the reference trajectory, from Eq. (2.12) equals to [28]:

$$\langle u^2(s) \rangle = 2\beta_u(s) \langle J_u \cos^2 \psi_u(s) \rangle. \qquad (2.17)$$
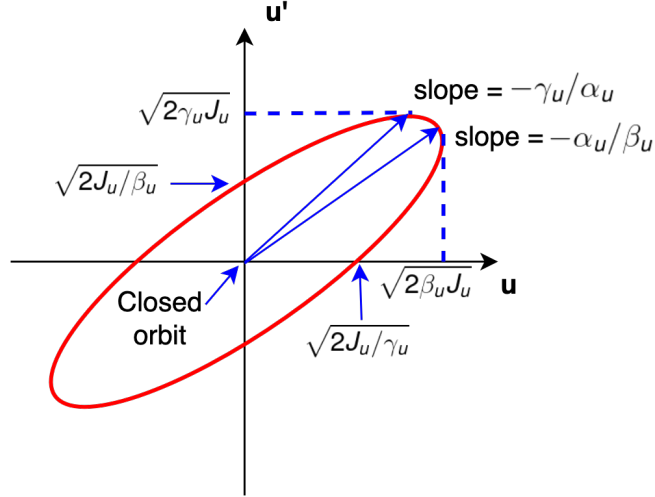
Figure 2.2: Phase space co-ordinates (u, u') turn by turn, for a particle moving along the ring but at a particular position s which is characterised by the following twiss parameters $[\alpha_u(s), \beta_u(s), \gamma_u(s)]$.

Assuming that the angle and action variables are uncorrelated Eq. (2.17) becomes [28]:

$$\langle u^2(s) \rangle = 2\beta_u(s) \langle J_u \rangle \langle \cos^2 \psi_u(s) \rangle. \tag{2.18}$$

Considering that the angle variables are uniformly distributed from 0 to 2π [28]:

$$\langle \cos^2 \psi_u(s) \rangle = \int_{s_0}^{s_0+C_0} \cos^2 \psi_u(s) ds = \int_0^{2\pi} \cos^2 \psi_u(\phi) d\phi = \frac{\pi}{2\pi} = \frac{1}{2}, \tag{2.19}$$

where for the integration the phase advance ϕ is used instead of the location s along the ring for convenience.

Inserting Eq. (2.19) in Eq. (2.17) gives [28]:

$$\langle u^2(s) \rangle = \beta_u(s) \epsilon_u^{\text{geom}}, \tag{2.20}$$

where

$$\epsilon_u^{\text{geom}} = \langle J_u \rangle \tag{2.21}$$

is the geometric emittance of the bunch. Assuming again that the action and angle variables are uncorrelated and that the latter are uniformly distributed from 0 to 2π,

Eq. (2.12) and Eq. (2.13) results to [28]:

$$\langle u(s)u'(s)\rangle = -\alpha_u(s)\epsilon_u^{\text{geom}}, \tag{2.22}$$

$$\langle u'^2(s)\rangle = \gamma_u(s)\epsilon_u^{\text{geom}}. \tag{2.23}$$

Combining the above equations, the geometric emittance is expressed in terms of the particles' distribution as [28]:

$$\epsilon_u^{\text{geom}} = \sqrt{\langle u^2(s)\rangle\langle u'^2(s)\rangle - \langle u(s)u'(s)\rangle^2} \tag{2.24}$$

For a Gaussian distribution with $\langle u\rangle = 0$, Eq. (2.20) becomes [28]:

$$\sigma_u(s) = \sqrt{\beta_u(s)\epsilon_u^{\text{geom}}}, \tag{2.25}$$

where σ_u is the transverse rms beam size. Note that Eq. (2.25) is also valid for a distribution with $\langle u\rangle \neq 0$. The ϵ_u^{geom} is often called the rms emittance since it is the contour that encloses one standard deviation of the particles' distribution in phase space.

An alternative definition of the rms emittance is introduced below based purely on the beam distribution, and in particular on the covariance matrix (see Eq. (A.11)) of its second order moments:

$$\Sigma = \begin{pmatrix} \text{Cov}(u,u) & \text{Cov}(u,u') \\ \text{Cov}(u,u') & \text{Cov}(u',u') \end{pmatrix} = \begin{pmatrix} \sigma_u^2 & \text{Cov}(u,u') \\ \text{Cov}(u,u') & \sigma_{u'}^2 \end{pmatrix}, \tag{2.26}$$

where $\text{Cov}(u,u')$ the covariance between the position u and the angle u' as defined in Eq. (A.9), σ_u and σ_u' the standard deviation of u and u' respectively. The rms emittance is the determinant of the matrix of Eq. (2.26):

$$\epsilon_u^{\text{geom}} = \sqrt{\det\Sigma}. \tag{2.27}$$

It is worth noting that for the simulation studies presented in this thesis, the

emittance is computed using the statistical definition introduced in Eq. (2.27). In the experimental studies, the emittance is obtained from the rms beam size at a point in the beamline where the beta function is known following Eq. (2.25). These two methods of computing the emittance are considered equivalent for the studies presented in this thesis.

According to Liouville's theorem [28], assuming that there are no interactions between the particles and that the energy of the beam is not changing, the geometric emittance remains constant and therefore is an invariant of bunch motion (similarly to the action J_u for the single-particle motion). The geometric emittance does not remain constant during acceleration. Instead, the normalised emittance defined as [28]:

$$\epsilon_u = \beta_0 \gamma_0 \epsilon_u^{\text{geom}}, \tag{2.28}$$

is conserved during acceleration and is often used as an alternative to the geometric emittance, especially in situations where the beam undergoes acceleration or deceleration. It is highlighted here, that throughout this thesis the term "emittance" will refer to the rms normalised emittance.

Despite Liouville's theorem, in a real accelerator there are various phenomena that change the emittance, such as [31]: scattering by residual gas, intra-beam scattering, stochastic or electron cooling, synchrotron radiation emission, filamentation due to non-linearities of the machine, space charge and noise effects. The studies in this thesis focus on the emittance growth due to noise effects.

Transfer maps and linear transfer matrix

The motion of the particles through accelerator components can be represented by transfer maps. A transfer map is a set of functions that yields the final set of phase space coordinates as a function of the initial one. The transfer maps can be found from the equations of motion, which can be obtained from Hamilton's equations. For each component, the Hamiltonian that describes its full dynamics is used. Further details on this approach can be found in [28].

The transfer maps of the linear magnetic elements, such as dipoles and quadrupoles

can be written in terms of matrices. The Twiss parameters can be used to describe the linear transport of a particle in the accelerator from the position s_0 to the s_1 using the matrix formalism as follows [30]:

$$\begin{pmatrix} u \\ u' \end{pmatrix}_{s_1} = M_u(s_1|s_0) \begin{pmatrix} u \\ u' \end{pmatrix}_{s_0}, \tag{2.29}$$

where $u = (x, y)$. The linear transfer matrix from the position s_0 to the s_1, $M_u(s_1|s_0)$, can be expressed in terms of the Courant-Snyder parameters as [30]:

$$
\begin{aligned}
M_u(s_1|s_0) &= \begin{pmatrix} \sqrt{\dfrac{\beta_u(s_1)}{\beta_u(s_0)}}(\cos\Delta\psi_u + \alpha_u(s_0)\sin\Delta\psi_u) & \sqrt{\beta_u(s_0)\beta_u(s_1)}\sin\Delta\psi_u \\ -\dfrac{1+\alpha_u(s_0)\alpha_u(s_1)}{\sqrt{\beta_u(s_0)\beta_u(s_1)}}\sin\Delta\psi_u + \dfrac{\alpha_u(s_0)-\alpha_u(s_1)}{\sqrt{\beta_u(s_0)\beta_u(s_1)}}\cos\Delta\psi_u & \sqrt{\dfrac{\beta_u(s_0)}{\beta_u(s_1)}}(\cos\Delta\psi_u + \alpha_u(s_1)\sin\Delta\psi_u) \end{pmatrix} \\
&= \begin{pmatrix} \sqrt{\beta_u(s_1)} & 0 \\ -\dfrac{\alpha_u(s_1)}{\sqrt{\beta_u(s_1)}} & \dfrac{1}{\beta_u(s_1)} \end{pmatrix} \begin{pmatrix} \cos\Delta\psi_u & \sin\Delta\psi_u \\ -\sin\Delta\psi_u & \cos\Delta\psi_u \end{pmatrix} \begin{pmatrix} \dfrac{1}{\sqrt{\beta_u(s_0)}} & 0 \\ \dfrac{\alpha_u(s_0)}{\sqrt{\beta_u(s_0)}} & \sqrt{\beta_u(s_0)} \end{pmatrix},
\end{aligned}
$$

$$\tag{2.30}$$

where $\Delta\psi_u = \psi_u(s_1) - \psi_u(s_0)$ is the betatron phase advance between the two locations, while $\alpha_u(s_i)$ and $\beta_u(s_i)$ are the Twiss parameters at the location s_i, where $i = (0,1)$. Transfer matrices provide a very convenient approach to accelerator beam dynamics, and they will be used extensively throughout this thesis to study the motion of the particles in the accelerator lattice.

Off-momentum effects: dispersion

Up to now, the discussion was limited to on-momentum particles $\delta = 0$: their momenta equals the reference momentum, p_0. In a real beam, however, the momenta of the individual particles are spread around the reference momentum, p_0. The "momentum spread" is described by the rms momentum deviation, σ_δ. For reference, for the studies in the SPS machine presented in this thesis, σ_δ is in the order of magnitude of 10^{-4} to 10^{-3}. Particles with $\delta < 0$ ($\delta > 0$) are deflected stronger (less) by the dipole magnets than the reference particle due to lower (higher) magnetic rigidity.

For the off-momentum particles the solutions of Eq. (2.8) have the following form:

$$x(s) = x_H(s) + x_D(s), \tag{2.31}$$

where $x_H(s)$ is the solution shown in Eq. (2.12) for $u = x$ and corresponds here to betatron oscillations around the on-momentum closed orbit. The function $x_D(s) = D_x(s)\delta$ defines the off-momentum closed orbit.

The parameter $D_x(s)$ is the dispersion function which can be expressed as:

$$D_x''(s) + K_x(s)D_x(s) = \frac{1}{\rho(s)}, \tag{2.32}$$

where $K_x(s) = \frac{1}{\rho^2(s)} + k_2(s)$ like in Eq. (2.11). As an example, the rms horizontal dispersion of the SPS machine is about 1.8 m (model value). The dispersion introduces a coupling between the longitudinal and transverse planes. Here the discussion is limited to the horizontal plane since typically only vertical dipolar fields are considered in a synchrotron[2].

Particles with non-zero δ travel along the accelerator performing betatron oscillations not around the reference trajectory but around a different closed orbit as illustrated in Fig. 2.3 which depends on their momentum deviation, δ.
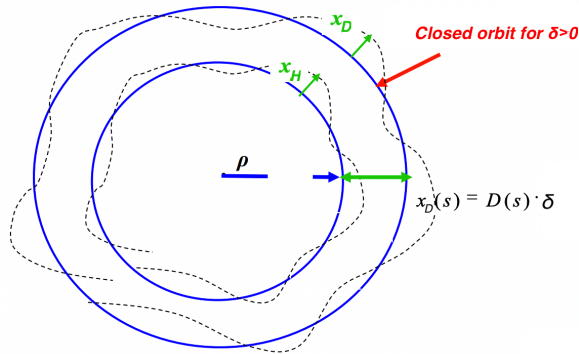
Figure 2.3: The closed orbit and the betatron oscillations around it in the presence of dispersion [32]

For Gaussian beam distributions with $\langle\delta\rangle = 0$, the rms beam size defined in Eq. (2.25) can be re-written so that it includes the dispersive contribution as

---

[2]A corresponding discussion can be done for the vertical plane to obtain the vertical dispersion but it is out of the scope of this thesis.

follows [28]:

$$\sigma_x(s) = \sqrt{\beta_x(s)\epsilon_x^{\text{geom}} + D_x(s)^2\sigma_\delta^2}. \tag{2.33}$$

In a real machine, vertical dispersion can be introduced by sources such as steering errors of the dipole or quadrupole magnets [33]. For reference, the rms vertical dispersion in the SPS machine is measured to be about 10 cm. Note that the above analysis is valid also for the vertical plane.

Off-momentum effects: chromaticity

Additionally, off-momentum particles receive different focusing in the quadrupoles. This effect is known as chromaticity and is defined as the variation of the betatron tune Q_u with the relative momentum deviation δ. This is a result of the fact that particles with $\delta < 0$ ($\delta > 0$) are focused more (less) strongly from the quadrupoles due to their smaller (larger) magnetic rigidity. The tune shift introduced by the chromaticity for each particle, $\Delta Q_u(\delta) = Q_u - Q_{u0}$, is:

$$\Delta Q_u(\delta) = \sum_{n=1}^{m} \frac{1}{n!} Q_u^{(n)} \delta^n, \tag{2.34}$$

where:

$$Q_u^{(n)} = \left.\frac{\partial^n Q_u}{\partial \delta^n}\right|_{\delta=0}, n \in \mathbb{N}, \tag{2.35}$$

denotes the chromaticity of order n. The studies in this thesis, are limited to the chromaticity at the first order in δ ($n = 1$) which is often called linear chromaticity. For the linear chromaticity the parameter Q_u' is also often used. Note that the betatron tune shift of Eq. (2.34) is referred to as an "incoherent" tune shift, since each particle is affected differently, depending on its individual momentum deviation. Similarly to the tune, the chromaticity is a property of the machine lattice.

The linear chromaticity can be controlled with the use of sextupole families, which are typically placed in high dispersion regions, as follows [28]:

$$Q_x' = -\frac{1}{4\pi} \int_{s_0}^{s_0+C_0} \beta_x(k_1 + D_x k_2)ds, \tag{2.36}$$

and

$$Q'_y = \frac{1}{4\pi} \int_{s_0}^{s_0+C_0} \beta_y (k_1 + D_x k_2) \, ds, \tag{2.37}$$

for the horizontal and vertical planes, respectively. Note that the first terms, proportional to k_1 correspond to the natural chromaticity generated by the quadrupole magnets, while the second terms correspond to the chromaticity correction induced by the sextupoles.

Octupole magnets

The octupole plays an important role in the studies of the thesis. The transfer map for an octupole is:

$$\Delta x' = -\frac{1}{6} k_3 L_3 (x^3 - 3xy^2), \tag{2.38}$$

$$\Delta y' = -\frac{1}{6} k_3 L_3 (y^3 - 3yx^2), \tag{2.39}$$

where $k_3 L_3$ is the integrated strength of the octupole of length L_3. Equations (2.38) and (2.39) are valid for the thin lens approximation. In that case, the rest of the co-ordinates (x, y, z, δ) do not change as the particle passes through the magnet.

As described in Chapter 10 of [34] the term $-\frac{1}{6} k_3 L_3 u^3$, with $u = (x, y)$, introduces an additional phase advance in the motion of each particle, which eventually over one turn is translated to a change in their tune given by [34]:

$$\Delta Q_u = \frac{1}{16\pi} k_3 L_3 \beta_u(s)^2 J_u. \tag{2.40}$$

It can be seen that a different change in the tune is introduced for each particle depending on their individual action, J_u. Note, that the above change of the tune is a result of a single octupole around the machine at a location s and beta function $\beta_u(s)$.

This property, of providing incoherent betatron tune spread in a controlled way is used extensively in this thesis. For reference, the octupole magnets are typically used to increase the transverse tune spread of the beam particles to avoid instability effects[3].

---

[3]Beam instabilities in an accelerator are a result of the interplay of the wakefields (introduced in Section 2.3) and a perturbation (e.g. noise) on equations of motion of the beam particles. Their

In the SPS and LHC rings, the octupoles are installed in families (called focusing and defocusing) in order to avoid the excitation of resonances[4]. They are usually referred to as "Landau octupoles" since they are used to create a betatron tune spread that provides the mechanism of Landau damping [36] (to stabilise the beam).

The general formula which describes the linear betatron detuning with transverse amplitude introduced by multiple octupoles around the machine is [37]:

$$\Delta Q_x(J_x, J_y) = 2(\alpha_{xx} J_x + \alpha_{xy} J_y), \tag{2.41}$$

$$\Delta Q_y(J_x, J_y) = 2(\alpha_{yy} J_y + \alpha_{yx} J_x), \tag{2.42}$$

where α_{xx}, α_{yy} and $\alpha_{xy} = \alpha_{yx}$ are the detuning coefficients. The detuning coefficients depend on the octupoles' strength and the beta functions at their location [37]. Note that the detuning with the transverse action (or amplitude) is an incoherent effect as it depends on the individual action of each particle.

2.2.2 Longitudinal motion

In the longitudinal plane, the motion is parallel to the reference trajectory and is described by the co-ordinates (z, δ). In the next paragraphs, the discussion is limited to the longitudinal motion in a synchrotron storage ring operating at the ultra-relativistic regime (like the machines of interest in this thesis) and only to the concepts that are needed for understanding the studies. The discussion in this section is more limited than for the transverse motion since the work presented in the thesis mostly concerns transverse beam dynamics. A complete discussion can be found in Chapter 9 of [29] and in [28].

Revolution period and frequency

The time that the reference or synchronous particle needs to complete one complete revolution around the accelerator is called the revolution period, T_{rev}.

---

detailed study is out of the scope of this thesis, however, more details can be found in [35].

[4]Resonances in circular accelerators are a result of perturbation terms in the equation of motion once the perturbation frequency matches the frequency of the particles' oscillatory motion. The topic of resonances is out of the scope of this thesis, however, more details can be found in Chapter 16 of [29].

The revolution frequency is $\omega_{\text{rev}} = 2\pi/T_{\text{rev}}$ or $f_{\text{rev}} = 1/T_{\text{rev}} = v_0/C_0 = \beta_0 c/C_0$, where v_0 is the speed of the reference particle, β_0 the relativistic beta, c the speed of light and C_0 the circumference of the accelerator.

Equations of motion

In a synchrotron storage ring, the motion in the longitudinal plane is controlled by the RF cavities. They provide a longitudinal electric field, which can be described by:

$$E_{\text{RF}}(z) = E_A \sin(2\pi f_{\text{RF}} z + \phi_s), \tag{2.43}$$

where E_A is the amplitude of the electric field, f_{RF} is the frequency of the RF system, and ϕ_s is the phase of the synchronous or reference particle.

The frequency of the RF field needs to be synchronous with the revolution frequency, such that the synchronous particle arrives with the same phase at the cavity again after one turn. Therefore the frequency of the RF field is a multiple of the revolution frequency: $\omega_{\text{RF}} = h2\pi f_{\text{rev}}$. The parameter h (number of RF cycles per revolution) is called the harmonic number and defines the number of stable synchronous particle locations in the ring [38].

The RF cavities provide a change in the energy deviation of the individual particles as a function of their longitudinal position z within the bunch ($z = 0$ the location of the synchronous particle and $z > 0$ the head of the bunch). The equations of motion for a particle passing through a system of synchronised RF cavities located around the accelerator in the ultra-relativistic regime can be expressed as [28]:

$$z' = \frac{dz}{ds} = -\eta_p \delta, \tag{2.44}$$

$$\delta' = \frac{d\delta}{ds} = -\frac{qV_{\text{RF}}}{cp_0 C}\left(\sin\phi_s - \sin\left(\phi_s - \frac{\omega_{\text{RF}} z}{c}\right)\right). \tag{2.45}$$

Equation (2.44) assumes that we can average the change of the z co-ordinate over the circumference of the machine. This approximation is valid for slow synchrotron motion compared to the revolution period and for small oscillation amplitude compared to the RF wavelength[28].

Equation (2.45) assumes that the energy deviation, $\delta_E = \frac{E - E_0}{E_0} \approx \delta$. This approximation is valid for particles with small momentum deviation and for machines operating at the ultrarelativistic regime [28].

The parameter η_p is called phase split factor and describes the relative change in the revolution frequency of a particle with respect to its momentum spread and can be written as:

$$\eta_p \equiv \frac{\Delta f / f_{\text{rev}}}{\delta},\tag{2.46}$$

where Δf is the change of the revolution frequency of each individual particle. Further details can be found in [28].

Synchrotron oscillations

Following the above-described equations of motion, the off-momentum particles will perform oscillations around a stable location in the longitudinal plane. They are also known as synchrotron oscillations and are typically orders of magnitude slower than the betatron oscillations. For example, a complete synchrotron oscillation may take many ($\sim$100) turns, in contrast to the betatron oscillations (of which there are usually many complete oscillations per turn).

The possible stable locations around which the synchrotron oscillations are performed are defined by the harmonic number h. The set of particles that oscillate around the same stable point will be referred to as a "bunch". Note that the harmonic number h defines the maximum number of bunches that can be stored in the ring.

Synchrotron tune

The synchrotron tune, Q_s, is defined as the number of synchrotron oscillations performed during one complete revolution around the machine and is computed as follows [28]:

$$Q_s = \frac{1}{2\pi}\sqrt{-\frac{eV_{\text{RF}}}{cp_0}\frac{\omega_{\text{RF}}C_0}{c}\eta_p\cos\phi_s}.\tag{2.47}$$

2.3 Collective effects: Wakefields

Up to now, the motion of the particles was studied neglecting the interaction between them within the bunch. Collective effects in an accelerator describe the phenomena in which the motion of the particles depends on their interaction with each other through electromagnetic fields. Examples are beam-beam interactions, space charge effects, wakefields, and intra-beam scattering [39]. The collective effects usually become critical for high-intensity beams as they can lead to instabilities[5] which then may degrade beam quality, or lead to beam losses. In either case, the performance of the accelerator can be adversely affected. The discussion here is limited to the description of the wakefields which are relevant for the studies presented in this thesis. A complete overview of the collective effects can be found in [28, 39, 40].

For the following discussion, it is appropriate to introduce the terms incoherent and coherent effects. Incoherent effects (microscopic approach) affect the individual particles. Any theory or model of incoherent effects has to treat the beam as a collection of a large number of individual particles, each with its own behaviour. In contrast, coherent effects can be understood in terms of their impact on the beam as a whole.

Wakefields

The charged particles within a beam interact electromagnetically with their surroundings in the beam pipe such as the resistive vacuum pipe walls, the RF cavities, etc. If these structures are not smooth (presence of discontinuities) or not perfectly conducting the interaction with the charged particles will result in electromagnetic perturbations called wakefields. The wakefields act back on the beam affecting the beam dynamics.

The longitudinal and transverse wakefields can often be treated separately. In the following only the transverse components will be discussed as the focus of the thesis is on the transverse beam dynamics.

---

[5]For example a beam is unstable when one of its co-ordinates $(x, x', y, y', z, \delta)$ undergoes exponential growth. Further details on the beam instabilities can be found in [35]

Consider two particles of charge q_1 and q_2 moving with ultra-relativistic speed through a structure of length L as shown in Fig. 2.4. The particle of charge q_1 is the source particle while the witness particle[6] of charge q_2 travels behind it at a constant distance z. $(\Delta x_1, \Delta y_1)$ are the transverse offsets of charge q_1, and $(\Delta x_2, \Delta y_2)$ are the transverse offsets of charge q_2 from the symmetric axis of the beam pipe. From the interaction of the source particle with the structure a wakefield is generated.
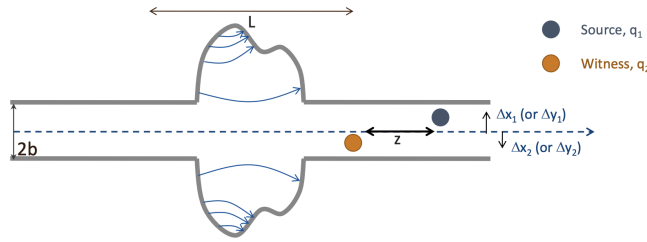
Figure 2.4: Wakefield interaction, where the source particle (blue) affects the witness particle (yellow) travelling at a distance z behind it [41]. $(\Delta x_1, \Delta y_1)$ and $(\Delta x_2, \Delta y_2)$ are the transverse offsets of the source and witness particles respectively.

The wakefields in the time domain are described with the concept of wakefunctions, $W_u(z)$, where $u = (x, y)$ denotes the horizontal and vertical plane, respectively. The wakefunction can be expressed as a series of its multipole components as follows:

$$W_u(\Delta u_1, \Delta u_2, z) = W_u^{\text{const}}(z) + W_u^{\text{dip}}(z)\Delta u_1 + W_u^{\text{quad}}(z)\Delta u_2 + o(\Delta u_1, \Delta u_2), \quad (2.48)$$

where $u = (x, y)$ and $W_u^{\text{const}}(z)$, $W_u^{\text{dip}}(z)$, $W_u^{\text{quad}}(z)$ are the transverse constant, dipolar, and quadrupolar wakefunctions respectively. The higher order term $o(\Delta u_1, \Delta u_2)$ is not considered in the work presented here.

The dipolar and quadrupolar wakefunctions were named after the way they act on the witness particle. The dipolar wakefunction acts like a dipole magnet: its impact is the same regardless of the transverse position of the witness particle; it depends only on the position of the source particle. The quadrupolar wakefunction acts like a quadrupole magnet: its impact increases linearly with the transverse position of the witness particle (independent of the .position of the source particle).

---

[6]In studying collective effects, the terms "source particle" and "witness particle" are sometimes used for particles generating wakefields and particles affected by the wakefields, though in reality all charges act as sources of wakefields, and are affected by them

The constant term can change the closed orbit while the dipolar and quadrupolar terms can modify the tunes [42]. The dipolar term is often referred to as a driving term for coherent instabilities. The quadrupolar term is often referred to as the detuning term as it modifies the betatron frequencies of individual particles.

The effect of the wakefields on the witness particles can be modeled as the following kicks on the transverse normalised momentum [43]:

$$\Delta u_2' = -q_1 q_2 [W_u^{\text{const}}(z) + W_u^{\text{dip}}(z)\Delta u_1 + W_u^{\text{quad}}(z)\Delta u_2], \qquad (2.49)$$

If the structure leading to the wakefield is axially symmetric, then the constant term of the wakefunction is zero.

Note that in the ultrarelativistic regime (which is the regime of the work presented in this thesis) the wakefields from a source particle act only on the particles behind it, hence the term "wake". Wakefields can also act back on the charge generating them when that charge returns to a given location in a storage ring over successive turns.

Beam coupling impedance

The beam coupling impedance is the frequency spectrum of the wakefields in a given component or section of the accelerator. The impedance can be obtained from the wake function through a Fourier transform [40]:

$$W_u(z) = -\frac{i}{2\pi} \int_{-\infty}^{+\infty} Z_u(\omega) e^{i\omega z/c} d\omega, \qquad (2.50)$$

$$Z_u(\omega) = \frac{i}{c} \int_{-\infty}^{+\infty} W_u(z) e^{-i\omega z/c} dz, \qquad (2.51)$$

where $u = (x, y)$, i is the imaginary unit and c is the speed of light.

In order to study the beam dynamics effects due to wakefields, impedance models of the particle accelerators have been developed (using both measurements and electromagnetic simulations) including the contributions from the individual elements in the accelerator. Details on how an impedance model is built can be found in [42].

Head-tail modes

The Vlasov equation [44] is often used to describe the beam motion in the presence of wakefields as it allows its mode representation (in frequency domain): the beam motion is described by a superposition of modes. Solving the Vlasov equations for the coupled system between the particle motion (synchrotron and betatron) and wakefield kicks the eigenmodes and eigenfrequencies are obtained. These modes are often referred to as head-tail modes as they are related to the betatron phase shift between the head and tail of the bunch in a synchrotron. The head-tail modes can either be stable, damped, or excited; in the latter case, they evolve into instabilities. For the beam to become unstable the wakefield kicks (source of energy) need to be synchronized with the bunch motion (e.g. with chromaticity) [41].

The head-tail modes can be described with the mode indices m and l which denote the transverse and the longitudinal (or azimuthal) mode numbers [40]. In the following, modes with $m = 1$ will be considered and they are often referred to as transverse modes [40]. Figure 2.5 shows a graphical representation of the azimuthal modes for $m = 1$.
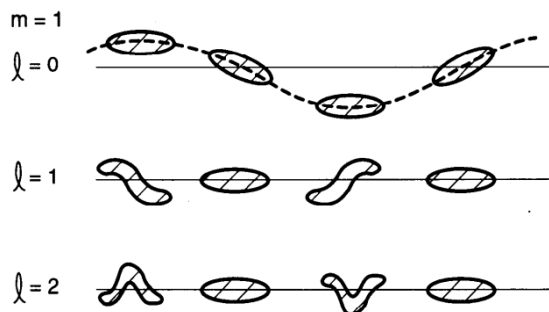
Figure 2.5: Graphical representation of the lowest azimuthal modes in the longitudinal beam structure, for $m = 1$ as the bunch oscillates transversely [40]. The x-axis represents time.

In this thesis, the terms "mode" or "head-tail mode" will refer to the azimuthal modes[7].

As shown in Fig. 2.5 for the head-tail mode 0 ($l = 0$), the bunch moves transversely as a rigid unit or the head-tail mode 1 ($l = 1$), the bunch oscillates transversely but

---

[7]The modes' radial structure in the longitudinal plane is described by their radial modes [40]. They are not considered nor discussed here as they are out of they are beyond the scope of the work presented in this thesis.

the head and the tail of the bunch move 180° out of phase.

Sacherer formulae and complex coherent frequency shift

One of the impedance-induced effects, that is relevant for the studies of the thesis, is the complex tune shift. The complex tune shift can be computed analytically based on the Vlasov formalism [44] through the use of perturbation theory. Formulae expressing the results were derived by Sacherer [45, 46].

The head-tail modes introduce an exponential dependence on the amplitude of the bunch centroid as follows [43]:

$$u(t) \propto e^{i(\Omega_{u0}^{(l)}+\Delta\Omega_u^{(l)})t} = e^{i(\Omega_{u,0}^{(l)}+\Delta\Omega_{u,\mathrm{re}}^{(l)})t} e^{-\Delta\Omega_{u,\mathrm{im}}^{(l)}t}, \qquad (2.52)$$

where $\Omega_{u0}^{(l)}$ is the real-valued, unperturbed frequency of the head-tail mode l, and $\Delta\Omega_u^{(l)} = \Delta\Omega_{u,\mathrm{re}}^{(l)} + i\Delta\Omega_{u,\mathrm{im}}^{(l)}$ is the complex coherent frequency shift introduced by the beam impedance. From Eq. (2.52) it can be seen that the real part $\Delta\Omega_{u,\mathrm{re}}^{(l)}$ modifies the oscillation frequency. The second term $e^{-\Delta\Omega_{u,\mathrm{im}}^{(l)}t}$ illustrates that the amplitude of the motion grows for $\Delta\Omega_{u,\mathrm{im}}^{(l)} < 0$ (unstable bunch) and is damped for $\Delta\Omega_{u,\mathrm{im}}^{(l)} > 0$ (stable bunch).

The complex coherent frequency shift for the mode l for a bunched beam is (Chapter 6 in. [40]):

$$\Delta\Omega_u^{(l)} = \Omega_{u0}^{(l)} - \omega_{u0} - l\omega_s = -\frac{1}{4\pi}\frac{\Gamma(l+1/2)}{2^l l!}\frac{N_b r_0 c^2}{\gamma_0 T_{\mathrm{rev}}\omega_{u0}\sigma_z}iZ_{\mathrm{eff}}, \qquad (2.53)$$

where ω_{u0} and ω_s are the unperturbated betatron and synchrotron frequencies, $\Gamma(x)$ is the gamma function, N_b is the number of particles in the bunch, $r_0 = 1.535 \cdot 10^{-16}$ cm is the clasical radius of the proton, c is the speed of light, γ_0 is the relativistic gamma, T_{rev} is the revolution period, σ_z is the rms bunch length, i is the imaginary unit and Z_{eff} is the effective impedance.

The effective impedance expresses the effect of the impedance defined in Eq. (2.51) on the beam dynamics. The effective impedance Z_{eff} can be computed as

follows [40]:

$$Z_{\perp\text{eff}}^{(l)} = \frac{\sum_{p=-\infty}^{+\infty} Z_{\perp}^{(l)}(\omega_p) h_l(\omega_p - \omega_\xi)}{\sum_{p=-\infty}^{+\infty} h_l(\omega_p - \omega_\xi)}, \tag{2.54}$$

where $\omega_p = (p + Q_u)\omega_{\text{rev}}$ is the discrete spectrum of the transverse bunch oscillations with $-\infty < p < +\infty$ for a single bunch (which is the case in the following studies) or several bunches oscillating independently and $\omega_\xi = Q_u'\omega_{\text{rev}}/\eta_p$ is the chromatic angular frequency with η_p being the phase slip factor.

Last, h_l, is the power spectral density (definition in Appendix B) of a Gaussian bunch of l azimuthial mode. h_l is described by:

$$h_l(\omega) = (\omega \sigma_z/c)^{2l} e^{-(\omega \sigma_z/c)^2}, \tag{2.55}$$

where σ_z is the rms bunch length and c the speed of light.

It should be highlighted that all the parameters inserted in Eq. (2.53), Eq. (2.54) and Eq. (2.55) should be converted in CGS (centimetre–gram–second) units. For the conversion from SI to CGS system the following relations are useful:

$$1[\Omega] = \frac{1}{9} \cdot 10^{-11}[\text{s}]/[\text{cm}], \tag{2.56}$$

where Ω (Ohm) is the SI unit of resistance.

Finally, the imaginary part of the impedance, leads to a real coherent frequency shift which can be expressed in tune units as follows [47]:

$$\Delta Q_u^{(l)} = \frac{\Delta\Omega_{u,\text{re}}^{(l)}}{\omega_{\text{rev}}}, \tag{2.57}$$

where $\Delta\Omega_{u,\text{re}}^{(l)}$ the real part of the complex tune shift as defined in Eq. (2.53). The real part of the impedance, leads to an imaginary coherent frequency shift which is also known as the growth (+ sign) or damping (- sign) rate of the mode l and is given by [47]:

$$1/\tau_u^{(l)} = -\frac{\Delta\Omega_{u,\text{im}}^{(l)}}{T_{\text{rev}}}, \tag{2.58}$$

where $\Delta\Omega_{u,\text{im}}^{(l)}$ the imaginary part of the complex tune shift as defined in Eq. (2.53).

The real coherent tune shift introduced by the beam transverse impedance plays a crucial role in the studies with Crab Cavities discussed in the following.

2.4 Optics models for accelerators

For the study of beam dynamics, it is essential to know the detailed arrangement of the magnets (position and strength) in the lattice, which will be referred to as optics. The optics also provide information on the Twiss parameters and phase advances along the ring.

MAD-X [48] is a code which is used extensively for the design and simulation of the accelerators at CERN. The official optics repositories of the CERN machines can be found in [49].

SPS optics

The studies presented in this thesis are performed for the SPS optics called Q26 optics (as the integer part of the tune in both planes is 26). The model for the Q26 optics can be found in the official CERN repository [50] and will be referred to as the nominal SPS model in this thesis. The values of the optics parameters in what follows correspond to the model values unless stated otherwise.

2.5 Tracking simulation codes

In this section the two tracking simulation codes used in this thesis to study the noise-induced emittance growth are presented. Both codes are macroparticle tracking libraries that simulate the particle motion in the six-dimensional (6D) phase space $(x, x', y, y', z, \delta)$.

2.5.1 PyHEADTAIL

PyHEADTAIL [51] is an open-source 6D macroparticle tracking code, developed at CERN, which was originally designed to study collective effects in circular machines and to be easily extensible with custom elements. Details on its implementation and its features can be found in [52, 53]. In principle, the tracking is performed between

interaction points around a circular accelerator at which the particles' receive kicks from magnetic elements or from collective effects.

Below the main steps for setting up a simulation are listed:

1. **Machine initialisation:** The accelerator ring is split into a number of segments of equal length, after each of which there is an interaction point[8] (IP). At the interaction points, the macroparticles experience kicks from various accelerator components (feedback system, multipoles, etc) or from collective effects such as the wakefields.

   The machine parameters, such as the circumference, the betatron and synchrotron tunes, the Twiss, and the dispersion values at the interaction points are defined.

2. **Bunch initialisation:** A particle bunch is represented by a collection of macroparticles, each of which represents a clustered collection of physical particles. Each macroparticle is described by four transverse (x, x', y, y') and two longitudinal coordinates (z, δ), a mass and an electric charge. For the studies presented in this thesis 10^5 macroparticles are sufficient for an accurate representation of the bunch, unless it is stated otherwise. There are various distributions available. In this thesis the simulations are performed using a Gaussian distribution in both transverse and longitudinal planes.

3. **Transverse tracking**: In the transverse plane, the macroparticles are transported from one interaction point to another (e.g. grom IP0 to IP1) following the matrix formalism of Eq. (2.29). The linear transfer matrices, M, introduced in Eq. (2.30) take into account the optics parameters at the beginning and the end of the corresponding segment. It should be noted that if no detuning source is added (see next step) the matrix M is the same for all particles.

4. **Chromaticity and detuning with transverse amplitude:** The chromaticity

---

[8]It should be clarified that this is not an "interaction point" in the sense of collision between counter-circulating beams.

(up to higher orders) and amplitude detuning are implemented as a change of the phase advance of each individual particle as follows (example for the horizontal plane):

$$\Delta\psi_{x,i\text{IP0}\rightarrow\text{IP1}} = \Delta\psi_{x,\text{IP0}\rightarrow\text{IP1}} + (Q_x'\delta_i + \alpha_{xx}J_{x,i} + \alpha_{xy}J_{y,i})\frac{\Delta\psi_{x,\text{IP0}\rightarrow\text{IP1}}}{2\pi Q_x}, \quad (2.59)$$

where $i = 1,...,N_{\text{mp}}$ with N_{mp} being the number of macroparticles, $\Delta\psi_{x,\text{IP0}\rightarrow\text{IP1}}$ is the phase advance for all macroparticles defined in the previous step, Q_x' the linear horizontal chromaticity, α_{xx} and α_{xy} are the detuning coefficients, while J_x and J_y are the horizontal and vertical actions of the macroparticle.

5. **Longitudinal tracking:** The longitudinal coordinates are updated once per turn after solving numerically the equations of motion introduced in Eq. (2.44) and Eq. (2.45). The motion can be linear or not (non-linear RF system). The studies presented in this thesis use the linear longitudinal tracking.

6. **Transverse impedance effects:** In PyHEADTAIL, wakefield kicks are used to implement the effect of the transverse impedance in the time domain. To improve the computational efficiency, the total impedance of the full machine is lumped at one of the interaction points along the ring and the kicks are applied to the macroparticles once per turn. Additionally, instead of computing the wakefield kicks from each particle to the rest individually, the bunch is divided into a number of slices longitudinally and the macroparticles in each slice receive a wakefield kick generated by the preceding slices[9] [54]. This is illustrated schematically in Fig. 2.6. A large number of slices is required such as the wakes can be assumed constant within the slice. A high number of macroparticles is also needed in order to avoid statistical noise effects caused by undersampling [52]. For the studies presented, 500 slices are used over a range of three rms bunch lengths in both directions from the bunch centre with the bunch being represented by 10^6 macroparticles (instead of 10^5 required for simulations without impedance

---

[9]This is valid in the ultrarelativistic scenario when no wakefield is generated in front of the bunch. The condition applies to the SPS experiments described in this thesis, performed at 270 GeV.

effects).

(a) Without slicing

(b) With slicing

Figure 2.6: Longitudinal bunch slicing for the implementation of wakefield kicks in PyHEADTAIL. Without the slicing technique (left) the wake kicks on the red macroparticle are generated from all the green macroparticles resulting in computationally expensive simulations. Instead, when the bunch is sliced longitudinally (right) the wake kicks on the macroparticles in the red slice i are generated by the macroparticles in the green slices j, decreasing significantly the computation time. The figures are courtesy of M. Schenk [53].

Every turn, the change on the u' co-ordinate, where $u = (x, y)$, of all the macroparticles in slice j by the effect of the wakefields generated by all slices i is modeled as follows [52]:

$$\Delta'_{u,j} = -\frac{e^2}{p_0 c} \sum_{k=j+1}^{N_{\text{slices}}} N_k W_u(k(z_i - z_j))\langle u_k \rangle, \qquad (2.60)$$

where N_{slices} is the number of longitudinal slices, N_k and $\langle u_k \rangle$ the number of macroparticles at the centre of mass in u plane in the kth slice.

The wake functions are available from the detailed impedance model of the machine, which is obtained from a combination of theoretical computations and electromagnetic simulations and can be imported in PyHEADTAIL in form of tables [52]. Typically, the impedance model of an accelerator is provided normalised with the average value of the horizontal and vertical beta functions over the machine at the respective plane. Therefore the transverse beta functions at the location where the wakefield kicks are applied on the beam must equal these average values.

7. **Data acquisition:** The updated macroparticle coordinates after each turn are available at IP0 for post-processing. Typically, 10^5 turns are required for the noise-induced emittance growth simulations presented in this thesis.

Figure 2.7 shows a graphic representation of the accelerator model and the tracking procedure supporting the steps described above.
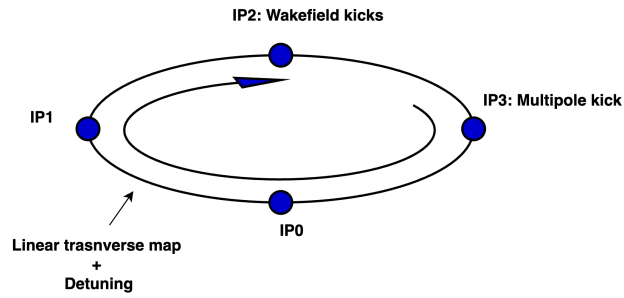
Figure 2.7: Graphical representation of the accelerator model and tracking procedure in PyHEADTAIL In this example, the ring is split into four segments separated by the interaction points (IPs). Wakefield and multipole kicks are applied to the macroparticles in IP2 and IP3. The macroparticles are transported between the IPs by a linear transfer map (which can include detuning effects) in the transverse plane. The longitudinal coordinates are updated once per turn.

2.5.2 Sixtracklib

Sixtracklib [55] is a library for performing single charged particle simulations developed at CERN. It simulates the motion of the particles in the six-dimensional (6D) phase space. The individual trajectories are computed taking into account the interactions with all the magnetic elements in the machine using the detailed design optics model described in Section 2.4. The particles advance from one element to the other with transfer maps which are obtained from the Hamiltonians that describe each element e.g. drift, dipoles, quadrupolar, high-order multipoles, RF cavities, etc. Note that thin lens approximation is used. Simulations with Sixtracklib are time efficient as the library can run on Graphical Processing Units (GPUs). Further details on Sixtracklib implementation and usage can be found in [56] and [57].

Since the Sixtracklib code was not used as extensively as PyHEADTAIL for the studies of this thesis, no further description is provided here, but the reader is referred to the references mentioned above.

3 | Theory of Crab Cavity RF noise-induced emittance growth

This section describes the theoretical formalism which predicts the transverse emittance growth in the presence of CC RF noise. First, it introduces the concept of noise in accelerator physics. The second section focuses on the CC amplitude and phase noise and it provides the equations to predict the noise-induced emittance growth. The last section comments briefly on the experiments that were carried out in KEKB: the work at KEKB constitutes the only experimental study of the effect of crab cavity RF noise prior to the work performed in the SPS.

3.1 Noise

In particle accelerators, the presence of noise in components controlling the beam or observing the beam behavior is a concern. Random fluctuations in the electric and magnetic fields seen by the beam can lead to emittance growth, orbit instability, and in extreme cases, particle loss. Examples of noise sources are ripples in the power converters which lead to fluctuations of the magnetic fields, ground motion, and various elements in the accelerator structure such as the transverse damper and the Crab Cavities.

Emittance growth

The thesis focuses on the problem of noise-induced emittance growth, which has been studied extensively in the past [58, 59, 27]. In principle, if the spectrum of the noise, overlaps with the sidebands of the betatron frequencies, $(k \pm q_u)f_{\text{rev}}$ (where k is an integer, q_u is the fractional part of the transverse betatron tune with $u = (x, y)$ denoting the horizontal and vertical planes respectively, and f_{rev} is the revolution frequency), it drives coherent betatron oscillations. For these betatron oscillations to result in emittance growth requires the presence of a tune spread.

The mechanism behind the emittance growth is that the tune spread leads to a phase mixing of the particles within the bunch causing decoherence of the betatron oscillations, which then results in emittance growth [58]. It should be highlighted, that for all the studies presented in this thesis, the decoherence rate is fast compared to the growth of betatron oscillations and thus the emittance growth rate is independent of the exact value of betatron tune spread [58]. For machines with working points far from non-linear (high-order) betatron resonances, the emittance growth is linear with time and proportional to the power spectral density of the noise spectra at the betatron frequencies, $(k \pm q_u) f_{\text{rev}}$, mentioned above [58]. This scenario holds for the work of this thesis. The definition of the power spectral density can be found in Appendix B.

White noise

In the studies presented in this thesis (simulations, theoretical and experimental studies), it is considered that the beam is subject to white noise. In signal analysis, white noise is a random signal with the same amplitude (intensity) at all frequencies, which results in a uniform power spectral density. This is a good approximation for noise resulting from random fluctuation of the magnetic fields in an accelerator [58] and for the noise in the LHC CCs [27]. Further details on the noise used in the experimental and simulation studies of this thesis are provided in Sections 4.3 and 5.2.

For the computational analysis (i.e. simulation studies), it is considered that the particle motion is influenced by the noise once per turn [58, 59, 27]. To this end, the white noise signal is sampled at a finite number of points (equal to the number of turns considered for the computational study) which are called discrete time steps. In this case, the white noise can be considered as a sequence of uncorrelated random values taken from a Gaussian distribution with zero mean and given standard deviation. For reference, the power spectral density of such a white noise signal that was used for the simulations that will be presented in this thesis can be found in Fig. 5.3. More details on the continuous and discrete time analysis can be found in Appendix B.

Dipole noise

From the various noise sources that are present in an accelerator, this thesis focuses on the dipolar noise and on the CC noise. Dipolar noise, which typically is originated by random displacements of a quadrupole magnet or by fluctuations in the current of a dipole magnet [58], affects all particles in the same way, i.e. the noise kick is constant along the bunch. On the other hand, the way the CC noise affects the particles depends on their longitudinal position within the bunch.

In this paragraph, the modeling of dipole noise is introduced as it constitutes the basics for understanding the more complex effects of CC noise. The details on the CC noise (which is the main focus of the work presented here) are discussed further in a dedicated section (see Section 3.2).

Past studies [58, 59] have shown that the dipole white noise can be modeled as a sequence of random kicks (stochastic process) that affect the particles within a bunch by changing their transverse angle each turn as follows:

$$\Delta u'_j = \theta_j, \tag{3.1}$$

where $j = \{0, \dots N_{\text{turns}}\}$ denotes the turn number with N_{turns} being the total number of turns that the beam experiences the noise and $u = (x, y)$ denoting horizontal or vertical position co-ordinate. The parameter θ_j corresponds to the noise kick and is the jth element of a set of N_{turns} samples, drawn from a Gaussian distribution (with size N_{turns}) with zero mean and standard deviation σ_θ. This way it is ensured that the noise kicks are uncorrelated.

The standard deviation σ_θ characterises the strength of the noise. As discussed in Appendix B (see Eq. (B.21)) for a white noise spectrum, it is related to its power spectral density, S_θ, as follows:

$$S_\theta = \frac{\sigma_\theta^2}{f_{\text{rev}}}, \tag{3.2}$$

where f_{rev} is the revolution frequency of the machine.

The power spectral density, S_θ, is expressed in terms of the square of the amplitude

of the signal per unit frequency. The noise is applied in the angle co-ordinates, hence the units of the power spectral density are rad^2/Hz. In Eq. (3.2) the noise appears independent of the frequency since for the white noise spectrum the power spectral density is the same for all frequencies.

In this thesis, the term "noise" will refer to white noise, which can be modeled with the above-mentioned stochastic process.

3.2 Crab Cavity noise and emittance growth

The presence of noise in the CC low-level RF system is an issue of major concern for the HL-LHC project as it results in transverse emittance growth and subsequently in loss of luminosity. To this end, in 2015, P. Baudrenghien and T. Mastoridis developed a theoretical model [27] which predicts this transverse emittance growth induced by CC noise focusing in the HL-LHC scenario. In particular, the model assumes a hadron machine, zero synchrotron radiation damping, long bunches (in the order of cm), and white RF noise (discrete spectral lines are excluded). Additionally, it is assumed that the phase of the CC is set such that the zero-crossing of the voltage coincides with the longitudinal centre of the bunch.

Since we will refer to the theoretical model of P. Baudrenghien and T. Mastoridis [27] frequently throughout the thesis we will often use the term "Mastoridis–Baudrenghien model" for simplicity.

The Mastoridis–Baudrenghien model is also applicable to the SPS (where the same conditions apply), where the CCs will be tested before their installation in the HL-LHC (Section 1.3). The equations and formulas from this model that are essential for the understanding of the studies are discussed below.

3.2.1 Crab Cavity amplitude and phase noise

The unperturbed instantaneous CC voltage can be written as:

$$V_{\text{CC}}(t) = V_{0,\text{CC}} \sin\left(2\pi f_{\text{CC}} t + \phi_{\text{CC}}\right), \qquad (3.3)$$

3. Theory of Crab Cavity RF noise-induced emittance growth

where $V_{0,CC}$ is the peak amplitude of the CC voltage, f_{CC} the CC frequency, and ϕ_{CC} the CC phase. The following analysis will consider $\phi_{CC} = 0$ as this is the case for most of the studies presented in this thesis unless it is stated otherwise. To this end, the above equation becomes:

$$V_{CC}(t) = V_{0,CC} \sin\left(2\pi f_{CC} t\right), \tag{3.4}$$

Equation (3.4) can be re-written as a function of the longitudinal position within the bunch z instead of time t as follows:

$$V_{CC}(z) = V_{0,CC} \sin\left(\frac{2\pi f_{CC}}{\beta_0 c} z\right), \tag{3.5}$$

where β_0 is the relativistic parameter and c is the speed of light. In the presence of modulations in amplitude and phase Eq. (3.5) becomes:

$$V_{CC}(z) = V_{0,CC}(1 + \Delta A) \sin\left(\frac{2\pi f_{CC}}{\beta_0 c} z + \Delta\phi\right), \tag{3.6}$$

where $\Delta\phi$ is the deviation from the nominal phase, $2\pi f_{CC} z/(\beta_0 c)$, and will be referred to as phase noise in the following. $\Delta A = \Delta V_{0,CC}/V_{0,CC}$ is the relative deviation from the nominal amplitude $V_{0,CC}$ and will be referred to as amplitude noise. The units of $\Delta\phi$ are radians while ΔA has no units as it defines a scaling factor applied to the amplitude, rather than stating directly the change in the amplitude.

In the calculation of the RF noise effects, it is assumed that RF phase and amplitude noises are uncorrelated. The validity of this hypothesis depends on the actual architecture of the low-level RF responsible for the regulation of the cavity field. The low-level RF system for the HL-LHC CCs is presently being designed at CERN. Further details can be found in Ref. [15] of the above-mentioned publication of P. Baudrenghien and T. Mastoridis [27], but discussing them in more detail is out of the scope of this thesis.

To this end, and following the analysis in [27] and in accordance with Eq. (3.1) the

change of the trajectory of each particle within a bunch as a result of the phase and amplitude CC RF noise can be modeled as follows:

$$\text{\textbf{Amplitude noise:}} \; \Delta u'_j = \frac{eV_{0,\text{CC}}}{E_b} \Delta A_j \sin\left(\frac{2\pi f_{\text{CC}}}{c\beta_0} z_j\right), \tag{3.7}$$

$$\text{\textbf{Phase noise:}} \; \Delta u'_j = +\frac{eV_{0,\text{CC}}}{E_b} \Delta \phi_j \cos\left(\frac{2\pi f_{\text{CC}}}{c\beta_0} z_j\right), \tag{3.8}$$

where $j = \{0, \dots N_{\text{turns}}\}$ denotes the turn number with N_{turns} being the total number of turns that the bunch experiences the noise and e is the elementary charge. Furthermore, u', with $u = (x, y)$, is the angle co-ordinate and z the longitudinal co-ordinate of each particle as defined in Eq. (2.2). The parameters ΔA_j and $\Delta \phi_j$, are the jth elements of a set of N_{turns} samples, drawn from Gaussian distributions of size N_{turns}, with zero mean and standard deviation of $\sigma_{\Delta A}$ and $\sigma_{\Delta \phi}$, respectively. A typical value of σ_A and σ_ϕ that will be used in the simulations later is 2.7×10^{-3}. It is reminded that σ_ϕ is expressed in radians, while σ_A has no units.

The power spectral density of these noise kicks for a white noise spectrum can be computed as follows (see discussion in Appendix B and Eq. (B.21)):

$$S_{\Delta A} = \frac{\sigma_{\Delta A}^2}{f_{\text{rev}}}, \tag{3.9}$$

and

$$S_{\Delta \phi} = \frac{\sigma_{\Delta \phi}^2}{f_{\text{rev}}}, \tag{3.10}$$

where f_{rev} is the revolution frequency. $S_{\Delta A}$ is the power spectral density of the amplitude noise and is expressed in Hz^{-1}, while $S_{\Delta \phi}$ is the power spectral density of the phase noise and is expressed in $\text{rad}^2\text{Hz}^{-1}$.

Figures 3.1 and 3.2 show schematically the effects of the amplitude and phase noise (respectively) on the crab cavity voltage, and on the particles within a single bunch. It can be seen that in the presence of amplitude noise the head and the tail of the bunch are kicked in opposite directions which results in intra-bunch oscillations. On the other hand, in the presence of phase noise, the particles in the bunch receive kicks that are in phase. This results in a shift of the bunch centroid which is dipole (or head-tail mode 0) motion.
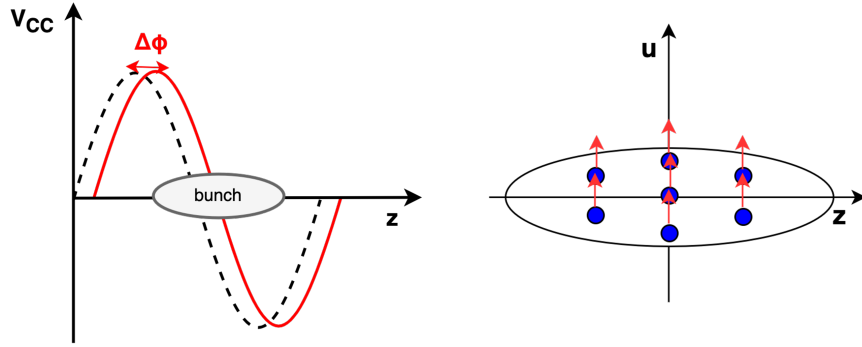
Figure 3.1: Modulation in amplitude or amplitude noise (left) and its impact on the particles within the bunch (right). The blue dots represent the individual particles while the red arrows indicate the direction of the noise kicks which act on them.
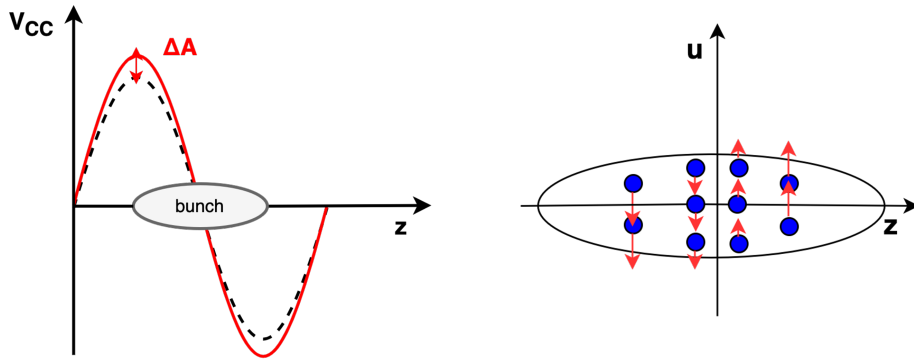
Figure 3.2: Modulation in phase or phase noise (left) and its impact on the particles within the bunch (right). The blue dots represent the individual particles while the red arrows indicate the direction of the noise kicks which act on them.

For the LHC, HL-LHC, and SPS CCs the amplitude and phase RF noise are represented by white noise spectra. In that case, they can be considered as a sequence of uncorrelated random variables taken from a Gaussian distribution with zero mean and standard deviation $\sigma_{\Delta A}$ and $\sigma_{\Delta\phi}$, respectively. The variances, $\sigma_{\Delta A}^2$ and $\sigma_{\Delta\phi}^2$ equal the total noise power (see Appendix B.2 for definitions).

3.2.2 Emittance growth formulas

The theoretical formalism for predicting the transverse emittance growth in the presence of CC RF amplitude and phase noise was derived in [27]. The derivation assumes a single bunch is crossing the crab cavity and the phase of the CC is set such that the zero-crossing of the voltage coincides with the longitudinal centre of the bunch, as well as no coupling between the transverse planes and constant

energy (no acceleration). The noise kicks are represented as a stochastic process with a uniform spectrum across the betatron tune distribution.

Taking these conditions into account, the emittance growth resulting from amplitude noise is derived as [27]:

$$\frac{d\epsilon_u^{\text{geom}}}{dt} = \beta_{u,\text{CC}} \left(\frac{eV_{0,\text{CC}} f_{\text{rev}}}{2E_b} \right)^2 C_{\Delta A}(\sigma_\phi) \sum_{k=-\infty}^{+\infty} S_{\Delta A}[(k \pm \bar{q}_u \pm \bar{q}_s) f_{\text{rev}}]. \tag{3.11}$$

For phase noise, the emittance growth is derived as [27]:

$$\frac{d\epsilon_u^{\text{geom}}}{dt} = \beta_{u,\text{CC}} \left(\frac{eV_{0,\text{CC}} f_{\text{rev}}}{2E_b} \right)^2 C_{\Delta\phi}(\sigma_\phi) \sum_{k=-\infty}^{+\infty} S_{\Delta\phi}[(k \pm \bar{q}_u) f_{\text{rev}}]. \tag{3.12}$$

In these formulas, which are valid for both transverse planes as $u = (x, y)$, $\beta_{u,\text{CC}}$ is the transverse beta function at the location of the CC, $V_{0,\text{CC}}$ the CC voltage, f_{rev} the revolution frequency of the beam, E_b the beam energy, and $\bar{q}_u$ and $\bar{q}_s$ the mean of the betatron and synchrotron tune distribution[1] where q_u, q_s (with lower case) denote the fractional part of the betatron and synchrotron tunes, respectively. $S_{\Delta A}$ and $S_{\Delta\phi}$ are the power spectral densities (PSD) of the noise at all the betatron and synchrobetatron (for the amplitude noise case) sidebands and they are expressed in units of Hz^{-1} and $\text{rad}^2\text{Hz}^{-1}$, respectively. In particular, $k \in \mathbb{Z}$ is the harmonic number of the revolution frequency and the $\pm$ signs refer to the upper (+) and lower (−) sidebands at each multiple of the revolution frequency, kf_{rev}.

The definition of the power spectral density along with the fundamental terminology for the signal-processing can be found in Appendix B. As all the studies presented in this thesis are done with white noise, the power spectral densities can be computed using Eqs. (3.9) and (3.10).

The terms $C_{\Delta A}$ and $C_{\Delta\phi}$ are correction terms to account for the bunch length:

$$C_{\Delta A}(\sigma_\phi) = e^{-\sigma_\phi^2} \sum_{l=0}^{+\infty} I_{2l+1}(\sigma_\phi^2), \tag{3.13}$$

$$C_{\Delta\phi}(\sigma_\phi) = e^{-\sigma_\phi^2} \left[I_0(\sigma_\phi^2) + 2 \sum_{l=1}^{+\infty} I_{2l}(\sigma_\phi^2) \right], \tag{3.14}$$

---

[1]For white noise spectra the effect of noise is independent of the actual tune distribution, hence the use of the mean quantities. The generic formulas can be found in [27].

with σ_ϕ the rms bunch length, in radians, with respect to the CC frequency f_{CC}, and $I_n(x)$ the modified Bessel function of the first kind.

Figure 3.3 illustrates the correction term for different values of bunch length for amplitude (left) and phase noise (right). The SPS nominal bunch length used in the CC tests is indicated by an orange dot for reference.
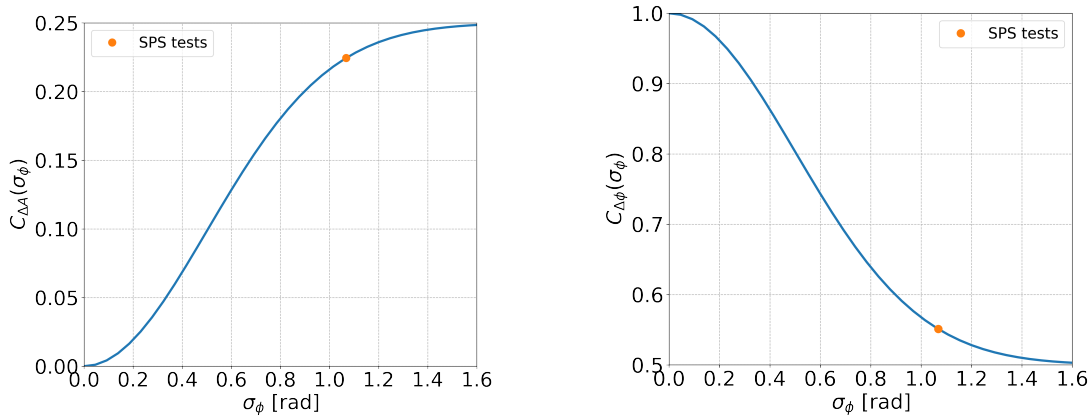
Figure 3.3: Correction term for amplitude (left) and phase noise (right) over a range of bunch length values.

3.3   Studies in KEKB

CCs have been tested in the past with lepton beams at KEKB in Japan [20, 21, 22]. The tests included studies of the effects of RF noise in the CC on the beam. However, there were significant differences in KEKB, compared to SPS, LHC, and HL-LHC. In particular, the studies in KEKB were conducted for lepton bunches, rather than hadron bunches. The bunch length in KEKB was smaller by an order of magnitude than in SPS or HL-LHC: this means that the effects of amplitude noise would be negligible in KEKB. Furthermore, synchrotron radiation in lepton storage rings provides significant damping. Finally, the RF noise in KEKB was characterised by a single spectral line, rather than white noise. Due to these differences, the studies performed at KEKB [60] are not applicable to the studies presented in this thesis and will thus not be discussed in more detail.

Now that the theoretical formulas for the CC RF noise-induced emittance growth have been introduced, they will be used through the following chapters for comparison against numerical simulations and experimental measurements (in

the SPS) for developing confidence in the theoretical model and its predictions for the HL-LHC.

4 | Experimental studies from 2018: emittance growth from Crab Cavity noise

In Chapter 3 the theoretical model (Mastoridis–Baudrenghien model) for the transverse emittance growth caused by amplitude and phase noise in a CC was discussed. On September 5, 2018, a dedicated experiment was conducted in the SPS to benchmark this model against experimental data and check the analytical predictions. In particular, the aim was to inject artificial noise into the CC RF system and compare the measured emittance growth rates with the theoretically computed ones. In this chapter, the measurement results from the SPS are presented and discussed. However, since a similar experiment has not been performed before, this chapter not present only the emittance growth measurements but it also discusses in detail the experimental conditions and the available measurements of other parameters of interest such as the CC voltage, the RF noise spectra, the bunch length, and the bunch intensity, aiming to provide a complete overview.

Section 4.1 provides some information on the installation of the CCs in the SPS that is essential for the studies in this thesis and elaborates on some considerations regarding their operation in the SPS. Section 4.2 describes the machine setup and the beam configuration for the emittance growth measurements. This includes a summary of the preparatory studies conducted in the previous years. In Section 4.3 information on the noise injected in the CC RF system is provided while in Section 4.4 the beam-based measurement of the CC voltage is presented. The measurements of transverse emittance growth are presented in Section 4.5, and the complementary measurements of bunch length and intensity in Section 4.6. Section 4.7 compares the measured transverse emittance growth with the

predictions of the Mastoridis–Baudrenghien model. The conclusions of the first experimental campaign with CC noise in SPS are drawn in Section 4.8.

4.1 Crab Cavities in the SPS

For the SPS tests of 2018 two prototype CCs of the Double Quarter Wave (DQW) type[1], which will be referred to as CC1 and CC2 throughout this thesis, were fabricated at CERN and were assembled in the same cryomodule. For their installation, available space was found at the SPS Long Straight Section 6 (SPS-LSS6) zone. As this section is also used for the extraction of the beam to the LHC, the cryomodule was placed on a mobile transfer table [61] which moved the cryomodule in the beamline for the CC tests and out of it for the usual SPS operation, without breaking the vacuum.

The main CCs' parameters are listed in Table 4.1. Their location along the SPS ring is also indicated, in case someone would like to repeat the analysis described in this thesis.

Table 4.1: Crab Cavities design parameters for the SPS tests.

Parameter	Value	
	CC1	**CC2**
Crabbing plane	vertical	vertical
s-location*	6312.72 m	6313.32 m
CC voltage, $V_{0,\text{CC}}$	≤ 3.4 MV	≤ 3.4 MV
CC frequency, $V_{0,\text{CC}}$	400.78 MHz	400.78 MHz
Horizontal / vertical beta function, $\beta_{x,\text{CC}}$ / $\beta_{y,\text{CC}}$	29.24 m / 76.07 m	30.31 m / 73.82 m
Horizontal / vertical alpha function, $\alpha_{x,\text{CC}}$ / $\alpha_{y,\text{CC}}$	-0.88/ 1.9	-0.91 / 1.86
Horizontal / vertical dispersion, $D_{x,\text{CC}}$ / $D_{y,\text{CC}}$	-0.48 m / 0 m	-0.5 m / 0 m

 * The s-location is referred to the location of the elements along the SPS ring with respect to the start of the lattice i.e. element QF.10010 which is a focusing quadrupole. The s-location is given to allow the studies to be reproduced.

4.1.1 Considerations about the Crab Cavity operation

The experimental studies presented in this thesis were performed with the CCs operating at a fixed frequency of 400.78 MHz (unless it is stated otherwise) and at a target peak voltage of about 1 MV. Even though the CC modules installed in the SPS

---

[1]The RFD type CCs are expected to be ready by the end of 2022 - beginning of 2023.

can operate at a maximum voltage of 3.4 MV (see Table 4.1), the experiments were performed with a peak voltage of 1 MV since for that value the stable CC operation for long periods was ensured. Further details on the hardware aspects of the CC operation in the SPS are not discussed here as they are out of the scope of this thesis.

Energy ramp

SPS receives the proton beam at 26 GeV from the PS. It was found that the ramp to higher energies could not be performed with the CC switched on, since during the acceleration one of the vertical betatron sidebands was crossing the CC frequency resulting in resonance excitation and beam loss [62, 63]. Changing the CC frequency during the ramp so that it stays synchronous with the beam was not an option due to hardware limitations [63]. Therefore, the acceleration had to be performed with the CC switched off and its voltage set up only after the energy of interest has been reached.

Synchronization between main SPS RF and Crab Cavity

In order to maintain the CC waveform time-aligned with the circulating bunch, the CC operating at 400.78 MHz needs to be synchronized with the main SPS RF system operating at around 200 MHz. Due to the larger bandwidth of the SPS main RF system, the CC was used as a master. Therefore the CC was operating at a fixed frequency, while the main accelerating cavities were adjusted to the exact half of the CC frequency so that they become synchronous with the CC waveform. For studies at higher energies, the synchronisation took place at the end of the energy ramp shortly a few seconds after the CC was switched on [62].

4.2   Experimental configuration and procedure

4.2.1   Preparatory experimental studies

For studying the long-term emittance evolution a special mode of operation with bunches beams was set up in the SPS, which is called "coast" (in other machines, it is referred to as storage ring mode). In this mode, the bunches circulate in the

machine at constant energy for long periods, from a few minutes up to several hours, similar to the HL-LHC case.

To make sure that the SPS can be used as a testbed for the emittance growth studies with CCs, an extensive preparatory campaign was carried out between 2012-2017 [64, 65, 66]. The primary concern was emittance growth due to sources other than voluntarily injected noise, which will be referred to as "background emittance growth" in this thesis. The background emittance growth needs to be well characterised and be kept sufficiently small in order to distinguish and understand the contribution from the CC noise.

From these studies, it was concluded that the background emittance growth is smallest at high energies, with low chromaticity and with bunches of low intensity [66]. The highest energy for which the SPS could operate in coast was 270 GeV and thus the experiments were performed at this energy. That limitation was due to limited cooling of the magnets to transfer away the dissipated power in the resistive magnets when operating at high energy and thus at large currents for long periods. Moreover, as the background emittance growth was found to be a single bunch effect, four bunches were used. That choice was made to reduce the statistical uncertainty of the measurements but not to increase the beam intensity.

4.2.2   Machine and beam configuration

During the experiment, the Landau octupoles were switched off. Nevertheless, a residual non-linearity was present in the machine mainly due to multipole components in the dipole magnets [67, 68]. The transverse feedback system was also switched off. No measurements of chromaticity are available from the day of the experiment. However, it was ensured that the chromaticity was corrected to small positive values. Last, only one CC, CC2, was used for simplicity and it operated at 1 MV. The main machine and beam parameters used for the emittance growth measurements in 2018 are listed in Table 4.2.

Table 4.2: Main machine and beam parameters for the emittance growth studies with CCs in SPS in 2018.

Parameter	Value
Beam energy, E_b	270 GeV
Revolution frequency, f_{rev}	43.375 kHz
Main RF voltage / frequency, V_{RF} / f_{RF}	3.8 MV / 200.39 MHz
Horizontal / vertical betatron tune, Q_{x0} / Q_{y0}	26.13 / 26.18
Horizontal / vertical first order chromaticity, Q'_x / Q'_y	~ 1.0 / ~ 1.0
Synchrotron tune, Q_s	0.0051
CC2 voltage / frequency, $V_{0,\text{CC}}$ / f_{CC}	1 MV / 400.78 MHz
Number of protons per bunch, N_b	3×10^{10} p/b*
Number of bunches	4
Bunch spacing	525 ns
Bunch length, $4\sigma_t$	1.8 ns*
Horizontal / vertical normalised emittance, ϵ_x / ϵ_y	2 μm / 2 μm*
Horizontal / vertical rms tune spread, ΔQ_x^{rms} / ΔQ_y^{rms}	1.9×10^{-5} / 2.1×10^{-5} †

* The value corresponds to the requested initial value at the start of each coast. The measured evolution of the parameter through the experiment is presented in the Sections 4.5 and 4.6.
† Here the rms betatron tune spread includes only the contribution from the detuning with amplitude present in the SPS machine. The calculations for the listed values can be found in Appendix C.1.

4.2.3   Experimental procedure for emittance growth measurements

The emittance growth experiment took place on September 5, 2018, and was given a total time window of about 6 hours (start:~10:30, end:~17:00). In order to characterize the CC noise induced emittance growth, different levels of controlled noise were injected into the low-level RF system and the bunch evolution was recorded for about 20-40 minutes (for each noise setting). A new beam was injected every time the quality of the beam was seen to be degraded e.g. very large beam size. Overall, the experiment was conducted over three coasts. In the following, the different noise settings will be denoted as "Coast$N$-Setting$M$", where N stands for the coast number and M for the different noise levels applied in each coast in chronological order. After the experiment, the measured growth rates would be compared with the theoretically expected values from the Mastoridis–Baudrenghien model (described in Chapter 3).

4.3   Injected RF noise

The noise injected in the CC RF system was a mixture of amplitude and phase noise up to 10 kHz. The phase noise was always dominant. The noise levels were measured with a spectrum analyzer E5052B [69] and are expressed as $10\log_{10}\mathscr{L}(f)$ [dBc/Hz]. $\mathscr{L}(f)$ follows the IEEE definitions in [70] is the standard measure for characterising instabilities in the frequency domain. It should be emphasised that $\mathscr{L}(f)$ as defined in [70] is two-sided, which means that it has both positive and negative frequencies and as a real signal is symmetric around the DC component, $f = 0$ Hz. However, since the spectrum analyser E5052B displays the logarithmic quantity $10\log_{10}\mathscr{L}(f)$, only the positive frequencies are displayed.

The relation between the measured noise levels and the power spectral densities in Eq. (3.11) and Eq. (3.12) following the IEEE conventions [70] is given by $S_{\Delta A, \Delta \phi}(f) = \mathscr{L}(f)$ (see Table A.1 in [70]), with $S_{\Delta A}$ in Hz^{-1} and $S_{\Delta \phi}$ in $\mathrm{rad}^2\mathrm{Hz}^{-1}$.

Figure 4.1 spectra of the measured of amplitude (left) and phase (right) noise acquired during the experiment. The spectrum analyzer E5052B [69], was connected to the RF antenna inside the CC which monitors the amplitude and the phase of its field. To this end, the voltage induced by the passage of the bunch through the CC was visible in the measured spectra: spikes at high frequencies and in particular at harmonics of the revolution frequency.
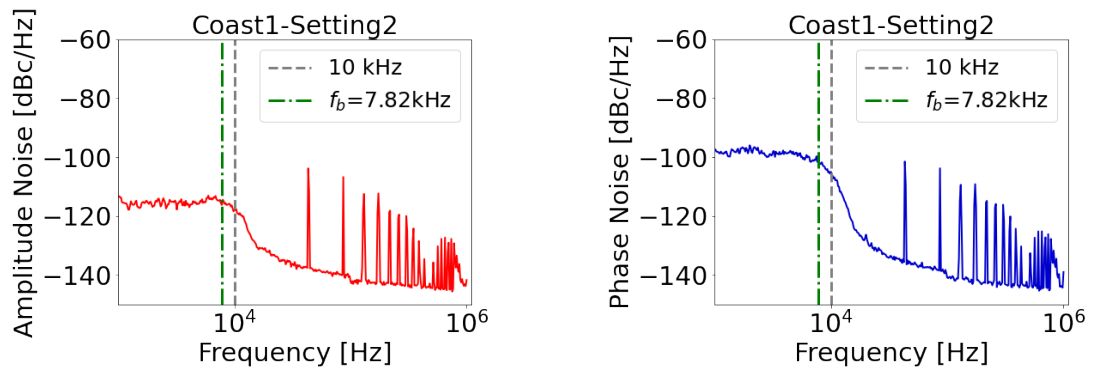
Figure 4.1: Example amplitude (left) and phase (right) noise spectra measured with a spectrum analyzer E5052B [69] during the emittance growth studies with CCs in SPS. The noise extends up to 10 kHz (grey dashed line) overlapping the first betatron sideband at ~8 kHz (green dashed line). The spikes at high frequencies correspond to the harmonics of the revolution frequency and are a result of the beam-induced signal from its passage through the CC.

4.3.1 Expected emittance growth from the Mastoridis–Baudrenghien model

Here, some comments on the use of the Eq. (3.11) and Eq. (3.12) for predicting the emittance growth rate from the above-described noise spectra injected in the CC RF system are made.

First, the emittance growth in the vertical plane is considered since the CC module (DQW) installed in the SPS provides a vertical deflection on the beam. As already discussed in Chapter 3 the noise-induced emittance growth in the vertical plane depends on the noise power at the vertical betatron and synchrobetatron sidebands for the phase and amplitude noise respectively (see Eq. (3.12) and Eq. (3.11)). During the experiment (see parameters listed in Table 4.2): $q_y = 0.18$, $f_{\text{rev}} = 43.38\,\text{kHz}$, and $q_s = 0.0051$.

The upper and lower sidebands of the first and second vertical betatron sidebands are observed in the following frequencies:

$$\text{k} = 0: \ (0 \pm q_y)\, f_{\text{rev}} = \pm 0.18 \times 43.38\,\text{kHz} \approx \pm 7.8\,\text{kHz}, \tag{4.1}$$

$$\text{k} = \pm 1: \ (\pm 1 \pm q_y)\, f_{\text{rev}} = (\pm 1 \pm 0.18) \times 43.38\,\text{kHz} \approx \begin{cases} -51.2\,\text{kHz and} -35.6\,\text{kHz}, & \text{for } k = -1 \\ 51.2\,\text{kHz and } 35.6\,\text{kHz}, & \text{for } k = 1 \end{cases}. \tag{4.2}$$

The upper and lower sidebands of the first and second vertical synchrobetatron sidebands are observed in the following frequencies:

$$\text{k} = 0: \ (0 \pm q_y \pm q_s)\, f_{\text{rev}} = (\pm 0.18 \pm 0.0051) \times 43.38\,\text{kHz} \approx \pm 8.02\,\text{kHz and} \pm 7.6\,\text{kHz}. \tag{4.3}$$

$$\text{k} = \pm 1: \ (\pm 1 \pm q_y \pm q_s)\, f_{\text{rev}} = (\pm 1 \pm 0.18 \pm 0.0051) \times 43.38\,\text{kHz} \approx$$

$$\approx \begin{cases} -35.35, -35.79, -50.96, -51.40\,\text{kHz}, & \text{for } k = -1 \\ 35.35, 35.79, 50.96, 51.40\,\text{kHz}, & \text{for } k = 1 \end{cases}. \tag{4.4}$$

It is evident, that the noise spectra injected in the CC RF, which extends with approximately constant power spectral density up to 10 kHz, overlaps and

primarily excites only the first betatron and synchrobetatron sidebands, for $k = 0$ (upper and lower).

To this end, for the experimental conditions of 2018 Eq. (3.11) and Eq. (3.12) can be re-written as follows:

$$\frac{d\epsilon_u^{\text{geom}}}{dt} = 4 \times \beta_{u,\text{CC}} \left(\frac{e V_{0,\text{CC}} f_{\text{rev}}}{2E_b} \right)^2 C_{\Delta A}(\sigma_\phi) S_{\Delta A}, \tag{4.5}$$

and

$$\frac{d\epsilon_u^{\text{geom}}}{dt} = 2 \times \beta_{u,\text{CC}} \left(\frac{e V_{0,\text{CC}} f_{\text{rev}}}{2E_b} \right)^2 C_{\Delta \phi}(\sigma_\phi) S_{\Delta \phi}. \tag{4.6}$$

for amplitude and phase noise, respectively. The multiplication factors 4 and 2, show the contribution from to the first synchrobetatron and betatron sidebands at the frequencies computed in Eqs. (4.3) and (4.1), respectively.

It is reminded, that the power spectral densities $S_{\Delta A}$ and $S_{\Delta \phi}$ appear independent of the frequency since the noise spectra are considered constant up to $\pm 10\,\text{kHz}$. They can be computed from the measured spectra expressed in $10 \log_{10} \mathscr{L}$ [dBc/Hz] through the relation $S_{\Delta A, \Delta \phi} = \mathscr{L}$ introduced earlier in this section.

Power spectral density values of interest

To smoothen the power spectra around the frequency of interest, i.e. the first betatron sideband, f_b, the average of the power spectral density values over a frequency range of $\pm 500\,\text{Hz}$ around it is considered. The uncertainty is obtained from the standard deviation over that range. For simplicity, the power spectral density is assumed to be the same at the betatron and synchrobetatron sidebands since they lie very close to each other.

The emittance growth measurements were performed with seven different noise levels. The values of the phase and amplitude noise for each setting are listed in Table 4.3.

Effective phase noise

In order to make a meaningful comparison between the different levels of noise,

the concept of effective phase noise is introduced: this is the phase noise level that would lead to the same emittance growth as that from both phase and amplitude noise according to Mastoridis–Baudrenghien model.

For the calculation of the effective phase noise the averaged bunch length for each case is used (bunch length measurements at Section 4.6). The uncertainty on the effective phase noise is computed following the standard procedure of the propagation of the uncertainty (introduced in Appendix A.3). The calculated effective phase noise values for the experimental conditions are also listed in Table 4.3. The values shown correspond to the results using the parameters of the first bunch. However, the difference between the values for the other bunches is very small and is also within the displayed uncertainties. The noise levels mentioned in the following analysis of the experimental data correspond to the calculated effective phase noise.

Table 4.3: Phase and amplitude noise levels injected in the CC RF system for the emittance growth studies of 2018. The listed values correspond to the average power spectral density values over a frequency range of $\pm\,500\,$Hz around the first betatron sideband, f_b. The calculated effective phase noise for the parameters of the first bunch are also listed.

	$10\log_{10}\mathscr{L}$(f) [dBc/Hz]		
	Phase noise	**Amplitude noise**	**Effective phase noise**
Coast1-Setting1	-122.6 $\pm$0.6	-128.1 $\pm$ 0.6	-121.8 $\pm$ 0.5
Coast1-Setting2	-101.4 $\pm$ 0.8	-115.2 $\pm$ 0.6	-101.3 $\pm$ 0.8
Coast2-Setting1	-115.0 $\pm$ 0.8	-124.1 $\pm$ 0.5	-114.6 $\pm$ 0.7
Coast2-Setting2	-111.4 $\pm$ 0.6	-115.7 $\pm$ 0.4	-110.2 $\pm$ 0.5
Coast3-Setting1	-110.9 $\pm$ 0.9	-116.9 $\pm$ 0.4	-110.1 $\pm$ 0.8
Coast3-Setting2	-106.4 $\pm$ 0.3	-112.9 $\pm$ 0.6	-105.8 $\pm$ 0.3
Coast3-Setting3	-101.4 $\pm$ 0.7	-106.9 $\pm$ 0.5	-100.6 $\pm$ 0.6

4.4   Measurement of Crab Cavity voltage

As mentioned above, CC2 operated at 1 MV. Before the start of the emittance growth measurements, this value was validated with beam-based measurements from the Head-Tail monitor [71]. The Head-Tail monitor measures the transverse displacement within the bunch which can be used to reconstruct the CC voltage experienced by the beam. A detailed description of the post-processing procedure

is provided in Appendix D.

The beam-based measurement of the CC voltage can only be performed right after the acceleration ramp at 270 GeV and not during the coast mode for reasons that are explained in Appendix D. Therefore, the CC voltage was measured at the beginning of the emittance growth experiment.The CC settings remained unchanged for the rest of the experimental procedure.

The beam-based measurement of the CC voltage (reconstructed from the Head-Tail monitor) is displayed in Fig. 4.2 with red color. The horizontal axis shows the longitudinal position in nanoseconds with respect to the center of the bunch as it passes through the Head-Tail monitor. The voltage amplitude, $V_{0,\mathrm{CC}}$, is obtained from a sinusoidal fit (blue solid line in Fig. 4.2) on the reconstructed voltage, $V_{\mathrm{CC}}(t)$, from the Head-Tail monitor reading. The standard procedure of least squares fitting (see Appendix section A.2) is followed. In particular, $V_{\mathrm{CC}}(t)$ is fitted with the following three-parameter (A, θ, d) model function which also provides the CC phase and voltage offset:

$$f(x) = A \sin\left(2\pi f_{\mathrm{CC}} x + \theta\right) + d, \tag{4.7}$$

where A is the amplitude, θ is the phase and d is the vertical offset of the measured CC voltage. In Eq. (4.7) the CC frequency, f_{CC}=400.78 MHz, and is not a parameter of the fit since its operational value is fixed and well known.

The offset parameter, d, is added to the model function as measurements from other dedicated studies[2] that took place during this first experimental campaign with CCs in the SPS have shown that the reconstructed CC voltage, $V_{\mathrm{CC}}(t)$, is not centered around zero. A possible explanation for the asymmetry is that it is a result of the cable response of the Head-Tail monitor pick up [72]. However, its origin is not yet fully understood and will have to be addressed in the future. Furthermore, it was found that the vertical offset varied between the different dedicated studies and it outweighs the uncertainty on the voltage amplitude obtained by the

---

[2]A total of seven different dedicated experiments with CCs took place in SPS in 2018 in order to address various questions on the operation of the CC with proton beams [62]. The emittance growth experiment was the fifth in chronological order.
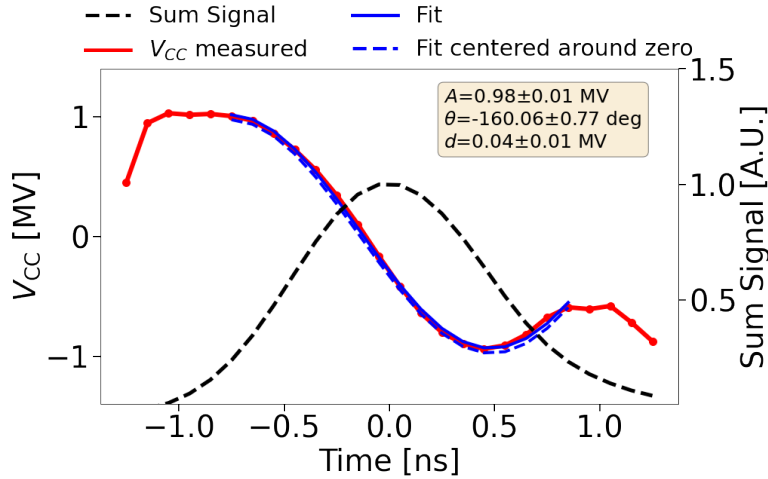
Figure 4.2: Beam-based measurement of the CC voltage as reconstructed from the Head-Tail monitor before the emittance growth measurements in 2018 (red). The sinusoidal fit on the reconstructed voltage to obtain the CC voltage amplitude is also shown (blue solid line). The fit result is given in the yellow box. The measured voltage amplitude, $V_{0,\text{CC}}$, was found to be 0.98 MV while its uncertainty, d, was measured at 0.04 MV. The measured voltage value agrees well with the requested value of 1 MV.

sinusoidal fit. To this end, in this thesis, this vertical offset d, will be defined as the uncertainty of the measured voltage amplitude.

In order to obtain results that correspond to the experimental conditions the following constraints are imposed to the fit. First the voltage amplitude, A, is requested to always be positive and higher than 0.7 MV. Furthermore, the part of the signal that corresponds to the tails of the bunch is excluded from the fit in order not to degrade its quality. Consequently, only the part of the signal for which the corresponding normalised sum signal of the Head-Tail monitor[3] (black dashed line) is above 0.4 is used for the fit.

The results of the sinusoidal fit are illustrated in the yellow box in Fig. 4.2. The measured CC voltage is: $V_{0,\text{CC}} = A \pm d = 0.98 \pm 0.04$ MV. The measured value is very close to the targetd value of 1 MV.

From the sinusoidal fit, the CC phase was found to be about -160° while the set value of the CC phase was 0° and thus there is a phase offset between the set value of the CC phase and of the voltage actually experienced by the beam.

---

[3]The sum signal is the longitudinal line density. Further details are provided in Appendix D.

Since this analysis was performed at a later time, the value of the phase offset was not known during the measurement and hence it could not be corrected. Nevertheless, simulation studies performed with Sixtracklib have shown that for the long bunches ($\sigma_z \sim 14$ cm) that were used for the tests in 2018, the phase offset of the CC has no significant impact on the phase noise[4] induced emittance growth [73].

The procedure of measuring the voltage amplitude from the Head-Tail monitor reading and calibrating the phase offset was optimised and automated so that it could be performed during the experiment, for the campaigns that took place in 2022 (see Chapter 7.4.1).

4.5 Emittance growth measurements

This section presents the transverse emittance growth measurements with CC RF noise. It discusses first the measurement of the beam emittance with the SPS Wire Scanners (WS) and then it provides an overview of the emittance growth measurements for the four bunches over all the different noise settings.

4.5.1 SPS Wire Scanners

The SPS is equipped with wire scanners (WS) to measure the transverse beam emittance. The SPS Wire Scanner system is described in detail in [74, 75]. For the SPS tests in 2018, the emittance was measured with Wire Scanners both for the horizontal and vertical plane (BWS.51995.H and BWS.41677.V respectively).

The working principle is shown in Fig. 4.3. A thin wire rapidly moves across the proton beam and a shower of secondary particles is generated. The signal from the secondary particles is detected by a system of scintillator and photomultiplier (PM) detectors outside of the beam pipe. By measuring the photomultiplier current as a function of wire position over multiple turns the transverse beam profile is reconstructed.

---

[4]It is reminded here that for the emittance growth experiments the CC RF phase noise was always dominant.
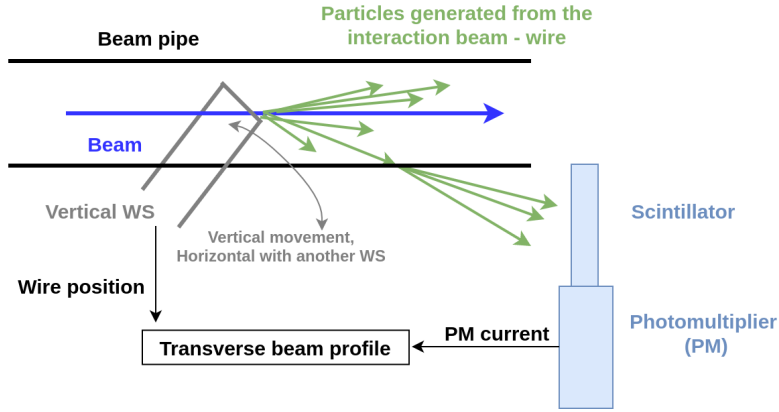
Figure 4.3: Sketch of the SPS rotational wire scanners [75]. The wire moves across the proton beam generating secondary particles which are then detecting by a scintillator and a photomultiplier. From the measured photomultiplier current the beam profile is reconstructed.

Fitting of transverse profiles

Assuming Gaussian beams and for $u = (x, y)$ being the index that corresponds to the horizontal and vertical plane respectively, the rms beam size, σ_u, is obtained following the standard procedure of least squares fitting (see Appendix A.2). In particular, the measured beam profiles from each scan are fitted with the following four-parameter (P, k, μ, σ_u) Gaussian function:

$$f(x) = k + P e^{-\frac{(x-\mu)^2}{2\sigma_u^2}},\tag{4.8}$$

where k is the signal offset of the photomultiplier, P is the signal amplitude, μ is the mean of the gaussian distribution, and σ_u is the standard deviation. The uncertainty of the measured rms beam size, $\Delta\sigma_u$, is defined as the error of the fit of the σ_u parameter (see Appendix A.2).

An example of the beam profile measured from the SPS Wire Scanner at a specific time is shown in Fig. 4.4 (light blue dots) along with the gaussian fit (orange line).

Computing the normalised beam emittance

The formula for computing the normalised beam emittance from the beam size, σ_u is given by:

$$\epsilon_u = \frac{\sigma_u^2}{\beta_{u,WS}}\beta_0\gamma_0,\tag{4.9}$$
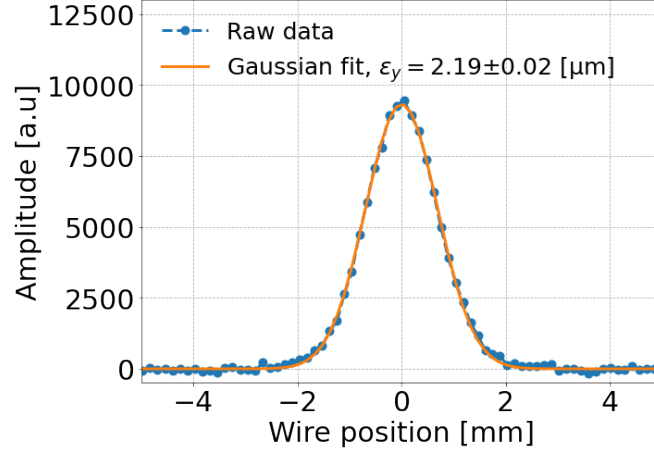
Figure 4.4: Vertical beam profile obtained from the BWS.41677.V instrument. The measured data points (light blue) are fitted with a four-parameter Gaussian (orange) to obtain the beam size. The calculated emittance and its uncertainty are also shown.

where σ_u is the rms beam size, $\beta_{u,WS}$ the beta function at the Wire Scanner location, and β_0, γ_0 the relativistic parameters. Note that $u = x, y$ is the index that respectively corresponds to the horizontal and vertical plane.

Assuming that the relativistic parameters are well known, the uncertainty of the computed emittance, $\Delta\epsilon_u$, depends on the uncertainty of the measured beam size, $\Delta\sigma_u$ and of the beta function at the location of the Wire Scanner, $\Delta\beta_{u,WS}$, as follows:

$$\Delta\epsilon_u = \sqrt{\left(\frac{\partial\epsilon_u}{\partial\sigma_u}\right)^2 \Delta\sigma_u^2 + \left(\frac{\partial\epsilon_u}{\partial\beta_{u,WS}}\right)^2 \Delta\beta_{u,WS}^2} = \epsilon_u\sqrt{\left(\frac{2\Delta\sigma_u}{\sigma_u}\right)^2 + \left(\frac{\Delta\beta_{u,WS}}{\beta_{u,WS}}\right)^2}. \quad (4.10)$$

For the computation of the emittance values from the CC experiment of 2018, the following points were considered. First, in the 2018 SPS operational configuration, the dispersion was small at the Wire Scanner location and thus its contribution to the beam size was considered to be negligible[5]. Moreover, for the studies at 270 GeV beam energy, $\beta_0\gamma_0$ equals 287.8 and the beta functions were 81.5 m and

---

[5]BWS.51995.H location in 2018 was located at a low-dispersion region $D_x < 0.5$ m [76]. At 270 GeV, the energy spread, δ, is of the order of 10^{-4}. Thus, from Eq. (2.33) the horizontal normalised emittance from the dispersion is expected at the order of 9×10^{-3} μm. Comparing to the observed beam size during the CC tests of a few microns the dispersion is negligible and hence it will not be considered in the following. This is also confirmed by past studies [76]. The measured vertical dispersion has a similar value with the horizontal [77] hence its contribution in the measured vertical emittance will also not be considered in the following

4. Experimental studies from 2018: emittance growth from Crab Cavity noise

62.96 m at the locations of the horizontal and vertical Wire Scanner, respectively. The uncertainty on the beta functions at the location of the Wire Scanner, $\Delta\beta_{u,WS}$, is 5% in both planes, which represents the rms beta-beating in the SPS [78].

It is worth noting here that during each measurement with the Wire Scanner the beam profile is actually acquired twice as the wire crosses the beam in the forward direction (IN scan) and then in the reverse direction (OUT scan). For the 2018 measurements the emittance values obtained from IN and OUT scans, $\epsilon_{\text{IN}} \pm \Delta\epsilon_{\text{IN}}$ and $\epsilon_{\text{OUT}} \pm \Delta\epsilon_{\text{OUT}}$, were found to be very similar. In the analysis of the 2018 measurements, the average emittance from the two scans, $\epsilon_{\text{avg}} = \langle\epsilon_{\text{IN}}, \epsilon_{\text{OUT}}\rangle$, is used. The uncertainty in the average, $\Delta\epsilon_{\text{avg},1}$, is given by [79]:

$$\Delta\epsilon_{\text{avg},1} = \frac{|\epsilon_{\text{IN}} - \epsilon_{\text{OUT}}|}{2\sqrt{2}}. \tag{4.11}$$

The propagated uncertainty from the measurement errors, $\Delta\epsilon_{\text{IN}}$ and $\Delta\epsilon_{\text{OUT}}$, is given by:

$$\Delta\epsilon_{\text{avg},2} = \frac{1}{2}\sqrt{\Delta\epsilon_{\text{IN}}^2 + \Delta\epsilon_{\text{OUT}}^2}. \tag{4.12}$$

Assuming that $\Delta\epsilon_{\text{avg},1}$ and $\Delta\epsilon_{\text{avg},2}$ are independent, the combined uncertainty in the average, $\Delta\epsilon_{\text{avg}}$, is given by:

$$\Delta\epsilon_{\text{avg}} = \sqrt{\Delta\epsilon_{\text{avg},1}^2 + \Delta\epsilon_{\text{avg},2}^2}. \tag{4.13}$$

Finally, some emittance increase is expected during each wire scan, due to multiple Coulomb scattering. This effect has been extensively studied in [76]. For the rotational SPS Wire Scanners and the energy of 270 GeV, at which the CC experiments were performed, the expected emittance growth from the Wire Scanner is expected to be a few nanometeres per scan in both transverse planes [76] which is very small with respect to the emittance values of a few micrometers. Nevertheless, a conservative number of scans were carried out, ~20 scans per plane during ~1 hour, in order to minimise the contribution from this effect.

4.5.2 Experimental results

In this section, an overview of the emittance growth measurements is presented. Figure 4.5 displays the bunch-by-bunch transverse emittance evolution throughout the total duration of the experiment. The three different coasts are distinguished in this plot with the blue dashed vertical lines. The values of the effective phase noise are also displayed (see Table 4.3), while the moments when the noise level changed are shown with the grey vertical lines. The four different colors (blue, orange, red, and green) correspond to the four different bunches. For the bunches the notation "bunch N" will be used, where $N = \{1, 2, 3, 4\}$ according to their position in the bunch train. The error bars of the emittance values correspond to the uncertainty computed using Eq. 4.13. However, as they are very small compared to the scale of the plots they are barely visible. Last, the emittance growth rates, $d\epsilon_u/dt$, for each setting and for each bunch are displayed at the bottom of each plot along with their uncertainties. The growth rates are obtained following the standard procedure of weighted least squares fitting (see Appendix A.2). In particular, the measured beam profiles from each scan are fitted with the following polynomial:

$$p(x) = c_0 + c_1 \times t, \tag{4.14}$$

where t is the time in seconds, c_0 corresponds to the initial value of the emittance, while c_1 is the emittance growth rate, $d\epsilon_u/dt$. The uncertainties of the emittance growth rates correspond to the error of the fit (see Appendix A.2).

First observations and comments

Figure 4.5 demonstrates a clear emittance growth in the vertical plane which is expected due to the vertical CC. However, the CC noise is observed to induce growth also in the horizontal emittance as a result of residual coupling in the machine. Thus, the total emittance growth given by $d\epsilon_x/dt + d\epsilon_y/dt$ will be considered in the following. PyHEADTAIL simulations confirmed that in the presence of coupling the emittance growth induced by the CC noise is distributed between the horizontal and vertical planes [80].
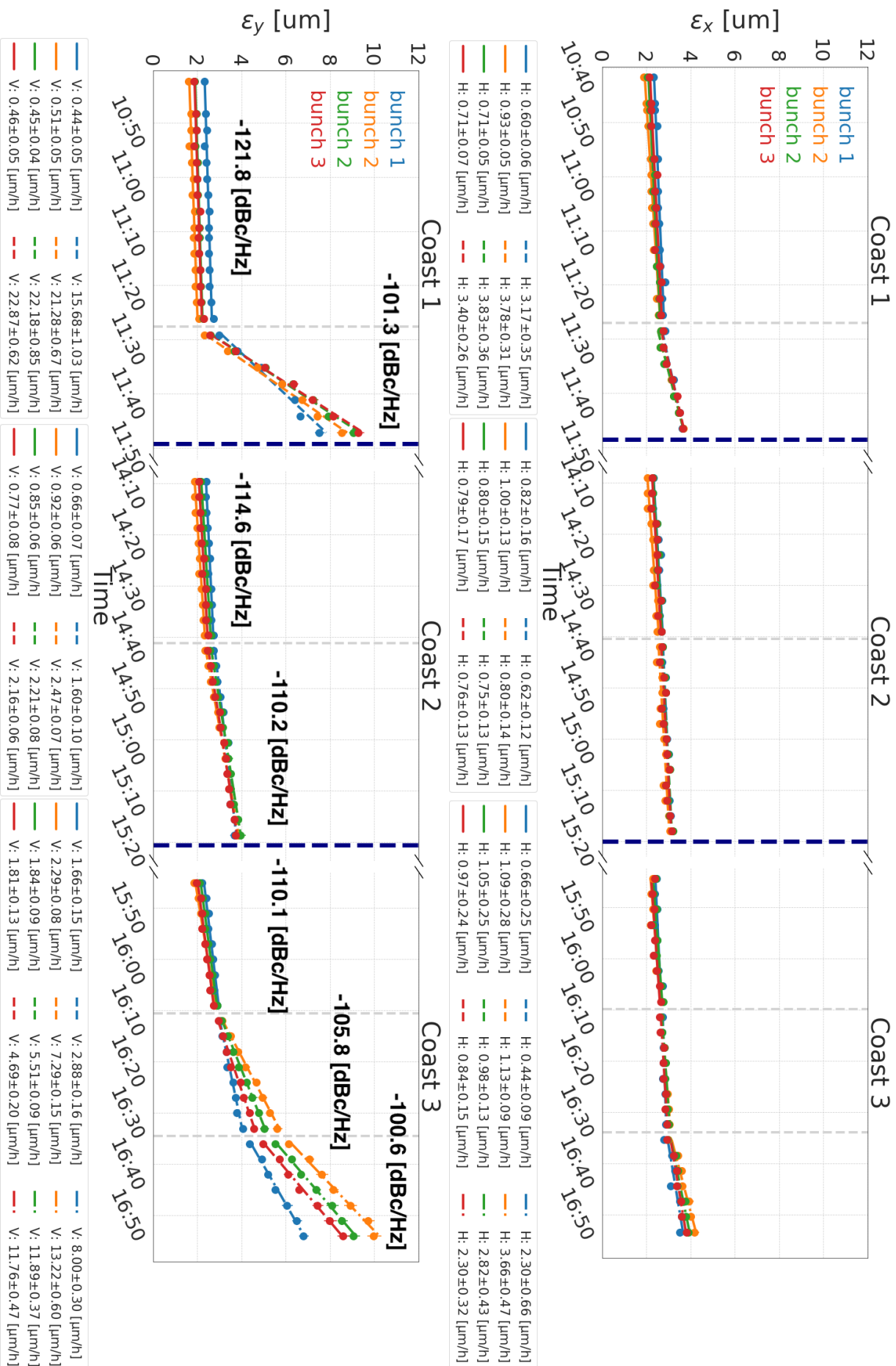
Figure 4.5: Bunch by bunch horizontal (top) and vertical (bottom) emittance evolution during the experiment on September 5, 2018. The four different colors indicate the different bunches. The different applied noise levels are also shown while the moments when the noise level changed are indicated with the grey vertical dashed lines. The emittance growth rates along with their uncertainties for the seven different noise settings are displayed at the legend at the bottom of the plots.

Furthermore, both the phase and amplitude noise levels for Coast1-Setting1 were found to be below the noise floor of the CC. Therefore, the transverse emittance growth observed during that case is a result of other sources (background emittance growth, see Section 4.2.1) and will be considered as the background growth rate in the analysis below.

Summary plot

Figure 4.6 provides a clearer view of the measurements presented in Fig. 4.5. It displays the measured emittance growth rates for each one of the four bunches for the different levels of injected noise. The horizontal error bars correspond to the uncertainty of the effective phase noise (see Section 4.3) while the vertical error bars correspond to the uncertainty of the total transverse emittance growth calculated from the uncertainties of the horizontal and vertical growth rates following the standard procedure of the propagation of the uncertainty (see Appendix A.3).
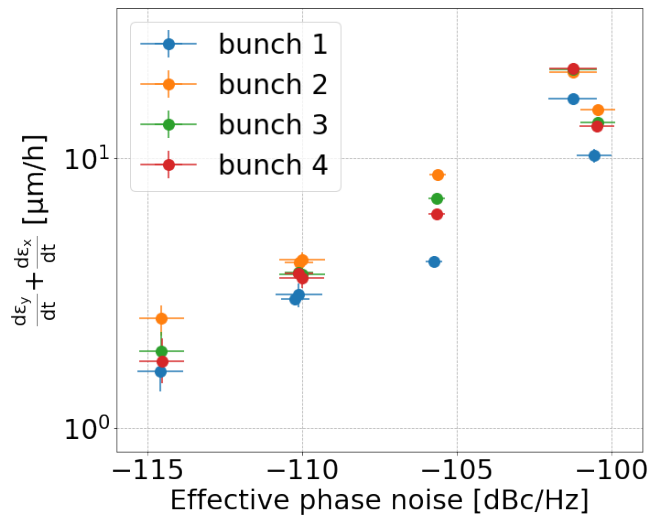
Figure 4.6: Summary plot of the emittance growth study with CC noise in 2018. The transverse emittance growth rate, for the four bunches, is shown as a function of the different levels of applied noise.

From the plot it becomes clear that the measured emittance growth was different for the four different bunches. Furthermore, the first bunch (blue) had systematically the smallest growth rate.

An attempt to understand these observations will be presented in the following section, based on a possible correlation between the transverse emittance growth

and the beam evolution in the longitudinal plane.

4.6   Bunch length and intensity measurements

The measurements of the bunch length and intensity that took place in parallel with the emittance growth measurements are presented in this section. The goal is to get a more complete insight of the experimental conditions and possibly explain the different emittance growth rates observed for the four bunches which was discussed in the previous section.

4.6.1   ABWLM and Wall Current Monitor

The bunch length was measured with two different instruments, the ABWLM[6] [81] and the Wall Current Monitor [82]. Both ABWLM and Wall Current Monitor acquire the longitudinal bunch profiles, but the ABWLM has a higher bandwidth compared to the Wall Current Monitor. In the ABWLM the bunch length is obtained by performing a gaussian fit on the acquired profiles. Only the calculated bunch length values are available but not the profiles themselves. For the Wall Current Monitor the bunch length is estimated by computing the full width half maximum of the profiles and then using it to estimate the standard deviation of a Gaussian distribution. The longitudinal profiles and the calculated bunch lengths are available for each acquisition. Furthermore, the Wall Current Monitor provides additional information on the relative bunch position with respect to the center of the RF bucket, which will also be used in the following analysis. No further details on the operation of these instruments are discussed here as the offline analysis was not performed by the author.

The intensity values obtained from the ABWLM and the Wall Current Monitor are obtained by integration of the longitudinal bunch profiles. Since there is no available calibration for this procedure the measured intensity cannot be expressed in protons per bunch. To this end, the intensity evolution is presented normalised with the initial intensity value (see Fig. 4.9).

---

[6](A for RF, B for Beam, W for Wideband, L for Longitudinal, M for Measurement)

4.6.2 Bunch length measurements

The bunch length measurements that took place during the CC noise induced emittance growth studies are shown in the bottom plot in Fig. 4.7. The small markers correspond to the data acquired with the ABWLM while the bigger markers correspond to the data acquired with the Wall Current Monitor. The color code corresponds to the four different bunches. The blue dashed vertical lines distinguish the three different coasts, while the grey vertical lines indicate the moments when the noise level changed. Four main observations can be made.
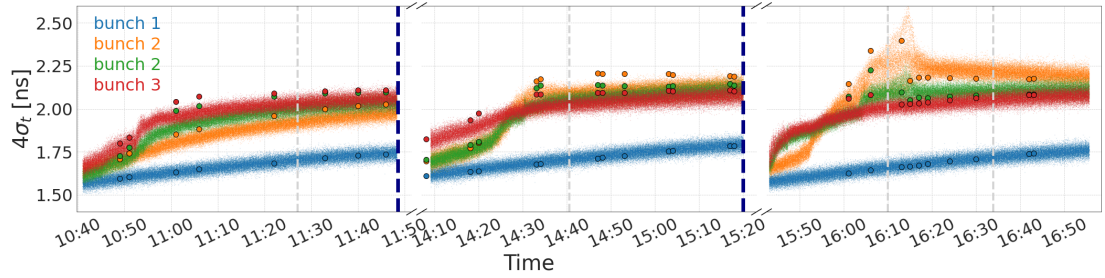
Figure 4.7: Bunch length evolution measured with the ABWLM (small markers) and the Wall Current Monitor (bigger markers) during the CC noise-induced emittance growth experiment.

First, the plot demonstrates a very good agreement between the ABLWM and the Wall Current monitor. Second, a bunch length increase of ~9 %/h is observed for bunch 1 (blue) in all the three coasts. This rate, which is computed from the ABWLM data, is similar as observed previously in the SPS for similar machine conditions [65]. Third, the bunch length increase for the last three bunches (2, 3, and 4) is larger than the increase for bunch 1. However, bunches 2, 3, and 4 seem to be longitudinally unstable as sudden jumps appear in their bunch length evolution and this could explain the faster bunch length increase. Last, no correlation is observed between the bunch length evolution and the change of noise level. In order to validate that bunches 2, 3, and 4 are unstable, the longitudinal profiles acquired with the Wall Current Monitor are studied in the next paragraph.

4.6.3 Longitudinal profile measurements

Two example longitudinal profile acquisitions from the Wall Current Monitor are discussed here as they can provide further insight on the sudden jumps observed

in the bunch length values for bunches 2, 3, and 4. The selected acquisitions correspond to the moments where the sudden jumps are performed in the second and third coast and are shown in Fig 4.8[7]. The relative bunch position with respect to the center of the RF bucket of each bunch for an acquisition period of 7 ms is also illustrated in the bottom plots of Fig. 4.8 for completeness.
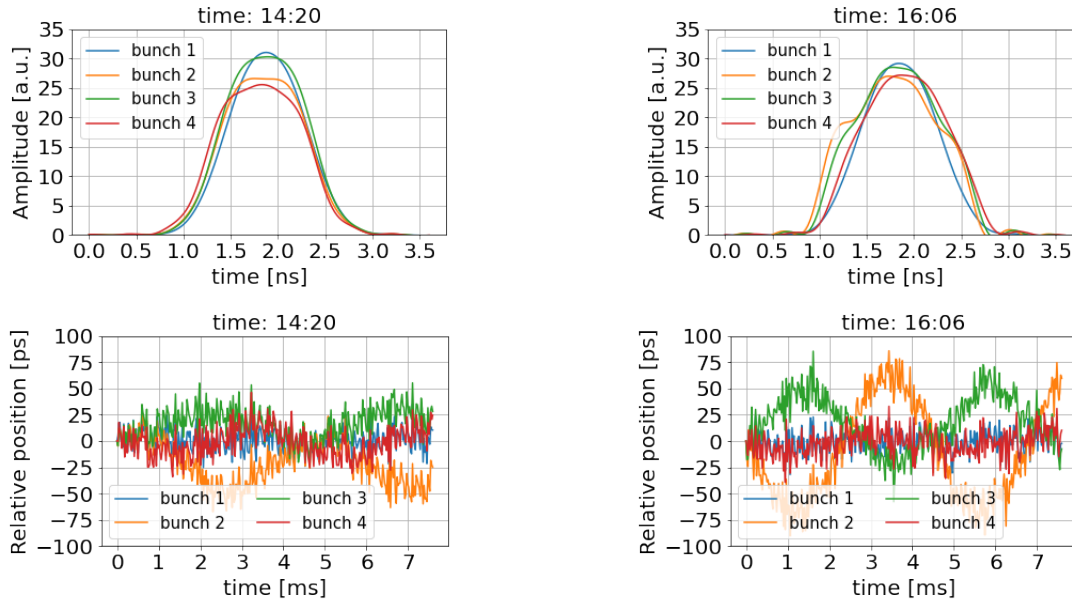
Figure 4.8: Longitudinal profiles (top) and relative bunch position with respect to the center of the RF bucket (bottom) acquired with the Wall Current Monitor. The acquisitions correspond to the times when the sudden jumps in the bunch length evolution are observed (see Fig. 4.7).

The oscillations of the relative bunch position (bottom) of the bunches 2,3 and 4 (orange, green, and red) indicate that the bunches are longitudinally unstable. This is also reflected in the longitudinal profiles (top) which appear distorted. It is believed that this longitudinal instability is caused by the fact that the bunches 2,3, and 4 were out of the sampling gate of the phase loop pickup [83]. For this reason, the following analysis focuses on bunch 1, which was not affected by the instability.

4.6.4 Intensity measurements

The bunch-by-bunch intensity measurements that were performed along the experiment with artificial noise injected in the CC RF system are displayed in Fig. 4.9. In particular, the intensity values normalised with the initial value are

---

[7]The analysis method for the profiles and the relative bunch position shown in Fig. 4.8 was provided by M.Schwarz.

shown for each bunch. The four different bunches are indicated with the four different colors. The acquisitions from both the ABWLM and the Wall Current Monitor are illustrated with the small and bigger markers, respectively.
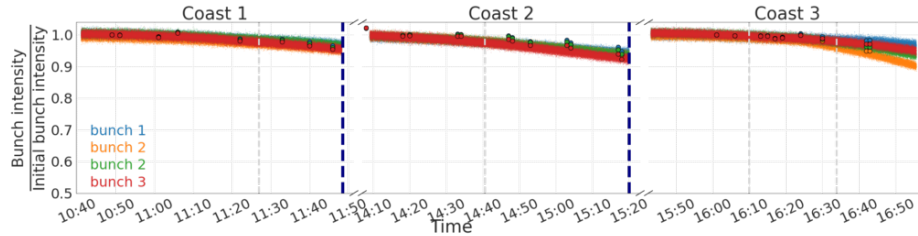
Figure 4.9: Intensity evolution as measured with ABLWM (smaller markers) and with the Wall Current Monitor (bigger markers) during the experiment with CC noise in 2018.

The following observations can be made. First, there is a very good agreement between the measurements from the ABLWM and the Wall Current Monitor. Second, losses of ~2-4 %/h, computed from the ABLWM acquisitions, are observed for bunch 1 (blue) in all the three coasts. This rate is even smaller than observed in the SPS in coast studies without external noise (~10 %/h) [65]. Last, more significant losses are observed for the longitudinally unstable bunches (bunch 2,3, and 4). However, this is not of concern as the last three bunches will not be included in the following analysis.

4.7 Comparison of measured transverse emittance growth with the Mastoridis–Baudrenghien model

This section focuses on the main objective of the experiment which was the comparison of the measured transverse emittance growth with the expected values as computed from the Mastoridis–Baudrenghien model introduced in Chapter 3. As already discussed (Section 4.6.3), the comparison considers only bunch 1 as the other three bunches were found to be longitudinally unstable.

Figure 4.10 compares the measured (blue) and the theoretically calculated (black) emittance growth rates of bunch 1 for the different noise levels. For the comparison, the background emittance growth rate from other sources (measured during Coast1-Setting1, as discussed in Section 4.5) is subtracted from the

measured values. In particular, the background emittance growth was measured as $0.6\,\mu$m/h and $0.44\,\mu$m/h for the horizontal and vertical plane respectively. One should keep in mind that background subtraction has practically no impact for high noise levels. Instead, it is significant for small noise levels.

The expected emittance growth due to CC noise was estimated for all noise settings using Eq. (3.12). The emittance growth was computed for the beam energy of 270 GeV, considering the vertical beta function at the location of the CC2 of 73.82 m and the revolution frequency of SPS which is 43.37 kHz. For each setting, the measured noise power spectral densities (i.e. effective phase noise) and the average bunch length over each observation window were used in the calculation. These values are listed in the first two columns of Table 4.4.

The horizontal error bars, for both measured and calculated growths, correspond to the uncertainty of the effective phase noise values (see Table 4.3). The vertical error bars for the measured emittance growth are defined as the error of the linear fit on the emittance values (see Section 4.5). The vertical error bars on the theoretically calculated emittance growth rates are computed following the standard procedure of propagation of the uncertainty. It should be mentioned here that only the uncertainties on the effective phase noise (~13% on average for bunch 1) are included in the uncertainty propagation. The beam energy and the revolution frequency are assumed to be well known with negligible uncertainty, while the uncertainties of the rest of the parameters: bunch length, CC voltage and beta function (~ 2%, 0.01%, and 5% respectively) are not included as they are much smaller than those of the noise.

From Fig. 4.10 it becomes evident that the theory systematically overestimates the measured emittance growth rates. The averaged discrepancy over all noise levels is a factor of 4: numerical values are given in Table 4.4. It is worth mentioning, that the simulated emittance growth for the experimental conditions (even though it is not shown in the plot) is in very good agreement with the theory and does not agree with the measured data.
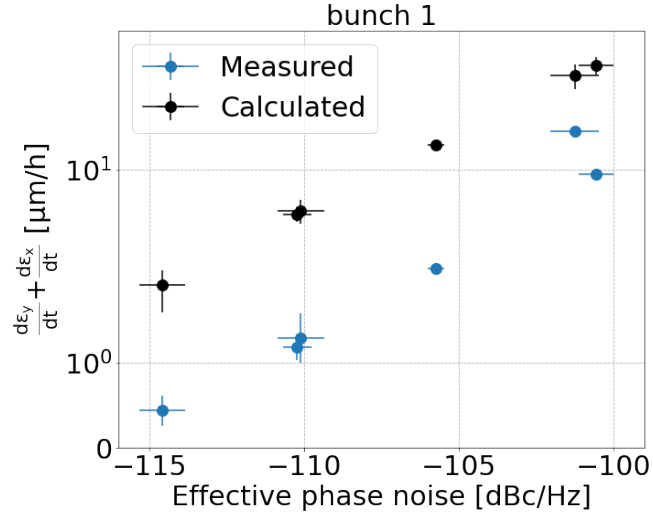
Figure 4.10: Summary plot of the emittance growth study with CC noise in 2018 focused on bunch 1 only. The measured emittance growth rate (blue) and the expected growths from the theoretical model (black) are shown as a function of the different levels of applied noise.

Table 4.4: Comparison between the measured and the calculated transverse emittance growth rates for bunch 1 for the different noise levels, and average bunch length for each case.

$10\log_{10}\mathscr{L}(\mathbf{f})$ [dBc/Hz]	$\langle\sigma_\phi\rangle$ [rad]	Growth rate [μm/h]	
		Measured	Calculated
-114.6	1.05	0.44	1.9
-110.2	1.10	1.18	5.10
-110.1	1.03	1.28	5.38
-105.8	1.06	2.28	14.50
-101.3	1.08	17.81	40.55
-100.6	1.09	47.42	9.26

4.8 Conclusions and outlook

The objective of the first experimental campaign with CC noise in the SPS was to benchmark the available theoretical model of Mastoridis–Baudrenghien against measurements. For this reason, a dedicated experiment took place in the SPS in September of 2018, with different levels of artificial noise injected in the CC RF system. Four bunches circulated in the machine for long periods of time and their emittance evolution was recorded and compared with the theoretical predictions.

The experiment demonstrated that the transverse emittance of all four bunches

increased for stronger noise. However, during the analysis it was found that only the first bunch of the train was stable in the longitudinal plane. For this reason, only the data from the first bunch were used for the comparison with the theoretically calculated emittance growth rates from the Mastoridis–Baudrenghien model. The comparison showed that the theory overestimates the measurements by a significant factor of 4. The reason behind this discrepancy needs to be understood as the predictions of the theoretical model will be used to define limits and acceptable noise levels for the HL-LHC CCs. Therefore, the next chapters focus on explaining the observed discrepancy.

5 | Investigation of the discrepancy between emittance growth theory and experimental data

In Chapter 4 the analysis of the experiment data from the CC experiments in 2018 was presented. It was found that the Mastoridis–Baudrenghien model [27] which predicts the emittance growth in the presence of noise in the CC RF system overestimates the corresponding measurements by a factor of 4 on average. The reason behind this discrepancy needs to be understood in order to gain confidence in the predictions of the Mastoridis–Baudrenghien model in order to correctly define the acceptable noise levels for the low-level RF system of the HL-LHC project. Therefore, this observation triggered a series of studies which are presented in this chapter.

This chapter is structured as follows: First, in Section 5.1 parametric studies based on the theoretical model are presented, exploring the sensitivity of the emittance growth rates to the CC voltage and bunch length. In the following two sections, the theory is benchmarked against two different simulation tools: PyHEADTAIL (in Section 5.2) and Sixtracklib (in Section 5.3). Finally, the main observations and conclusions are discussed in Section 5.4.

The PyHEADTAIL and Sixtracklib simulation results that are presented in this chapter were performed at an early stage of this PhD project. In particular they were performed before the thorough analysis of the experimental data described in Chapter 4. To this end, the simulations were performed for beam and machine conditions similar to the ones of the SPS during the tests with CCs in 2018, but with some small deviations in the bunch length and the beta function at the location of the CC, the value of linear chromaticity and the synchrotron tune. However, it

should be highlighted, that since the objective of these studies was to benchmark the Mastoridis–Baudrenghien model against different simulation codes these small differences in the parameters do not affect the validity of the study. This statement is validated by the simulation studies that will be presented in Chapter 7 which were undertaken with more accurate parameters for the 2018 experiment.

5.1   Parametric studies based on the theoretical model

The basics of the existing theoretical model (Mastoridis–Baudrenghien model) which describes the emittance growth in the presence of amplitude and phase noise in CCs in a storage ring have been introduced in Chapter 3. In this section, the Mastoridis–Baudrenghien model is used to study the sensitivity of the noise-induced emittance growth on the CC voltage and rms bunch length. The objective of the study is to investigate if the uncertainty in the measurements of these two variables could explain the observed discrepancy of a factor ~4 between measured emittance growth and the analytically predicted values (see Section 4.7).

The parametric studies in this section were performed for parameters similar to the experimental configuration of 2018: beam energy of 270 GeV, vertical beta function of 73 m (at the location of CC2), and phase and amplitude noise of -111.4 and -115.7 dBc/Hz respectively (Coast2-Setting2). The phase and amplitude noise are considered here independently, instead of the effective phase noise, due to the different dependence of the correction term (see Fig. 3.3).

5.1.1   Sensitivity to bunch length

Using Eqs. (3.11) and (3.12) with the above-mentioned parameters and CC voltage, $V_{0,\mathrm{CC}}$ =1 MV the normalised vertical emittance growth is computed as a function of different values of bunch length over a range from 0.001 ns to 2.5 ns (expressed in $4\sigma_t$). The results are illustrated in Fig. 5.1.

A clear dependence of the vertical emittance growth on the bunch length is observed. However, there is only a strong dependence for bunch lengths within a certain range. In the regime of the measured bunch length during the CC

experiment for bunch 1 (~1.6 ns- 2.0 ns) the sensitivity to the bunch length is very small and cannot explain the factor of about 4 that was observed between measurements and theoretical predictions in SPS CC tests in 2018.
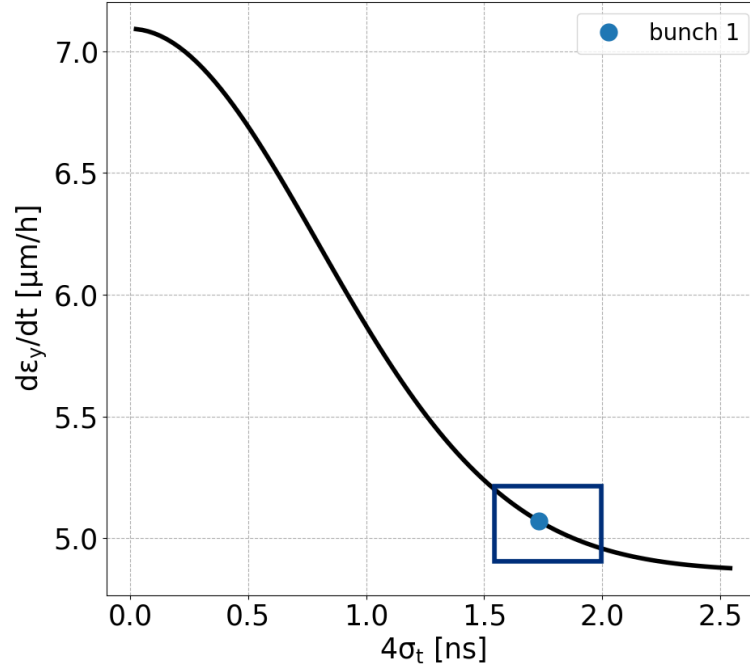
Figure 5.1: Vertical emittance growth for different bunch length values computed using the analytical formulas Eqs. (3.11) and (3.12) for the experimental configuration of 2018. The blue dot shows the average bunch length over all coasts in 2018. The blue box around it gives the upper and lower limits of its measurements.

5.1.2 Sensitivity to CC voltage

Here, the sensitivity of the vertical emittance growth is studied for the parameters mentioned above and bunch length of $4\sigma_t = 1.7$ ns. The vertical emittance growth is computed again analytically using Eqs. (3.11) and (3.12) over a range of CC voltage values equally spaced from 0.6 to 1.3 MV.

Figure 5.2 illustrates the computed vertical emittance as a function of the CC voltage. From the analysis in 2018, the calibration of the CC voltage (which showed 1 MV) was not straightforward. However, from the plot it is evident that even if the actual voltage was 30% lower due to measurement errors this would lead to just a factor of 2 lower vertical emittance growth. An error of this scale is not realistic. To this end, it is concluded that uncertainties on the beam-based

measurements of the CC voltage cannot explain the experimental observations of 2018, where there was a factor 4 between measured and predicted emittance growth.
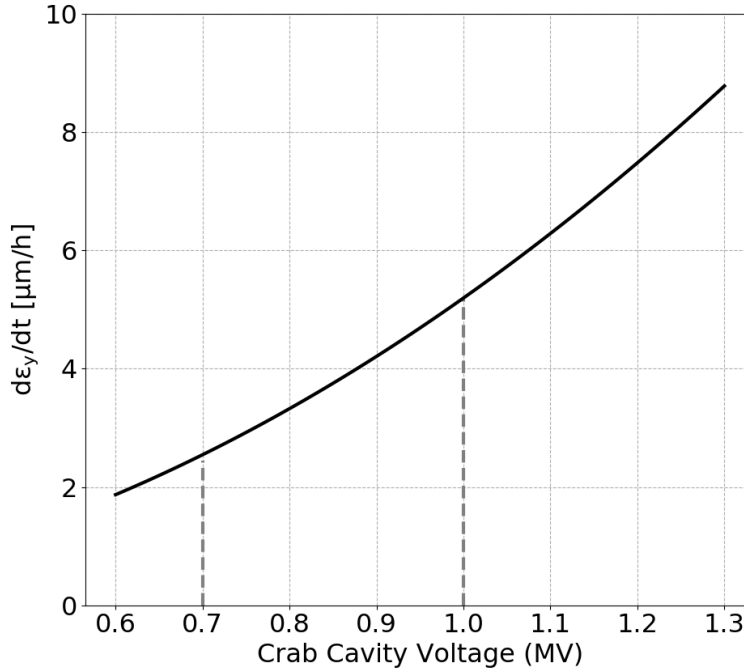
Figure 5.2: Vertical emittance growth for different values of CC voltage computed using the analytical formulas Eq. (3.11) and (3.12) for the experimental configuration of 2018.

5.2   Benchmarking theory against PyHEADTAIL

As mentioned in Chapter 3 the Mastoridis–Baudrenghien model which predicts the emittance growth driven by CC RF phase and amplitude noise was benchmarked against simulation results with the HEADTAIL [27] simulation tool. In this section, the predictions of the model are benchmarked against the PyHEADTAIL simulation tool. PyHEADTAIL is the implementation of the HEADTAIL (which was written in C/C++ language) in Python, so that it can be more easily maintained and extended [53]. Further details on the PyHEADTAIL are provided in the introductory Subsection 2.5.1.

The parameters used for setting up the linear transfer map, the longitudinal tracking, and the initialisation of the beam distribution are shown in Table 5.1: they are similar to the parameters in the SPS CC experiments of 2018. The accelerator

ring consists of one segment, with one interaction point, where the beam receives the noise kicks from the CC every turn. In particular, at that location, the angle variable, y', of each particle within the bunch is updated every turn following the description of Eqs. (3.7) and (3.8) for modeling the phase and amplitude noise respectively. The vertical angle co-ordinate is updated to study the vertical emittance growth following the experiments of 2018 where the CC module that was used provided a vertical deflection to the bunches. Nevertheless, the beam dynamics are the same in the horizontal plane.

The simulations were performed for both phase and amplitude CC RF noise. The noise level was chosen to be much stronger than the levels used in the experiment of 2018 in order to observe a reasonable emittance growth in the 10^5 turns simulated. For reference, this corresponds to about 2.5 s in the SPS machine.

In particular, the simulations were performed using a sequence of noise kicks with length $N_{\text{turns}} = 10^5$, mean 0 and standard deviation of $\sigma_{\Delta\phi} = 2.7 \times 10^{-3}$ rad for phase noise and $\sigma_{\Delta A} = 2.7 \times 10^{-3}$ for amplitude noise. This corresponds to a total noise power of $\sigma_{\Delta\phi}^2 = 7.3 \times 10^{-6}$ rad^2 and $\sigma_{\Delta A}^2 = 7.3 \times 10^{-6}$ or to a power spectral density of 1.68×10^{-10} rad^2/Hz or 1/Hz (for phase and amplitude noise respectively).

In the simulations, the beam particles encounter the phase or amplitude noise kicks once per turn. This means that the sampling frequency of the noise spectrum in the frequency domain equals, $f_s = f_{\text{rev}} = 43.37$ kHz. Thus, the frequency spectrum of the noise applied in the simulations extends from $-f_s/2 \approx -22$ kHz to $+f_s/2 \approx 22$ kHz. This is visible in the power spectra of the sequence of amplitude and phase noise kicks (discrete-time signal) which are plotted in Fig. 5.3. The power spectral densities are computed using Eq. (B.10).

Following the discussion in Section 4.3.1 it is evident that the noise applied in the simulations also overlaps and excites the first betatron and synchrobetatron sidebands. Therefore, to predict the vertical emittance growth from CC RF and amplitude and phase noise according to Mastoridis–Baudrenghien model, one can use the simplified Eqs. (4.5) and (4.6), respectively.

The simulations were performed for a single bunch. The initial bunch was

5. Investigation of the discrepancy between emittance growth theory and experimental data
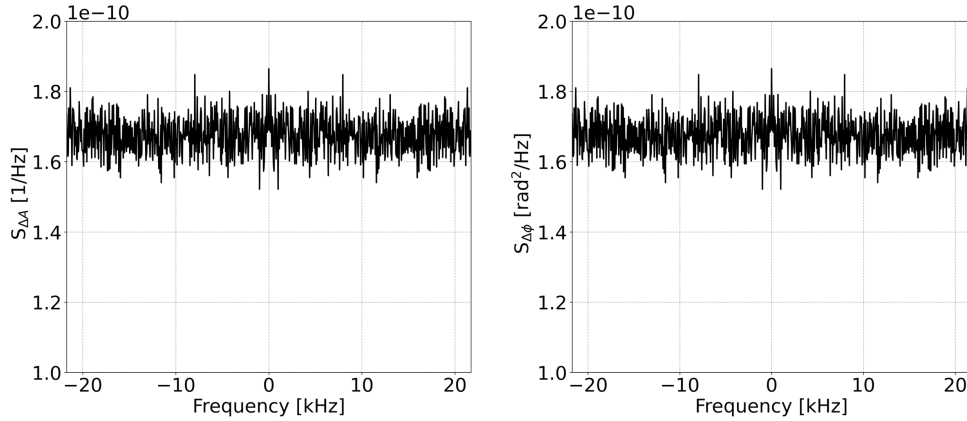
Figure 5.3: Power sepctra of the CC amplitude (left) and phase (right) noise used in the PyHEADTAIL simulations.

generated with Gaussian distributions in transverse and longitudinal planes[1]. The bunch intensity of 3×10^{10} protons was represented by 10^5 macroparticles.

The beta function at the location of the interaction point was chosen to be the value at the location of CC1 for both horizontal and vertical planes (values are listed in Table 5.1). At the same location, the Twiss parameter alpha and the dispersion were chosen to be zero. This is a valid assumption for the studies since these parameters have no direct impact on the noise-induced emittance growth [27]. This is also confirmed, with simulations with the Sixtracklib code which are presented in the following section. The Sixtracklib simulations use the detailed optics of the machine for the tracking. It will be shown that the emittance growth rates from the two simulation tools are in good agreement.

The mechanism responsible for the emittance growth in the presence of noise is the spread of the betatron tunes [58]. As explained earlier (in Section 3.1) the tune spread leads to a phase mixing of the particles within the bunch causing a decoherence of the betatron oscillations which then results in emittance growth [58]. The time scale of the decoherence equals the inverse of the betatron frequencies [58]:

$$\tau_{\text{decoh}} = \frac{1}{2\pi f_{\text{rev}} \Delta Q_u^{\text{rms}}}, \tag{5.1}$$

---

[1]The longitudinal distribution in reality is not a Gaussian but it was found that the shape of the longitudinal profile has no significant impact on the predicted emittance growth rates. These studies were performed by T. Mastoridis and P. Baudrenghien [84]. The simulation studies presented in this thesis used a Gaussian longitudinal distribution following the studies presented in Ref. [27].

80

Table 5.1: Simulation parameters used to benchmark the theoretically predicted emittane growth in Chapter 5.

Parameter	Value
Beam energy, E_b	270 GeV
Machine circumference, C_0	6911.56 m
Horizontal / vertical betatron tune, Q_{x0} / Q_{y0}	26.13 / 26.18
Synchrotron tune, Q_s	0.0035
Number of bunches	1
Rms bunch length, σ_z	15.5 cm
Horizontal / vertical normalised emittance, ϵ_x / ϵ_y	2 μm / 2 μm
Horizontal / vertical beta function, $\beta_{x,CC1}/\beta_{y,CC1}$	29.24 m / 76.07 m [†]
Number of macroparticles, N_{mp}	10^5
Number of turns, N_{turns}	10^5

[†] Model values for the Q26 optics.

where $u = (x, y)$ indicates the horizontal or vertical plane, f_{rev} the revolution frequency, and ΔQ_u^{rms} the rms betatron tune spread. The latter can be computed by Eqs. (C.6) and (C.7) for the vertical and horizontal planes respectively.

Therefore, it becomes clear that in order to observe some emittance growth a source of tune spread must be included in the simulations. For the simulations presented here detuning with transverse amplitude is introduced as described in Section 2.5.1, by applying a change of the phase advance of each individual particle depending on its action variable and the detuning coefficients. Detuning in both transverse planes is thus introduced for horizontal detuning coefficient $\alpha_{xx} = 179.35/$m, vertical detuning coefficient $\alpha_{yy} = -30.78/$m and for cross-term coefficient $\alpha_{yx} = -441.34/$m. These coefficients were computed using MAD-X [48] for the nominal SPS lattice (introduced in Section 2.4) and for $Q'_{x,y} = 0.5$. It should be noted that the detuning in the vertical plane is the value of interest since the emittance evolution will be investigated in the vertical plane. Using Eq. (C.6) for the above mentioned coefficients and the initial transverse actions of the bunch yields $\Delta Q_y^{rms} \approx 7 \times 10^{-6}$.

For the emittance growth studies to be valid the simulation time should be much longer than the decoherence time defined in Eq. (5.1). For the above value of rms vertical tune spread, the decoherence time is computed to be $\tau_{decoh} \approx 0.5$ s. Therefore, the simulation time of about 2.5 s is reasonable for these studies.

5. Investigation of the discrepancy between emittance growth theory and experimental data

The tracking was performed for 10^5 turns and the geometric emittance was computed every 100 turns (for computational efficiency) using the statistical definition introduced in Eq. (2.27). The normalised emittances were obtained using Eq. (2.28). To reduce the statistical uncertainty of the results, due to the way the noise kicks are applied, the simulation was performed for 30 different runs. The initial bunch distribution and the sequence of the uncorrelated noise kicks were randomly regenerated every run (a different seed was used in the random generator).

The PyHEADTAIL simulation results are summarised in Fig. 5.4. The simulated vertical emittance evolution in the presence of amplitude noise (left) and phase noise (right) is plotted as a function of time. For both noise types, the theoretically predicted emittance growth (computed using Eqs. (4.5) and (4.6) for the above mentioned parameters) is shown with the red line. The dark orange and dark blue lines show the evolution of the averaged emittance values over the different runs. The shaded areas, (light orange and light blue color), depict the standard deviation of the different emittance values over the 30 runs. The emittance growth rate is obtained with a linear fit to the averaged normalised emittance values over the simulation time. The slope that corresponds to the emittance growth rate obtained by this fit is also drawn in the plot in black color. The uncertainty on the slope of the fit is displayed in the legend.

It is worth commenting, that the emittance growth rates here are expressed in nm/s instead of μm/h that was used for the experimental results. This is due to the time scale of the simulations.

It can be seen, that for the amplitude noise case there is excellent agreement between the theoretical prediction, from Mastoridis–Baudrenghien model, and the simulated emittance growth rate. For the phase noise case, the agreement between expected and simulated emittance growth is very good. The simulated growth appears slightly lower than the theoretical predictions. However, this difference is insignificant compared to the factor of about 4 observed between the theory and the measurements of 2018. A possible reason for the small discrepancy between simulation and theory is the very small tune spread. Later simulations with larger
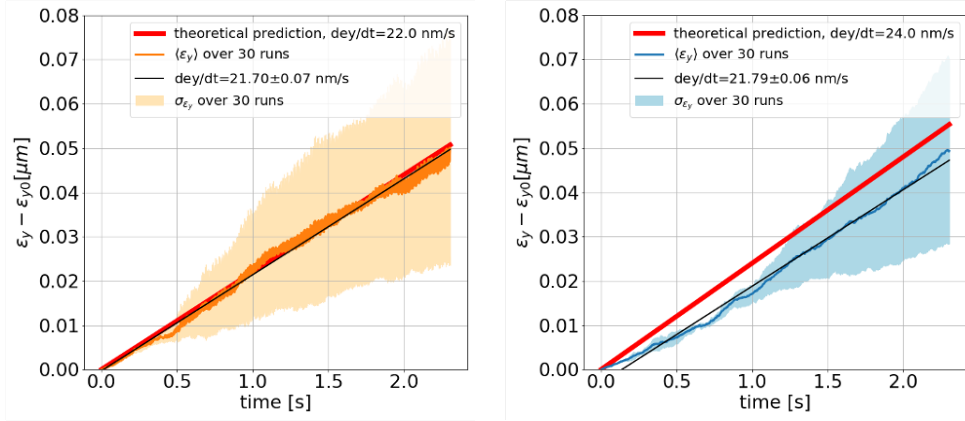
Figure 5.4: Vertical emittance growth driven by CC RF amplitude noise (left) and phase noise (right) as simulated with PyHEADTAIL for a configuration close to the experimental conditions of the SPS CC tests in 2018.

vertical tune spread (closer to the realistic tune spread in the SPS during the 2018 experiments (see Section 6.3)) show excellent agreement between the PyHEADTAIL results and the theoretically computed values. Nevertheless, this small difference does not affect the conclusions drawn from the results, as will be shown in the following chapters.

In general, it can be concluded that the transverse emittance growth driven by CC RF noise obtained by PyHEADTAIL simulations is in good agreement with the theoretically expected values from the Mastoridis–Baudrenghien model. In the following section, the theory is benchmarked against a more complete simulation tool, Sixtracklib.

5.3 Benchmarking theory against Sixtracklib

This section summarises the results of validating the Mastoridis–Baudrenghien theoretical model against numerical simulations with Sixtracklib [55]. The additional comparison between theory and simulation is motivated by the fact that PyHEADTAIL and theory may miss some beam dynamics effects that could explain the discrepancy between their results and the experimental observations of 2018. Sixtracklib is a more complete simulation tool than PyHEADTAIL as the tracking simulations use the detailed optics of the machine and therefore is considered appropriate for this study. Calculations can be performed on GPU decreasing the

required computational time. For the simulations presented in this section the nominal SPS model for Q26 optics will be used [49] as introduced in Section 2.4 except if it is stated otherwise.

5.3.1 Emittance growth simulations with CC noise modeled as transverse kicks on the angle co-ordinate.

The emittance growth simulations presented in the previous section were repeated with Sixtracklib instead of PyHEADTAIL. This basically means that the detailed optics of the SPS machine elements including non-linear elements are used for the tracking instead of modelling the ring as a simple transfer map with one interaction point where the CC kick is applied. The nominal SPS lattice of MAD-X is used: dipoles, quadrupoles, and chromatic sextupoles as discussed in Section 2.4. It can be found in the GitLab repository of [49]. The linear chromaticity was adjusted to be in the range $1 < Q'_{x,y} < 2$. The relevant machine and beam parameters are listed in Table 5.1.

The rms betatron tune spread here is slightly higher than 7×10^{-6} that was computed in the previous section, due to the larger values of linear chromaticity. To this end, tracking for 10^5 turns is reasonable also for these studies. The initial distribution of 10^5 particles follows a gaussian both in transverse and longitudinal planes.

The emittance growth was simulated in Sixtracklib in the presence of both amplitude and phase noise. The noise kicks were implemented as kicks on the vertical angle co-ordinate of each particle following the previous PyHEADTAIL simulations. The noise kicks were applied on the beam at the location of CC1. The power spectral density of the noise at the betatron frequency was 1.68×10^{-10}/Hz and rad^2/Hz for amplitude and phase noise respectively. This corresponds to a total noise power of $\sigma^2_{\Delta A} = 7.3 \times 10^{-6}$ and $\sigma^2_{\Delta \phi} = 7.3 \times 10^{-6}$ rad^2 respectively.

The emittance and emittance growth values were computed with the same procedure followed for the previous PyHEADTAIL simulations (see Section 5.2). Figure 5.5 summarizes the simulated emittance growth driven by amplitude (left) and phase noise (right). For both types of noise, the theoretical prediction of the

emittance growth is shown by the red line. The dark blue and dark orange lines show the evolution of the averaged emittance values over 30 different runs. The shaded areas, shown with light blue and light orange colors, depict the standard deviation of the emittance values over the 30 different runs. The emittance growth rate is obtained with a linear fit to the averaged normalised emittance values over the simulation time. The resulting fits are shown in the plots as black lines. The uncertainty on the slope of the fit is displayed in the legend.

Figure 5.5: Vertical emittance growth driven by CC RF amplitude noise (left) and phase noise (right) as simulated with Sixtracklib simulation tool for a configuration close to the experimental conditions of the SPS CC tests in 2018. The CC noise is modelled as uncorrelated kicks on the angle variables of the particle every turn following Eqs. (3.8) and. (3.7) for phase and amplitude noise, respectively.

From these plots, it becomes evident that there is an excellent agreement between the theoretically predicted vertical emittance growth and the simulation results with Sixtracklib. The emittance growth rates from Sixtracklib simulations are also in agreement with the results from PyHEADTAIL. To this end, it is concluded that taking into account the detailed optics including machine non-linearities of the SPS cannot explain the discrepancy between expected and measured emittance growth that was observed in the SPS CC tests in 2018.

Finally, the spread between the emittance values obtained from the different runs in Sixtracklib and PyHEADTAIL simulations is commented here. By comparing Figs. 5.4 and 5.5 it is evident that in the presence of phase noise (right) the spread of the emittance growth between the different simulation runs is similar. However, in the presence of amplitude noise (left) the spread of the emittance growth between different runs is significantly smaller in Sixtracklib results compared to

the PyHEADTAIL results. It should be noted, however, that the simulated emittance growth is quite small and even small differences in the two codes could lead to different behavior and might explain the different results. For example, in Sixtracklib simulations non-linear elements are included. On the contrary in PyHEADTAIL non-linear elements are not included and the amplitude detuning is introduced as a change in the phase advance of each individual particle. Nevertheless, the codes agree on the average emittance growth rate and this issue does not affect the conclusions drawn from the results presented in this thesis.

5.3.2   Implementation of Crab Cavity in Sixtracklib

Sixtracklib provides the possibility to perform tracking simulations in the presence of an actual CC element on which noise can be added, instead of modelling only the transverse momentum kicks due to phase and amplitude noise in the RF system of the cavity (as was done in PyHEADTAIL). This provides the opportunity to study the CC RF noise-induced emittance growth in a more realistic scenario and therefore it will be used for the rest of the simulations presented in this chapter.

In Sixtracklib the CC is represented by the "RF-Multipole" element [55] that has the properties of a multipole magnet oscillating at a specified frequency. To simulate the vertical CC, the multipole field component corresponds to a skew RF dipole.

When a particle passes through this element, the change in the vertical angle of each particle is the following:

$$\Delta y'_j = \frac{eV_{0,\mathrm{CC}}}{p_0 c} \cos\left(\phi_{\mathrm{RF-Mult}} - \frac{2\pi f_{\mathrm{CC}}}{c}\frac{z}{\beta_0}\right), \tag{5.2}$$

where $j = 0, ..., N_{\mathrm{turns}}$ denotes the turn number with N_{turns} being the total number of turns that the beam passes through the element. In Eq. (5.2), y' is the vertical angle co-ordinate and z is the longitudinal co-ordinate of each particle, $\phi_{\mathrm{RF-Mult}}$ is the phase of the RF-Multipole, f_{CC} is the CC frequency, c is the speed of light, e the elementary charge, β_0 is the relativistic beta, $V_{0,\mathrm{CC}}$ is the amplitude of the CC voltage and p_0 the reference momentum.

Before using this element for the emittance growth simulations its implementation

in Sixtracklib was tested. The CC element installed at a location s_0, acts like a single dipole field error with a strength depending on the longitudinal position z of the particle. To this end, the induced orbit shift from the CC (represented by the RF-Multipole element) as detected at another location s_1 is benchmarked against the theoretically expected orbit shift.

The theoretically expected orbit shift can be computed with Eq. (5.3). Equation (5.3), which is obtained from Eq. (1) from chapter 4.7.1 in [85], gives the vertical orbit shift (in meters) from the CC kick (at the location s_0), at the location s_1 as follows:

$$\Delta y_{,s_1} = \frac{\sqrt{\beta_{y,s_1}}}{2\sin(\pi Q_{y0})}\Delta y' \sqrt{\beta_{y,s_0}}\cos(\pi Q_{y0} - |\psi_{y,s_1} - \psi_{y,s_0}|), \tag{5.3}$$

which after inserting, $\Delta y'$ from Eq. (5.2) for any turn becomes:

$$\Delta y_{,s_1} = \frac{\sqrt{\beta_{y,s_1}\beta_{y,s_0}}}{2\sin(\pi Q_{y0})}\left(\frac{eV_{0,\mathrm{CC}}}{p_0 c}\cos\left(\phi_{\mathrm{RF-Mult}} - \frac{2\pi f_{\mathrm{CC}}}{c}\frac{z}{\beta_0}\right)\right)\cos(\pi Q_{y0} - |\psi_{y,s_1} - \psi_{y,s_0}|),$$
$$\tag{5.4}$$

where Q_{y0} is the vertical tune, β_{y,s_0} and β_{y,s_1} are the vertical beta function at the locations s_0 and s_1 respectively and $|\psi_{y,s_1} - \psi_{y,s_0}|$ is the vertical phase advance in radians between the locations s_0 and s_1.

Figure 5.6 plots the vertical co-ordinate at the location s_1 (orange) after tracking 1000 particles for 500 turns with Sixtracklib in the presence in the presence of the above-mentioned CC element (which is installed at the location of CC1, location s_0). The locations s_1 is the start of the lattice, which for this study it was considered to be the horizontal rotational Wire Scanner, BWS.51995.H. The simulations took place using an initial Gaussian bunch distribution in the six-dimensional phase space. The initial normalised emittances were ϵ_x=2.5 μm and $\epsilon_y = 2.5 \times 10^{-6}$ μm for the horizontal and vertical plane respectively. The distribution was chosen to be so small in the vertical plane so there is practically no initial offset which facilitates the observation of the orbit shift. The most relevant parameters are

5. Investigation of the discrepancy between emittance growth theory and experimental data

listed in Table 5.2.

The orbit shift computed analytically using Eq. (5.4) is also plotted in Fig. 5.6 (blue) for the same parameters used in the simulation. The orbit shift was computed over a range of equally spaced z co-ordinates from -0.6 to 0.6 m ($\sim 3\sigma_z$ of the initial distribution used in the simulations).
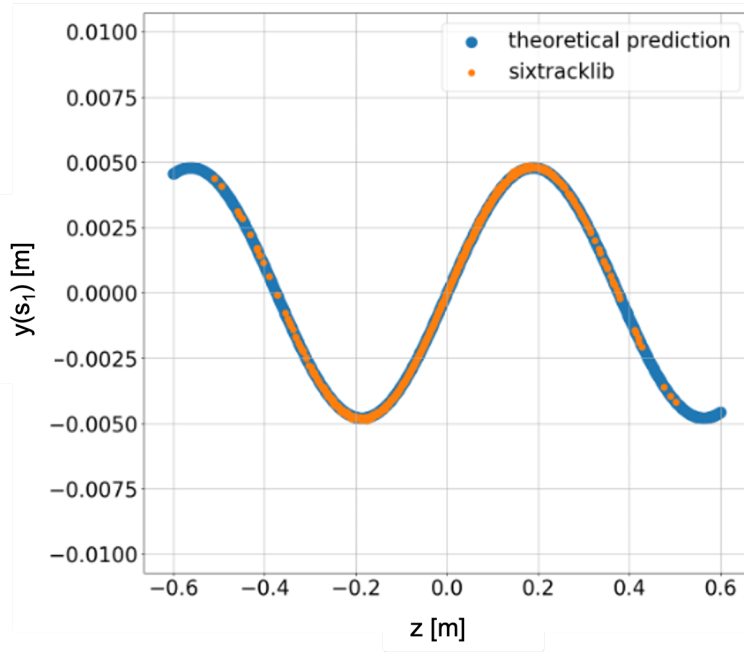
Figure 5.6: Vertical orbit shift at the location of the horizontal Wire Scanner (SPS.BWS.51995.H.) induced by the CC element as computed analytically (blue) and from tracking simulations with Sixtracklib (orange).

By looking at Fig. 5.6 it is concluded, that using Sixtracklib the result of CC element on the orbit is as expected from the analytical calculations.

The amplitude and phase noise in the CC element are modelled as the following change of the vertical angle of each particle (modifying Eq. (5.2)):

$$\Delta y'_j = \frac{e(V_{0,CC} + \Delta V_{0,CC\,j})}{p_0 c} \cos\left(\left(\phi_{\text{RF-Mult}} + \Delta\phi_j\right) - \frac{2\pi f_{CC}}{c}\frac{z}{\beta_0}\right), \tag{5.5}$$

where $j = 0, ..., N_{\text{turns}}$ denotes the turn number with N_{turns} being the total number of turns that the beam passes through the element. Furthermore, $\Delta\phi_j$ is the deviation from the nominal phase (phase noise level), and $\Delta V_{0,CC\,j}$ is the deviation from the nominal amplitude $V_{0,CC}$ (amplitude noise level) at the jth turn.

Table 5.2: Parameters for computing the vertical orbit shift induced by the CC element (at the location s_0) at the location of the horizontal Wire Scanner (SPS.BWS.51995.H.), s_1.

Parameter	Value
Beta function at the Wire Scanner, β_{y,s_1}	27.47 m
Phase advance to the Wire Scanner*, ψ_{y,s_1}	0
Beta function at the CC1, $\beta_{y,CC1}$	76.07 m
Phase advance to the CC1*, $\psi_{y,CC1}$	$4.05 \times 2\pi$
Vertical betatron tune, Q_{y0}	26.18
Beam energy, E_b	26 GeV
Rms bunch length, σ_z	0.22 m
Rms momentum spread, σ_δ	1e-4
CC voltage, $V_{0,CC}$	3 MV
CC frequency, f_{CC}	400 MHz
RF-Multipole phase, $\phi_{RF-Mult}$	90 deg[†]

* The phase advances are measured from the start of the lattice which is considered the element SPS.BWS.51995.H that is the horizontal rotational Wire Scanner.
[†] It was found that in the definition of the RF-Multipole the phase of the cavity is shifted by 90 degrees compared to the standard (theoretical) CC kick.

In the following simulations (unless it is stated otherwise) the parameters $\Delta\phi_j$ and $\Delta V_{0,CC_j}$ are the jth elements of a set of N_{turns} samples, drawn from Gaussian distributions of size N_{turns}, with mean zero and standard deviation of $\sigma_{\Delta\phi}$ and $\sigma_{\Delta V_{0,CC}}$ respectively. The typical values that will be used in the following simulations for phase and amplitude noise respectively are: $\sigma_{\Delta\phi} = 2.7 \times 10^{-3}$ rad and $\sigma_{\Delta V_{0,CC}} = 0.0027$ MV.

The parameter $\Delta V_{0,CC_j}$ is related to the relative deviation from the nominal amplutude ΔA_j of Eq. (3.7) as follows: $\Delta A_j = (\Delta V_{0,CC_j}/V_{0,CC})c$. Consiquently, one can write: $\sigma_{\Delta A} = (\sigma_{V_{0,CC}}/V_{0,CC}) = 2.7 \times 10^{-3}$. These values result in power spectral densities at the betatron frequency of: $S_{\Delta_A}(f_b) = 1.68 \times 10^{-10}$/Hz for amplitude noise and $S_{\Delta_\phi}(f_b) = 1.68 \times 10^{-10}$ rad^2/Hz for phase noise (same as in the simulations presented already in this chapter).

5.3.3 CC noise-induced emittance growth in the presence of local CC scheme

In this section, the emittance growth driven by CC RF noise is simulated with Sixtracklib in the presence of a local CC scheme. As previously mentioned, in the

5. Investigation of the discrepancy between emittance growth theory and experimental data

local CC scheme (Fig. 1.4) two CCs are used with opposite phases, to cancel out the orbit distortion.

The benchmark with the local scheme is performed as it is closer to the case that was studied previously: where the CC RF noise is modelled as noise kicks in the transverse angle co-ordinate of the individual particles. Both configurations avoid introducing any orbit distortion from the CCs.

The simulation studies presented in Section 5.3.1 were repeated here but this time the CCs (represented by the RF-Multipole) were implemented and switched on. Both CC1 and CC2 operated at $1\,$MV, for $\phi_{\text{RF}-\text{Mult},1}$=90 deg and $\phi_{\text{RF}-\text{Mult},2}$=270 deg. Figure 5.7 shows that the orbit shifts from two CCs operating in opposite phases cancel out as expected. The results shown are obtained from Sixtracklib simulations that were conducted following the same procedure as the equivalent study presented in Section 5.3.2 (see Fig. 5.6.)
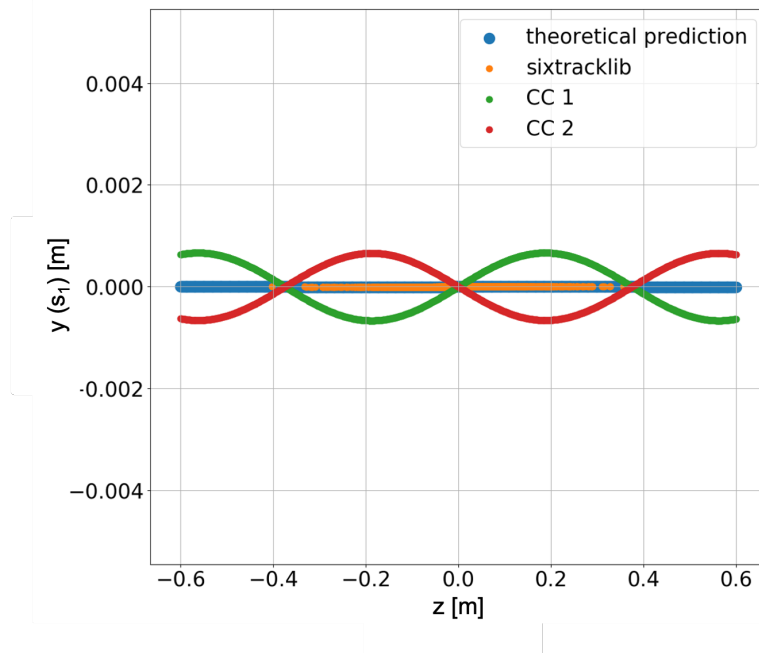
Figure 5.7: Vertical orbit shift at the location of the horizontal Wire Scanner (SPS.BWS.51995.H.) as obtained with Sixtracklib tracking through the nominal SPS lattice. *Green:* Only CC1 operates at $1\,$MV and $\phi_{\text{RF}-\text{Mult},1}$=90 deg. *Red:* Only CC2 operates at $1\,$MV and ϕ_{CC2}=270 deg. *Orange:* The two CCs operate at the same voltage but in opposite phase: $\phi_{\text{RF}-\text{Mult},1}$=90 deg and $\phi_{\text{RF}-\text{Mult},2}$=270 deg. *Blue:* Orbit shift calculated analytically using Eq. (5.4).

For the emittance growth simulations, the noise was applied only in CC1. The

amplitude and phase noise were treated separately and for the simulation parameters a growth of 22 nm/s and 24 nm/s is expected respectively. The simulation results are illustrated in Fig. 5.8.
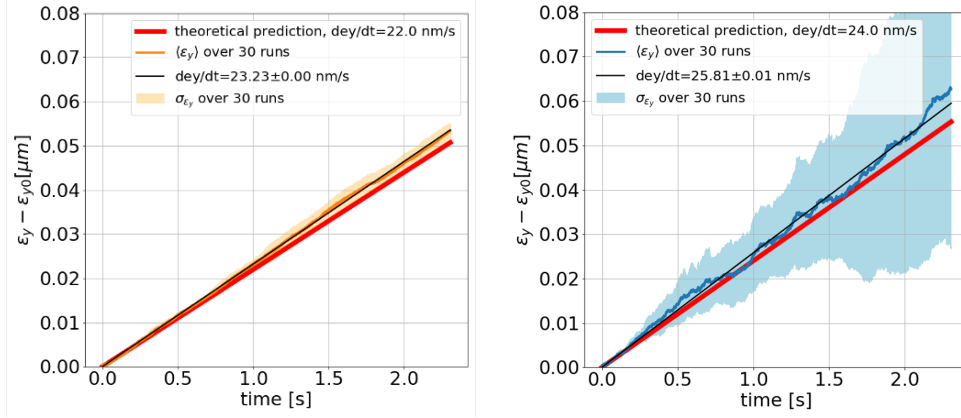
Figure 5.8: Vertical emittance growth driven by CC RF amplitude noise (left) and phase noise (right) as simulated with Sixtracklib simulation tool for a configuration close to the experimental conditions of the SPS CC tests in 2018 but for a local CC scheme. The CC noise is applied on CC1, following Eq. (5.5).

The simulations show an excellent agreement between the theoretically computed and simulated growth rates for both noise types. They also demonstrate that the modelling of the noise as kicks on the angle co-ordinate provides equivalent results to "real" noise which is applied through the CC (represented by the RF-Multipole) of Sixtracklib.

5.3.4 CC noise induced emittance growth in the presence of global CC scheme

Here, the simulations presented above were repeated but for a global CC scheme. As already mentioned, in the global CC scheme only one CC (represented by the RF-Multipole element) is in operation and the closed orbit shift is present during the circulation of the bunch around the machine. This scheme is the realistic case for the experiments of 2018, where for the emittance growth measurements only one CC was used.

For the simulations presented here, CC2 was switched off. CC1 operated at 1 MV, for $\phi_{\text{RF}-\text{Mult},1}$=90 deg. The noise was applied as described in Eq. (5.5) for the same noise levels as before. For this study, where only one CC is switched on, its voltage is

slowly increased to the chosen value of 1 MV, so that the new closed orbit includes the full CC kick. Without this dynamic ramping, an emittance blow-up is observed during the first turns in the simulation. Previous studies have shown that using a ramp of 200 turns is sufficient to avoid emittance blow-up. The first 200 turns are excluded from the linear fit used to obtain the emittance growth rates.

Figure 5.9 illustrates the simulated emittance growth driven by amplitude (left) and phase (right) noise in the presence of a global CC scheme. Once again, an excellent agreement is observed with the theoretically expected growth and also with the simulated growth rates for the different configurations discussed previously in this chapter.
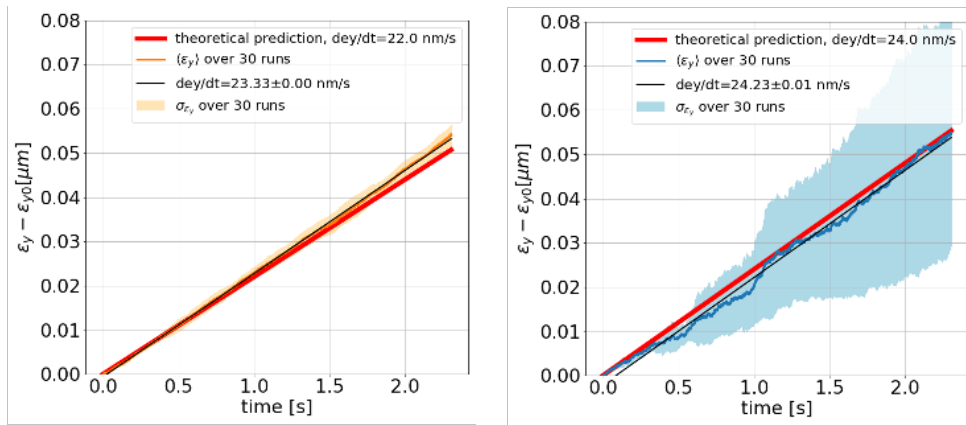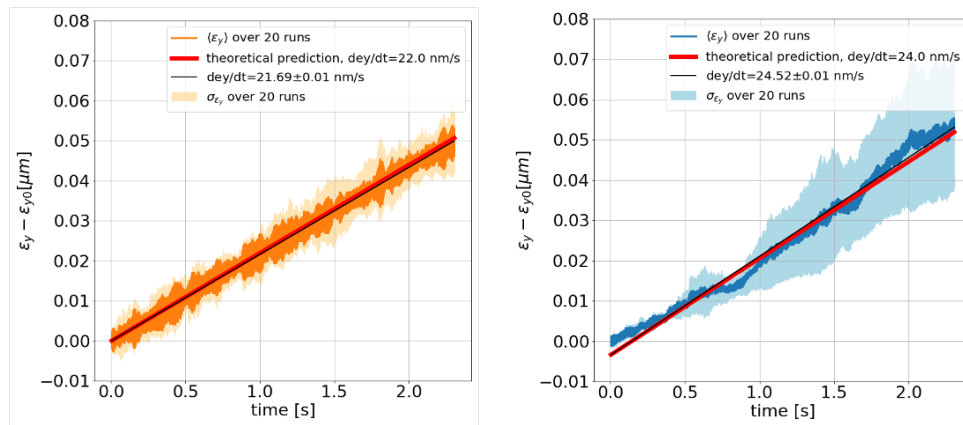

Figure 5.9: Vertical emittance growth driven by CC RF amplitude noise (left) and phase noise (right) as simulated with Sixtracklib simulation tool for a configuration close to the experimental conditions of the SPS CC tests in 2018 but for a global CC scheme. The CC noise is applied on CC1 which operates at 1 MV, following Eq. (5.5), while CC2 is switched OFF.

5.3.5 CC noise induced emittance growth with the measured noise spectrum

All the simulations discussed up to now were performed considering a white noise spectrum where the sequence of the uncorrelated random noise kicks were taken from a Gaussian distribution. However, as discussed in Section 4.3, measurements are available of the phase and amplitude noise that were injected in the CC RF system for the emittance growth studies in the SPS in 2018.

Here, the simulation studies presented in the previous Subsection 5.3.4 (with global

CC scheme) were repeated but this time the emittance growth is simulated using the measured noise spectrum.

The phase and amplitude noise spectra from Coast3-Setting3 (see Fig. 5.10) were used since they were the strongest noise levels from all the coasts. To this end, one can ensure the observation of reasonable emittance growth in our simulation time, which for this particular set of simulations was increased to ~10 s (5×10^5 turns).
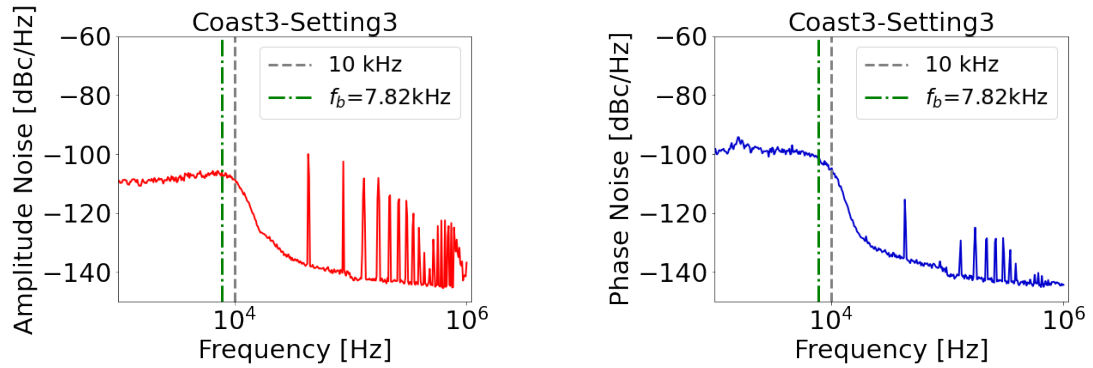
Figure 5.10: Example amplitude (left) and phase (right) noise spectra measured with a spectrum analyzer E5052B [69] during the emittance growth studies with CCs in SPS. The noise extends up to about 10 kHz (grey dashed line) overlapping the first betatron sideband at ~8 kHz (green dashed line). The spikes at high frequencies correspond to the harmonics of the revolution frequency and are a result of the bunch crossing.

Additionally, some of the simulation parameters were refined to be closer to the experimental conditions of 2018. In particular, the synchrotron tune and bunch length were set to Q_s = 0.0051 and σ_z = 0.138 m. Following the experimental configuration of 2018, CC1 was switched off, while CC2 operated at 1 MV (with the voltage being slowly ramped up during the first 200 turns). For reference, the vertical beta function at the location of CC2 is 73.8 m.

The measured spectra of Fig. 5.10 were converted to a discrete time series that can be used in the numerical simulations as described in Appendix B.3.

In Fig. 5.11 the simulation results where the phase and amplitude noise from Coast3-Setting3 are applied separately on CC2 are summarised. Once again, the agreement between the theory and the simulations is excellent for both cases.

By looking at the plots, it is evident that there is significantly less variation in the emittance growth rates over the different runs. This is due to the fact that, as
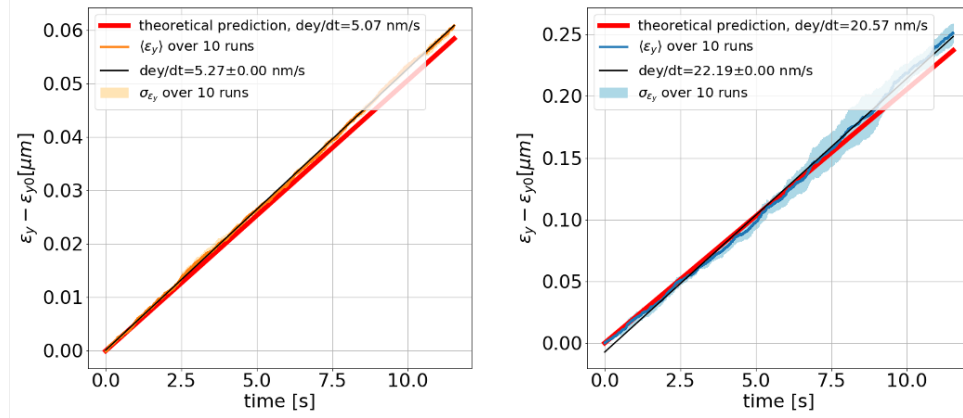
Figure 5.11: Vertical emittance growth driven by CC RF amplitude noise (left) and phase noise (right) as simulated with the Sixtracklib simulation tool for a configuration close to the experimental conditions of the SPS CC tests 2018. The measured phase and amplitude noise spectra from Coast3-Setting3 are used for the simulations. The CC noise is applied on CC2 which operates at 1 MV, following Eq. (5.5), while CC1 is switched off.

discussed in Appendix B.3, in the time series generated by the measured spectra the random factor is included in the set of random phases which leads to much less deviation in the values than the sequence of white noise kicks where the random factor is in their amplitude. To this end, the simulation here is repeated for just 10 different runs to reduce the uncertainty.

Finally, the same simulation is repeated in the presence of both amplitude and phase noise together. The results are shown in Fig. 5.12 where it is clear that the agreement with the analytically predicted rates is very good.

5.3.6 CC noise induced emittance growth with the non-linear SPS model

The nominal SPS model includes only the non-linear fields produced by the chromatic sextupoles. However, one of the most important sources of non-linearities in SPS are the higher-order multipole components of its main dipole magnets. In this subsection, their impact on the beam dynamics studies is considered, as a possible contribution to the observed discrepancy between predicted and measured emittance growth rates in the presence of CC RF noise. To this end, the multipole components of the SPS main dipoles should be included in
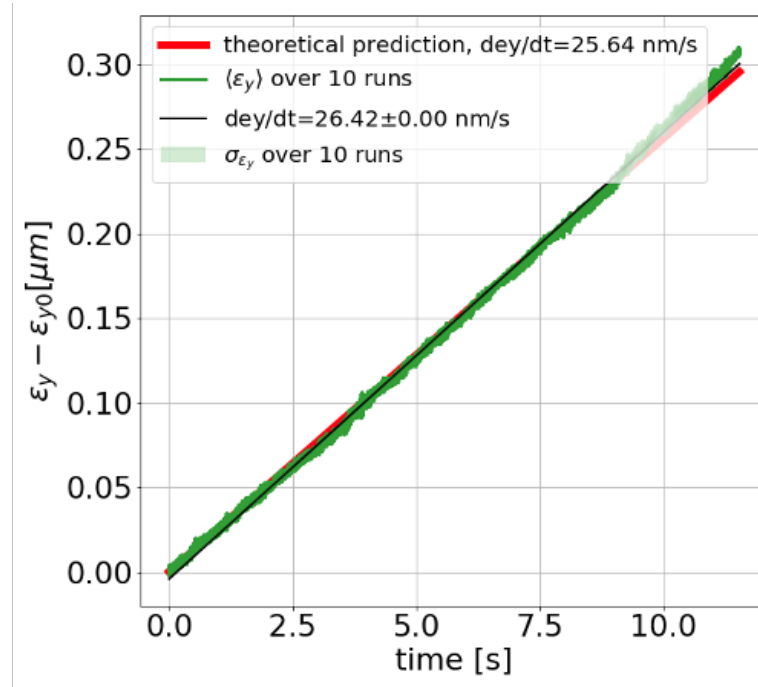
Figure 5.12: Vertical emittance growth driven by CC RF amplitude and phase noise as simulated with the Sixtracklib simulation tool for a configuration close to the experimental conditions of the SPS CC tests 2018. The measured phase and amplitude noise spectra from Coast3-Setting3 are used for the simulations. Both types of noise are applied on CC2 which operates at 1 MV, following Eq. (5.5), while CC1 is switched off.

the nominal SPS model that was used up to now.

Magnetic measurements of the precise multipole errors of the SPS main dipoles are not available. On this ground, a non-linear optics model of the SPS has been established with beam-based measurements of the chromatic detuning over a range of momentum deviation [67, 68]. The optics model was obtained by assigning systematic multipole components to the main lattice magnets, in the nominal model of SPS, in order to reproduce the tune variation with momentum deviation as it was measured in the real machine. The calculations were performed with MAD-X.

The values of the multipole components up to the seventh order obtained from this method are given in Table 5.3 where, (b_3^A, b_3^B) (b_5^A, b_5^B) and (b_7^A, b_7^B) stand for the sextupolar, decapolar and decatetrapolar multipoles respectively. Note that different values have been obtained for each of the two different kinds of SPS main dipoles (MBA and MBB) which are marked with the indices A and B respectively.

5. Investigation of the discrepancy between emittance growth theory and experimental data

Table 5.3: Multipole errors from SPS non-linear model, at 270 GeV [68].

Multipole	Value
b_3^A, b_3^B	$8.1 \times 10^{-4}\,\mathrm{m}^{-2}$, $1.1 \times 10^{-3}\,\mathrm{m}^{-2}$
b_5^A, b_5^B	$9.2\,\mathrm{m}^{-4}$, $-10\,\mathrm{m}^{-4}$
b_7^A, b_7^B	$1.3 \times 10^5\,\mathrm{m}^{-6}$, $1.4 \times 10^5\,\mathrm{m}^{-6}$

These values were assigned to the main dipoles of the SPS and the simulations presented in Section 5.3.5 were repeated. The simulations were performed in the presence of the measured phase noise spectrum only which was dominant during the SPS experiments in 2018. The results are displayed in Fig. 5.13. It is clear that there is a very good agreement between the theory and the simulations when the non-linear model of SPS is used. Hence, it is concluded that since the theoretical estimate does not take into account the multipole errors, the inclusion of these errors has no significant impact on the emittance growth rates
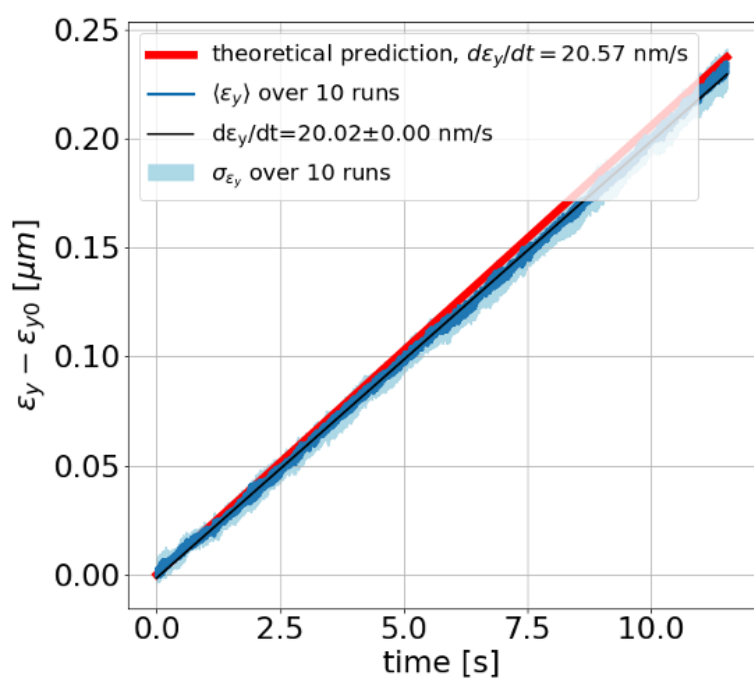
Figure 5.13: Vertical emittance growth driven by CC RF phase noise as simulated with Sixtracklib simulation tool for a configuration close to the experimental conditions of the SPS CC tests 2018. The measured phase and amplitude noise spectra from Coast3-Setting3 are used for the simulations. The non-linear model (including multipole components of the main dipole magnets) of the SPS machine was used for the tracking. Both types of noise are applied on CC2 which operates at 1 MV, following Eq. (5.5), while CC1 is switched off.

5.4 Conclusions and outlook

The work presented in this chapter focused on investigating possible explanations for the discrepancy of a factor of about 4 observed between the theoretically predicted and measured emittance growth driven by CC RF noise during the experiments of 2018 in the SPS. The following points were checked:

- Sensitivity to possible uncertainties in the measured parameters and in particular in the CC voltage and bunch length.

- Benchmarking of the theory with two different simulation codes: PyHEADTAIL and Sixtracklib.

- Sensitivity of the simulated emittance growth to the detailed optics and the presence of a real CC element.

- Sensitivity to the measured noise spectrum.

- Sensitivity to the non-linearities of the SPS lattice.

All these factors were excluded as possible sources of the discrepancy since for all of these study cases the simulated emittance growth demonstrated an excellent agreement with the theoretically predicted values using the Mastoridis–Baudrenghien model. It was also confirmed that the detailed optics of the SPS, its non-linearities and the orbit shift induced by the CC (represented by the RF-Multipole element in Sixtracklib) have no impact on the CC RF noise-induced emittance growth. To this end, in the next chapters, the simulations will be performed with the PyHEADTAIL simulation tool which also provides the possibility of including collective effects (such as the impedance), which were not addressed so far in the context of these studies.

6 | Simulation studies: Emittance growth suppression mechanism from the beam transverse impedance

During the dedicated experiment that took place in the SPS in 2018 with the CCs, the measured emittance growth due to CC RF noise was found to be a factor of four (on average) lower than expected from the theory (see Section 4.7). The reason for this discrepancy remained unresolved for some time, as detailed follow-up studies (see Chapter 5) investigated and excluded a number of possible explanations for the discrepancy. It was recently found, that the beam transverse impedance, which is not included in the theory [27] used for the comparison with the measurements may impact the noise-induced emittance growth and explain the experimental observations. Here, the damping mechanism from the beam transverse impedance is investigated in PyHEADTAIL simulations.

The structure of this chapter is as follows: Section 6.1 provides information on the impedance model of the SPS machine and benchmarks its implementation in PyHEADTAIL against theoretical calculations. In Section 6.2 the simulation setup for the emittance growth studies is discussed and the beam and machine parameters (following the 2018 CC experiment) are listed. Section 6.3 presents simulation results which showed for the first time that the transverse beam impedance (which was not included in the theory [27] and the simulations up to now) significantly suppresses the noise-driven emittance growth. Furthermore, PyHEADTAIL simulations were carried out aiming to characterise the effect of the emittance growth suppression in order to understand the mechanism behind it. These studies are presented in Section 6.4. The suppression mechanism is

investigated through parametric studies and with studies in the frequency domain in Section 6.5. Finally, the main results are summarised in Section 6.6

6.1 SPS transverse impedance model

The PyHEADTAIL studies presented in this chapter are performed including the detailed transverse impedance model of the SPS machine [86]. This model has been developed through a combination of theoretical computations and electromagnetic simulations and was benchmarked with beam-based measurements [54, 87, 88, 89]. It includes the contributions from all the individual elements in the SPS lattice, i.e. the resistive wall, the indirect space charge, the kickers, the RF cavities (200 MHz and 800 MHz), the step transitions, and the horizontal and vertical Beam Position Monitors [89]. As discussed in Section 2.5.1, the model needs to represent the global impedance of the full machine. Thus, the total impedance is obtained by summing up the impedance of each element weighted with the beta function at its location and dividing the sum by the value of the beta function at which the wakefield kick is applied in the simulations, which is chosen to be the average beta function around the machine. For the Q26 optics, the average horizontal and vertical beta functions are 42.09 m, and 42.01 m, respectively. Figure 6.1 shows the complete transverse impedance model of the SPS machine with the dipolar (blue) and quadrupolar (orange) terms plotted separately.

Wake functions

As already discussed in Section 2.5.1, in order to include the impedance effects in PyHEADTAIL simulations the real-value wakefields in the time domain are used in order to update the angle co-ordinate of the particles according to Eq. (2.60). The total transverse dipolar (blue) and quadrupolar (orange) wake functions for both planes of the SPS can be found in the GitLab repository of [86] and they are plotted in Fig 6.2.

For reference, the impedance model is used as an input in the Sacherer formula (Eq. (2.53)) for analytical estimations while the wake functions are used as an input
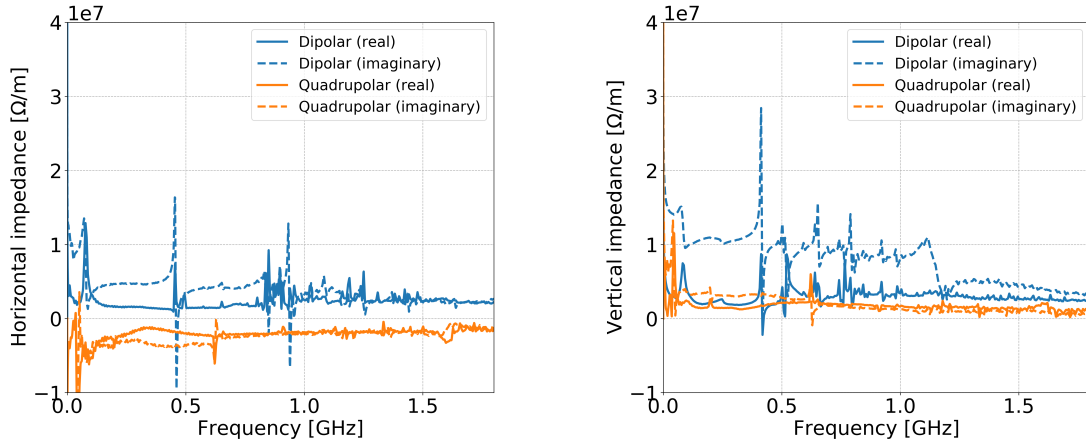
Figure 6.1: Horizontal (left) and vertical (right) impedance model of the SPS. The contributions from the wall, the kickers and the step transitions are visible at the low frequencies (up to ~ 0.4 GHz). The impedance of the RF cavities and the Beam Position Monitors (BPMs) correspond to the peaks observed between ~0.4-1 GHz.
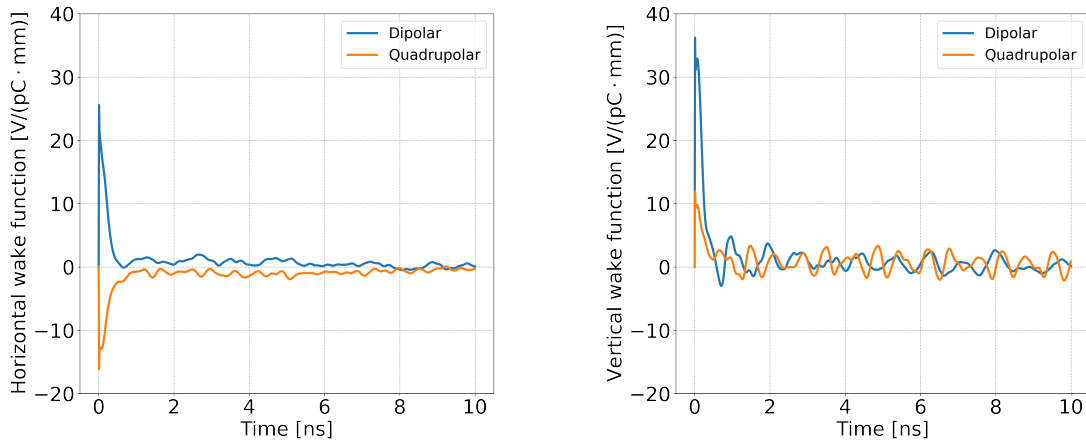
Figure 6.2: Horizontal (left) and vertical (right) wakefunctions of the SPS. The wake functions are available in the public GitLab repository of [86]. For comparison the bunch length in the SPS CC experiments is ~ 1.85 ns ($4\sigma_{\mathrm{t}}$).

in simulation codes such as PyHEADTAIL.

Last, these wake functions are obtained with an inverse Fast Fourier Transform algorithm (iFFT) on the impedance model as described in the references provided above.

6.1.1 Testing the implementation in PyHEADTAIL

As discussed in Section 2.3 the imaginary part of the impedance leads to a coherent tune shift which depends on the bunch intensity. One of the most common ways to test the correct implementation of the impedance model in a tracking simulation

code is to benchmark the simulated intensity-dependent coherent tune shift with the theoretically predicted behavior (using Eqs. (2.53) and (2.57)).

Typically, in tracking simulations, the coherent tune is obtained by applying a frequency analysis technique to the oscillations of the centroid of the particle distribution (the center of mass of the bunch). Here, the analysis is limited to the coherent mode $l = 0$, as the study of mode $l = 0$ is sufficient for the purpose of the studies presented here. For simplicity in the following the term "coherent tune" will refer to the coherent tune of mode $l = 0$.

Simulations setup

The parameters used for setting up the linear transfer map, the longitudinal tracking, and the beam initialisation are shown in Table 6.1 and are the ones used in the SPS CC experiment of 2018. The ring is modelled by a linear transport map, with one interaction point at which the beam interacts with the wakefields. At that location, the horizontal and vertical beta functions equal the corresponding average beta functions over the SPS machine (see Section 2.5.1). The latest transverse wakefield model (as of February 2019 in [86]) of the SPS was used.

The initial bunch was generated with Gaussian distributions in transverse and longitudinal planes. The bunch population of the different intensity values was represented by 5×10^5 macroparticles and the number of slices of the longitudinal distribution was 500.

For all the PyHEADTAIL simulation studies presented in this thesis, the Twiss parameter $\alpha_u(s)$ and the dispersion function $D_u(s)$ equal zero. This is a valid assumption for the studies as these parameters have no direct impact on the effects under investigation.

To facilitate the observation of the coherent tune, the bunch was initialised with a static offset of $0.15\sigma_{x,y}$ in both transverse planes, so that it performs dipole oscillations around the machine. The parameter $\sigma_{x,y}$ is the rms transverse beam size (see Eq. (2.25)) at the only interaction point along the ring i.e. at the location where the beam interacts with the wakefields. It was tracked for 600 turns and the coherent tune was computed using a NAFF algorithm [90, 91], which provides a

6. Simulation studies: Emittance growth suppression mechanism from the beam transverse impedance

Table 6.1: PyHEADTAIL simulation parameters used to study impedance induced effects for the SPS.

Parameter	Value
Beam energy, E_b	270 GeV
Machine circumference, C_0	6911.5623 m
Horizontal / vertical betatron tune, Q_{x0} / Q_{y0}	26.13 / 26.18
Synchrotron tune, Q_s	0.0051
Number of bunches	1
Rms bunch length, $4\sigma_t$	1.7 ns [*]
Horizontal / vertical normalised emittance, ϵ_x / ϵ_y	2 μm / 2 μm
Average horizontal / vertical beta function, $\langle\beta_x\rangle/\langle\beta_y\rangle$	42.09 m / 42.01 m [†]
Number of macroparticles, N_{mp}	5×10^5
Number of longitudinal slices, N_{slices}	500

[*] This value corresponds to the average measured bunch length of bunch 1 over all the coasts of 2018. The value for bunch 1 is used here since it was the only stable bunch in the SPS CC tests of 2018.
[†] Model values for the Q26 optics.

refined FFT analysis on the turn-by-turn centroid motion. The Python implementation, NAFFlib, can be found in [92]. The coherent tune shift was computed by subtracting the obtained tune value from the unperturbed coherent tune (in the absence of impedance) which equals the Q_{u0} value.

Last, the dependence of the coherent tune on the bunch intensity value was studied in the absence of other detuning effects (such as chromaticity or detuning with transverse amplitude).

The simulation was repeated for a range of bunch intensities, N_b, equally spaced from 0 to 5×10^{10} protons per bunch. This range was chosen to be in the vicinity of the bunch intensity of the CC experiments of 2018, where N_b was 3×10^{10} protons per bunch. $N_b = 0$ is not a realistic value. However, it is used here as the reference point for which the coherent betatron tune shift equals zero. The simulation results are compared with the theoretically expected tune shifts in Fig. 6.3.

The theoretically expected values are computed from Eqs. (2.53) and (2.57) for $l = 0$ and using only the imaginary part of the impedance. Given that $\Gamma(1/2) = \sqrt{\pi}$ and $Q_u = \omega_{u0}/\omega_{\text{rev}}$ equation Eq. (2.53) becomes:

$$\Delta\Omega_u^{(0)} = \Omega_{u0}^{(0)} - \omega_{u0} = \frac{\sqrt{\pi}}{4\pi}\frac{N_b r_0 c^2}{\gamma_0 \frac{2\pi}{\omega_{\text{rev}}}\omega_{u0}\sigma_z}Z_{\text{eff,im}} = \frac{N_b r_0 c^2}{8\pi^{3/2}\gamma_0 Q_u \sigma z}Z_{\text{eff,im}} \qquad (6.1)$$

All the parameters inserted in Eq. (6.1) need to be converted into cgs (centimetre–gram–second) units. The coherent betatron tune shift is computed by inserting the result of Eq. (6.1) in Eq. (2.57) such that:

$$\Delta Q_u = \frac{\Delta\Omega_u^{(0)}}{\omega_{\text{rev}}}.$$

$$(6.2)$$
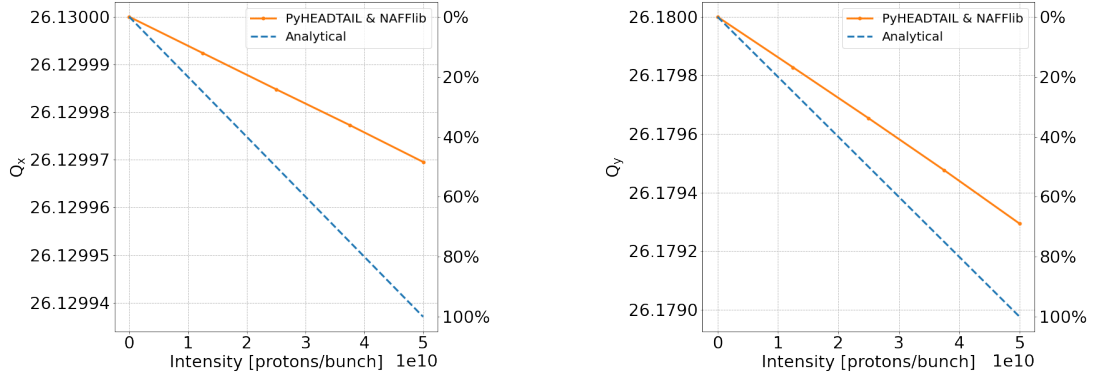
Figure 6.3: Horizontal (left) and vertical (right) coherent tunes as a function of intensity in the presence of the beam coupling SPS impedance obtained using analytical formula (blue dashed line) and PyHEADTAIL tracking simulations (orange line). The impedance model and the wake functions used are available in [86].

Figure 6.3 shows that the coherent tune shift from the analytical model does not agree with simulation results. In particular, the wakefields used in the PyHEADTAIL simulations result in between roughly 50% and 70% of the coherent tune shift computed analytically using the corresponding impedance. This discrepancy has not been observed previously, such a comparison has not been conducted for such low intensities (the usual intensity range for this type of study is in the order of 10^{11} protons per bunch [93]) and short bunches. The analytical predictions from the Sacherer formula have been successfully benchmarked against beam measurements [94, 95] which indicates that there is an issue with the model of the wakes or with their implementation in the simulation. Given the fact that the studies with CCs are sensitive to the coherent tune shift[1] (and its dependence on the beam intensity), it is important to identify the cause of the discrepancy between the simulation and analytical results and to resolve it.

---

[1] The sensitivity of the dynamics with CCs to the coherent tune shifts will be discussed later in this chapter.

6. Simulation studies: Emittance growth suppression mechanism from the beam transverse impedance

After several studies and discussions with the experts on the topic[2] it was identified that higher accuracy of the impedance model is needed at the lower frequencies. Thus, the wakefields of the resistive wall and the step transitions were refined by being computed analytically directly in time domain so that no FFT is involved. The details of this work are not discussed here as they are out of the scope of this thesis and they were not performed by the author. The re-computed wake functions (of the resistive wall and the step transitions) along with the rest of the components of the original model can be found in [96] and it will be referred to as the "updated wakefields" model.

The coherent betatron tune as a function of intensity obtained using PyHEADTAIL and the updated wakefields model is plotted in Fig. 6.4 in comparison with the analytical predictions from the Sacherer formula. In both transverse planes, the results from the simulations and the theory are in very good agreement ($\leq 5\%$) which is within the uncertainty that one can expect from the model implementation.
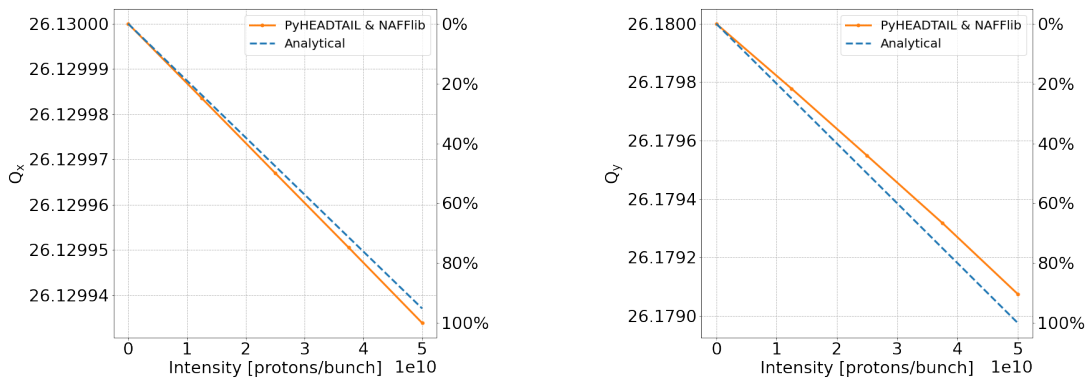
Figure 6.4: Horizontal (left) and vertical (right) coherent tunes as a function of intensity in the presence of the beam coupling SPS impedance obtained using analytical formula (blue dashed line) and PyHEADTAIL tracking simulations (orange line). The impedance model is available in. [86]. The PyHEADTAIL simulations use the "updated wakefields model" (in contrast with the results of Fig. 6.3) which can be found in [96].

The above figure demonstrates that the updated wakefields model is reliable and validates the implementation in PyHEADTAIL. Therefore it will be used to study the interplay of the CC noise-induced emittance growth with impedance induced effects. These studies are presented in the following chapter.

---

[2]In particular with Carlo Zannini, carlo.zannini@cern.ch.

6.2   Emittance growth simulations setup

The simulations that were performed to investigate the impact of the beam coupling impedance on the CC RF noise-induced emittance growth were performed following the procedure and using the parameters that are described below. Any change in the choice of parameters, e.g. for some of the parametric studies, will be mentioned at the appropriate point.

The parameters used for setting up the linear transfer map, the longitudinal tracking, and the beam initialisation are shown in Table 6.1 and are the ones used in the SPS CC experiment of 2018. The ring is modelled by two linear transfer maps and two interaction points. Kicks representing noise from the crab cavities are applied at the first interaction point, and wakefield kicks are applied at the second. The updated wakefields model [96] of the SPS was used.

At the location of the CC RF noise kick the horizontal and vertical beta functions equal the values at the location of the CC2 which was used in the experiments of 2018. At the location where the wakefield kicks are applied the transverse beta functions equal the corresponding average beta functions over the SPS machine (see Section 2.5.1). The simulations are performed for the Twiss parameter $\alpha_u(s)$ and the dispersion function $D_u(s)$ equal zero. This is a valid assumption for the studies as these parameters have no direct impact on the effects under investigation.

The emittance growth studies were performed for the intensity of 3×10^{10} protons per bunch in accordance with the 2018 experiments. The bunch population was represented by 5×10^5 macroparticles and the number of longitudinal slices was 500. The emittance growth was also simulated without including the wakefields. For the latter case, the bunch population was represented by 10^5 particles. The studies were performed using an initial Gaussian bunch distribution in the six-dimensional phase space. This is a good approximation for the bunches used in the experimental studies of 2018.

At the location of the CC, the change of the angle, y', of each particle within the

6. Simulation studies: Emittance growth suppression mechanism from the beam transverse impedance

bunch as a result of phase and amplitude CC RF noise is modelled according to Eqs. (3.7) and (3.8) for amplitude and phase noise respectively. The simulations performed for a total noise power of $\sigma_{\Delta A}^2 = 7.3 \times 10^{-6}$ and $\sigma_{\Delta\phi}^2 = 7.3 \times 10^{-6}\,\mathrm{rad}^2$ except if it is stated otherwise. This noise level, which corresponds to power spectral density at the betatron frequency of $1.68 \times 10^{-10}\mathrm{rad}^2/\mathrm{Hz}$ or $1/\mathrm{Hz}$ for phase and amplitude noise respectively is much stronger than the ones of the actual CC RF system and was chosen such as it results in a reasonable growth in the simulation time of 10^5 turns (it corresponds to ~2.5 seconds in the SPS). The higher noise level in the simulation means that the emittance growth over 10^5 turns is comparable to the emittance growth observed over the full measurement time in the SPS experiments. This approach is valid due to the linear growth of emittance with time and the linear scaling with the noise level [27]. The parameters used for the implementation of the CC RF noise kick in the simulations are shown in Table 6.2.

Table 6.2: PyHEADTAIL simulation parameters used for the implementation of the CC RF noise kicks for the emittance growth studies. This table is complementary of Table 6.1.

Parameter	Value
Horizontal / vertical beta function, $\beta_{x,\mathrm{CC}}/\beta_{y,\mathrm{CC}}$	30.31 m / 73.82 m
CC frequency, f_{CC}	400.78 MHz
Total amplitude and phase noise power, $\sigma_{\Delta A}^2 / \sigma_{\Delta\phi}^2$	7.3×10^{-6} / $7.3 \times 10^{-6}\,\mathrm{rad}^2$

Last, the emittance growth simulation studies were performed for non-zero linear chromaticity and non-zero detuning with the transverse amplitude. Both effects were introduced as changes in the phase advance of the individual particles according to Eq. (2.59). The value of the linear chromaticity, $Q'_{x,y} = 0.5$ was used for most of the studies according to the experimental conditions of 2018. Higher-order chromaticities are negligible. The values of the detuning coefficients will be given in the following sections.

In the following sections, the emittance growth rates will be expressed in nm/s due to the simulation time scale and will be referred to as the growth of the normalised emittance values to be in agreement with the analysis of the measured data in Chapter 4.

6.3 Suppression of noise induced emittance growth by the beam coupling impedance

A first set of emittance growth simulations were performed for the beam and machine conditions of the 2018 experiments. The parameters are listed in Tables 6.1 and 6.2 and the detailed procedure is described in Section 6.2.

As mentioned in Chapter 4 the Landau octupoles were switched off during the 2018 CC experiment. Nevertheless, multipole components in the dipole magnets of the SPS, as well as the chromatic sextupoles create some non-linearities [67, 68]. The rms tune spread in the vertical plane from these non-linearities is computed at ~2-3 $\times 10^{-5}$. In order to reproduce this tune spread value in the simulations, the vertical amplitude detuning coefficient was set at $\alpha_{yy} = 2000/$m. For simplicity, the horizontal and cross-term coefficients were both set to zero, $\alpha_{xx} = \alpha_{yx} = 0$.

The simulations were performed with CC phase noise as it was the dominant type of noise in the 2018 experiment, with a power spectral density of 1.68×10^{-10}rad^2/Hz which corresponds to a total noise power of $\sigma_{\Delta\phi} = 7.3 \times 10^{-6}$ rad^2. For this noise power a growth rate of about 25 nm/s is expected (exciting the first betatron sidebands at ± 7.8 kHz, see further discussion in Section 3.2.2).

The geometric emittance value was computed every 100 turns (for computational efficiency) using the statistical definition which can be found in Eq. (2.27). The emittance growth rate was computed by performing a linear fit to the normalised emittance values over the simulation turns ($N_{\text{turns}} = 10^5$). Twenty simulation runs were conducted, to reduce the uncertainty of the results. The initial bunch distribution and the sequence of the uncorrelated noise kicks were regenerated randomly for every run. The mean and the standard deviation (including the uncertainty on the slope of the fit) were computed over all the simulation runs.

The simulations were performed with and without wakefield kicks, to study the impact of machine impedance on the emittance growth induced by CC RF phase noise. The results are illustrated in Fig. 6.5. The average emittance evolution (over

6. Simulation studies: Emittance growth suppression mechanism from the beam transverse impedance

the 20 different runs) in the absence of impedance effects is shown with dark blue color while in the presence of impedance effects with the dark orange color. The shaded areas with light blue and light orange colors show the standard deviation over the 20 runs. The simulated emittance growth without the wakefields is in very good agreement with the theoretically expected value of ~25 nm/s (black dashed line). However, once the impedance model is included the phase noise-induced emittance growth is strongly suppressed.
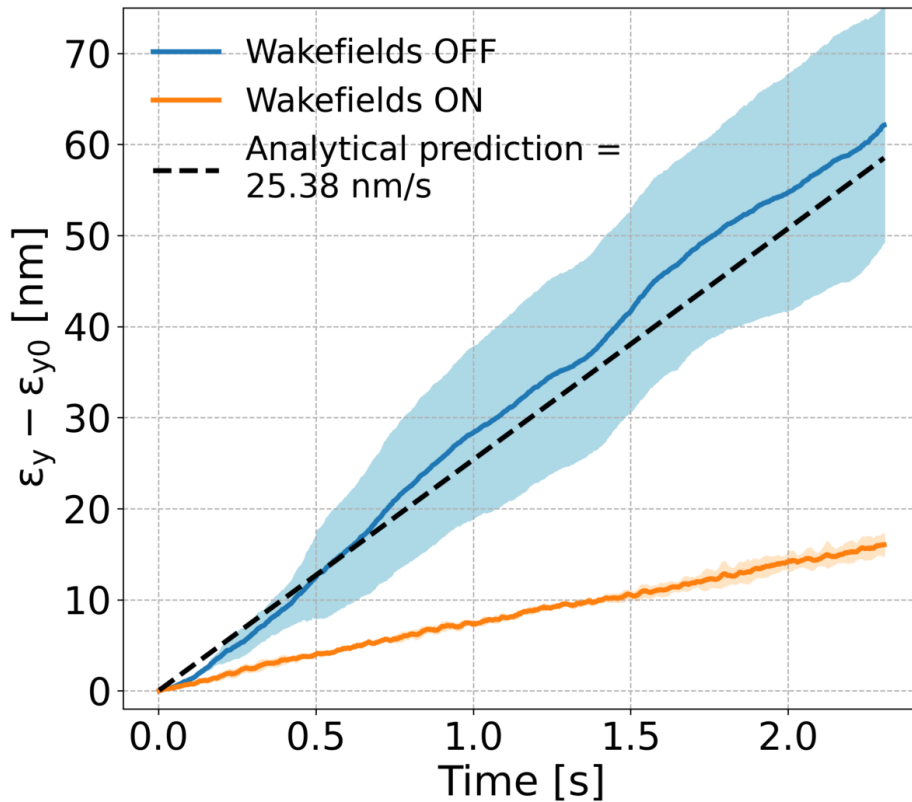
Figure 6.5: Simulatued transverse emittance growth driven by CC RF phase noise without (blue) and with (orange) the impedance effects for the beam and machine conditions of the CC tests in SPS during 2018. The results were obtained from 20 different runs. The average emittance evolution is shown with the dark colors, while the shaded areas show the standard deviation of the emittance values over the 20 runs.

It is worth noting that the large spread in the emittance growth rates over the different simulation runs in the absence of wakefields is a result of the very small tune spread. The wakefields introduce some additional tune spread, on top of the one from the vertical tune shift with amplitude, which reduces the uncertainty of the simulated growth rates. For reference, the rms vertical betatron tune spread introduced by the wakefields was found to be about 5.5×10^{-5} in PyHEADTAIL

108

tracking simulations.

To conclude, PyHEADTAIL simulations showed for the first time that the transverse beam impedance (which is not included in the Mastoridis–Baudrenghien model) has a significant impact on the emittance growth driven by CC RF noise. The effect of the suppression of noise-induced emittance growth from the impedance has not been observed before. To characterise this effect and to be able to understand the mechanism behind it, a series of exploratory studies were conducted and are discussed in the following section.

6.4   Characterisation of the emittance growth suppression by the impedance

In this section, we discuss the results of the exploratory simulation studies which investigate the suppression of the CC RF noise-induced emittance growth by the transverse beam coupling impedance. The goal is to characterise the effect and understand the mechanism behind it.

The simulations were conducted following the same pattern as the case discussed in the previous section. Nevertheless, the main relevant parameters for each case will also be listed in the corresponding section.

6.4.1   Sensitivity of CC RF phase noise induced emittance growth to amplitude-dependent tune shift

As the machine non-linearities were not explicitly characterised during the experiment, the dependence on the octupole-like amplitude dependent tune spread was studied. Instead of using an actual octupolar (non-linear) element which would cause excitation of a resonance, the amplitude dependent tune shift was modelled as a change to the phase advance of the particles depending on their individual betatron action as discussed in Eq. (2.59). More specifically, the dependence on the detuning coefficient in the vertical plane, α_{yy}, was studied. For the studies presented here and in the following sections of this chapter, the

horizontal detuning coefficient and the cross-term were left at zero for simplicity, i.e. $\alpha_{xx} = \alpha_{xy} = 0$. The sensitivity on the cross-term is discussed in Chapter 7.

The simulations were performed with and without the SPS impedance model to study its impact on the emittance growth induced by CC noise. Figure 6.5 shows the dependence of the average growth rates (over the 20 different runs) on the amplitude detuning coefficient, α_{yy}. The error bars indicate the standard deviation over the 20 runs. The secondary horizontal axis shows the resulting rms tune spread computed using Eq. (C.6). Incoherent tune shifts from sources other than the detuning with transverse amplitude are not included. The sensitivity to chromaticity is studied later, while the incoherent tune shift from the impedance itself is very small ($\sim 5.5 \times 10^{-5}$ rms value) compared to the one introduced by the Landau octupoles.
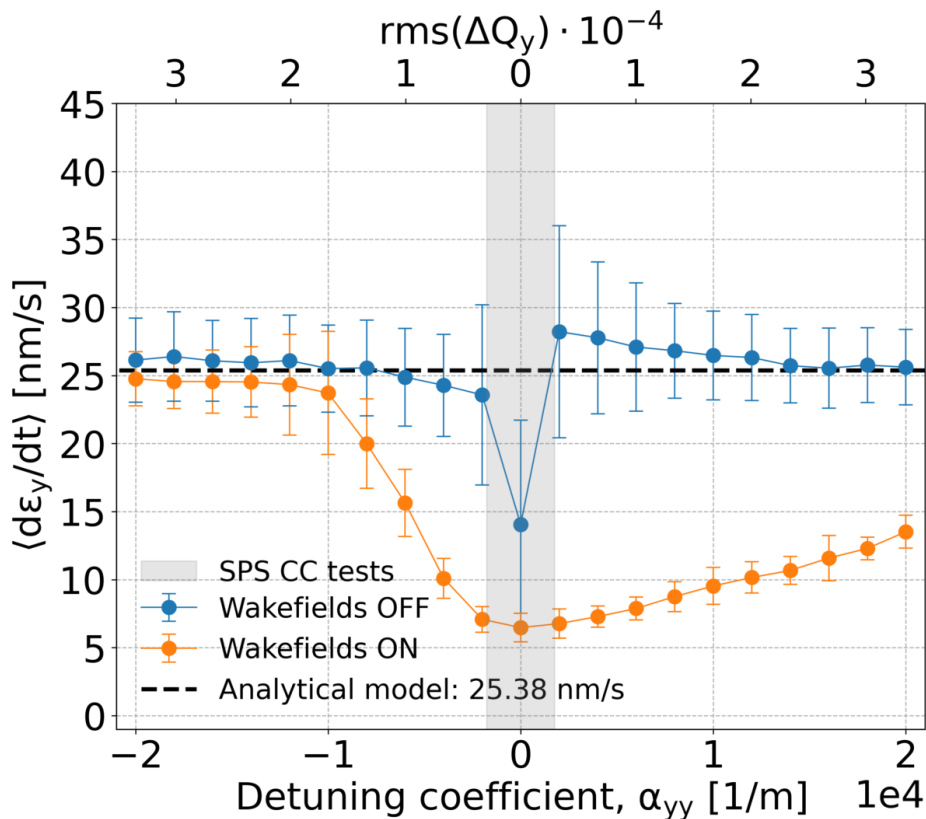
Figure 6.6: Simulated transverse emittance growth driven by CC RF phase noise (as a function of detuning coefficient), without (blue) and with (orange) impedance effects. The error bars represent the standard deviation over 20 different runs of the simulation.

It can be seen, that when the wakefield kicks are not applied to the beam, the

emittance growth rate agrees very well with the value predicted by Eq. (4.6) and (within the reproducibility of the simulation) is independent of the detuning coefficient value. However, for $\alpha_{yy} = 0$ some emittance growth is observed. This is unexpected since for zero tune spread there is no decoherence and thus no emittance growth is expected. A possible explanation for this could be that the orbit shift from the CC noise kick over the bunch length is not linear, which might result in phase mixing of the particles within the bunch causing decoherence of the betatron oscillations and hence emittance growth. Regarding the fact that the observed emittance growth appears smaller than expected from the Mastoridis–Baudrenghien model, a possible explanation could be that the tune spread (introduced by the non-linearities of the CC kicks) is very small and results in a slow decoherence (see Eq. (5.1)) meaning that the 2.5 s of simulation time are not sufficient to obtain valid results.

Figure 6.5 shows a clear suppression of the transverse emittance growth when the wakefield kicks are included, depending on the tune spread, and is asymmetric between positive and negative detuning coefficients. Over a realistic range of tune spread values (estimated with MAD-X [48] including the non-linearities of SPS [67, 68] and $Q'_{x,y} = 0.5$, and shown by the grey shaded area in Fig. 6.5) the suppression reaches up to a factor 4-5. This suppression is very close to that observed in the experiments and suggests that the impedance effects might explain the discrepancy between the measured and theoretically estimated emittance growth rates.

6.4.2 Amplitude noise

The simulations discussed here were performed with and without the SPS impedance model in the presence of CC RF amplitude noise, with a total power of $\sigma^2_{\Delta A} = 7.3 \times 10^{-6}$ which corresponds to a power spectral density of 1.68×10^{-10}/Hz. The total power of the amplitude noise equals the one of the phase noise used in the previous section. The results are shown in Fig. 6.7.

It can be seen that the emittance growth rate agrees very well with the value predicted by Eq. (4.5) and (within the reproducibility of the simulation) is
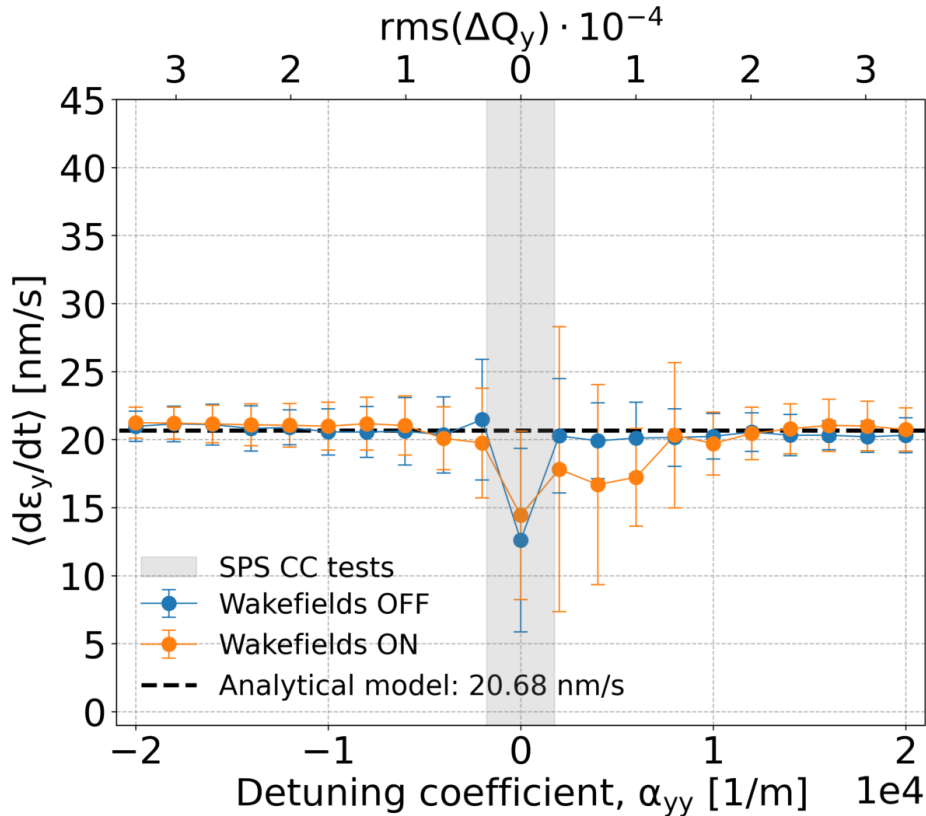
Figure 6.7: Simulated transverse emittance growth driven by CC RF amplitude noise (as a function of detuning coefficient), without (blue) and with (orange) impedance effects. The error bars represent the standard deviation over 20 different simulation runs.

independent of the tune spread value both when the wakefields are included and when they are not. In other words, the simulations demonstrate that the emittance growth driven by CC RF amplitude noise is not suppressed by impedance-induced effects.

The difference in the PyHEADTAIL simulations between the CC RF phase and amplitude noise could be explained by the fact that the phase noise (which is similar to a dipolar noise kick but with a high order distortion) is associated with the head-tail mode 0, while the amplitude noise is associated with the head-tail mode 1. The hypothesis, that the emittance growth suppression from impedance induced effects is related to head-tail mode 0 will be discussed in detail in the following sections and was also tested experimentally in 2022.

6.4.3 CC operating at 200 MHz

In the HL-LHC the main RF system and the CCs will operate at the same frequency ($f_{CC} = f_{RF-LHC}$=400 MHz). To replicate, this scenario in the SPS, the sensitivity on the amplitude-dependent tune spread was simulated assuming a CC frequency of 200 MHz, i.e. $f_{CC} = 200$ MHz, which equals the frequency of the main accelerating RF system of the SPS (see Table 4.2).

The simulations were performed with and without wakefield kicks, in the presence of both amplitude and phase noise with power spectral density of 1.21×10^{-10}rad^2/Hz ($\sigma^2_{\Delta A} = 7.3 \times 10^{-6} \times 0.72$) and 3.06×10^{-10}/Hz ($\sigma^2_{\Delta\phi} = 7.3 \times 10^{-6} \times 1.82$) respectively. The noise strength was scaled so that it results in ~ 25 nm/s to be comparable with the initial studies presented in Section 6.3.

The PyHEADTAIL simulation results are summarised in Fig. 6.8. The first plot (left) displays the amplitude detuning dependent emittance growth in the presence of amplitude noise while the second plot (right) shows the emittance growth in the presence of phase noise.

(a) Amplitude noise

(b) Phase noise

Figure 6.8: Simulated transverse emittance growth driven by CC RF noise, assuming a CC frequency of 200 MHz, without (blue) and with (orange) the impedance effects as a function of tune spread. The error bars represent the standard deviation over 20 different runs of the simulation.

Comparing Fig. 6.8 (left) and Fig. 6.7 it becomes evident that the behavior of the amplitude noise induced emittance growth is consistent for CC operating at 200 MHz and 400 MHz (both with and without wakefields). In neither case is there

any significant suppression of the emittance growth from amplitude detuning while the obtained growth rates agree very well with the theoretical predictions from Eq. (3.11).

Comparing Fig. 6.8 (right) and Fig. 6.5 it can be seen that emittance growth driven by CC phase noise in the absence of wakefield kicks (blue) is in excellent agreement for the CC operating at 200 MHz and 400 MHz. However, for the case with zero amplitude detuning, $\alpha_{yy} = 0$, almost zero emittance growth is observed for $f_{CC} = 200$ MHz. This could be explained by the fact that for f_{CC}=200 MHz, the CC wavelength (~5 ns) is much longer than the bunch length ($4\sigma_t$=1.7 ns). Thus, the bunch is affected mostly by the linear part of the CC kick, which does not lead to phase mixing of the bunch particles and emittance growth. This reasoning is in agreement with the discussion in Section 6.4.1.

Comparing the simulations in the presence of wakefields, the dependence of the emittance growth suppression is similar when the CC operates at 200 MHz and 400 MHz. However, in the case of f_{CC}=200 MHz the emittance growth suppression appears stronger and reaches up to a factor of 10 instead of just 4-5 in the case of f_{CC}=400 MHz. This observation agrees with the hypothesis that the emittance growth suppression by impedance-induced effects is related to rigid bunch motion (head-tail mode 0). In particular, since for f_{CC}=200 MHz, the CC wavelength is much longer than the bunch length the CC kick is closer to a pure dipole excitation.

6.4.4   Pure dipolar noise

To validate that the effect of the suppression of the noise-driven emittance growth from the beam coupling impedance is associated with the dipolar motion (head-tail mode 0), the same simulations as in the previous section were conducted but instead of the longitudinally dependent noise kicks a pure dipolar noise kick was applied on the beam. The dipolar noise kick was modelled by the transformation of Eq. (3.1) for $\sigma_\theta^2 = 7.3 \times 10^{-6} \times 2$ which corresponds to a power spectral density of 3.36×10^{-10} rad^2/Hz. The noise strength was scaled so that it results in ~25 nm/s to be comparable with the initial studies presented in Section 6.3.

Figure 6.9 shows the noise-induced vertical emittance growth as a function of amplitude-dependent tune spread with and without the presence of wakefield kicks. In the absence of wakefields (blue) the emittance growth appears independent of the tune spread, while for $\alpha_{yy} = 0$ no emittance growth is observed. This is expected, since for zero betatron tune spread there is no decoherence and thus no emittance growth.

In the presence of wakefield kicks (orange) strong suppression of emittance growth is observed. The suppression reaches up to a factor of 10 for the small values of amplitude detuning (within the gray area which indicates the tune spread present in the SPS during the 2018 CC experiments). The fact that the suppression of the emittance growth is enhanced in the presence of dipolar noise, is another indication that the phenomenon is associated with the head-tail mode 0.
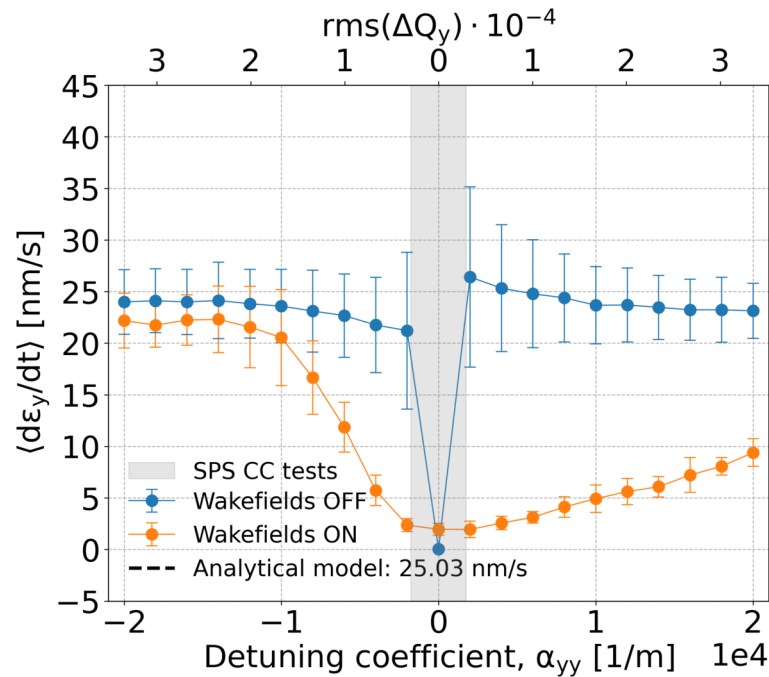
Figure 6.9: Simulated transverse emittance growth driven by a pure dipolar noise kick without (blue) and with (orange) the impedance effects as a function of tune spread. The error bars represent the standard deviation over 20 different runs of the simulation.

6.4.5 Sensitivity to linear chromaticity

The PyHEADTAIL simulations discussed up to now cover the case for linear chromaticity $Q'_{x,y} = 0.5$, which is believed to be the case for the emittance growth

6. Simulation studies: Emittance growth suppression mechanism from the beam transverse impedance

measurements in SPS in 2018. To understand the effect of the linear chromaticity on the suppression of the noise-induced emittance growth from the SPS impedance the same simulations as in Section 6.3 were repeated for a range of different chromaticities. In particular, five different values were studied: $Q'_{x,y} = 0.0, 0.5, 1.0, 2.5, 5.0$. The study is limited to small positive chromaticity values following past experimental chromaticity scans for emittance growth studies, $Q'_{x,y} < 10.0$ [66, 64]. An additional reason for not extending the study to the negative chromaticity values is that they would lead to head-tail mode 0 instability induced by the impedance, since the SPS experiments were performed above transition[3] [40].

The simulations for this subsection were performed using the setup and the parameters of Section 6.3 (i.e. for a crab cavity frequency of 400 MHz with phase noise). The results of the scan in $Q'_{x,y}$ are displayed in Fig. 6.10, where each subfigure shows the results for one chromaticity value, increasing in value from top left to bottom right.

In the absence of impedance effects (blue), the CC RF noise-induced emittance growth rates appear independent of both the amplitude detuning coefficient and the value of linear chromaticity. This is in agreement with the predictions of the Mastoridis–Baudrenghien model for the white noise spectrum.

In the presence of impedance effects (orange), suppression of the emittance growth is observed for all the studied values of linear chromaticity. An examination of the results shows that the impact of the linear chromaticity on the maximum suppression, which is observed for $\alpha_{yy} = 0$, is negligible. Yet, the simulated emittance growth rates exhibit a slightly different dependence on the vertical detuning coefficient, α_{yy}, for each of the five chromaticity values. This difference appears mainly for the negative values of α_{yy}. In particular, it appears that for increasing linear chromaticity, the provided tune spread from amplitude detuning

---

[3]The transition energy is defined by the lattice of the machine. Below transition energy particles with positive energy offset have a higher revolution frequency than the synchronous particle because they have a higher velocity. Above transition, the particles with positive energy offset have a smaller revolution frequency because they travel on a longer path around the machine and the velocity difference between the particles is comparably small. Further details can be found in [28], however, a further discussion is out of the scope of this thesis.

(a) $Q'_{x,y}=0.0$

(b) $Q'_{x,y}=0.5$

(c) $Q'_{x,y}=1.0$

(d) $Q'_{x,y}=2.5$

(e) $Q'_{x,y}=5.0$
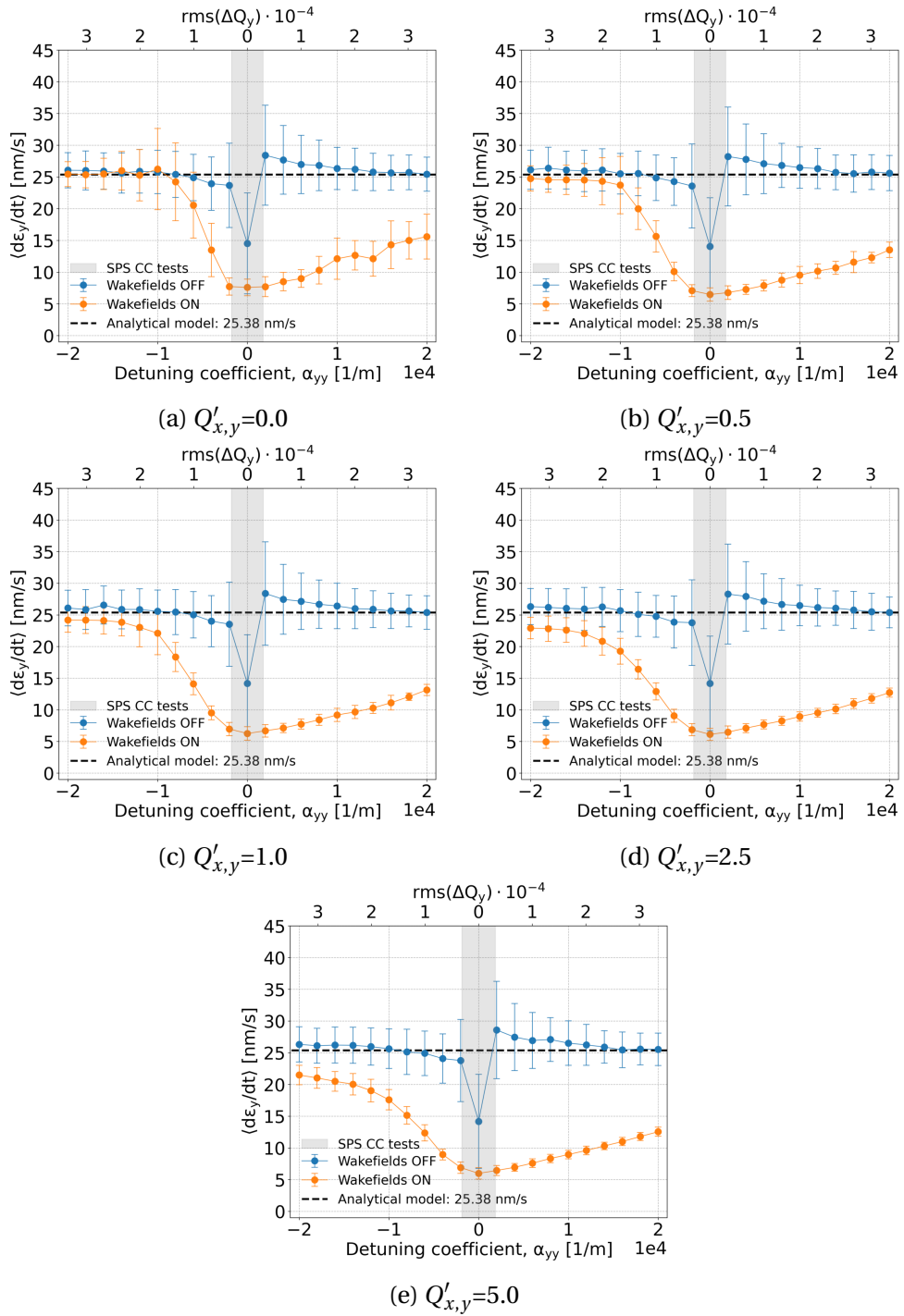
Figure 6.10: Simulated transverse emittance growth driven by CC RF phase noise, assuming a CC frequency of 400 MHz, without (blue) and with (orange) the impedance effects as a function of tune spread is shown for five different values of linear chromaticity increasing from top left to bottom right.

is becoming less sufficient for recovering the emitance growth rates expected from the Mastoridis–Baudrenghien model. Nevertheless, for the regime of the realistic SPS tune spread (grey stripe) the dependence of the suppression factor on the chromaticity appears negligible. The fact that there are no exact chromaticity measurements available from the SPS CC tests of 2018 is thus not an issue.

The weak dependence of the emitance growth rates (for different values of the detuning coefficient) on the chromaticity is not surprising as the damping or growth time of head-tail mode 0, is chromaticity-dependent. Nevertheless, overall, it can be concluded that there is no strong sensitivity of the suppression induced by the beam coupling impedance to the linear chromaticity.

6.4.6 Disentangling quadrupolar and dipolar impedance contributions

The simulation described in Section 6.3 is repeated taking into account the quadrupolar (detuning) and dipolar (driving) terms of the wakefields separately, in order to investigate their individual contribution to the phenomenon of emitance growth suppression. This is easily achievable since in the SPS impedance model the quadrupolar and dipolar terms are provided separately (see Section 6.1).The linear chromaticity for this study was set to $Q'_{x,y}$=0.5 units.

The results are summarised in Fig. 6.11. The upper plots illustrate the individual effect of the dipolar (left) and quadrupolar (right) terms of the SPS wakefields on the noise-induced emitance growth while the bottom plot shows the combined effect of the two terms. For each study case, the simulation results without including the impedance effects are also shown (blue) for reference. As usual, without including the impedance, the simulated growth rates appear independent of the vertical detuning coefficient and are in very good agreement (within the errorbars) with the theoretical predictions of the Mastoridis–Baudrenghien model which does not take into account impedance effects.

Looking at the emitance growth rates obtained in the presence of wakefield kicks (orange), it becomes evident that the dipolar contribution (Fig. 6.11a) results in a
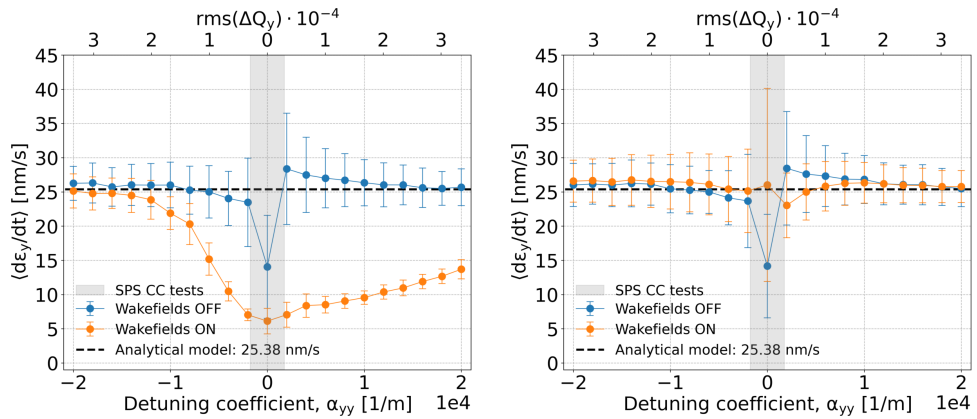
(a) Only dipolar (driving) impedance contribution.

(b) Only quadrupolar (detuning) impedance contribution.
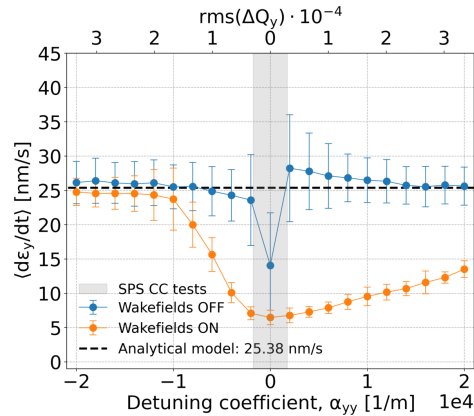
(c) Dipolar (driving) and quadrupolar (detuning) impedance contribution.
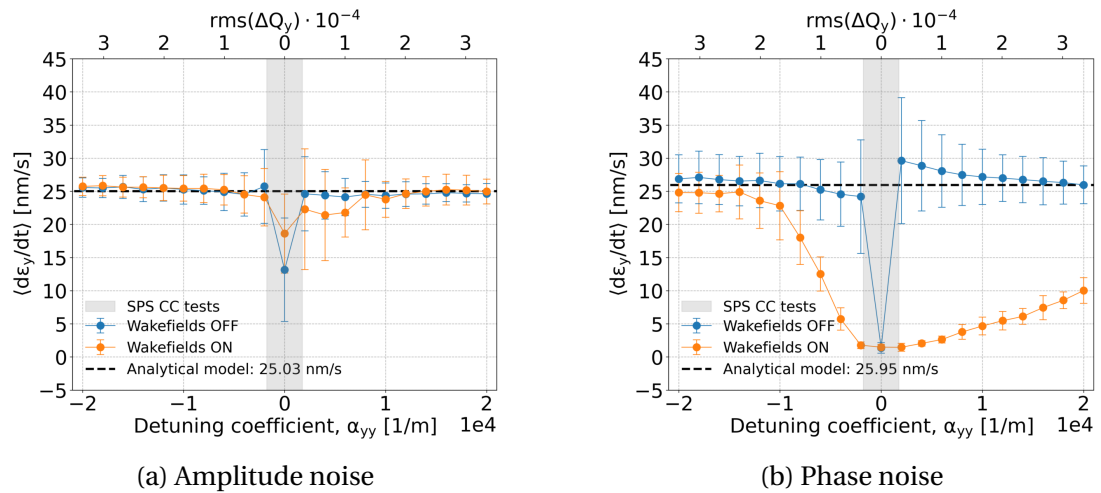
Figure 6.11: Simulated transverse emittance growth driven by CC RF phase noise, for a CC frequency of 400 MHz, without (blue) and with (orange) the impedance effects as a function of tune spread. *Top*: Simulation results with only the dipolar (left) and quadrupolar (right) impedance contribution. *Bottom*: Simulation results with the dipolar and quadrupolar impedance contributions combined.

strong suppression of the emittance growth which has the same dependence on the tune spread with the simulations that include both the dipolar and quadrupolar terms. In contrast, the emittance growth remains unaffected when only the quadrupolar contribution is taken into account (Fig. 6.11b). Thus, it is evident, that the effect of the suppression is a result of the dipolar term of the impedance.

The significance of the dipolar term is that it leads to coherent tune shift (see Section 2.3). Therefore, these simulation results show that the observed suppression of the noise-induced emittance growth is associated with the coherent tune shift from the dipolar impedance contribution. This suggestion and consequently the mechanism behind the observed suppression will be further explored in the next section.

6.5 Suppression mechanism

6.5.1 Similar effects studied in the past and motivation

As concluded in Section 6.4, the effect of the emittance growth suppression from the beam coupling impedance is associated with the coherent tune shift, caused by the dipolar impedance term. This triggered the idea, that the overlap between the coherent tune and the incoherent betatron tune spectrum could explain the observed effect of the suppression.

The motivation for this idea came from past theoretical studies [97, 98], which showed that in hadron colliders the efficiency of the feedback system at suppressing the emittance growth depends on the overlap between the frequency of the coherent mode and the incoherent tune spectrum. In particular, it was observed that the decoherence of dipole oscillations is drastically suppressed if the coherent tune of the beam is outside of the incoherent tune spectrum. This theory has been verified by numerical simulations and experimental studies for LHC [99, 100, 101]. For reference, additional simulation studies for the LHC case which deal with the above-mentioned phenomenon of decoherence suppression can be found

in [102, 103].

However, in the previous studies, the frequency of the coherent modes was shifted by the beam-beam effect[4] and not by the beam coupling impedance. Adjusting the theoretical approach of [97] for the impedance-induced tune shift was not straightforward.

Development of a new theoretical model

The experimental results of 2018 and the simulation studies with the SPS impedance model described above and in the following, motivated the development of a theoretical description for the suppression of the noise-induced emittance growth from the beam transverse impedance [105, 106].

This theory, developed by X. Buffat, is a simplification of the approach of Y. Alexahin (in the context of beam-beam interactions) [98]. In particular, X. Buffat adapted Y. Alexahin's approach for configurations featuring linear detuning and a complex tune shift from a collective force.

This theory predicts that the emittance growth driven by an external noise source can be significantly reduced by a collective force [105]. To observe the emittance growth suppression a damping force is necessary. The emittance growth suppression is enhanced in configurations where the real tune shift is larger than the spread of the betatron frequencies, i.e. the coherent mode emerges from the incoherent spectrum [105].

This theory supports the studies presented in this thesis. It also explains the asymmetry in the dependence of the emittance growth suppression for positive and negative detuning coefficients observed in PyHEADTAIL simulations. Moreover, it was used to fit the experimental data measured during the experiment with dipole noise (see Section 7.9) with very promising results [106].

In the following paragraphs, the suppression mechanism of the CC RF noise-induced emittance growth suppression by the transverse impedance is

---

[4]Beam-beam effects, are the ones induced by the perturbation of the two beams in a collider as they cross each other. Further details on these effects and the beam-beam interaction can be found in [104] but their analysis is out of the scope of this thesis.

further explored with tracking simulations using PyHEADTAIL.

6.5.2   Intensity scans

To test the hypothesis that the observed suppression of the emittance growth is a result of the separation of the coherent mode from the incoherent spectrum the emittance growth in the presence of CC RF phase noise and impedance is studied as a function of the bunch intensity. As illustrated in Section 6.1.1 the shift of the coherent tune increases (in absolute value) linearly for increasing intensity.

The simulation was performed for the beam and machine conditions of the 2018 CC experiments in the SPS as described in Section 6.3. The CC RF phase noise kick that was acting on the beam had a power spectral density of $1.68 \times 10^{-10} \text{rad}^2/\text{Hz}$, which results in an emittance growth of about $25 \, \text{nm/s}$.

In Section 6.3, it was shown that in order to reproduce the realistic rms tune spread ($\sim 2 - 3 \times 10^{-4}$) that was present in SPS during the 2018 experiments (from intrinsic non-linearities), the vertical amplitude detuning coefficient should be $|\alpha_{yy}|$=2000/m, which results however in a comparably small tune spread and thus results in a strong suppression of the emittance growth. Therefore, the intensity scan was performed for α_{yy}=6000/m which reduces the emittance growth suppression, while remaining close to the realistic machine conditions of 2018.

The study was conducted over a range of bunch intensities from 0 to 5×10^{10} protons per bunch. This range was chosen to be similar to the CC experiments in SPS in 2018, where the initial intensity for each coast was 3×10^{10}-3.5×10^{10} protons per bunch. The initial intensity was measured with the Fast Beam Current Transformer (FBCT) and the Beam Current Transformer (in particular with the device SPS.BCTDC.41435) which are installed in SPS. Both devices have the same working principle but different bandwidths. They measure the beam-induced current in their ferrite core and transform it to the number of protons per beam. Further details on their working principle and operation can be found in [107, 108].

The results of the intensity scan are summarised in Fig. 6.12, where the simulated emittance growth rate is plotted as a function of intensity. The spread of the initial

Figure 6.12: PyHEADTAIL simulations illustrating the effect of the beam intensity on the transverse emittance growth driven by CC RF phase noise in the presence of impedance effects. The grey area shows the range of the initial intensity values measured during the SPS CC tests in 2018.

intensity values during the SPS CC experiment of 2018 is given by the grey area for reference. For small intensity values, $<\sim 0.7\times10^{10}$ protons per bunch, the emittance growth rates appear to be little affected by any change in intensity and are close to the theoretically expected value of 25 nm/s. However, for intensity slightly larger than $\sim 0.7\times10^{10}$ protons per bunch there is a sudden drop in the obtained emittance growth rates. After that point, the emittance growth rates seem to decrease with increasing intensity. This dependence seems to saturate for larger intensity values, $>\sim 2.5\times10^{10}$ protons per bunch. It becomes apparent that the intensity value of the SPS CC tests (blue line) is well inside the regime of strong suppression.

The important observation of this study is that the dependence of the suppression of the emittance growth on the intensity is consistent with a suppression mechanism based on the overlap between the coherent betatron tune and the incoherent tune spread distribution. To further validate this hypothesis, simulations were performed aiming to examine the frequency spectrum of the bunch, which should reveal more information on the overlap of the coherent mode frequency and the incoherent spectrum. These simulations will be discussed in the

next subsection.

6.5.3   Spectral analysis of the bunch centroid motion

Here, the incoherent spectrum of the bunch is investigated for different intensities in an attempt to visualise and hence confirm that the mechanism for the suppression of the emittance growth is related to the separation of the coherent mode from the incoherent spectrum. The incoherent spectrum can be obtained from Fourier analysis of the turn-by-turn centroid motion. This method can be also found in the bibliography as Schottky noise method [109] and is often used for beam diagnostics as it can reveal information on important parameters such as tunes and chromaticity, and of course the incoherent tune spectrum.

For the spectral analysis studies presented here, the simulations presented previously (Section 6.5.2) were repeated but without applying any noise kick on the bunch to minimise the external perturbations and obtain a clear tune spectrum resulting from the wakefields and the detuning with amplitude only. This approach was chosen since the objective of the study is to see how the coherent tune is located compared to the incoherent betatron tune spectrum. The six-dimensional Gaussian distribution was now generated with an initial vertical offset of 0.2 times the rms vertical beam size. The reason behind this is that due to the offset the beam will undergo betatron oscillations with a sufficiently large amplitude to facilitate the Fourier analysis. Furthermore, this type of simulation requires longer tracking than the emittance growth studies, 10^6 turns instead of 10^5, for better resolution in the frequency domain. Finally, 5×10^4 macroparticles were sufficient[5] for this type of simulation which reduced significantly the computational time of the simulation. The spectra that will be discussed below were obtained by applying the NAFF algorithm (introduced in Section 6.1.1) to the turn-by-turn data.

The results are displayed in Fig. 6.13 which shows the vertical spectrum of the centroid (coherent) oscillation of the bunch for different intensity values, selected from the range studied in the previous Subsection 6.5.2, choosing cases for which

---

[5]Following similar studies in [110] and exploratory studies confirmed that the number of macroparticles used does not affect the quality of the results.

the separation of the coherent tune from the incoherent spectrum is clearly visible. Each subplot shows the power spectral density of the motion of the centroid as a function of the frequency in tune units for a given intensity value, which increases from the top left to the bottom right. The frequency of the coherent mode is shown with the vertical magenta line and it corresponds to the frequency with the highest amplitude.
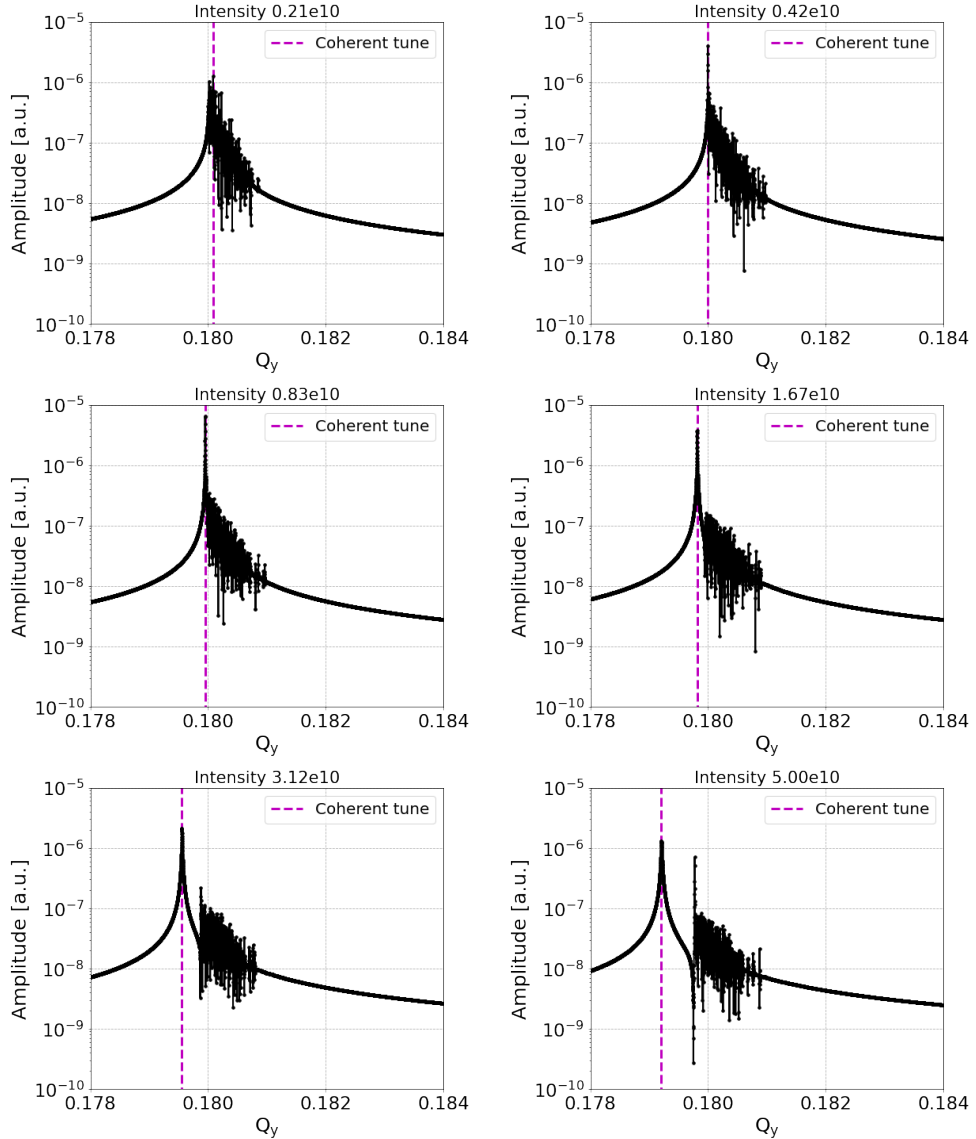
Figure 6.13: Simulated frequency spectra of the vertical bunch centroid motion on a logarithmic scale in the presence of the SPS transverse impedance model, calculated over 10^6 turns with 5×10^4 macroparticles for different values of intensity increasing from top left to bottom right.

Comparing Fig. 6.13 with Fig. 6.12 it becomes evident that:

- The two upper spectra, where the coherent mode lies inside the incoherent

spectrum, reside in the regime of no emittance growth suppression.

- The two middle spectra, where the coherent mode emerges from the incoherent spectrum, reside in the regime where the emittance growth suppression increases for higher intensity values.

- The two bottom spectra, where the coherent mode is well separated from the incoherent spectra, reside in the regime where the dependence on the intensity saturates.

The above observation, confirms that the transverse impedance separates the coherent tune from the incoherent spectrum and this is related to the effective suppression of the CC phase noise induced emittance growth.

According to the studies of Y. Alexahin [97] (which were performed in the context of the beam-beam modes) the separation of the coherent mode from the incoherent spectrum results in a suppression of the decoherence of the dipole oscillations and thus of the dipole and/or phase-noise-induced emittance growth. What happens is that only part of the energy from the noise kicks is absorbed by the incoherent spectrum and drives incoherent motion leading to irreversible emittance growth. The rest of the energy is absorbed by the coherent mode, which is damped [6] by the impedance (for the experimental conditions of small positive chromaticity) without leading to emittance growth.

A similar effect seems to be happening in the case studied here, where the impedance induced tune shift pushing the coherent tune of the bunch outside of the incoherent spectrum results in the suppression of decoherence and thus of the CC noise induced emittance growth. A recent theoretical description of this phenomenon, triggered by the studies presented in this thesis was developed by X. Buffat [105, 106].

---

[6]The damping rate of the coherent tune (mode 0) for the experimental parameters of 2018, was estimated to be 3.6 1/turns using Eq. (2.58)

6.5.4 Dependence on bunch length

In this section, the emittance growth in the presence of CC RF phase noise and impedance is studied as a function of the bunch length. The goals of this study are: first, to complete the set of parametric studies presented already in this chapter; and second, to identify possible limitations on observing the effect of the emittance growth suppression introduced by the bunch length. The latter is very important for the second experimental campaign with CCs in the SPS that took place in early 2022 and that will be discussed in further detail in the following chapter.

This parametric study was conducted for the experimental beam and machine conditions of 2018 as shown in Tables 6.1 and 6.2, and described in Section 6.3. The CC RF phase noise kick that was acting on the beam had a power spectral density of $1.68 \times 10^{-10}\,\mathrm{rad}^2/\mathrm{Hz}$, which results in an emittance growth rate of about $25\,\mathrm{nm/s}$. The vertical amplitude detuning coefficient was set to α_{yy}=2000/m in order to reproduce the realistic rms tune spread ($\sim 2-3 \times 10^{-5}$) that was estimated for SPS during the 2018 experiments (from intrinsic non-linearities). The study was performed for a range of bunch lengths ($4\sigma_t$) from 0 to $4\,\mathrm{ns}$. In practice, no simulations were conducted for zero bunch length as it is not a realistic value.

Simulations are performed with and without wakefields. The PyHEADTAIL simulation results are summarised in Fig. 6.14, together with the predictions of the Mastoridis–Baudrenghien model (which does not include the effects of machine impedance).

Figure 6.14 illustrates, as expected, that the simulation results without the wakefields (blue) are in very good agreement with the theoretical predictions (black model), within the error bars. However, there is some systematic difference, of a few microns per hour, between the mean emittance growth obtained from the simulations and the theory, which shrinks for longer bunches. The reason for this is not understood but it was not investigated further since for the regime of realistic bunch lengths values for the SPS experiments (grey stripe) the difference is insignificant and it does not affect the conclusions drawn from these studies.
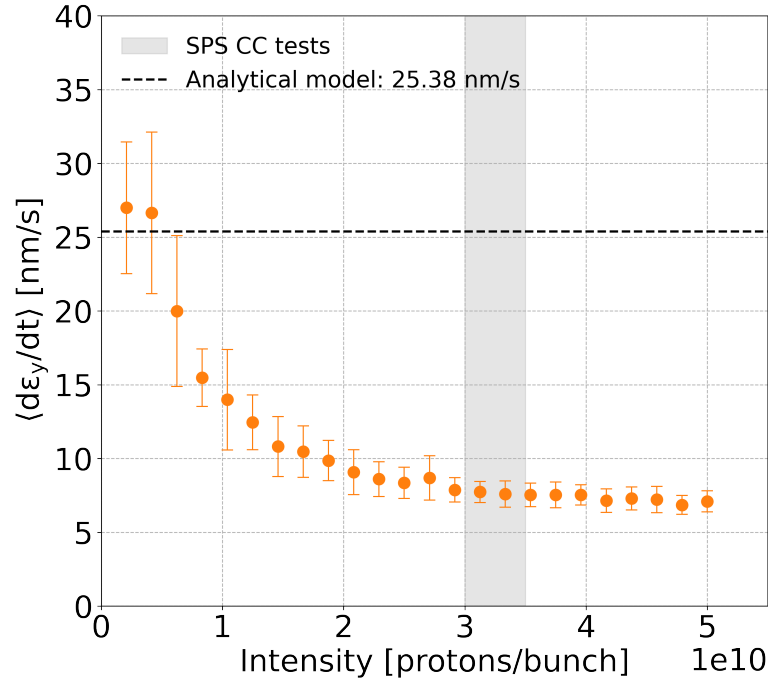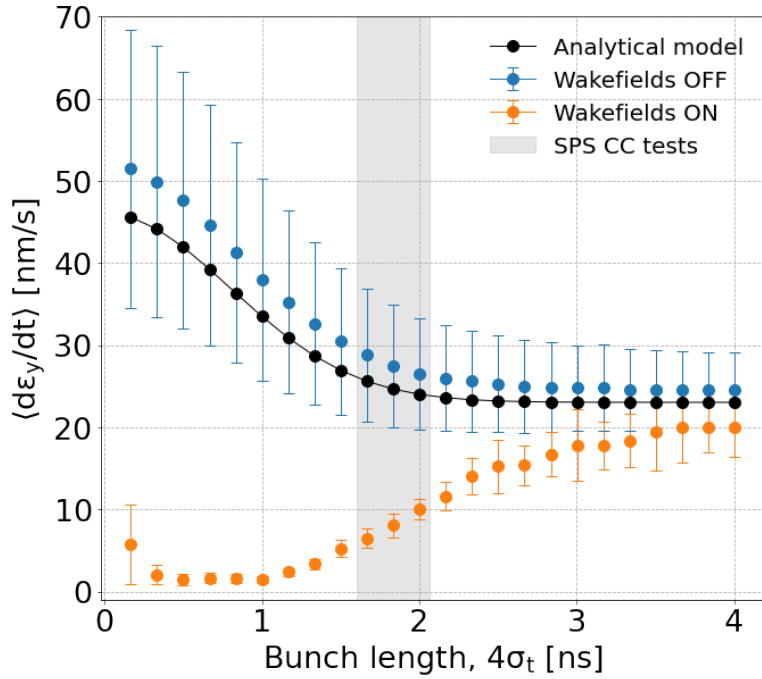
Figure 6.14: PyHEADTAIL simulations illustrating the impact of the bunch length on the transverse emittance growth driven by CC RF phase noise in the absence (blue) and in the presence (orange)of impedance effects. The analytically predicted emittance growth rates (not including impedance effects) are also shown (black). The regime of the realistic bunch length values during the SPS CC tests of 2018 is depicted with the grey stripe.

In the presence of wakefields (orange), there is a clear dependence of the suppression of emittance growth on the bunch length. In particular for bunch length values smaller than 1 ns the suppression appears very strong and is roughly independent of the precise value of the bunch length. For longer bunches, up to about 3.5 ns ($4\sigma_t$) the suppression factor appears to decrease with the bunch length. For bunches longer than 3.5 ns ($4\sigma_t$) the dependence of the emittance growth on the bunch length seems to saturate, and the emittance growth rates are also in agreement with the theoretical model which does not include the contribution from the wakefields. The suppression of the emittance growth is reduced for larger bunch lengths: this is consistent with the mechanism discussed in Sections 6.5.2 and 6.5.3, since the separation of the coherent tune from the incoherent tune spread is also reduced at larger bunch length. The behavior of the dependence, which is inversely proportional to the bunch length value is explained by the fact that the coherent tune shift from the impedance is also inversely proportional to the bunch length. In other words, for short bunches the coherent

tune shift from the impedance is strong and thus the coherent mode emerges from the incoherent spectrum leading to the strong emittance growth suppression. For larger bunch lengths the shift of the coherent mode is weaker resulting in weaker suppression which eventually saturates once the coherent mode lies inside the incoherent spectrum.

Finally, the first point of the simulation results with the wakefields seems to not follow the otherwise smooth dependence on the bunch length. Also, a much bigger spread of the emittance growth between the different runs is observed. A possible explanation could be that for very short bunches the wake potential used for the simulations may not be a completely accurate representation of the actual wakefields in the machine.

6.6   Conclusions

PyHEADTAIL simulations showed for the first time that the transverse beam impedance (not included in the theory nor in the numerical simulations so far) has a significant impact on the emittance growth driven by RF noise in the crab cavities. In particular, it was found that the transverse impedance can suppress the crab cavity noise-induced emittance growth once the coherent tune, which is shifted by the impedance, moves out of the incoherent tune spectrum. It turns out that, when the coherent tune is outside the incoherent tune spread, the rate of decoherence of betatron oscillations is reduced, leading to a suppression of the noise-induced emittance growth rate as shown by recently developed theoretical models [105, 106]. This mechanism, which has been observed in the past as a result of beam-beam interactions, is related to the transverse dipole oscillation of the beam. To this end, the suppression is not observed for amplitude but only for phase noise-induced emittance growth.

For the beam and machine conditions as in the 2018 SPS experiment, the simulations with the complete SPS transverse impedance model revealed a strong emittance growth suppression of about a factor 4-5, which agrees with the experimental observations and hence it appears to explain the observed

discrepancy with the Mastoridis–Baudrenghien theoretical model of (see Chapter 4).

The PyHEADTAIL simulations also revealed a strong dependence of the emittance growth suppression factor on the amplitude-dependent tune shift, as it modifies the incoherent tune spectrum. This behaviour can be tested in the SPS with the use of the Landau octupoles. Based on this, an experiment was planned and took place in the SPS in 2022, aiming to reproduce the dependence of the emittance growth suppression on the amplitude detuning. Further details and the results of this additional experimental campaign with CCs in the SPS are presented in the next chapter.

7 | Experimental studies from 2022: investigation of the effect of impedance on noise-induced emittance growth

7.1 Motivation

As discussed in the previous chapter, PyHEADTAIL simulations including the SPS impedance model suggest that the beam coupling impedance leads to an effective suppression of the CC RF phase noise induced emittance growth through the separation of the coherent tune from the incoherent spectrum. This emittance growth suppression, which is related to the coherent (dipole) motion, can reach up to a factor of 4-5 for the experimental conditions of the first experimental campaign with CCs that took place in the SPS in 2018 and seems to be the explanation for the experimental observations (see Section 4.5.2).

This emittance growth suppression effect has not been observed before. To this end, another experimental campaign took place in the SPS in 2022 where the main objective was to validate experimentally the above-mentioned suggested emittance growth suppression mechanism. If successful, it would constitute the first experimental investigation and validation of this effect. Moreover, achieving a good understanding of the 2018 results is essential for developing confidence in the theoretical model and its predictions for the HL-LHC.

The experimental campaign of 2022 was organised in five experiments which aimed to investigate in the SPS machine the effect of the impedance on the noise-induced emittance growth. The first four experiments were carried out with artificial noise

injected in the CC RF system. The fifth experiment took place with a pure dipolar noise source: the transverse damper. This chapter reports on the preparation, the methodology, and the results of these experiments.

7.2 Machine and beam configuration

The emittance growth measurements in 2022 were performed in "coast" mode at 270 GeV following the same setup as in 2018 (see Section 4.2) and very similar machine and beam conditions. The most relevant parameters are listed in Table 7.1. The listed values of the transverse normalised emittance, of the bunch length, and of the intensity correspond to the requested initial values of each coast. The measured values of these parameters will be commented in the following sections and the detailed measurements through the experiments are available in Appendix E.

Table 7.1: Main machine and beam parameters for the emittance growth studies in SPS in 2022.

Parameter	Value
Beam energy, E_b	270 GeV
Main RF voltage / frequency, V_{RF} / f_{RF}	5 MV / 200.39 MHz
Horizontal / vertical betatron tune, Q_{x0} / Q_{y0}	26.13 / 26.18
Horizontal / vertical first order chromaticity, Q_x' / Q_y'	0.0-1.0 / 0.0-1.0
Synchrotron tune, Q_s	0.0051
Number of protons per bunch, N_b	3×10^{10} p/b*
Number of bunches	1
Bunch length, $4\sigma_t$	1.83 ns*
Horizontal / vertical normalised emittance, ϵ_x / ϵ_y	2 µm / 2 µm*
Horizontal / vertical rms tune spread, $\Delta Q_x^{\mathrm{rms}}$ / $\Delta Q_y^{\mathrm{rms}}$	1.9×10^{-5} / 2.1×10^{-5} ‡
CC1 voltage / frequency, $V_{0,\mathrm{CC}}$ / f_{CC}	1 MV / 400.78 MHz

* These values correspond to the requested initial values at the start of each coast.
‡ Here the rms betatron tune spread includes only the contribution from the detuning with amplitude present in the SPS machine. More details along with the calculations for the listed values can be found in Appendix C.1.

The emittance growth measurements of 2018 indicated that the betatron coupling in the SPS was small but not zero. On this ground, for the experimental campaign of 2022, there was an effort to reduce the betatron coupling in the SPS. The betatron coupling correction was performed before the start of the emittance growth measurements on May 16, 2022, using the skew quadrupoles to minimise

the tune signal from the horizontal (vertical) plane in the FFT measurements of the vertical (horizontal) plane. It is assumed that the settings of the skew quadrupoles remained unchanged for all of the five experiments.

Recalling that the last three (out of four) bunches in the 2018 experimental campaign were unstable, the experiments in 2022 were carried out with a single bunch. This choice allowed also to have better control on the beam conditions, avoiding possible effects from interactions between the bunches[1].

In the experimental campaign of 2018, CC2 was used. On the contrary, in 2022 the experiments with CC RF noise were conducted with CC1 for the reasons discussed in Section 7.4.1.

Finally, the emittance values were measured with the SPS Wire Scanners according to the procedure discussed in Section 4.5.1. In particular, the Wire Scanners SPS.BWS.51637.H and SPS.BWS.41677.V were used for measurements in the horizontal and vertical planes, respectively. These are new devices, installed in the machine as part of the LHC Injectors Upgrade (LIU) project [111]. For both devices the data points from the second photomultiplier were used (PM2)[2]. The beta functions of the respective plane at the locations of the Wire Scanners are β_x=79.29 m, and β_y=60.75 m. As explained earlier (see Section 4.5.1) during each measurement with the Wire Scanners the beam profile is acquired two times as the wire crosses the beam in the forward direction (IN scan) and then, 200 ms later, in the reverse direction (OUT scan). The analysis that is presented in this thesis, considers only the IN scan measurements for reasons that are discussed in the Appendix E.1.

---

[1]Even though these effects should be insignificant due to the large bunch spacing, see Table 4.2.

[2]Each Wire Scanner device is equipped with four PMs. Each one of them provides a better resolution of the amplitude signal of the secondary particles for a different regime. The choice of PM2 for the emittance growth studies in 2022 was done "online", during the experiment, by examining the obtained beam profiles.

7.3 Preparatory studies with PyHEADTAIL simulations

In preparation for the experiments with CC, the emittance growth in the presence of CC RF phase noise was simulated with PyHEADTAIL including the most up-to-date SPS impedance model [96] as a function of amplitude-dependent tune spread introduced by octupoles. In particular, the octupoles of the LOD family were considered as they act mostly in the vertical plane which is the plane of interest in these studies (vertical CC module). The beam and machine parameters are the ones reported in Table 7.1 which correspond to the experimental conditions of 2022. These preparatory studies were used to identify different regimes of the phenomenon of the emittance growth suppression by the beam transverse impedance for the experimental machine conditions and served as a guide for the planning of the experiments.

The emittance growth is induced by CC RF phase noise with a power spectral density of $1.68 \times 10^{-10} \, \mathrm{rad}^2/\mathrm{Hz}$ in the first betatron sideband which results in an emittance growth rate of about $25 \, \mathrm{nm/s}$. It should be highlighted that this noise level is much stronger than the levels of the injected artificial noise used in the experiment, in order for the emittance growth to be easily observed in the simulation time of just $2.5 \, \mathrm{s}$. Therefore, the goal of the experiments was to reproduce the simulated suppression factor and overall behavior. The simulation setup and the CC RF phase noise were simulated as discussed in Chapter 6.

The emittance growth was simulated over a range of k_{LOD}[3] values. In the simulations, no actual octupolar elements were used in order to avoid the excitation of resonances as discussed in Section 6.3. Instead, following the preceding PyHEADTAIL simulations, the effect of the Landau octupoles is introduced as a change in the phase advance of the individual particles depending on their individual actions and defined by the corresponding detuning coefficients. The study was performed for zero horizontal detuning coefficient, α_{xx}=0 since the

---

[3]The parameter k_{LOD} is the normalised strength of the LOD octupole family in the SPS and it corresponds to the k_3 definition of Eq. (2.5).

horizontal coefficient does not affect the vertical emittance growth assuming zero coupling between the two transverse planes. The values of the vertical, α_{yy}, and the cross-term, α_{yx}, coefficients were calculated using MAD-X [48] for each k_{LOD} value.

Figure 7.1 illustrates the dependence of the CC RF phase noise-induced emittance growth on the octupoles strength, in the absence (blue) and the presence (orange) of the wakefields. The analytical prediction of the Mastoridis–Baudrenghien model is also given to facilitate the identification of the suppression factor from the impedance (horizontal black dashed line). As usual, in the absence of wakefields, there is a very good agreement between the simulation results and the theoretical predictions. In the presence of wakefields, the expected dependence on the tune spread appears. The rms tune spread values (shown on the secondary horizontal axis) are computed taking into account both the α_{yy} and α_{yx} coefficients using Eq. (C.6).

The green and yellow areas indicate regimes where the octupoles require less than 200 A and 400 A respectively for their operation. The maximum operational current for the defocusing octupole family (LOD) in SPS is 400 A. However, due to their planned continuous operation in multiple coasts, the LOD current should stay below 200 A. The required current for the octupoles is computed from their strength, k_{LOD}, using Eq. (C.8)

From Fig. 7.1, we make the following observations:

1. For the octupoles switched off, k_{LOD}=0, a suppression factor of about 3 is observed.

2. The strong dependence of the emittance growth suppression on amplitude-dependent tune spread is observed for $|k_{\mathrm{LOD}}| \leq 20 \,/\mathrm{m}^4$.

   - The dependence is asymmetric between positive and negative octupole strengths. In particular, for negative octupole polarity the emittance growth suppression starts for smaller octupole strengths (in absolute value).
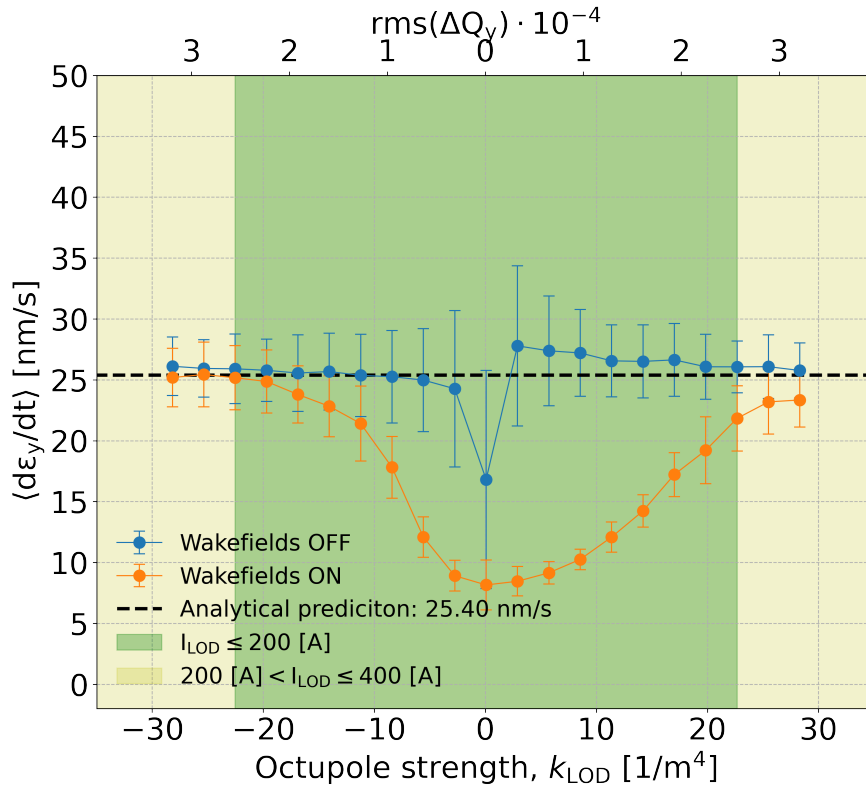
Figure 7.1: Transverse emittance growth driven by CC RF phase noise without (blue) and with (orange) the impedance effects as simulated using PyHEADTAIL. The error bars represent the standard deviation over 20 different runs of the simulation. The green and yellow areas indicate regimes where the octupoles require less than 200 A and 400 A respectively for their operation.

3. For $|k_{LOD}| > 20 \, /\text{m}^4$ the emittance growth rate expected from the Mastoridis–Baudrenghien model seems to be restored.

- Even for the strongest octupole strengths, $|k_{LOD}| \approx 30 \, /\text{m}^4$, the required current remains below 400 A. Consequently, no crucial limitations are introduced to the experiment from the octupoles operation.

7.4 Experiment I: dependence of Crab Cavity RF phase noise induced emittance growth rates on the noise power

For the experiment described here, the emittance growth was measured in the presence of four different noise levels (similar to the ones used in 2018) with the

Landau octupoles switched off. The objective was a) to reproduce the scaling of emittance growth observed in 2018 (see Fig. 4.6) and b) to benchmark the expected emittance growth suppression factor from PyHEADTAIL simulations with the impedance model. Experiment I took place in the SPS on May 16, 2022.

Four different levels of artificial noise were injected in the RF system of the CC as listed in Table 7.2 and the emittance was measured in coast mode every ~1.5 minute. For each noise level, a new bunch was injected so that all measurements took place with the same initial conditions. The duration of each coast varied from about 30 minutes for the low noise levels to about 20 minutes for the strong noise.

The linear chromaticity was corrected to about zero units in both the horizontal and vertical planes.

7.4.1 Calibration of the Crab Cavity phase offset and voltage measurement

The first step before the emittance growth measurements was to measure the CC voltage and calibrate the phase offset. It is reminded that in the experimental campaign of 2018, it was found that there was a phase offset between the set phase of the CC and the phase experienced by the beam (see Section 4.4). Even though simulation studies showed that for the long bunches used in the CC experiments the CC phase offset has no significant impact on the phase noise induced emittance growth [73] an automated procedure was developed for identifying and correcting this phase offset. The same procedure can also provide the amplitude of the CC voltage.

The calibration was performed by varying the phase setting of CC1 from -180° to +180° in steps of 30°. For each step, the z-dependent closed orbit offset along the bunch was acquired with the Head-Tail monitor and the CC voltage signal was reconstructed following the same procedure described in Section 4.4[4]. For each

---

[4]The calibration of the Head-Tail monitor which provides the normalisation factor that converts the measured intra-bunch offset to millimeters (more details in Appendix D.2) was repeated in 2022. The calibration factor for the Head-Tail monitor was measured to be 0.1037 in 2021(see Appendix D.3).

acquisition, the CC voltage at the center of the bunch, $t = 0$, was plotted as a function of the corresponding phase setting. The results of the phase scan for CC1 are summarised in Fig. 7.2 (blue dots). The three-parameter sinusoidal function of Eq. (4.7), which provides the amplitude, the phase and the vertical offset of the signal (A, θ, d) is used to fit the measured data.
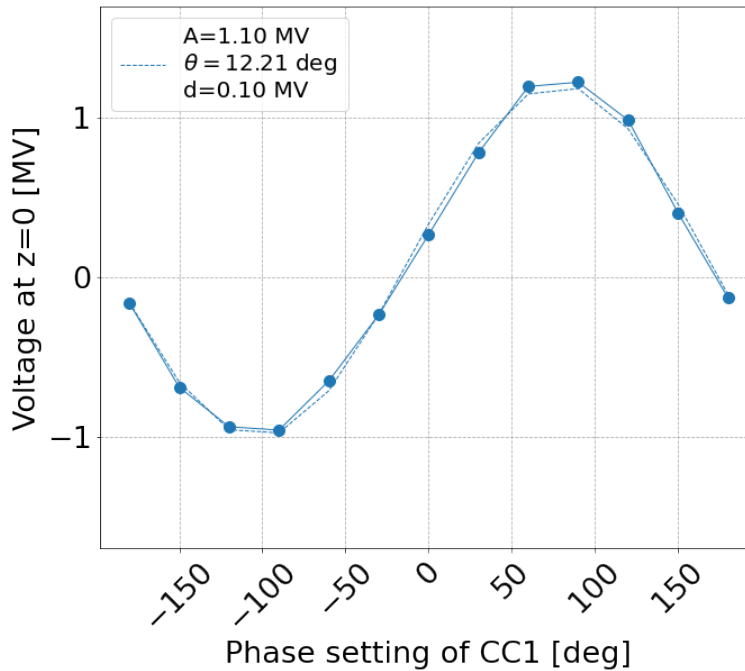
Figure 7.2: Calibration plot for CC1 as obtained during the experiment on 16 May 2022, displaying the CC voltage at the center of the bunch $t = 0$ for different phase values set in CC1.

The results of the sinusoidal fit (blue dashed line) are illustrated in the legend box in Fig. 7.2. From the beam-based measurements with the Head-Tail monitor, the phase offset was found to be $12.21°$. For the rest of the experiment, this phase offset was compensated so that the phase of the CC voltage experienced by the bunch is zero.

From the fit, the amplitude voltage of CC1 was found to be (following the discussion in Section 4.4): $V_{0,\mathrm{CC}} = A \pm d = 1.1 \pm 0.1\,\mathrm{MV}$, very close to the targeted one (1 MV). This approach of measuring the CC voltage experienced by the beam is preferred over the approach used in 2018, since now multiple Head-Tail acquisitions are taken into account contrary to the single acquisition used in 2018.

For reference, the calibration for CC1 took place at $270\,\mathrm{GeV}$ and it lasted for about

15 minutes (start: ~09:40, end: ~09:52).

Between ~11:39 and ~11:45 the same scan for CC2 was attempted. However, the cavity tripped systematically due to issues associated with the change of the RF phase. Fixing this issue would have been time-consuming, and was not possible due to the very limited machine time for the experiment. Therefore, for the measurements in 2022 CC1 was used.

7.4.2 Measurement of background growth rate in coast mode

After the calibration of CC1, the coast at 270 GeV was set up for the emittance growth measurements. First, the background emittance growth, with no additional noise injected in the CC and the Landau octupoles switched off was measured. The background emittance growth was found to be similar in both transverse planes: $d\epsilon_x/dt = 0.81 \pm 0.14\,\mu$m and $d\epsilon_y/dt = 0.84 \pm 0.25\,\mu$m in the horizontal and vertical planes respectively. This measured background emittance growth is illustrated in Fig 7.3 for both the horizontal (blue) and vertical (red) planes.
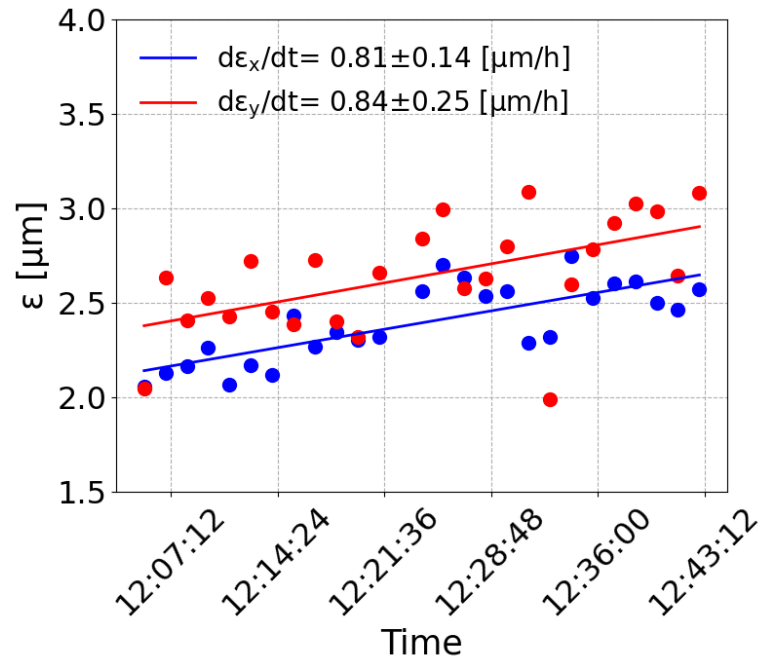
Figure 7.3: Horizontal (blue) and vertical (red) background emittance growth measured during the experiment with CC1 on May 16, 2022, with no artificial noise injected in the CC RF system and with the Landau octupoles switched off.

From the above figure, it is evident that there is a significant fluctuation in the

emittance values in both transverse planes. By looking at the beam profiles, no evidence (e.g. corrupted profiles, abnormal tails, large errors on the Gaussian fit results) was found to exclude some of the points. This fluctuation seems to be related to the new Wire Scanner instruments. As discussed with the experts it appears to be within the limitations of the instrument for these small emittance values. In order to reduce the sensitivity of the linear fit (from which the emittance growth rates are obtained) longer measurements are required (at least 40 minutes). For larger emittance growth rates, or in other words for larger emittance values, the effects of the fluctuations are mitigated.

At this point, it is worth noting that the emittance measurements presented in this chapter, are obtained using an automatic fitting algorithm (using the fitting function described in Eq. (4.8)) embedded in the applications which launch the Wire Scanners. All the results were also manually cross-checked to validate the quality of the fit following the procedure described in Section 4.5.1. The automatic algorithm does not provide the respective uncertainty of the computed emittance values, however, during the manual check of the profiles (which included the calculation of the uncertainties) it was found that the uncertainties on the computed emittance values are 2-3 orders of magnitude smaller than the emittance values themselves (see Appendix E.1). Therefore, their impact on the results of the linear fit applied to obtain the emittance growth rates is insignificant. Furthermore, the emittance growth rates are dominated by the fluctuation of the Wire Scanner acquisitions (as clearly shown in Fig. 7.3). To this end, the uncertainties on the emittance growth values are not included in the analysis to simplify the procedure.

Finally, for reference, the noise floor of the amplitude and phase noise of the CC at 8 kHz were measured to be -130.2 dBc/Hz and -125.7 dBc/Hz respectively. From the Mastoridis–Baudrenghien model the expected vertical emittance growth from those noise levels 0.2 μm/h from both noise types combined. this analytically computed rate was obtained for bunch length, $4\sigma_t = 1.83$ ns and the measured amplitude of the CC voltage of $V_{0,\text{CC}} = 1.1$ MV. The rest of the observed growth rates, is due to other sources which have not so far been identified (discussed in Chapter 4).

7.4.3 Injected Crab Cavity RF noise

The noise injected in the CC RF system was similar to the one used in the experimental campaign of 2018. Thus, the noise spectra extended up to 10 kHz overlapping and primarily exciting the first vertical betatron sideband only, at ~8 kHz. The phase noise was dominant, however, there was always some amplitude noise unavoidably injected into the CC RF system. The predicted transverse emittance growth from Mastoridis–Baudrenghien model can be computed using Eqs. (4.5) and (4.5) for amplitude and phase noise, respectively.

The power spectral density values at ~8 kHz of the four different levels of artificial noise measured during the experiment are listed in Table 7.2 along with the corresponding expected emittance growth rates from the Mastoridis–Baudrenghien theory. By looking at the table, it is evident that the contribution of amplitude noise to the total emittance growth was found to be small: about 7 % on average over all noise settings.

Table 7.2: Phase and amplitude noise levels injected in the CC RF system for the Experiment I in 2022 along with the analytically expected emittance growths. The listed noise values correspond to the power spectral density values at the first vertical betatron sideband, f_b, at ~8 kHz. The analytical emittance growth rates were computed using Eq. (4.5) and (4.6) for a bunch length of $4\sigma_t$=1.83 ns and the measured amplitude of CC voltage, $V_{CC,0}$=1.1 MV.

	$10\log_{10}\mathscr{L}$ (f) [dBc/Hz]		Analytical $d\epsilon_y/dt$ [μm/h]	
	Phase noise	**Amplitude noise**	**Phase noise**	**Amplitude noise**
Level 1	-115.2	-124.6	1.99	0.2
Level 2	-109.5	-120.5	7.39	0.51
Level 3	-104.7	-116.0	22.32	1.44
Level 4	-100.1	-111.0	64.35	4.54

7.4.4 Transverse emittance growth measurements

Four different levels of artificial noise were injected in the RF system of the CC as listed in Table 7.2 and the emittance evolution was recorded in coast mode at 270 GeV every ~1.5 minute. For each noise level, a new bunch was injected so that all measurements took place with similar initial conditions. The duration of each coast varied from about 30 minutes for the low noise levels to about 20 minutes for

the strong noise.

For the strong noise, less measurement time is sufficient since the growth rate obtained from the linear fit on the emittance values is less sensitive to the fluctuations in the Wire Scanner measurements. Additionally, for strong noise, the emittance reaches very quickly very large values, about 8-10 μm, which eventually degrades the quality of the transverse bunch profiles: they cannot be represented accurately by a Gaussian function.

For reference, the transverse emittance growth measurements lasted for about 2.5 hours (start: ~12:50, end: ~15:18). Figure 7.4 illustrates the transverse emittance growth measured during Experiment 1 in 2022 for the four different noise levels injected in the CC RF system increasing from top left to bottom right. These measurements are summarised in Fig. 7.5 which gives an overview of the vertical and horizontal emittance growth rates plotted as a function of the four different phase noise levels.

There is a clear emittance growth in the vertical plane which is stronger for higher noise, as expected. A growth in the horizontal emittance is also observed, but this appears to be independent of the growth in the vertical plane. This indicates that the use of the skew quadrupoles (discussed in Section 7.2) sufficiently minimised the betatron coupling. Consequently, even though in the 2018 analysis the total emittance growth given by $d\epsilon_y/dt + d\epsilon_x/dt$ was considered to account for effects of betatron coupling, in the 2022 analysis the growth in the horizontal and vertical planes will be treated separately.

7.4.5 Bunch length and intensity measurements

The bunch length measurements were performed with the Wall Current monitor. The bunch length evolution along each coast can be found in Appendix E.3.1. The average measured bunch length (over all coasts) was found to be about $4\sigma_t \approx$ 1.83 ns. During the coasts, an increase in the bunch length of ~5 %/h on average for each setting was observed. This small increase agrees with what is usually observed in the SPS in coast and will not be taken into consideration in the

(a) -115.2 dBc/Hz

(b) -109.5 dBc/Hz

(c) -104.7 dBc/Hz

(d) -100.1 dBc/Hz
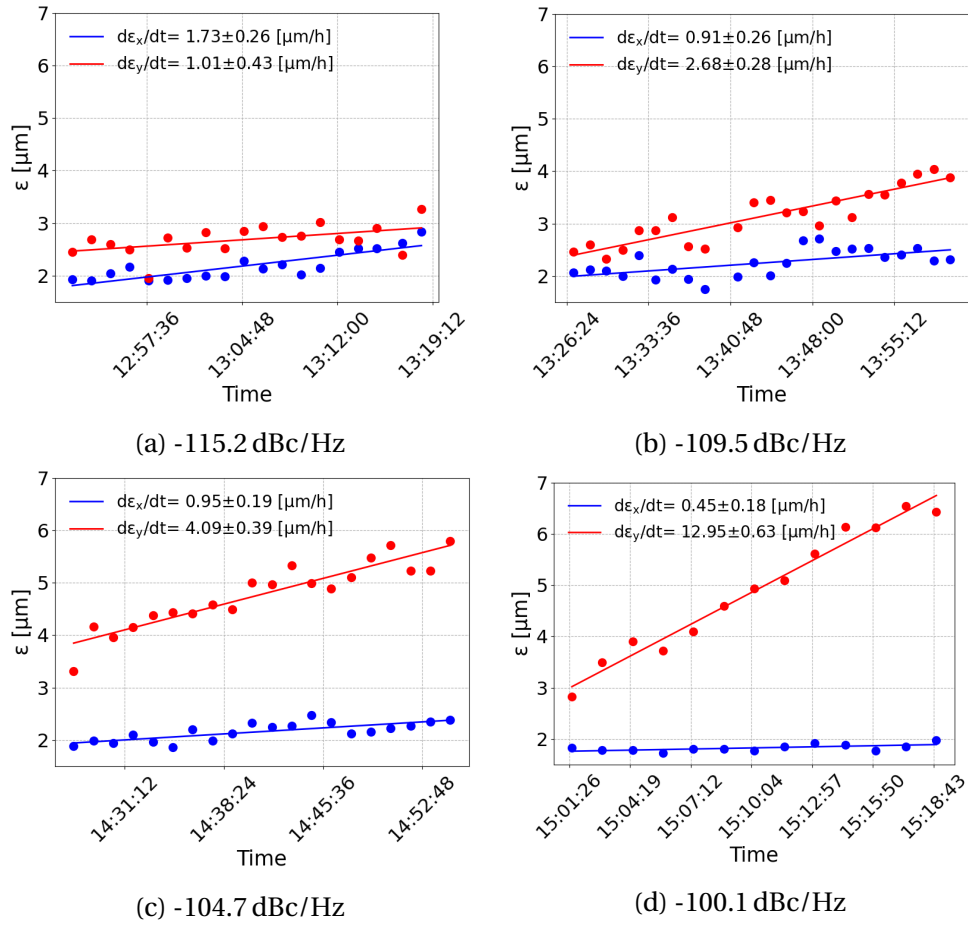
Figure 7.4: Horizontal (blue) and vertical (red) emittance evolution of a single bunch during Experiment I on 16 May, 2022. The different phase noise levels injected in the RF system of CC1, are shown in the caption for each plot.
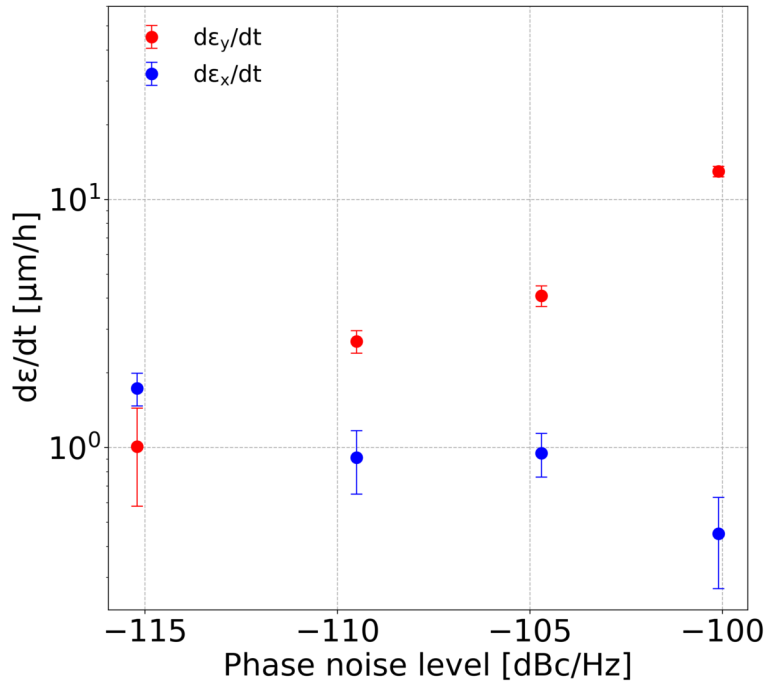
Figure 7.5: Overview plot of the emittance growth study during Experiment 1 with noise injected in the CC1 in 2022. The measured horizontal (blue) and vertical (red) emittance growth rates are shown as a function of the different power levels of applied phase noise. The error bars indicate the error of the linear fit to the emittance values (see Section 4.5).

following analysis.

The intensity measurements were performed with the Beam Current Transformer (BCTDC) [107, 108]. The bunch intensity along each coast can be found in Appendix E.4.1. The average intensity (over all coasts) was found to be about 2.9×10^{10} protons per bunch, very close to the requested values of 3.0×10^{10}. No significant losses were observed during the coasts, therefore the evolution of the intensity will not be taken into consideration in the analysis.

7.4.6 Comparison of the transverse emittance growth with the predictions of the Mastoridis–Baudrenghien model

Figure 7.6 compares the measured (red) and the theoretically calculated (black) vertical emittance growth rates for the different noise levels. For the comparison, the background growth rate measured in the vertical plane (see Section 7.4.2) of $0.84\,\mu$m/h is subtracted from the measured values. The subtraction of the

background has practically no impact on the high noise levels but it is significant for the small ones. The concept of effective phase noise that was used in the analysis of the 2018 experimental date is not used here. The reason is that in 2022 we know that the effect of the emittance growth suppression that we are investigating does not have the same behavior in the presence of amplitude and phase noise. To this end, the horizontal axis displays the four different phase noise values since they were dominant. However, the theoretically calculated values are obtained by inserting both the phase and the corresponding amplitude noise levels of Table 7.2 in Eqs. (4.6) and (4.5), respectively, for bunch length of $4\sigma_t = 1.83$ ns, energy of 270 GeV, the measured CC voltage amplitude $V_{0,\text{CC}} = 1.1$ MV, and the vertical beta function at the location of CC1, 76.07 m.
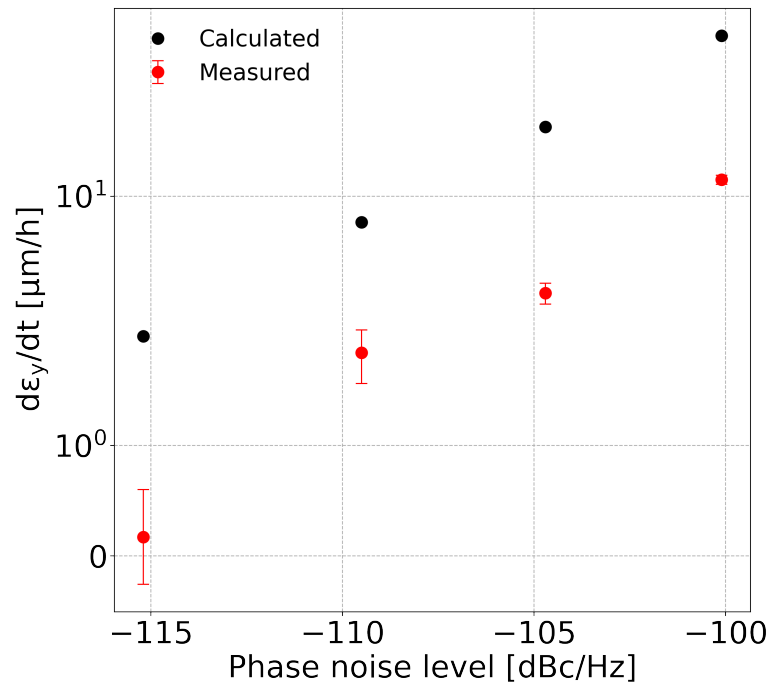
Figure 7.6: Summary plot of the emittance growth study with different noise levels injected in the RF system of CC1 during the Experiment I in 2022. The vertical measured emittance growth rate (red) and the expected emittance growth rates from the Mastoridis–Baudrenghien model (black) are shown as a function of the different levels of applied phase noise. The error bars indicate the error of the linear fit on the emittance values.

From Fig. 7.6 it becomes evident that the measured emittance growth rate increases for higher noise levels as expected. Furthermore, it is observed that the theory systematically overestimates the growth rates. The averaged discrepancy over all noise levels, but the first one, is a factor of about 6: numerical values are

given in Table 7.3. In the computation of the average, the measured emittance growth rates for the first noise level are not included. For the first noise level, the discrepancy between the measured emittance growth and the expected is a factor of 12. However, the uncertainty on the measured emittance growth is very big ($\sim$ 50% of the emittance growth rate itself).

Table 7.3: Comparison between the measured and the calculated transverse emittance growth rates for the different phase noise levels during the Experiment I in 2022. This table is complementary to Table 7.2.

Noise level	Growth rate [μm/h]	
	Measured	**Calculated**
Level 1	0.17	2.19
Level 2	1.84	7.9
Level 3	3.25	23.76
Level 4	12.11	68.9

To summarise, the Experiment I with different levels of noise injected in the CC RF system showed that:

- The measured emittance growth was found to scale with the noise power as expected from the Mastoridis–Baudrenghien model.

- The measured emittance growth rates were found to be systematically lower than the theoretically expected values. This observation is in accordance with the experimental observations of the 2018 campaign and validates the reproducibility of the experiment.

- The fact that the vertical emittance growth was found to be lower than the predictions of the Mastoridis–Baudrenghien model also shows a qualitative agreement with the PyHEADTAIL simulations including the SPS impedance model and the octupoles switched off (see Fig. 7.1 for $k_{\mathrm{LOD}} = 0$). However, the discrepancy between measured and theoretically expected values was found to be about a factor of 6 which is twice the suppression factor of 3 expected from the PyHEADTAIL simulations.

7.5 Experiment II: sensitivity of emittance growth rates to amplitude-dependent tune shift

In Experiment II, the emittance growth driven by CC RF noise was measured for one noise level over a range of octupole (LOD family) strengths. The goal was to explore the regime for $|k_{\mathrm{LOD}}| \leq 20 \,/\mathrm{m}^4$, where the dependence of the emittance growth suppression on the amplitude-dependent tune spread is expected to be strong (see Fig. 7.1). Experiment II took place in the SPS on May 16, 2022, right after Experiment I, for the same beam and machine conditions. The measurements of the CC voltage and of the background emittance growth were not repeated since the values measured in Experiment I are also valid for Experiment II.

The experiment was performed by injecting artificial noise in the CC RF system. In particular, the emittance growth was driven by phase noise of $-104.7 \,\mathrm{dBc/Hz}$ and by amplitude noise of $-116.0 \,\mathrm{dBc/Hz}$ at ~8 kHz (Level 4 in Table 7.2).

7.5.1 Transverse emittance growth measurements

In the limited time available for the experiment performing the full scan on the octupole strengths for $|k_{\mathrm{LOD}}| < 20 \,/\mathrm{m}^4$ was not feasible. Only five octupole strengths could be used, $k_{\mathrm{LOD}} = 0, \pm 5 \,/\mathrm{m}^4, 10 \,/\mathrm{m}^4$ and $15 \,/\mathrm{m}^4$. For each one of these octupole strengths the bunch evolution was recorded for about 20 minutes by acquiring repeated Wire Scanner measurements and then performing a linear fit. For the measurements of each octupole strength a freshly injected bunch was used so that the initial conditions each time are as similar as possible.

For reference, the transverse emittance growth measurements lasted for about 2.5 hours (start: ~15:25, end: ~17:05). The detailed measurements of the transverse emittance evolution for each octupole setting can be found in the Appendix. E.2.1.

Figure 7.7 shows an overview of the horizontal (blue) and vertical (red) measured emittance growth rates plotted as a function of the different octupole strengths. The error bars indicate the uncertainty of the linear fit on the emittance values

during each coast. The background emittance growth observed in the SPS without any noise injected in the CC1 ($d\epsilon_x/dt = 0.81\,\mu$m/h and $d\epsilon_y/dt = 0.84\,\mu$m/h) is subtracted from the measured values. The analytical prediction of the Mastoridis–Baudrenghien model (which does not include impedance induced effects) is also shown by the horizontal black line. The analytically predicted emittance growth rate of about 24 μm/h was computed for bunch length of $4\sigma_t = 1.83$ ns, energy of 270 GeV, the measured CC voltage amplitude $V_{0,\text{CC}} = 1.1$ MV, and the vertical beta function at the location of CC1, 76.07 m. The contribution from both phase and amplitude noise is included.
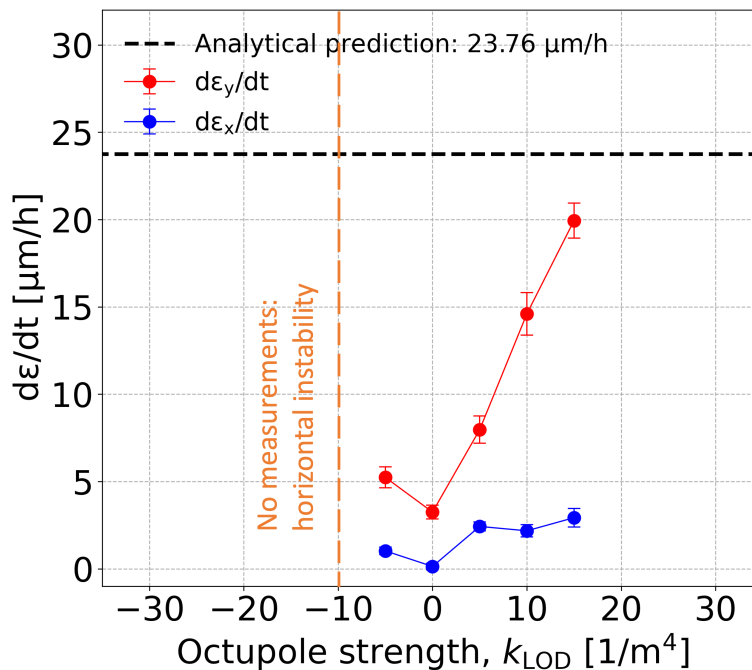
Figure 7.7: Overview of the horizontal (blue) and vertical (red) emittance growth driven by CC RF noise for different octupole settings measured during Experiment II, in 2022.

Similarly to the first part of the experiment (see Section 7.4), the emittance growth in the horizontal plane (of ~ 2-4 μm/h) seems independent of the emittance growth in the vertical plane. This indicates that the betatron coupling in the machine is minimised. Furthermore, Fig. 7.7 shows a clear dependence of the measured vertical emittance growth rate on the octupole strengths which agrees qualitatively with that expected from the simulations (see Fig. 7.1). Therefore, the results from Experiment II support the proposed explanation (in terms of the machine impedance) for the damping of the emittance growth from CC RF noise.

Horizontal instability

During Experiment II, there was an attempt to measure the emittance growth for $k_{\mathrm{LOD}} = -10$ /m^4. However, the bunch was found to be unstable in the horizontal plane which resulted in loss of the beam. The instability was observed in the turn-by-turn data acquired with the Base-Band tune (BBQ) measurement system of SPS [112], where the betatron oscillation amplitude appears to grow exponentially within a few seconds. This is illustrated in Fig. 7.8.
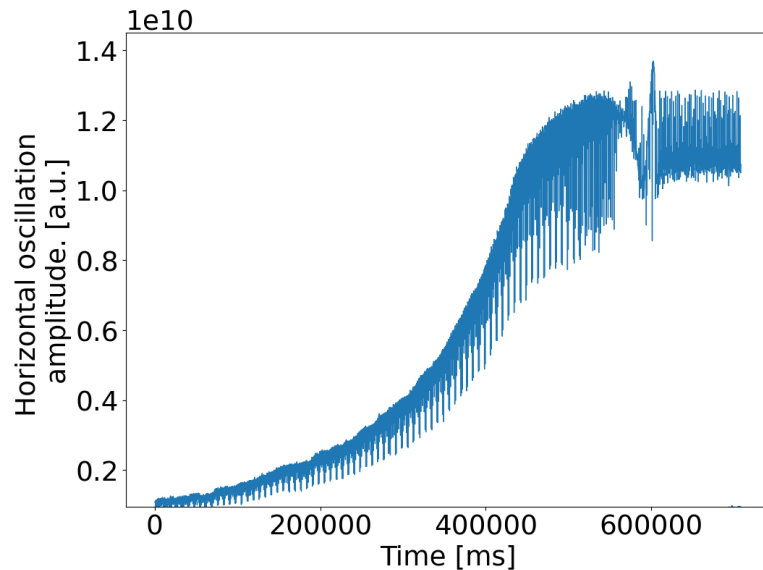
Figure 7.8: Example of the evolution of the horizontal oscillation of the bunch centroid during the CC measurements for $k_{\mathrm{LOD}} = -10$ /m^4 as captured by the BBQ instrument [112].

The setting of almost zero linear chromaticity is the most likely explanation for this instability. As mentioned in the introduction of this chapter, the linear chromaticity was set to slightly above zero instead of 0.5-1.0. This increased the probability of the chromaticity drifting to small negative values, which for machines like the SPS operating above transition can result in beam instabilities [113].

The instability was observed in the horizontal plane. A possible explanation could be that the betatron tune spread in the horizontal plane was not sufficient to stabilise the beam through the Landau damping mechanism[5] since the k_{LOD} families used for the experiment act mainly in the vertical plane.

---

[5]Landau damping is a stabilising mechanism that is applied against beam instabilities. It is demonstrated in the transverse planes in the presence of incoherent betatron tune spread. Further details can be found in [36, 43], however, a further discussion is out of the scope of this thesis.

7.5.2 Bunch length and intensity measurements

The bunch length evolution measured during Experiment II can be found in Appendix E.3.2 and the average bunch length was found to be $4\sigma_t = 1.83$ ns.

The measured intensity evolution is shown in Appendix E.4.2, and the average intensity was found to be about 2.9×10^{10} protons per bunch, very close to the requested value of 3.0×10^{10}.

7.6 Experiment III: emittance growth measurements in the presence of strong octupoles

In Experiment III, the emittance growth driven by CC RF noise was measured for one noise level for a range of octupole (LOD family) strengths. The goal was to explore mainly the regime for $|k_{\mathrm{LOD}}| \geq 20$ /m^4, where there should be no emittance growth suppression and the emittance growth is expected to agree with the predictions of the Mastoridis–Baudrenghien model (see Fig. 7.1). Experiment III took place in SPS on September 12, 2022 for very similar machine and beam conditions as Experiments I and II which can be found in Table 7.1. In Experiment III, CC1 was used.

The linear chromaticity was corrected to $Q'_{x,y} \approx 0.7$ in both transverse planes to ensure the coherent stability of the bunch even for large negative octupole strengths. It is reminded, that the occurance of horizontal coherent instabilities was a limiting factor in the emittance growth measurements of Experiment II, due to the almost zero values of linear chromaticity.

7.6.1 Calibration of the Crab Cavity phase offset and voltage measurement

The calibration of the CC1 offset and the measurement of the voltage were performed following the automated procedure described in Section 7.4.1. The results of the phase scan are summarised in Fig. 7.9 (blue dots).
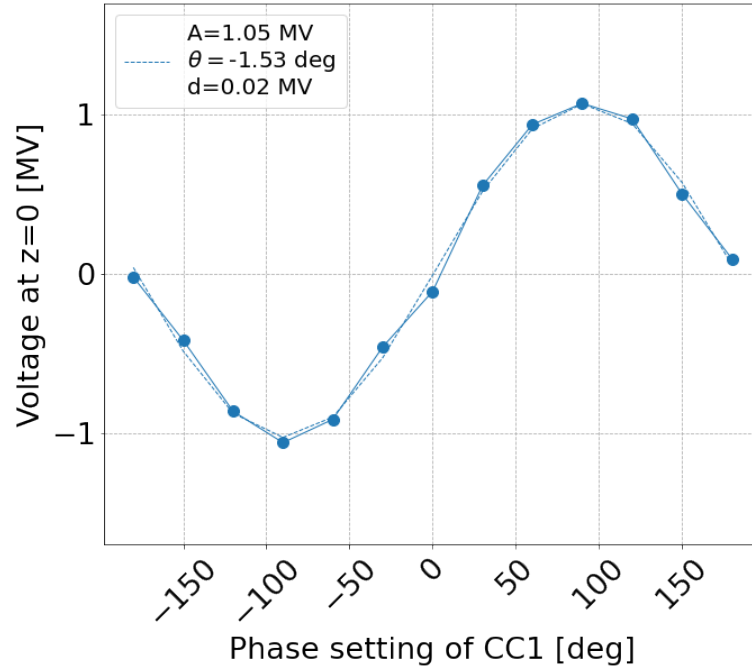
Figure 7.9: Calibration plot for the CC1 as obtained during the experiment on September 12, 2022, displaying the CC voltage at the center of the bunch $t = 0$ for different values of the set phase of CC1.

The results of the sinusoidal fit of Eq. (4.7) (blue dashed line) are given in the legend box of Fig. 7.9. From the beam-based measurements with the Head-Tail monitor the phase offset of CC1 was found to be $-1.54°$. For the rest of the experiment the CC phase was set to $+1.54°$ so that the phase of the voltage experienced by the bunch is zero.

The amplitude of the CC1 voltage was measured to be: $V_{0,\text{CC}} = A \pm d = 1.05 \pm 0.02\,\text{MV}$ very close to the targeted one of 1 MV.

7.6.2 Measurement of background emittance growth rate in coast mode

After the calibration of CC1, the coast at 270 GeV was set up for the emittance growth measurements. First, the background transverse emittance growth, with no additional noise injected in the CC RF system, was measured. This time, the background was measured with the Landau octupoles switched on, at $k_{\text{LOD}} = +30\,/\text{m}^4$. The background emittance growth was found to be: $d\epsilon_x/dt = 2.42 \pm 0.32\,\mu\text{m/h}$ and $d\epsilon_y/dt = 1.62 \pm 0.62\,\mu\text{m/h}$ in the horizontal and

vertical planes respectively. The measured background emittance growth is plotted in Fig. 7.11.
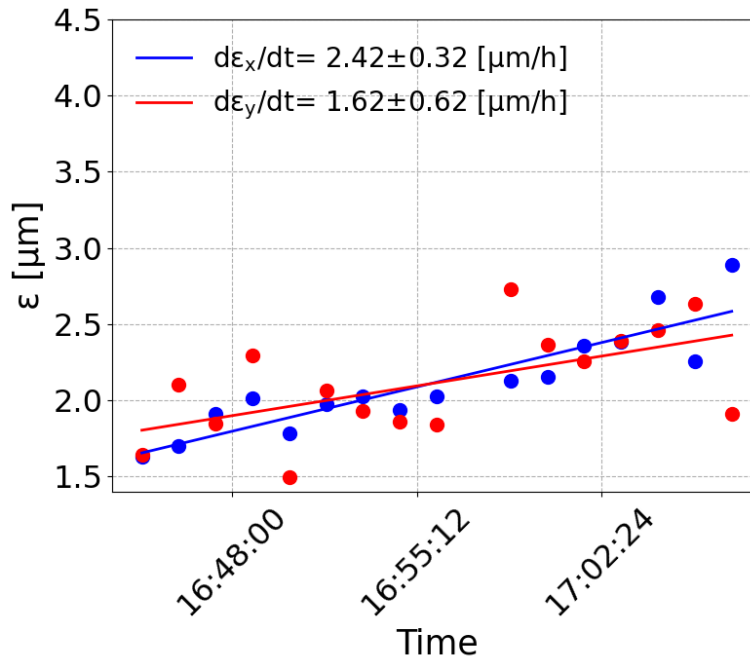
Figure 7.10: Horizontal (blue) and vertical (red) background emittance growth measured during the experiment with CC1 on September 12, 2022, with no artificial noise injected in the CC RF system and with $k_{\text{LOD}} = +30 \,/\text{m}^4$.

The background emittance growth was found to be higher than in May 16, 2022 (see Fig. 7.3). A possible explanation is that some growth in the transverse emittance could be driven by the operation of the Landau octupoles in very high currents. Some detailed investigation is required to identify the precise cause. However, due to the limited machine time, this issue should be addressed in future studies. Nevertheless, the background emittance growth is very small compared to the noise-induced emittance growth.

7.6.3   Injected CC RF noise

The experiment was performed by injecting artificial noise (similar to the one used for Experiment II) in the CC RF system. The noise was a mixture of both phase and amplitude noise with the phase noise being dominant. In particular, the amplitude and phase noise level at ~8 kHz were measured at $-123.3\,\text{dBc/Hz}$ and $-103.3\,\text{dBc/Hz}$, respectively. From the Mastoridis–Baudrenghien model (which does not include impedance-induced effects) these noise levels are expected to

result in a vertical emittance growth of $0.24\,\mu$m/h and $28.41\,\mu$m/h respectively. These rates are computed for the measured amplitude of the CC voltage, $V_{0,\mathrm{CC}} = 1.05$ MV and $4\sigma_t = 1.77$ ns (average measured bunch length over all coasts of Experiment III). It is evident that the contribution of the amplitude noise to the total emittance growth is negligible.

7.6.4   Transverse emittance growth measurements

The emittance growth induced by the above mentioned RF noise was measured for five different octupole strengths, $k_{\mathrm{LOD}} = \pm30\,/\mathrm{m}^4$, $\pm10\,/\mathrm{m}^4$ and $-20\,/\mathrm{m}^4$. The octupole strengths $|k_{\mathrm{LOD}}| \geq 20\,/\mathrm{m}^4$ are expected to restore the emittance growth rate to the values predicted by the Mastoridis–Baudrenghien model. For each octupole strength the bunch evolution was recorded for about 15-30 minutes by acquiring the emittance with repeated Wire Scanner measurements and then performing a linear fit on the emittance values. For the measurements of each setting a fresh bunch was used so that the initial conditions each time were as similar as possible.

For reference, the transverse emittance growth measurements lasted for about 2.5 hours (start: ~18:10, end: ~20:50). The detailed measurements of the transverse emittance evolution for each octupole setting can be found in the Appendix E.2.2.

Figure 7.7 shows an overview of the horizontal (blue) and vertical (red) measured emittance growth rates plotted as a function of the different octupole strengths. The error bars indicate the uncertainty of the linear fit on the emittance values during each coast. The background emittance growth observed in the SPS without any noise injected in the CC1 ($d\epsilon_x/dt = 2.42\,\mu$m/h and $d\epsilon_y/dt = 1.62\,\mu$m/h) is subtracted from the measured values. The analytical prediction of the Mastoridis–Baudrenghien model is also shown with the horizontal black line, including the contribution from both phase and amplitude noise.

The measured vertical emittance growth rates in the presence of strong octupoles appear to be relatively close to the emittance growth predicted by the Mastoridis–Baudrenghien model, which does not include the impedance effects.

7. Experimental studies from 2022: investigation of the effect of impedance on noise-induced emittance growth
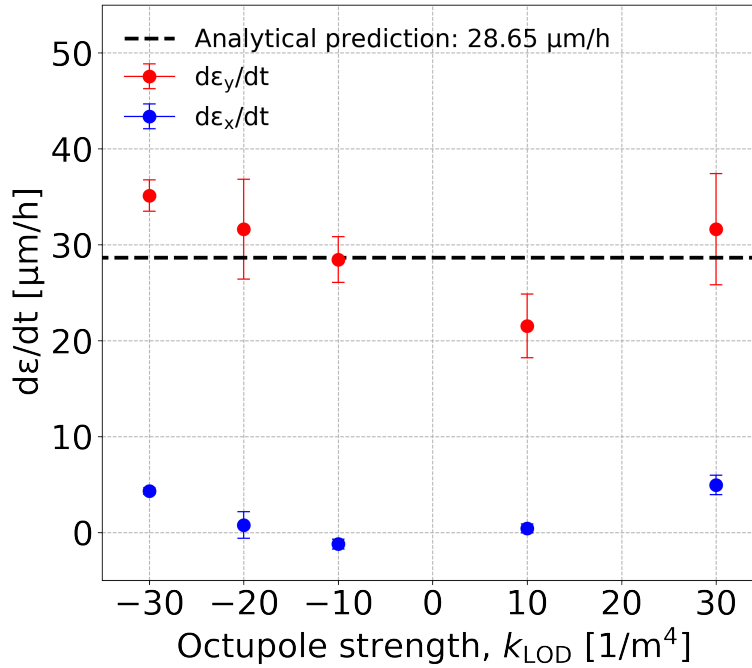
Figure 7.11: Measured horizontal (blue) and vertical (red) emittance growth driven by phase noise of -103.3 dBc/Hz injected in the RF system of CC1 for different octupole settings. The emittance growth predicted from the analytical model without taking into account the impedance-induced emittance growth suppression is $\sim 28\,\mu$m/h.

These experimental data are promising, since they agree qualitatively with the PyHEADTAIL simulations including the SPS impedance model which suggest that strong octupoles should be able to restore the emittance growth predicted by the Mastoridis–Baudrenghien model. However, there are quantitative discrepancies between the measurements and the analytical predictions: this will be discussed further in the following section which provides a direct comparison of the measured data with the PyHEADTAIL simulation results and the predictions of the Mastoridis–Baudrenghien model.

It is worth pointing out, that the vertical emittance growth for $k_{\mathrm{LOD}} = -10\,/\mathrm{m}^4$ was measured to be higher than for $k_{\mathrm{LOD}} = +10\,/\mathrm{m}^4$. This asymmetry on the emittance growth rates for positive and negative octupole strength agrees with the observables of the PyHEADTAIL simulations which include the impedance effects (see Fig. 7.1).

Finally, it is evident that the emittance growth in the horizontal plane increases for larger octupole strength (in absolute value). A possible explanation could be the operation of the Landau octupoles at very high currents. However, the precise

154

source of the growth in the horizontal plane is not yet identified and further dedicated measurements are needed to provide conclusive explanations on the source of the horizontal emittance growth.

7.6.5 Bunch length and intensity measurements

The bunch length evolution measured during Experiment II can be found in Appendix E.3.3 and the average bunch length was found to be $4\sigma_t = 1.77$ ns.

The measured intensity evolution is shown in Appendix E.4.3, and the average intensity was found to be about 2.5×10^{10} protons per bunch, which is smaller than the requested value of 3.0×10^{10}. The fact that Experiment III was performed with lower intensity does not affect the conclusions drawn from the studies. This is supported by PyHEADTAIL simulations which have shown that the dependence of the effect of the emittance growth suppression on the intensity saturates for intensities larger than $\sim 2.0 \times 10^{10}$ protons per bunch (see Fig. 6.12).

7.7 Comparison of experimental data with simulations and theory

Before discussing the direct comparison of the experimental data with simulations and theory, the complexity of the experimental campaign of 2022 should be highlighted. The experiments aimed at investigating the CC noise-induced emittance and its suppression by the beam coupling impedance as well as the dependence on the incoherent tune spread induced by the Landau octupoles. Preparatory simulation studies (see Chapter 6) indicated that these effects are sensitive to many parameters, including the bunch length, bunch intensity, beam energy, CC noise level, CC voltage, machine chromaticity, and betatron tune spread. A lot of uncertainties were introduced from the fact that the SPS operated in coast mode (which is not the usual operation mode), the machine experience with CCs of DQW type was very limited, the operation of octupoles at unusually high strengths (requiring high currents in the coils for extended periods), and the accuracy of the Wire Scanner measurements is limited for the small emittance

values of the experiment, which required to significantly increase the observation time.

Figure 7.12 provides a direct comparison of the measured vertical emittance growth with the simulation results from PyHEADTAIL including the SPS impedance model (discussed in Section 7.3). The measured vertical emittance growth is plotted from both Experiments II (magenta) and III (green), which were conducted in the SPS in May and September 2022, respectively. Both measured and simulated emittance growth rates are normalised to the corresponding analytical prediction.
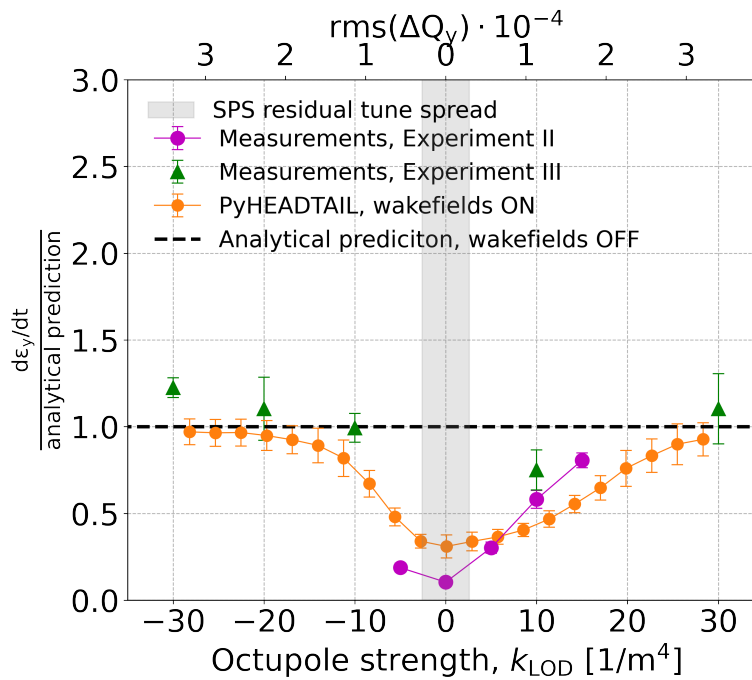
Figure 7.12: Measured (magenta-Experiment II, green-Experiment III) and simulated (orange) vertical emittance growth driven by phase noise injected in the RF system of CC1 for different octupole settings. Both measured and simulated emittance growth rates are normalised to the corresponding prediction from the Mastoridis–Baudrenghien model.

It can be seen, that overall there is a very good qualitative agreement between the measurements and the simulations. There is a clear dependence of the measured vertical emittance growth on the octupole strengths, which saturates for strong octupoles. Furthermore, for the large octupole values, the measured emittance growth is very close to the values predicted from the Mastoridis–Baudrenghien model. Thus, the experimental data support the hypothesis that the impedance can lead to damping of the CC noise induced emittance growth.

Additionally, the vertical emittance growth rate measured for k_{LOD}=10 /m^4 in Experiment II was found to be in agreement (within the error bars) with the emittance growth rate measured in Experiment III for the same octupole strength. This indicates the very good reproducibility of the measurements.

Regarding the degree of quantitative agreement, there is some uncertainty mainly for $|k_{\text{LOD}}| < 20$ /m^4 where the mechanism of the emittance growth suppression is effective. This is not surprising due to the complex nature of the effects. A possible factor that could explain the quantitative uncertainty is the contribution from space charge: this has not yet been studied but could affect the beam behaviour due to the additionally induced betatron tune spread. Space charge was not yet taken into account as its contribution is very small for the discussed experimental configurations. However, the betatron tune spread values in the regime of the studies are also very small, 10^{-6}-10^{-4}, which suggests that the space charge might play some role. This hypothesis can be investigated in simulation studies even though it is computationally challenging. Investigations of space-charge effects may be carried out in the future, but are beyond the scope of the present work. Another possible reason could be the fact that the simulated emittance growth was driven by CC RF phase only. On the contrary, the experimentally measured emittance growth in Experiment II (and the corresponding theoretical predictions) was driven by both CC RF phase and amplitude noise. As discussed in the previous sections, the phase noise was dominant however there was always some amplitude noise unavoidably injected into the CC RF system. The amplitude noise was much weaker and resulted in about 7% of the total emittance growth rate. The level of amplitude noise was not consistent throughout Experiments II and III, therefore introducing amplitude noise of a specific power in the simulations does not provide a unified approach. In order to have conclusive results, the level of quantitative agreement between simulations and measurements should be addressed in future studies.

The quantitative agreement in the regime of strong octupoles which should restore the emittance growth as predicted from Mastoridis–Baudrenghien model is in general very good. Only for $k_{\text{LOD}} = -30$ /m^4 the measured emittance growth

appears about 25% higher than the analytically predicted values. A possible explanation for this could be 10% higher CC voltage experienced by the beam than the one measured during the experiment[6]. An uncertainty of about 10% on the precise knowledge of the CC1 voltage amplitude is reasonable.

7.8 Experiment IV: emittance growth measurements driven primarily by amplitude noise

In Experiment IV, the emittance growth was driven primarily by CC RF amplitude noise. The experiment took place on September 12, 2022, right after Experiment III, hence the CC voltage amplitude and background emittance growth were not re-measured. The values measured for Experiment III will be used in the following analysis.

The experiment was performed by injecting artificial noise in the CC RF system. In particular, the amplitude and phase noise at $8\,\text{kHz}$ were measured to be $-102\,\text{dBc/Hz}$ and $-122\,\text{dBc/Hz}$, respectively. According to the Mastoridis–Baudrenghien model these noise levels are expected to result in about $32.25\,\mu\text{m/h}$ and $0.38\,\mu\text{m/h}$, respectively. These values were computed using Eq. (4.5) and (4.6), respectively, for amplitude of CC voltage, $V_{0,\text{CC}}$=1.05 MV and bunch length of $4\sigma_t$=1.75 ns.

7.8.1 Transvserse emittance growth measurements

The emittance evolution was measured for k_{LOD}=-30$\,$/m^4 and is illustrated in Fig. 7.13. The vertical emittance growth was measured to be $25.41\,\mu\text{m/h}$ (after subtracting the background emittance growth rate of $d\epsilon_y/dt = 1.62\,\mu\text{m/h}$). PyHEADTAIL simulations (see Section 6.4.2) suggest that in the emittance growth driven by CC RF amplitude noise is not suppressed and that is in agreement with the predictions of the Mastoridis–Baudrenghien model independently of the value of amplitude-dependent tune spread.

---

[6]For $V_{\text{CC},0}$ =1.15 MV an emittance growth of about $34\mu\text{m/h}$ is expected from Mastoridis–Baudrenghien model, which agrees with the measurements for $k_{\text{LOD}} = -30\,$/m^4.

Indeed, Experiment IV shows that the measured emittance growth rate is very close to the predictions of the Mastoridis–Baudrenghien model. The measurement appears about 20% lower than the predictions. However, this seems to be within the uncertainty one can expect from this experimental setup. Experiment IV is up to now the only available experimental study of the emittance growth driven by primarily amplitude noise and proton beams.
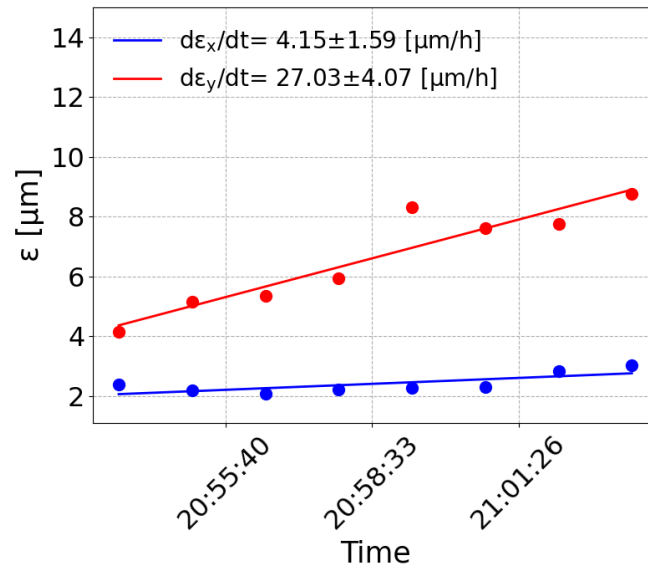
Figure 7.13: Horizontal (blue) and vertical (red) emittance growth measured during the experiment with CC1 on September 12, 2022

7.8.2 Bunch length and intensity measurements

The bunch length evolution measured during Experiment II can be found in Appendix E.3.4 and the average bunch length was found to be $4\sigma_t = 1.77$ ns.

The measured intensity evolution is shown in Appendix E.4.4, and the average intensity was found to be about 2.4×10^{10} protons per bunch, which is smaller than the requested value of 3.0×10^{10} protons per bunch. The intensity dependent effect of the emittance growth suppression is not valid in the presence of amplitude noise, hence the intensity value does not affect the conclusions drawn from the studies.

7.9   Experiment V: emittance growth driven by dipole noise

In Experiment V, the emittance growth driven by the transverse damper (acting as a pure dipolar noise source) was measured over a range of octupole (LOD family) strengths. The goal was to investigate the dependence of the emittance growth damping mechanism on the betatron tune spread in a setup without the uncertainties introduced by the CC operation in the SPS.

The damper provided noise excitation in the vertical plane, which remained constant over the different coasts of the experiment. The strength of the damper kick was not calibrated and therefore the analytically expected emittance growth could not be computed. However, the experimental data can be used to make qualitative comments about the suppression mechanism from the beam transverse impedance.

The emittance growth measurements were conducted in coast mode at 270 GeV for beam and machine parameters very similar to the CC experiments, which are listed in Table 7.1. Recalling the horizontal instability observed in Experiment II, the linear chromaticity was corrected to $Q'_{x,y} \approx 1$ in both transverse planes to ensure the transverse coherent stability of the beam.

For reference, the experiment lasted from about 23:50 on the May 16, 2022, until about 04:00 on the May 17, 2022.

7.9.1   Transverse emittance growth measurements

In the limited available machine time for the experiment seven octupole strengths could be tested: $+25 \text{ /m}^4, +15 \text{ /m}^4, +10 \text{ /m}^4, +5 \text{ /m}^4, 0 \text{ /m}^4, -15 \text{ /m}^4, -7.5 \text{ /m}^4$. For each octupole setting, the bunch evolution was recorded for about 10 minutes by acquiring repeated measurements with the Wire Scanners. The short duration of the measurements was a result of the strong noise excitation which resulted in a clear linear growth of the vertical emittance not dominated by the fluctuations of

the Wire Scanner acquisitions. This can be seen in the individual measurements of the transverse emittance evolution for each octupole setting, which are presented in the Appendix E.2.3. For the measurements of each setting a fresh bunch was injected.

The experimental results are summarised in Fig. 7.14. The measured horizontal (blue) and vertical (red) emittance growth are plotted as a function of the different octupole strengths. The error bars indicate the error of the linear fit on the emittance values during each coast. The background emittance growth without any noise excitation from the damper was not measured and thus is not subtracted from the displayed values. However, the impact of the background emittance growth (usually measured to be between 0.5-1μm/h in both transverse planes) is insignificant for the emittance growth rates of this study ($> 10\ \mu$m/m).
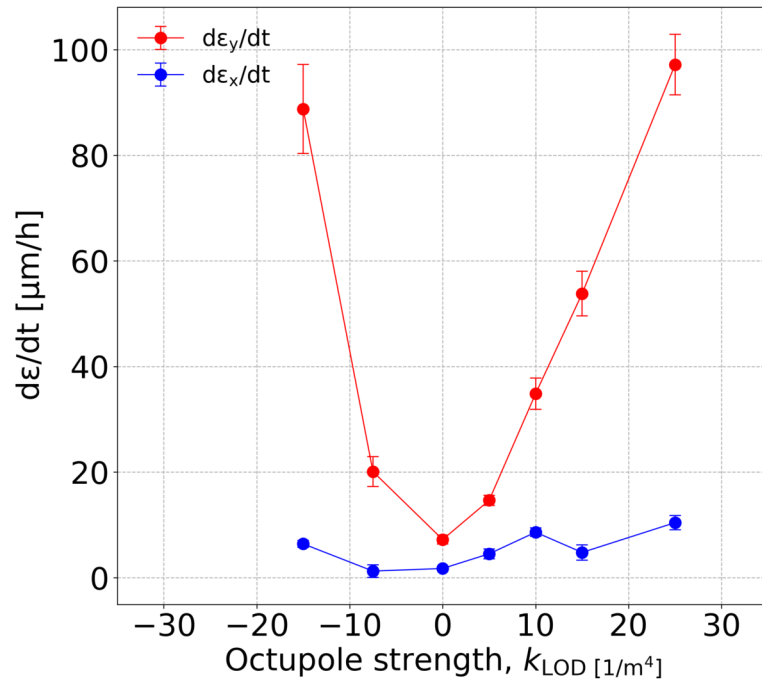
Figure 7.14: Measured horizontal (blue) and vertical (red) emittance growth driven by dipole noise introduced with the SPS transverse damper in the vertical plane for different octupole settings.

The emittance growth observed in the horizontal plane appears to be independent of the octupole strengths, agreeing with the observations during the experiments with CC noise.

In the vertical plane, there is a clear dependence of the measured emittance growth

on the strength of the octupoles as expected from PyHEADTAIL simulations including the SPS impedance model (see Fig. 6.9). The results of the experiment thus further support the hypothesis that the suppression of emittance growth observed from CC noise is a consequence of the machine impedance. However, it is not clear if the used octupole strength was sufficient to be beyond the suppression region. More data points with higher octupole strength would be needed to confirm whether this was the case, and further experiments to investigate the limits in more detail are planned in dedicated future experiments.

It is worth commenting, that the theoretical model developed by X. Buffat [105] describing the suppression of the noise-induced emittance growth from the beam transverse impedance was used to successfully fit these experimental data. Further details are discussed in [106].

7.10 Conclusions and outlook

In this chapter we have presented the results of the experimental campaign that took place in the SPS machine in 2022, aiming to validate experimentally the emittance growth suppression mechanism by the beam transverse impedance as predicted from PyHEADTAIL simulations. Five different experiments were conducted in total, which studied the emittance growth driven primarily by phase noise, amplitude noise, and a pure dipolar noise source.

Despite the limited available machine time and the numerous uncertainties resulting from the operation of the SPS outside of the usual mode, the experiment yielded useful data. The measured data from all the experiments were found to be in agreement with the suggested suppression mechanism of emittance growth.

The highlight was that the Experiments II and III, which were conducted in the presence of CC RF phase noise, reproduced qualitatively the dependence of the emittance growth suppression factor on the amplitude-dependent tune shift as predicted from PyHEADTAIL simulations. These studies provide a clear experimental validation of the emittance growth suppression mechanism from the transverse impedance. They also confirm that the suppression mechanism

explains the results of the 2018 experimental campaign. Furthermore, it was shown that in the presence of strong octupoles the measured emittance growth rates are very close to the predictions of the Mastoridis–Baudrenghien model, gaining confidence in its validity.

8 | Conclusions

The work presented in this thesis addressed the emittance growth driven by noise in the CC RF system, which is anticipated to limit the performance of the HL-LHC. The validity of the Mastoridis–Baudrenghien model, which predicts the CC RF noise-induced emittance growth was benchmarked against experimental data and its limitations were identified. Based on tracking simulations and experimental measurements it was shown that the beam transverse impedance can have a significant impact on the noise-induced emittance growth.

The studies presented in this thesis were conducted at the CERN SPS, where two prototype CCs were installed in 2018, to allow for tests with proton beams before their installation in the LHC.

The first beam dynamic studies with CCs and proton beams took place in 2018 in the SPS and are presented in this thesis. By analysing the emittance growth measurements it was found that CC RF noise-induced emittance growth was a factor four on average lower than predicted from the Mastoridis–Baudrenghien model. Follow-up studies excluded the possibility that the observed discrepancy was a result of some error in the analysis of the experimental data.

Tracking simulations with PyHEADTAIL revealed that the transverse beam impedance (not included in the Mastoridis–Baudrenghien model) affects the transverse emittance growth induced by CC RF noise and may therefore explain the experimental observations. In particular, PyHEADTAIL simulations including the accurate SPS impedance model demonstrated that the noise-induced emittance growth is suppressed by about a factor four for the 2018 experimental conditions. Detailed simulation studies were conducted to characterise this newly observed effect. It was identified that the emittance growth suppression is related purely to the rigid (or dipole) bunch motion (head-tail mode 0) of the beam, which is induced by the CC RF phase noise. It was also demonstrated that the

decoherence and thus the emittance growth is suppressed once the detuning induced by the impedance moves the coherent tune outside of the incoherent tune spectrum. Finally, it was shown that this emittance growth suppression mechanism depends on the amplitude-dependent betatron tune spread and that for large enough tune spread values the emittance growth predicted by the Mastoridis–Baudrenghien model can be restored.

An additional campaign took place in the SPS in 2022 and confirmed experimentally for the first time the suggested emittance growth suppression mechanism from impedance induced effects. In particular, the emittance growth driven primarily by CC RF phase noise was measured as a function of different values of amplitude-dependent betatron tune spread. The measurements were found to be in very good qualitative agreement with the expectations from PyHEADTAIL simulations including the SPS transverse impedance model for very similar machine and beam conditions. Some uncertainty on the quantitative agreement was observed, however, it is within the uncertainties expected from the experimental setup and the instruments used for the measurements. The emittance growth measured in the presence of large betatron tune spread was found to be very close to the predictions of the Mastoridis–Baudrenghien model gaining confidence in its validity.

8.1 Implications for HL-LHC

Since the main motivation of these studies was the use of the CCs in the HL-LHC, the implications of these results on the HL-LHC project are discussed. For reference, Table 8.1 summarises some of the main machine and beam design parameters for the SPS and HL-LHC machines.

Regarding the suppression mechanism from the beam coupling impedance
The mechanism of the emittance growth suppression from impedance (or beam-beam effects) due to the separation of the coherent modes from the incoherent spectrum is not expected to appear for the HL-LHC operational configuration for the following two reasons:

8. Conclusions

Table 8.1: Overview of the design parameters for the SPS and HL-LHC [9]. The listed values for the SPS correspond to its operation as a storage ring for studying the long-term emittance evolution. The listed values for the HL-LHC case are for beams at collision energy.

Parameter	SPS	HL-LHC
Circumference, C_0	6.9 km	26.7 km
Beam energy, E_b	270 GeV	7 TeV (per beam)
Rms bunch length, σ_z	12-16 cm	7.55 cm
Frequency of main RF system, f_{RF}	400 MHz	200 MHz
Number of bunches	1	2808 (per ring)
Intensity, N_b	3×10^{10} protons/bunch	2.2×10^{11} protons/bunch
Crab Cavity scheme	Global	Local
Beam-beam interaction	No	Yes
Interaction points	No	Yes
Crossing angle	No	Yes

- Past studies for the LHC and HL-LHC operational conditions, which feature complex bunch train structures, multiple interaction points with asymmetric phase advance, and non-zero chromaticity have shown that the coherent modes (dominated by the beam-beam interactions) are expected to lie inside the incoherent spectrum [114, 115].

- In the HL-LHC operational scenarios, the transverse feedback (ADT [116]) is switched on. Briefly, the ADT measures the bunch-by-bunch beam position every turn and tries to maintain zero centroid oscillations. For the foreseen gain values of this device, the damping time is much faster than the damping time from impedance in the potential (though unlikely) case where the coherent modes would emerge from the incoherent spectrum. This is supported by simulation results, which include noise (not CC RF noise), beam-beam interactions, wakefields, and the transverse feedback [115].

For these reasons, the simulation studies for the HL-LHC case were not strongly motivated in the context of this thesis.

Regarding the validity of the Mastoridis–Baudrenghien model

The experimental studies in the SPS during 2022 showed that for configurations where the coherent mode lies inside the incoherent betatron tune spread (like in the HL-LHC scenario) the transverse emittance growth was measured very close to

the predictions of Mastoridis–Baudrenghien model. Therefore, the work presented in this thesis gained confidence in the predictions of the model for the HL-LHC, and it can be used for defining limits on the acceptable noise levels for the HL-LHC CCs.

Plans for mitigating the emittance growth driven by Crab Cavity RF noise in the HL-LHC

In this paragraph, the current plans for mitigating the emittance growth driven by CC RF noise in the HL-LHC are discussed for the completeness of the thesis. Recall that the emittance growth suppression mechanism from the beam transverse impedance will not appear in the HL-LHC configuration.

The HL-LHC estimates [117] (based on the Mastoridis–Baudrenghien model) show that the expected emittance growth from noise present in the CC RF system is about $15.4\%/h$. In the presence of the transverse damper (assuming damping time of 10 turns) this emittance growth is reduced to about 5.3%/h. Note that these rates correspond to the emittance growth from both amplitude and phase noise.

However, the target value for emittance growth induced by CC RF noise for the HL-LHC is $2\%/h$ [24, 25, 26]. It becomes clear that an additional reduction of $3\%/h$ is required to meet the target value of the HL-LHC. Reducing the noise floor of the CC is technologically very challenging as it lies well below the noise floor of the main RF cavities [117].

Therefore, the further reduction from $\sim 5\%/h$ to $2\%/h$ could come from a proposed feedback system that uses transverse beam measurements. This system has already been proposed in 2019 but its necessity is underlined, since the identified emittance growth suppression mechanism from the beam transverse impedance cannot be used in the HL-LHC configuration. To provide some information, this CC feedback system would use an already existing pickup (the same as the transverse damper, ADT) and it could act on both amplitude and phase noise. Furthermore, the transverse damper and the feedback could be used together, to provide a more effective reduction of the emittance growth, but one should keep in mind that the result is not additive. This system is described in

detail in [118] and it is still under construction. Another alternative solution would be to operate HL-LHC with slightly flat optics (with different horizontal and vertical β^* values[1]) [119]. This configuration allows smaller beta functions in the crabbing plane at the locations of the CCs and thus the impact from the noise present in their RF system is smaller. To summarise, there is a lot of challenging and critical work currently in progress to reach the required $2\%/h$ emittance growth rate from CC RF noise.

---

[1]The β^* is often used to refer to the beta function at an interaction point.

A ┃ Definitions and methods of statistical analysis

A.1 Basic terminology

This appendix, introduces the basic terminology of statistical analysis and gives the definitions that are used in this thesis. The definitions follow the book by R. J. Barlow [120] where one can find a more detailed insight. Note that the use of the parameters x and y in this Appendix is not related to the co-ordinates introduced to describe the motion of the particles in the transverse plane.

A.1.1 Averages

Arithmetic mean

For a data set of N data $\{x_1, x_2, x_3, ..., x_N\}$ the arithmetic mean or just mean of the value of x is:

$$\langle x \rangle = \frac{1}{N} \sum_{i=1}^{N} x_i. \tag{A.1}$$

Below, two properties of the arithmetic mean are shown since they are used in this thesis.

- The mean of the sum of two variables x and y is equal to the sum of their means, ie:

$$\langle x + y \rangle = \langle x \rangle + \langle y \rangle \tag{A.2}$$

- If x and y are independent the mean of their product equals:

$$\langle x \cdot y \rangle = \langle x \rangle \cdot \langle y \rangle \tag{A.3}$$

Another notation for the arithmetic mean that is often found in bibliography is, $\bar{x}$.

Root mean square

In the classical definition in mathematics, the root mean square (rms) is an alternative to the arithmetic mean and is defined as:

$$x^{\mathrm{rms}} = \sqrt{\frac{x_1^2 + x_2^2 + x_3^2 + \dots + x_N^2}{N}} = \sqrt{\langle x^2 \rangle}. \tag{A.4}$$

A.1.2   Measuring the spread

Variance

For a data set of N data $\{x_1, x_2, x_3, \dots, x_N\}$ the variance of x expresses how much it can vary from the mean value, $\langle x \rangle$. The variance, $\mathrm{Var}(x)$, is defined as:

$$\mathrm{Var}(x) = \frac{1}{N} \sum_{i=1}^{N} (x_i - \langle x \rangle)^2. \tag{A.5}$$

Alternatively, the variance can be expressed in a simpler way as follows (see p.24-25 in [120]):

$$\mathrm{Var}(x) = \langle x^2 \rangle - \langle x \rangle^2. \tag{A.6}$$

Standard deviation

The square root of the variance is the standard deviation (std):

$$\sigma_x = \sqrt{\mathrm{Var}(x)} = \sqrt{\frac{1}{N} \sum_{i=1}^{N} (x_i - \langle x \rangle)^2}, \tag{A.7}$$

or as follows from Eq. (A.6):

$$\sigma_x = \sqrt{\langle x^2 \rangle - \langle x \rangle^2}. \tag{A.8}$$

The spread in a data set is usually expressed with the standard deviation instead of the variance, as the standard deviation has the same units as the variable x.

A.1.3   Data sets with more than one variables - Covariance

In the case that each element of the data set consists of a pair of variables, $\{(x_1, y_1),$ $(x_2, y_2), (x_2, y_2), ...(x_N, y_N)\}$ the covariance expresses the extend to which x and y tend to vary together. The covariance between x and y is defined as:

$$\text{Cov}(x, y) = \frac{1}{N} \sum_{i=1}^{N} (x_i - \langle x \rangle)(y_i - \langle y \rangle). \tag{A.9}$$

It can be seen that the covariance of variable x with itslef equals the variance. In particular, it is written:

$$\text{Cov}(x, x) = \sqrt{\frac{1}{N} \sum_{i=1}^{N} (x_i - \langle x \rangle)^2} = \text{Var}(x) = \sigma_x^2. \tag{A.10}$$

Covariance matrix

The covariance as defined above is only calculated between two variables. To express the covariance values of each pair of variables, the covariance matrix or Sigma matrix is introduced as follows and is:

$$\Sigma = \begin{pmatrix} \text{Cov}(x, x) & \text{Cov}(x, y) \\ \text{Cov}(y, x) & \text{Cov}(y, y) \end{pmatrix} = \begin{pmatrix} \sigma_x^2 & \text{Cov}(x, y) \\ \text{Cov}(y, x) & \sigma_y^2 \end{pmatrix}, \tag{A.11}$$

since the covariance between the same variables equals to the variance (Eq. (A.10)).

If the data set is a distribution the covariance matrix is a parameter of the distribution.

A.2   Least squares fitting

In sciences, many quantities can not be measured directly but can be inferred from measured data by fitting a model function to them. Common model functions are the Gaussian, polynomial, or sinusoidal. The fitting procedure followed in this thesis is called "least squares" and is described below, based on [121].

A. Definitions and methods of statistical analysis

Suppose that we have N data points (x_i, y_i) and that $y = f(x, \alpha, \beta)$ is the model function that describes the relationship between the points. The objective of the fit is to determine the optimal parameters α, β such as the model function describes best the data points. This is done by minimising the χ^2 statistics with respect to α and β:

$$\chi^2 = \sum_{i=1}^{N} [y_i - f(x_i, \alpha, \beta)]^2, \tag{A.12}$$

where y_i is the observed value and $f(x_i, \alpha, \beta)$ the expected value from the model. In other words, χ^2 is a measure of deviation between the measurement and the expected result, and thus its minimisation results in the best fit i.e. to the optimal parameters α, β.

Weighted least squares fitting

Suppose that we have N data points $(x_i, y_i \pm \Delta y_i)$, where Δy_i is the uncertaintyof y_i y, and that $y = f(x, \alpha, \beta)$ is the model function that describes the relationship between the points. To define the optimal parameters α, β taking into account the imapct of the uncertainty Δy_i, Eq. (A.12) is written as:

$$\chi^2 = \sum_{i=1}^{N} \frac{[y_i - f(x_i, \alpha, \beta)]^2}{\Delta y_i^2} \tag{A.13}$$

Uncertainty of the fit

The standard deviation of the fit results, $\sigma_\alpha, \sigma_\beta$, is estimated by the square root of the diagonal of their covariant matrix:

$$\begin{pmatrix} \sigma_\alpha^2 & \mathrm{Cov}(\alpha, \beta) \\ \mathrm{Cov}(\beta, \alpha) & \sigma_\beta^2 \end{pmatrix} \tag{A.14}$$

In this thesis, the uncertainties of the fit results, $\Delta\alpha, \Delta\beta$, are defined as the standard deviation, σ_α and σ_β, of the corresponding optimal parameters.

The values of the optimal parameters and their covariance matrix are computed in this thesis using the scipy.curve_fit [122] function of the Python programming language.

A.3   Propagation of uncertainty

Suppose that y is related to N independent variables $\{x_1, x_2, ..., x_N\}$ with the following function:

$$y = f(x_1, x_2, ..x_N). \tag{A.15}$$

If $\{\Delta x_1, \Delta x_2, ..., \Delta x_N\}$ the uncertainties of $\{x_1, x_2, ..., x_N\}$ respectively, the uncertainty of y, is given by [120]:

$$\Delta y = \sqrt{\left(\frac{\partial f}{\partial x_1}\Delta x_1\right)^2 + \left(\frac{\partial f}{\partial x_2}\Delta x_2\right)^2 + \cdots + \left(\frac{\partial f}{\partial x_N}\Delta x_N\right)^2} \tag{A.16}$$

B | Fundamentals of signal analysis and measurement

This appendix discusses the basic terminology of signal processing and gives the definitions which are used in this thesis. The focus is on Fourier transform and the power spectral density. First the most general mathematical definitions which concern signals continuous in time and with infinite time duration are discussed. Secondly, the definitions are given for signals sampled at a finite number of points, which are considered for the measurements and for the computational analysis. Furthermore, the quantities that are used most often for noise power spectrum measurements and their relationship to the mathematical definitions of the power spectral density are discussed. Finally, the way of applying a measured noise spectrum in numerical simulations is described.

B.1 Continuous-time analysis

Fourier transform

A physical process (or signal or time series) can be described in the time domain by a continuous function of time, e.g. $y(t)$, or else in the frequency domain, where the process is specified by giving its amplitude $\hat{y}$ as a function of frequency, e.g. $\hat{y}(f)$ with $f \in (-\infty, +\infty)$. In other words, $y(t)$ and $\hat{y}(f)$ are essentially different representations of the same function. In general, $\hat{y}(f)$ can be a complex quantity, with the complex argument giving the phase of the component at the frequency f.

One can switch between these two representations using the Fourier transform method. In this thesis the Fourier transform of a time series $y(t)$, which will be denoted in this document by $\hat{y}$, is defined as [123]:

$$\hat{y}(f) = \int_{-\infty}^{\infty} y(t)e^{-2\pi itf}dt, \tag{B.1}$$

where f stands for any real number. If the time is measured in seconds the frequency, f, is measured in Hertz.

The inverse Fourier transform, which is used to re-create the signal from its spectrum, is defined as [123]:

$$y(t) = \int_{-\infty}^{\infty} \hat{y}(f)e^{2\pi itf}df. \tag{B.2}$$

Power spectral density and total power

The power spectral density (PSD), $S_{yy}(f)$, of a signal (or a time series), $y(t)$ it describes the distribution of the power in a signal between its frequency components, and is defined as the Fourier transform of the autocorrelation function, $R_{yy}(t)$ [124]:

$$S_{yy}(f) = \hat{R}_{yy}(f) = \int_{-\infty}^{\infty} R_{yy}(\tau)e^{-2\pi i\tau f}d\tau. \tag{B.3}$$

The continuous autocorrelation $R_{yy}(\tau)$ is defined as the continuous cross-correlation integral of $y(t)$ with itself, at lag τ [125]:

$$R_{yy}(\tau) = (y * y)(\tau) = \int_{-\infty}^{\infty} \bar{y}(t)y(t+\tau)dt, \tag{B.4}$$

where $*$ denotes the convolution operation and $\bar{y}(t)$ represents the complex conjugate of $y(t)$.

According to the cross-correlation theorem [125]:

$$\hat{R}_{yy}(f) = \bar{\hat{y}}(f)\hat{y}(f) = |\hat{y}(f)|^2, \tag{B.5}$$

where $\hat{y}(f)$ is the Fourier transform of the signal as defined in Eq. (B.1).

From Eq. (B.3) and Eq. (B.5) the power spectral density of a signal $y(t)$ can be simply written as the square of its Fourier transform:

$$S_{yy}(f) = |\hat{y}(f)|^2, \tag{B.6}$$

with $f \in (-\infty, +\infty)$.

B.2 Discrete-time analysis

Discrete-time signals

Figure B.1 shows a part of a continuous signal $y(t)$. For signal measurements and computational analysis, signals (or time series) sampled at a finite number of points are considered. Such signals are called discrete-time signals and typically they are sampled at equal points in time. For example, in Figure B.1, it is assumed that the continuous signal, $y(t)$, is sampled at intervals Δt creating a set of N points. The length in time between the first and final sample is $T_{\text{total}} = N\Delta t$.
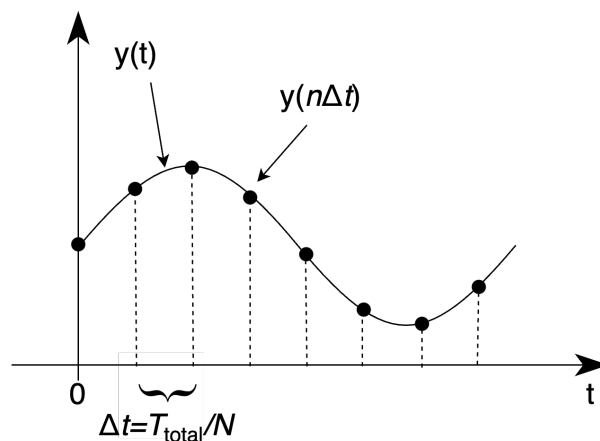
Figure B.1: Sampling of the continuous signal $y(t)$ at a finite number of points N. The sampled signal is the discrete-time signal $y(n\Delta t)$ with Δt the sampling interval and n an integer such that $n \in [0, N-1]$.

Discrete Fourier transform

Let us consider a discrete-time signal, y_n, which is sampled at N consecutive samples, $y_n = y(n\Delta t)$, with $n \in [0, N-1]$ such that Δt is the sampling interval. The following discussion considers that N is an odd integer. The Fourier transform for a

discrete-time signal, also known as discrete Fourier transform, is given by [123]:

$$\hat{y}_k = \sum_{n=0}^{N-1} y(n\Delta t)e^{-2\pi i \frac{kn}{N}}, \tag{B.7}$$

where the index k is an integer in the range $-\frac{N-1}{2}$ to $\frac{N-1}{2}$.

The components of the discrete Fourier transform are calculated at frequencies f_k that are integer multiples of $\Delta f = 1/T_{\text{total}} = f_s/N$, with $f_s = 1/\Delta t$ the sampling frequency. In that case, $f_k \in \left[-f_s/2, +f_s/2\right]$. An example of a discrete Fourier transform is shown in Fig. B.2.

(a) $y = \sin(2\pi f t)$, $f = 50\,\text{Hz}$ (b) Discrete Fourier transform
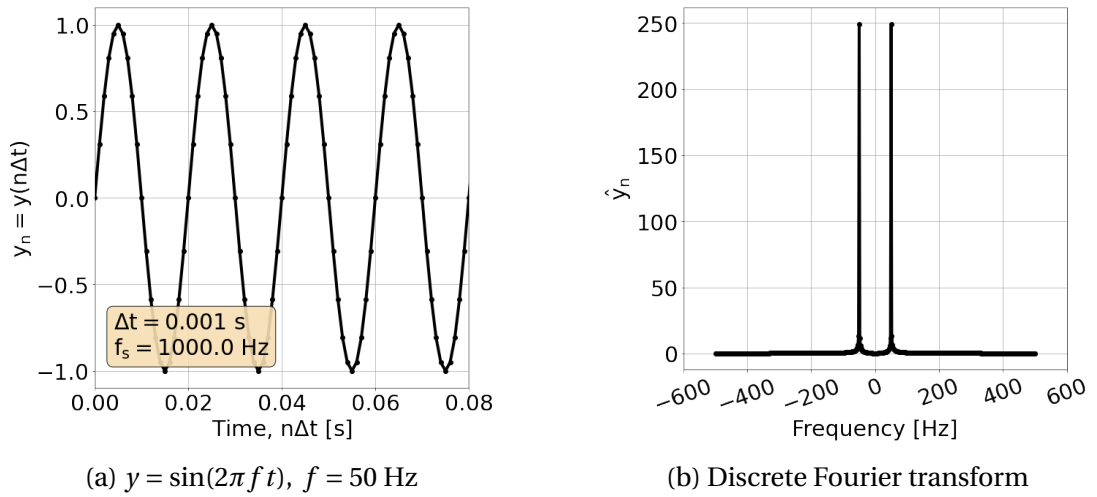
Figure B.2: Example of a signal sampled at discrete time intervals, and the corresponding discrete Fourier transform.

When using this convention the Fourier transform components outside of the above-mentioned frequency range are considered to be zero. Note that the zero frequency, $f_k = 0$, corresponds to $n = 0$. The positive frequencies, $0 < f_k < +f_s/2$ correspond to values $1 < n < (N-1)/2$ and the negative frequencies, $-f_s/2 < f_k < 0$ correspond to values $-f_s/2 < 0$. The value n $= (N-1)/2$ corresponds to both $f_k = -f_s/2$ and $+f_s/2$.

The inverse discrete Fourier transform is defined as:

$$y_n = y(n\Delta t) = \frac{1}{N} \sum_{k=-\frac{N-1}{2}}^{\frac{N-1}{2}} \hat{y}_k e^{2\pi i \frac{kn}{N}}, \tag{B.8}$$

where $n \in [0, N-1]$ and where n and k are both integers.

177

B. Fundamentals of signal analysis and measurement

The definitions given in Eq. (B.7) and Eq. (B.8) are consistent with those used in numpy, in the numpy.fft function [126] package of the Python programming language.

Power spectral density

Following Eq. (B.6) the power spectral density of a discrete-time signal should be estimated as follows:

$$S_{yy}(f_k) = C_{\mathrm{PSD}} \, | \, \hat{y}_k(f_k) \, |^2, \tag{B.9}$$

where $f_k \in \left[-f_s/2, +f_s/2 \right]$. C_{PSD} is a normalisation constant which is introduced in order to obtain the correct amplitudes at each frequency and thus the correct noise power. There are several different conventions for the choice of this normalization. In this thesis, the following normalization is considered:

$$S_{yy}(f_k) = \frac{1}{N^2 \Delta f} \, | \, \hat{y}_k(f_k) \, |^2, \tag{B.10}$$

where $\Delta f = 1/T_{\mathrm{total}}$ is the frequency resolution and N the number of samples.
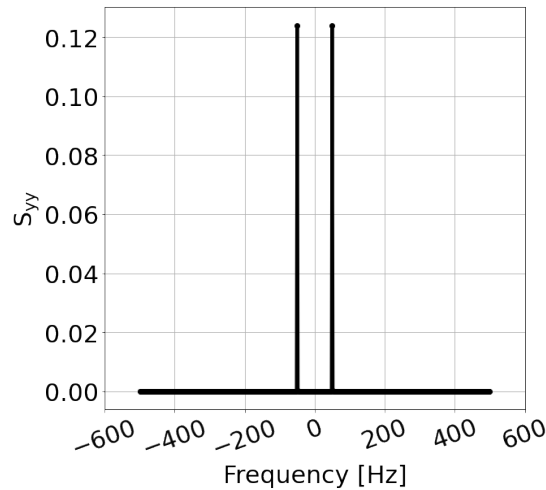
Figure B.3: Power spectrum of $y = \sin(2\pi f t)$, $f = 50\,\mathrm{Hz}$.

Figure B.3 shows an example power spectrum of the time-domain signal shown in Fig. B.2. It can be seen that the spectrum that results from the analysis above is two-sided, which means that it has both positive and negative frequencies. It is also symmetric around the DC component ($f = 0\,\mathrm{Hz}$), which is a property of a real signal.

The power spectral density is expressed in terms of the square of the amplitude of the signal per unit frequency. For example, for a signal defined in units of voltage, V, (e.g. from an oscillator) the units are V^2/Hz.

Normalisation factor for the power spectral density of a discrete-time signal

This paragraph discusses the choice of the normalisation factor $C_{PSD} = 1/(N^2\Delta f)$ for the power spectral density of a discrete-time signal defined in Eq. (B.9).

The discussion concerns noise signals with mean zero, which is the case for the noise spectra considered in the thesis. In particular the mean of the white noise spectra used in the simulation studies is zero by definition. The mean of the measured noise signal corresponds to the DC componenet which for the spectra discussed in this thesis was also considered at 0 Hz.

Consider the example of a discrete-time series $y_n = y(n\Delta t)$ where n is an integer such that $n \in [0, N-1]$. The y_n represents a sequence of successive points equally spaced in time, with zero mean, $\mu = 0$. The variance of this collection of N equally spaced values is given by:

$$\sigma^2 = \frac{1}{N} \sum_{n=0}^{N-1} |y_n|^2. \tag{B.11}$$

According to Parseval's theorem [125], the variance can be written as:

$$\sigma^2 = \frac{1}{N^2} \sum_{k=-\frac{N-1}{2}}^{\frac{N-1}{2}} |\hat{y}_k|^2, \tag{B.12}$$

where $\hat{y}_k$ is the discrete Fourier transform of y_n.

Using Eq. (B.3), the autocorrelation function $R_{yy}(\tau)$ for a continuous-time signal can be found from the inverse Fourier transform of $S_{yy}(f)$:

$$R_{yy}(\tau) = \int_{-\infty}^{\infty} \bar{y}(t)y(t+\tau)\,dt = \int_{-\infty}^{\infty} S_{yy}(f)e^{2\pi i t f}\,df. \tag{B.13}$$

For zero lag, this becomes:

$$R_{yy}(0) = \int_{-\infty}^{\infty} S_{yy}(f)\, df = \sigma^2. \tag{B.14}$$

This expresses the fact that the autocorrelation of a zero-mean stochastic process (such as y_n) is equal to the variance. It should be noted here that this integration over the spectral components yields the total power of the process.

For a discrete-time signal, we require that the power spectral density $S_{yy}(f_k)$ corresponds to the power spectral density for the continuous-time signal. In that case, Eq. (B.14) becomes:

$$\sigma^2 = \sum_{k=-\frac{N-1}{2}}^{\frac{N-1}{2}} S_{yy}(f_k)\Delta f. \tag{B.15}$$

From Eq. (B.12) and Eq. (B.15) this leads to:

$$\frac{1}{N^2}\sum_{k=-\frac{N-1}{2}}^{\frac{N-1}{2}} \left|\hat{y}_k\right|^2 = \sum_{k=-\frac{N-1}{2}}^{\frac{N-1}{2}} S_{yy}(f_k)\Delta f, \tag{B.16}$$

and hence:

$$\sum_{k=-\frac{N-1}{2}}^{\frac{N-1}{2}} \frac{\left|\hat{y}_k\right|^2}{N^2\Delta f} = \sum_{k=-\frac{N-1}{2}}^{\frac{N-1}{2}} S_{yy}(f_k). \tag{B.17}$$

Therefore, to satisfy the requirement that the power spectral density for the discrete-time signal corresponds to that for the continuous-time signal, we define the power spectral density for a discrete-time signal:

$$S_{yy}(f_k) = \frac{\left|\hat{y}_k\right|^2}{N^2\Delta f}. \tag{B.18}$$

Hence, the normalisation factor in Eq. (B.9) is chosen to be:

$$C_{\text{PSD}} = \frac{1}{N^2\Delta f}. \tag{B.19}$$

Computation of power spectral density for white noise signals

At this point, it is worth elaborating on the computation of the power spectral density, in the context of the noise effects in a synchrotron that are studied in this

thesis.

In Chapter 3 it was discussed that the noise effects are modeled as kicks which update the angle co-ordinates of the particles and which are applied to them once per turn and thus they consist of a discrete-time signal. The power spectral density of that noise signal is given by Eq. (B.15). Now, given the fact that in an accelerator the particles receive the noise kicks once per turn, the sampling frequency, f_s equals the revolution frequency, f_{rev}. This means that the frequency resolution, Δf, can be written as $\Delta f = f_s/N = f_{rev}/N$, where N is the number of samples (or size) in the noise signal.

Furthermore, the studies consider white noise, which is a random signal with the same amplitude (intensity) at all the frequencies which results in a uniform power spectral density. The white noise can be treated in the discrete-time domain as a sequence of uncorrelated random variables taken from a Gaussian distribution with mean zero and finite standard deviation, σ_{white}. Since by definition the power spectral density (for white noise signal) is the same in every frequency, Eq. (B.15) is re-written as:

$$\sigma_{white}^2 = NS_{yy}(f_k)f_{rev}/N = S_{yy}(f_k)f_{rev}, \qquad (B.20)$$

which becomes:

$$S_{yy}(f_k) = \frac{\sigma_{white}^2}{f_{rev}}. \qquad (B.21)$$

In other words, the power spectral density at a given frequency, f_k, for a white noise spectrum modeled as described above, equals the variance of the noise signal over the revolution frequency in the synchrotron.

B.3   Applying a measured noise spectrum in numerical simulations

This section discusses the steps required to convert a measured noise spectrum to a discrete-time series, i.e. a sequence of noise kicks, that can be used in tracking simulations. For the discussion, an example phase noise spectrum measured

during the CC tests in SPS in 2018 is used (see Fig. B.4a). Note that the steps are the same for an amplitude noise spectrum. The procedure involves converting the measured noise power to the power spectral density and then using the inverse Fourier transform to produce the discrete-time series of noise kicks.

In detail, the steps are as follows:

1. Convert the measured noise power $10\log_{10} \mathcal{L}(f_k)$ [dBc/Hz] to the power spectral density, $S_{\Delta\phi}(f_k)$, recalling that $S_{\Delta\phi}(f_k) = \mathcal{L}(f_k)$ (see Section 4.3). This is shown in Fig. B.4b. For now the discussion is limited to $f_k \in [1, 10^3]$ kHz. Note, that both $\mathcal{L}(f_k)$ and $S_{\Delta\phi}(f_k)$ have both negative and positive components and are symmetric around the DC component, $f_k = 0$ Hz (see Section 4.3).

2. Re-sample the noise spectrum. The measured noise power values are equally spaced in frequency on a logarithmic scale. A linear interpolation is needed so that they are equally spaced on a linear scale, every $\Delta f = f_s/N$. As discussed in Section 5.2, since the beam encounters the noise once per turn, the sampling frequency of the noise spectrum in the simulations equals the revolution frequency, $f_s = f_{\text{rev}}(= 43.38$ kHz for the SPS). Note that the frequency spectrum of the noise in the simulations and hence the linear interpolation extends up to $f_s/2$ as illustrated in Fig. B.4c. In our simulations, $N = 10^5$ turns are used. The result is shown in Fig. B.4c.

3. Compute the amplitude of the spectral components of the Fourier transform, $\left|\hat{\phi}_n(f_k)\right|$ according to Eq. (B.10).

4. Generate the phase information for each positive spectral component. By definition the power spectral density does not contain any information about the phase of the frequency components. Therefore, a random phase, $\theta(f_k)$, obtained from a uniform distribution between 0 and 2π is generated for each frequency.

5. Construct a one-sided frequency domain signal, $\hat{\phi}_n^{\text{os}}(f_k) = \left|\hat{\phi}_n(f_k)\right| e^{i\theta(f_k)}$. Once again this computation is done only for the positive spectral

components, with $f_k \in \left[\Delta f, +\frac{f_s}{2} \right]$.

6. Construct the two-sided Fourier transform spectrum. First, create the negative components of the Fourier transform by taking the complex conjugate of the positive components. Furthermore, the information for the zero frequency component (DC) is missing from the measured spectrum, since this extends from 1 kHz to 10 MHz. In order to do the conversion correctly, the zero frequency term is set to 0, so that $\hat{y}_n(0) = 0$. The two-sided Fourier transform is then given by:

$$\hat{\phi}_n(f_k) == \begin{cases} \left| \hat{\phi}_n^{\text{os}}(f_k) \right| \overline{e^{i\theta(|f_k|)}}, & f_k \in \left[-\frac{f_s}{2}, -\Delta f_s \right] \\ \left| \hat{\phi}_n^{\text{os}}(f_k) \right| = 0, & f_k = 0 \\ \left| \hat{\phi}_n^{\text{os}}(f_k) \right| e^{i\theta(|f_k|)}, & f_k \in \left[+\Delta f_s, +\frac{f_s}{2} \right] \end{cases} \tag{B.22}$$

It is clear that $\hat{\phi}_n(f_k)$ has both positive and negative frequencies and the magnitude is symmetric in f_k.

7. Finally, apply the inverse Fourier transform, Eq. (B.8), to $\hat{\phi}_n(f_k)$. The output is a random discrete time series, $\phi(n\Delta t)$ of N values sampled every $\Delta t = 1/f_s = 1/f_{\text{rev}}$.

8. The generated sequence of noise kicks, ϕ_n, that corresponds to the measured noise spectrum can be applied in the tracking simulations following the usual modeling described in Eq. (3.8). Now the parameter $\Delta\phi_j$ is the jth element of the ϕ_n sequence, where $j = \{0..., N_{\text{turns}}\}$ denotes the turn number of the simulation with N_{turns} being the total number of turns.

B.3.1 Validation of the time series reconstruction

This section describes the benchmarks that were carried out to ensure that the above procedure produces a valid time series for a set of noise kicks, for a given power spectrum.

(a) Phase noise spectrum measured with a spectrum analyzer E5052B.

(b) Measured phase noise spectrum in units rad^2/Hz.

(c) Linear interpolation of the measured noise spectrum.

(d) Amplitudes of the spectral components of the Fourier transform.
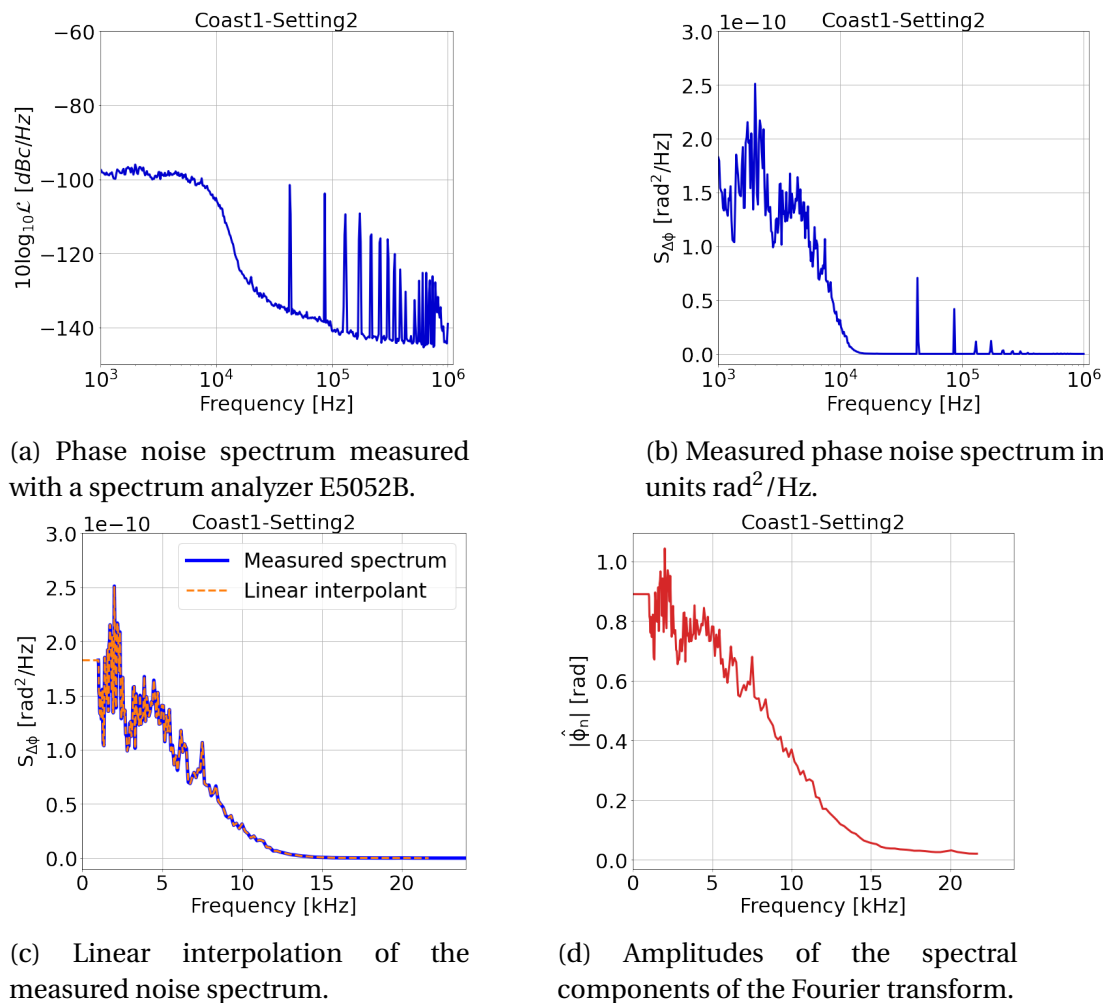
Figure B.4: Steps required to generate the sequence of noise kicks to be applied in the simulations from the measured noise spectrum.

Comparison of measured and reconstructed power spectrum

Figure B.5 shows the results of the first benchmark, comparing the measured power spectral density with the power spectral density computed from the generated time series ϕ_n. The two power spectra appear to be consistent with each other, which supports the validity of the method described above for generating the sequence of noise kicks from a given power spectrum.

PyHEADTAIL simulations

Another way to validate the method for producing a sequence of noise kicks from a measured power spectrum is to perform numerical simulations using the generated noise kicks, and compare the resulting emittance growth with the predictions from
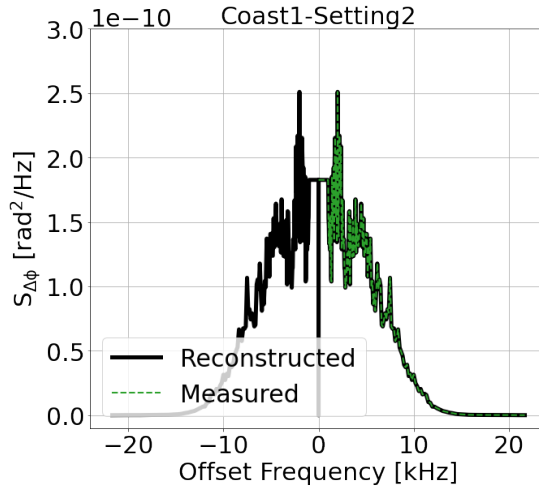
Figure B.5: Power spectral density computed from the time series ϕ_n produced from a measured power spectrum (black), compared with the original measured power spectrum (green).

an analytical model [27].

In the simulations, which were performed with PyHEADTAIL, the beam was tracked for 10^5 turns which correspond to about 2.5 s in the SPS. A kick representing the effect of the crab cavities was applied on each turn following Eq. (3.8). The noise kicks that the beam encounters every turn at the CC location were generated from the phase and amplitude noise spectra of Coast1-Setting2 of 2018 (Fig. 4.1).

It should be noted, however, that the sequence of noise kicks includes a random factor through the set of random phases $\theta(f_k)$. To reduce the uncertainty in the results, multiple simulation runs were conducted. The set of random phases was regenerated randomly for each of 10 runs with a different seed each time. For each run, the initial bunch distribution was also regenerated randomly 3 times. The mean and the standard deviation of the emittance values obtained from the tracking were computed over all runs. The emittance growth rate was computed by performing a linear fit to the mean of the emittance values.

Figures B.6a and B.6b show the emittance growth for the case of amplitude noise and phase noise respectively. The emittance evolution in the presence of both types of noise is also illustrated in Fig. B.6c. The simulated emittance growth rates show very good agreement with the predictions from the analytical model. The results again support the validity of the method for generating a sequence of noise kicks

from a measured noise power spectrum, described in this section.
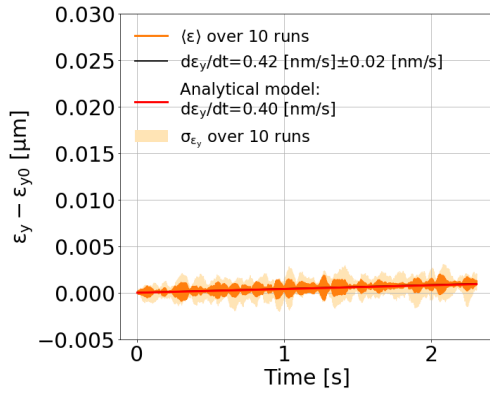
(a) Emittance growth in the presence of amplitude noise.
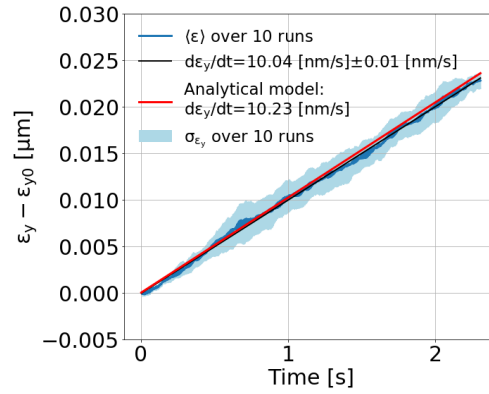
(b) Emittance growth in the presence of phase noise.
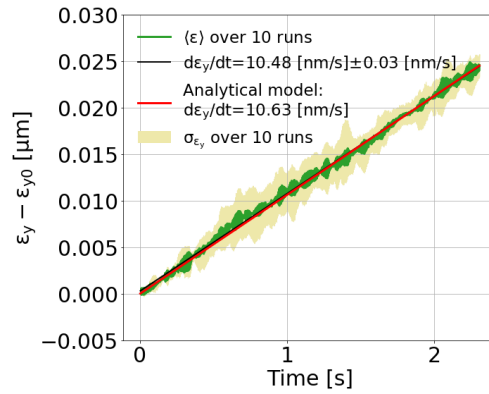
(c) Emittance growth in the presence of both amplitude and phase noise.

Figure B.6: Comparison between emittance growth found from simulations in PyHEADTAIL and emittance growth expected from an analytical model [27]. The emittance growth is driven by amplitude and phase noise, with kicks in the simulations generated from a measured power spectrum.

C | Estimating parameters for the SPS Crab Cavity tests

C.1 Detuning with amplitude

The linear betatron detuning with transverse amplitude introduced by the octupole families in an accelerator ring can be described by Eq. (2.40):

$$\Delta Q_x(J_x, J_y) = 2(\alpha_{xx}J_x + \alpha_{xy}J_y) \qquad (C.1)$$

$$\Delta Q_y(J_x, J_y) = 2(\alpha_{yy}J_y + \alpha_{yx}J_x) \qquad (C.2)$$

where α_{yy}, α_{xx} and $\alpha_{yx} = \alpha_{xy}$ are the detuning coefficients with units [1/m] and J_x, J_y are the action variables.

Rms detuning with amplitude

From the definition of variance, the variance of the vertical amplitude detuning is given by:

$$
\begin{aligned}
\mathrm{Var}(\Delta Q_y) &= \langle \Delta Q_y^2 \rangle - \langle \Delta Q_y \rangle^2 \\
&= \langle 2^2(\alpha_{yy}J_y + \alpha_{yx}J_x)^2 \rangle - \langle 2(\alpha_{yy}J_y + \alpha_{yx}J_x) \rangle^2 \\
&= 2^2 \left[\langle (\alpha_{yy}J_y + \alpha_{yx}J_x)^2 \rangle - \langle \alpha_{yy}J_y + \alpha_{yx}J_x \rangle^2 \right] \\
&= 2^2 \left[\langle (\alpha_{yy}J_y)^2 + 2\alpha_{yy}\alpha_{yx}J_yJ_x + (\alpha_{yx}J_x)^2 \rangle - (\langle \alpha_{yy}J_y \rangle + \langle \alpha_{yx}J_x \rangle)^2 \right] \\
&= 2^2 \left[\alpha_{yy}^2 \langle J_y^2 \rangle + 2\alpha_{yy}\alpha_{yx}\langle J_yJ_x \rangle + \alpha_{yx}^2 \langle J_x^2 \rangle - \alpha_{yy}^2 \langle J_y \rangle^2 - 2\alpha_{yy}\alpha_{yx}\langle J_y \rangle\langle J_x \rangle - \alpha_{yx}^2 \langle J_x \rangle^2 \right] \\
&= 2^2 \left[\alpha_{yy}^2 \langle J_y^2 \rangle + \underline{2\alpha_{yy}\alpha_{yx}\langle J_yJ_x \rangle} + \alpha_{yx}^2 \langle J_x^2 \rangle - \alpha_{yy}^2 \langle J_y \rangle^2 - \underline{2\alpha_{yy}\alpha_{yx}\langle J_yJ_x \rangle} - \alpha_{yx}^2 \langle J_x \rangle^2 \right] \\
&= 2^2 \left[\alpha_{yy}^2 (\langle J_y^2 \rangle - \langle J_y \rangle^2) + \alpha_{yx}^2 (\langle J_x^2 \rangle - \langle J_x \rangle^2) \right] \\
&= 2^2 \left[\alpha_{yy}^2 \mathrm{Var}(J_y) + \alpha_{yx}^2 \mathrm{Var}(J_x) \right]
\end{aligned}
$$

$$(C.3)$$

C. Estimating parameters for the SPS Crab Cavity tests

In the development of Eq. (C.3) the properties of the mean discussed in Eq. (A.2) and (A.3) are used.

Now, according to the discussion in Appendix A.1, the root mean square (rms) for the vertical amplitude detuning is defined here as:

$$
\begin{aligned}
\Delta Q_y^{\text{rms}} = \sigma_{\Delta Q_y} &= \sqrt{\text{Var}(\Delta Q_y)} \\
&= \sqrt{2^2 \left[\alpha_{yy}^2 \text{Var}(J_y) + \alpha_{yx}^2 \text{Var}(J_x) \right]} \\
&= 2\sqrt{\alpha_{yy}^2 (\sigma_{J_y})^2 + \alpha_{yx}^2 (\sigma_{J_x})^2} \\
&= 2\sqrt{\left[\alpha_{yy}(\sigma_{J_y}) \right]^2 + \left[\alpha_{yx}(\sigma_{J_x}) \right]^2},
\end{aligned}
\tag{C.4}
$$

where σ_{J_y} and σ_{J_y} stand for the standard deviation of the action variables J_y and J_x respectively

For a Gaussian distribution the actions, J_x and J_x follow an exponential distribution[1]. It is known that for an exponential distribution the mean equals the standard deviation. Therefore, Eq. C.4 can be written as follows:

$$
\Delta Q_y^{\text{rms}} = 2\sqrt{\left[\alpha_{yy}\langle J_y\rangle \right]^2 + \left[\alpha_{yx}\langle J_x\rangle \right]^2}.
\tag{C.5}
$$

Following Eq. (2.21), the rms betatron tune spread from amplitude detuning can be also written as:

$$
\Delta Q_y^{\text{rms}} = 2\sqrt{(\alpha_{yy}\epsilon_y^{\text{geom}})^2 + (\alpha_{yx}\epsilon_x^{\text{geom}})^2}.
\tag{C.6}
$$

Equivalently, the horizontal rms tune spread from amplitude detuning can be computed by:

$$
\Delta Q_x^{\text{rms}} = 2\sqrt{(\alpha_{xx}\epsilon_x^{\text{geom}})^2 + (\alpha_{yx}\epsilon_y^{\text{geom}})^2}.
\tag{C.7}
$$

of the lattice.

---

[1]The charge density function for a Gaussian beam in u, u', where $u = (x, y)$ is expressed in terms of the Twiss parameters as: $\rho(u, u') = e^{-(\gamma_u u^2(s) + 2\alpha_u(s)u(s)u'(s) + \beta_u(s)u'^2(s))/(2\epsilon_u^{\text{geom}})} = e^{-J_u/\epsilon_u^{\text{geom}}}$.

C.1.1 Residual rms tune spread in the SPS

Here the rms tune spread in the SPS that is present in the SPS with the Landau octupoles being switched off is estimated. For the estimation, only the detuning with transverse amplitude is considered.

As discussed in Section 5.3.6 a non-linear model of the SPS was developed through beam-based measurements including the contributions from the chromatic sextupoles and the SPS multipole components in the main dipoles [67, 68]. However, further experimental studies[127] indicated stronger amplitude detuning than predicted from these multiple components. The measured amplitude detuning can be approximated in simulations by switching on the Landau octupole families with strengths $k_{\mathrm{LOF}} = k_{\mathrm{LOD}} = 1 \,/\mathrm{m}^4$.

Using the values of the multipoles listed in Table 5.3 and setting the strength of both octupole families at $1 \,/\mathrm{m}^4$ the corresponding detuning coefficients are obtained with MAD-X [48]. In particular, $\alpha_{xx} = 923.45 \,/\mathrm{m}$, $\alpha_{yx} = -1122.451 \,/\mathrm{m}$, $\alpha_{yy} = 705.15 \,/\mathrm{m}$. It should be noted that these values are obtained for zero linear chromaticity in both transverse planes.

The tune spread is computed for the requested initial emittances for the emittance growth measurements of 2018 and 2021, $\epsilon_x = \epsilon_y = 2 \,\mu\mathrm{m}$. Using Eq. (2.28) it can be seen that these values correspond to geometric emittances of $\epsilon_x^{\mathrm{geom}} = \epsilon_y^{\mathrm{geom}} = 7.2 \,\mathrm{nm}$. By inserting these values of detuning coefficients and geometric emittances in Eq. (C.7) and Eq. (C.6) the rms tune spread is found to be, $\Delta Q_x^{\mathrm{rms}} = 1.9 \times 10^{-5}$ and $\Delta Q_y^{\mathrm{rms}} = 2.1 \times 10^{-5}$, in the horizontal and vertical planes respectively.

C.2 SPS octupoles calibration

In this section, the relation between the current and the strength of the focusing (LOF) and defocusing (LOD) SPS octupoles is described. First, the calibration curves (current, I_w, as a function of the strength, b_w, multiplied with the octuple length L_w, where $w =$ (LOD, LOF)) are extracted for both octupole families from the LHC

C. Estimating parameters for the SPS Crab Cavity tests

Software Architecture (LSA) [128]. They are shown in Figs. C.1 and C.2 for the LOF and LOD families, respectively. The parameter, b_w, is defined in Eq. (2.4) for $n = 3$. The lengths of the octupole magnets are: L_{LOF}=0.705 m and L_{LOD}=0.677 m.
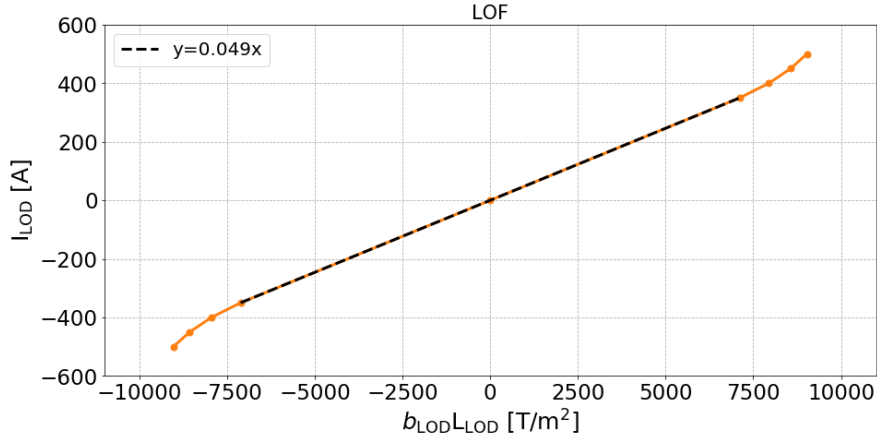
Figure C.1: Calibration curve for the LOF SPS family as obtained from LSA.
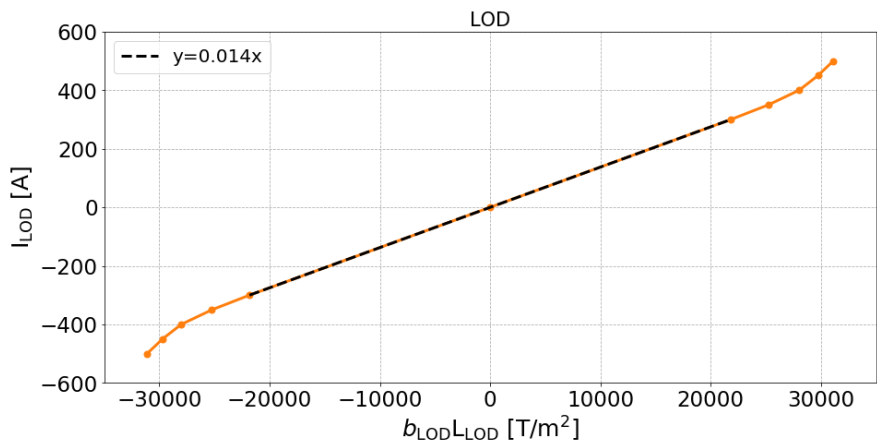
Figure C.2: Calibration curve for the LOD SPS family as obtained from LSA.

For the studies in the area of low to moderate current (up to 300 A) the relation between the current and the strength b_w appears to be linear. For the SPS experimental campaign of 2022, the octupoles operated in this regime. Therefore, focusing on the area of linear dependence is a valid approximation for the studies presented in this thesis.

Subsequently, the relation between the octupole current and strength is obtained by a linear fit on the above-discussed calibration curves which it is also shown in black color. From the fit, it occurs that:

$$I_{LOF} = 0.049 \times b_{LOF} \times 0.705 = 0.035 \times k_{LOF} \times B_1\rho \, [A], \tag{C.8}$$

$$I_{LOD} = 0.014 \times b_{LOF} \times 0.677 = 0.009 \times k_{LOD} \times B_1\rho \, [A], \tag{C.9}$$

where k_{LOF}, k_{LOD} correspond to the k_3 definition of Eq. (2.5) and $B_1\rho$ the magnetic rigidity.

D | SPS Headt-Tail monitor as the main diagonostic for the Crab Cavity studies

The SPS is equipped with a pick-up of approximately 2 GHz bandwidth allowing to resolve the intra-bunch motion. This instrument is called Head-Tail (HT) monitor and was originally designed for measuring chromaticity and transverse instabilities. However, in the SPS CC tests, the Head-Tail monitor was the main diagnostic device deployed for the demonstration of the crabbing and the reconstruction of the CC voltage as experienced by the beam. Its use as a crabbing diagnostic shall be explained here. The methods and procedures described in this section were developed at CERN and are described here for completeness.

In the first part of this section, some general information on the instrument along with example signals will be presented. Subsequently, the post-processing of the Head-Tail signal in the presence of the CC will be discussed. Last, the calibration of the CC voltage from the Head-Tail data is described and a schematic representation of the "crabbing" is displayed. The term crabbing is used here to describe the z-dependent orbit offset induced by the CC kick. The experimental data presented in this section were acquired on May 30, 2018 (time-stamp: 13:51:05), at the SPS injection energy of 26 GeV with only one CC, CC1, at phase $\phi_{CC} = 0$ (this means that a particle at the center of the bunch doesn't receive any transverse deflection). The energy of 26 GeV was chosen to provide a better understanding of the methods used as the orbit shift from the CC kick is stronger and thus more visible than at higher energies.

D.1 General information

The Head-Tail monitor [71] is a high bandwidth beam position monitor that can measure the transverse displacement within the bunch. It has a resolution of 100 ps while the length of the bunches is $4\sigma_t \sim 2$ ns [129]. This makes it ideal for the measurement of the intra-bunch offset caused from the CC kick. Its reading consists of the sum (Σ) and the difference (Δ) of the electrode signals of a straight stripline coupler (Fig. D.1) [130, 131] over a defined acquisition period. The sum signal is the longitudinal line density while the difference signal divided by the sum signal corresponds to the intra-bunch offset. The system operates on timescales such that the signals are given as a function of the position within the bunch. The center of the bunch as it passes through the Head-Tail monitor defines $t = 0$.
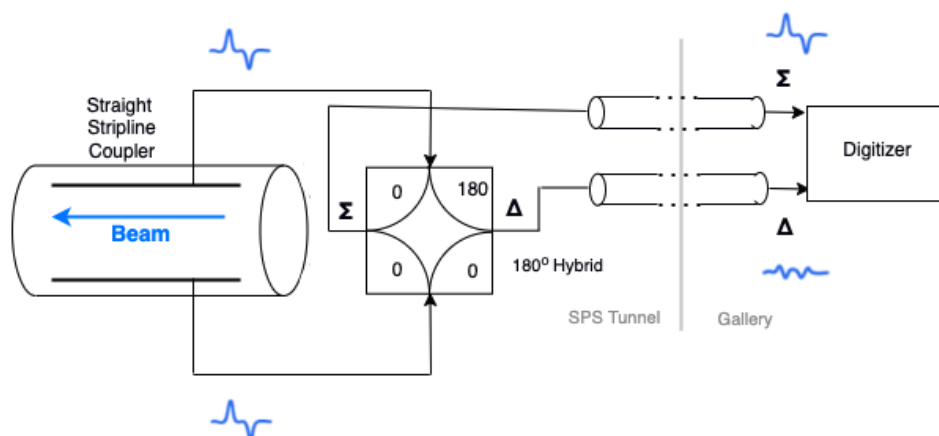
Figure D.1: Diagram of the SPS Head-Tail monitor [131]. The beam is passing through a straight stripline coupler which is followed by a 180° hybrid. This configuration provides the sum (Σ) and the difference (Δ) signal of the two electrodes.

The raw signals from the Head-Tail monitor require a specific post-processing procedure [131], in order to provide useful information. Figure D.2 shows some example signals obtained from the Head-Tail monitor after the basic post-processing is applied. Moreover, Fig. D.3 shows a 2D representation of the Head-Tail monitor reading. It is worth noting here that in the specific example a clear modulating pattern in time of the vertical intra-bunch offset signal is observed. This is a result of the phase slip between the CC and the main RF system because they are not yet synchronised during this specific measurement.
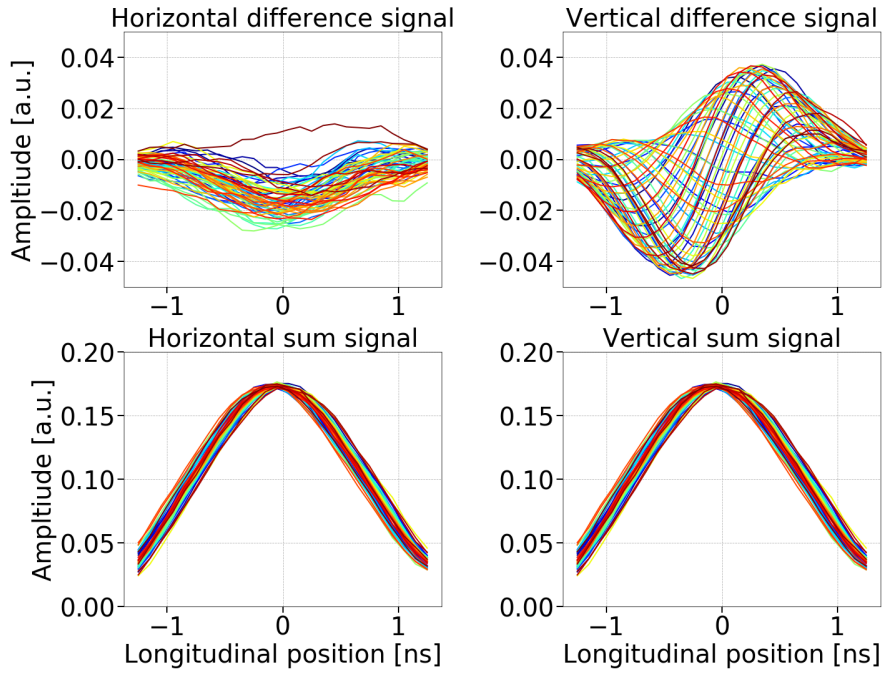
Figure D.2: Example difference and sum signals (top and bottom plots, respectively) from the Head-Tail monitor, in time scale, with respect to the longitudinal position within the bunch over several SPS revolutions, after the basic post processing [131] but before the baseline correction. The different colors indicate the signals from different turns (every 100 turns).

D.2 Post processing in the presence of Crab Cavities

To obtain useful information from the Head-Tail monitor signal in the presence of the CCs there are a few steps that differ from the standard post-processing procedure and they are described below.

D.2.1 Head-Tail monitor baseline correction

The Head-Tai monitor measurement has a baseline on the difference signal which needs to be removed. The baseline is a result of orbit offsets and non-linearities of the instrument and is constant from turn to turn [131]. Therefore, during the normal post-processing procedure (without CCs), the baseline is computed as the mean of the difference signals over all turns and then the correction is achieved by subtracting this static offset from the signal of each turn. However, in the SPS tests, where the CCs are well synchronised with the main RF system (Section 4.1.1), the crabbing signal is also a static intra-bunch position offset and thus would also be
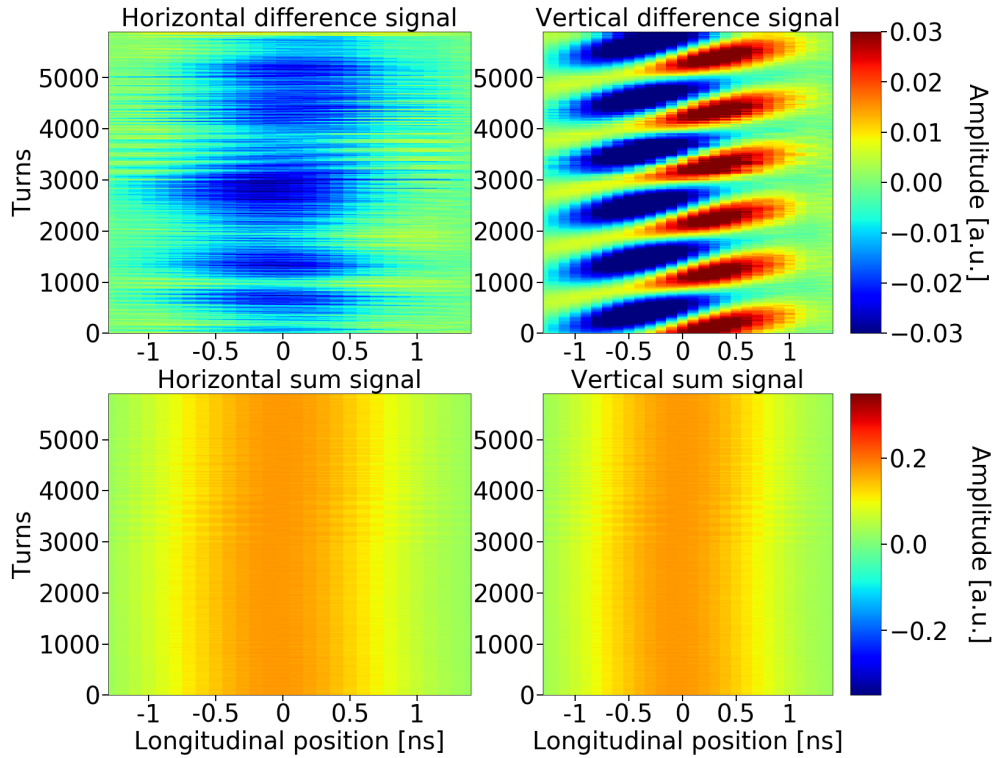
Figure D.3: 2D representation of example difference and sum signals with respect to the longitudinal position within the bunch obtained from the Head-Tail monitor over several SPS revolutions.

removed with the usual method. Because of technical limitations it was not feasible to switch off the CC for those kind of measurements. Thus, the following technique was used.

For the CC experiments a reference measurement had first to be made with the CC not being synchronous with the main RF system. The baseline was computed as the mean of the difference signals over this reference period and subsequently it was subtracted from the average of the difference signals acquired after the synchronisation (Fig D.4). The datasets before and after synchronisation are easily distinguishable in the 2D HT monitor reading as displayed in Fig. D.5.

Head-Tail monitor scaling

The last step to make the Head-Tail acquisitions meaningful is to convert the measured intra-bunch offset (the mean of the difference signals following phase synchronisation and baseline correction) from arbitrary units to millimeters. The scaling is achieved by dividing by the mean of the sum signals (which is a function of the position along the bunch and is calculated for each point individually over
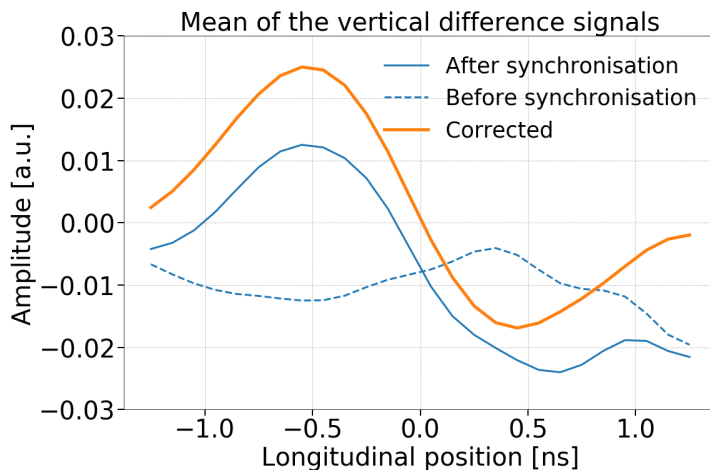
Figure D.4: Head-Tail monitor baseline correction for the SPS CC tests. The baseline signal (blue dashed line) refers to the mean of the difference signals acquired before the CC - main RF synchronisation. The measured signal (blue solid line) corresponds to the mean of the difference signal acquired after the synchronisation. Last, the corrected signal (orange solid line) is obtained after subtracting the baseline from the measured signal.
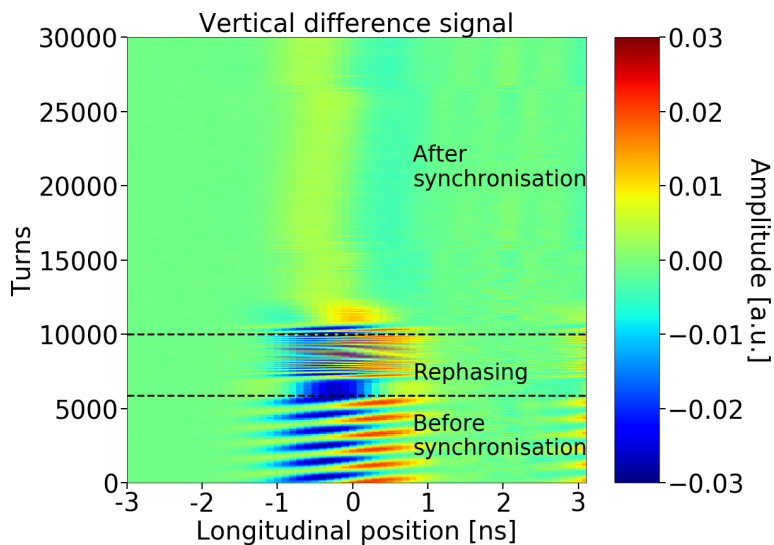
Figure D.5: Head-Tail acquisitions before and after the synchronisation of the SPS main RF with the CC.

many turns) after the synchronisation and with a normalisation factor which is provided by the calibration of the Head-Tail monitor [132]. The normalisation factor for the SPS was measured at 0.1052 in 2018 [133]. Figure D.6 shows the intra-bunch offset from the CC kick in millimeters and after the baseline correction.
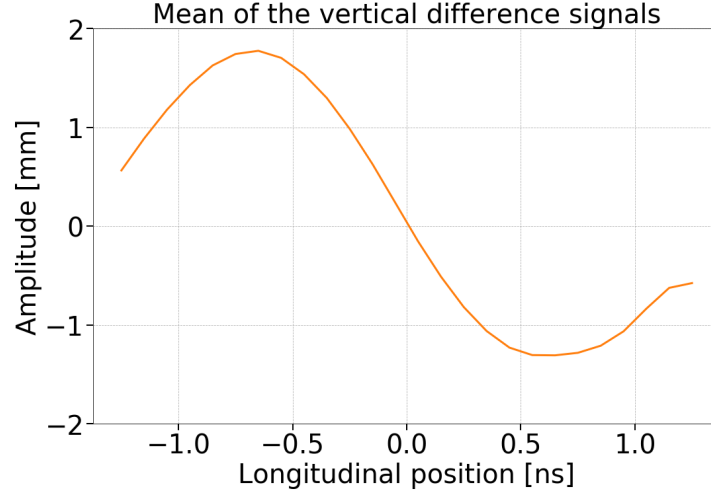
Figure D.6: Intra-bunch offset from the CC kick expressed in millimeters after the removal of the baseline.

D.2.2   Crab Cavity voltage reconstruction

This section discusses the reconstruction of the CC voltage from the HT monitor signal. First, Eq. (D.1) was used to calculate the CC kick, θ, required to reconstruct the measured intra-bunch offset. Equation (D.1), which is obtained from Eq. (1) from chapter 4.7.1 in [85], gives the vertical orbit shift from the CC kick, θ, at the Head-Tail monitor location as follows:

$$\Delta y_{,HT} = \frac{\sqrt{\beta_{y,HT}}}{2\sin(\pi Q_{y0})}\theta\sqrt{\beta_{y,CC}}\cos(\pi Q_{y0} - |\psi_{y,HT} - \psi_{y,CC}|),\qquad\text{(D.1)}$$

where β_y is the beta function, Q_{y0} is the tune, and $|\psi_{y,HT} - \psi_{y,CC}|$ is the vertical phase advance (in radians) between the CC and the Head-Tail monitor. The same applies for the horizontal plane. The subscripts Head-Tail and CC indicate quantities at the location of the Head-Tail monitor and CC respectively.

The CC voltage experienced by the beam is then reconstructed from the CC kick which is written as $\theta = -\frac{qV_{\mathrm{CC}}(t)}{E_b}$, where q is the charge of the particle, E_b the beam energy and $V_{\mathrm{CC}}(t) = V_{0,\mathrm{CC}}\sin(2\pi f_{\mathrm{CC}}t + \phi_{\mathrm{CC}})$ is the voltage that a particle experiences while passing through the CC. In the context where the Head-Tail monitor measures the signal as a function of time, t, the voltage in the above formula is expressed accordingly as $V_{\mathrm{CC}}(t)$, where $t = 0$ the center of the bunch as it passes through the
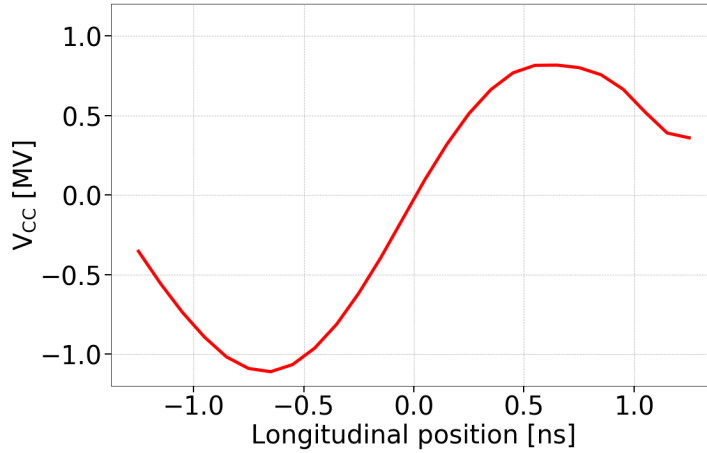
Head-Tail monitor.

Figure D.7: CC voltage reconstruction from the Head-Tail monitor.

It should be noted here, that the measured intra-bunch offset, $\Delta y_{,HT}$, is inserted in Eq. (D.1) after removing the baseline and converting it to millimeters as discussed in Section D.2. Figure D.7 illustrates the CC voltage computed from the Head-Tail signals shown already in this section. The corresponding beam and optic parameters are listed in Table D.1.

Table D.1: Parameters for computing the CC voltage from the example Head-Tail monitor measurements discussed in this chapter.

Parameter	Value
Beta function at the Head-Tail monitor, $\beta_{y,HT}$	49.19 m
Phase advance to the Head-Tail monitor*, $\psi_{y,HT}$	$15.68 \times 2\pi$
Beta function at the CC1, $\beta_{y,CC1}$	76.07 m
Phase advance to the CC1*, $\psi_{y,CC1}$	$23.9 \times 2\pi$
Vertical betatron tune, Q_{y0}	26.18
Beam energy, E_b	26 GeV

* The phase advances are measured from the start of the lattice which is considered the element QF.10010 which is a focusing quadrupole.

D.3 Head-Tail monitor calibration for the 2022 analysis

To give the measured intra-bunch offset (during the SPS CC tests) in units of millimeters, the Head-Tail monitor response is calibrated by performing orbit bumps (around the reference orbit) and measuring the normalised position[1] of the

---

[1]It is calculated as the difference signal divided by sum signal.

bunch in the vertical plane (plane of interest). More details on the calibration procedure are given in [132].

The calibration of the Head-Tail monitor response that took place in November 2021, is shown in Fig. D.8. After applying a linear fit to the measured data, it was found that a normalised position of 0.1037 corresponds to 1 mm.
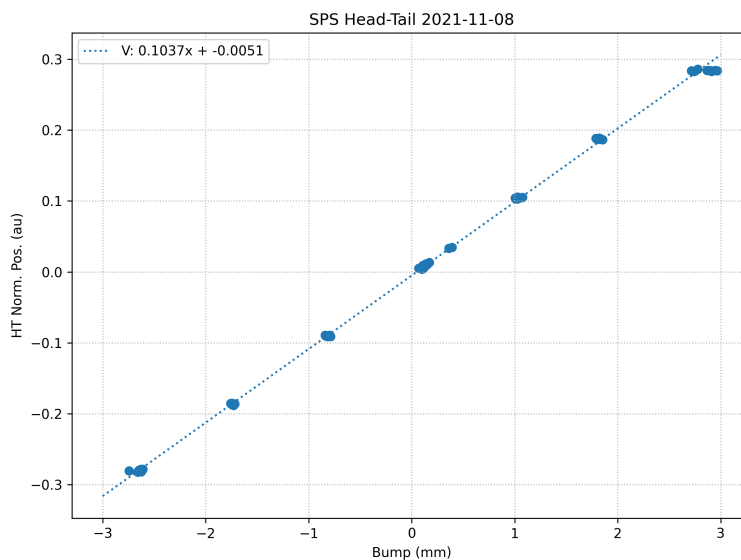
Figure D.8: Calibration of Head-Tail monitor from November 2021. This plot is courtesy of T. Levens.

E | Measurements from experimental studies in 2022

E.1 Example bunch profiles from Wire Scanner measurements

Uncertainties of the Gaussian fit

Figures E.2a and E.2b show two example horizontal and vertical beam profiles as obtained from the SPS.BWS.51637.H and SPS.BWS.41677.V instruments, respectively, during the experiment with CC1 in SPS in 2022. The data points from the IN (OUT) scan are shown with a blue (orange) color.

The measured data points (light blue) are fitted with a four-parameter gaussian (orange) following the procedure discussed in Section 4.5.1 to obtain the beam size. Thereafter, the emittance values and their uncertainties are computed from Eqs. (4.9) and (4.10) respectively. The results of the fit are also shown in the plots. It is evident that the calculated uncertainties are two orders of magnitude smaller than the corresponding emittance values themselves. This is the case for all acquisitions.

IN and OUT scans

As discussed in Section 4.5.1, during each measurement with the Wire Scanners the beam profile is acquired two times as the wire crosses the beam in the forward direction (IN scan) and then in the reverse direction (OUT scan). For the experiment of 2022, the OUT scan was performed just 200 ms after the IN scan. However, it was observed that there are significant discrepancies between the emittance measurements from IN and OUT scan, which in some cases reached up to 1 μm. By looking at the acquired profiles, e.g. in Fig. E.2a no apparent reason

(a) Horizontal beam profile.   (b) Vertical beam profile.

Figure E.1: Transverse beam profiles as obtained from SPS.BWS.51637.H during the CC experiment in the SPS in 2022. The data points from the IN (OUT) scan are shown with blue (orange) color.

was found to exclude or not one of the two scans.

A significant effort was done with the Wire Scanner experts during the emittance growth experiment trying to mitigate this effect without success due to limitations on the hardware of the current instrument that still need to be sorted out. Note that this issue was not observed in the 2018 measurements. A possible explanation is that the wire scanner acquisitions of 2022 provide lower number of points to reconstruct the bunch profiles (compare Figs. 4.4 against E.2b) increasing the uncertainty of the obtained emittances. The reason behind this, is that between 2018 and 2022 the wire scanners had undergone an upgrade which increased their speed while crossing the bunch. A possible solution to this issue would be to reduce the speed of the wire for the emittance growth experiments in coast mode. This is currently in discussion with the team responsible for the Wire Scanners of the SPS.

For the SPS CC tests in 2022, it was decided that the post-process analysis would be performed taking into account only the IN scan measurements since they appeared to have systematically less fluctuation than in the OUT scan. An example is provided in Fig. E.2 where it can be seen that the emittance values obtained from the OUT scan appear to be more fluctuating than the values from the IN scan. In this particular example, this is enhanced in the horizontal plane (blue). It is also clearly visible for the acquisitions during the first half of the coast. Furthermore, the acquisitions from the OUT scans led to corrupted profiles more frequently than

the IN scans.

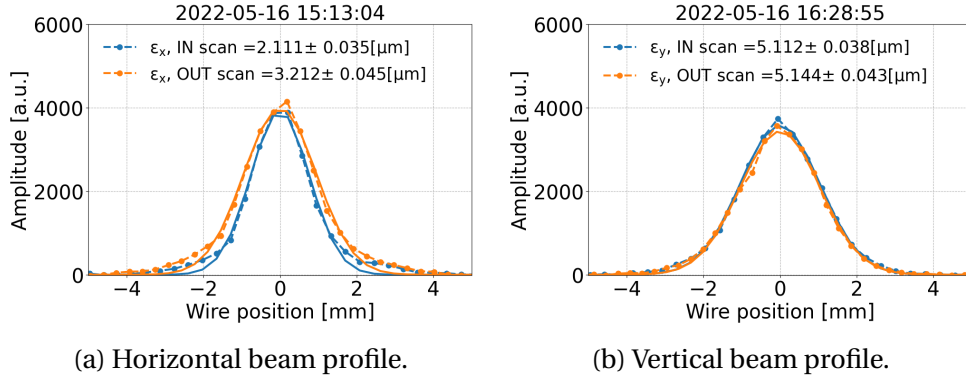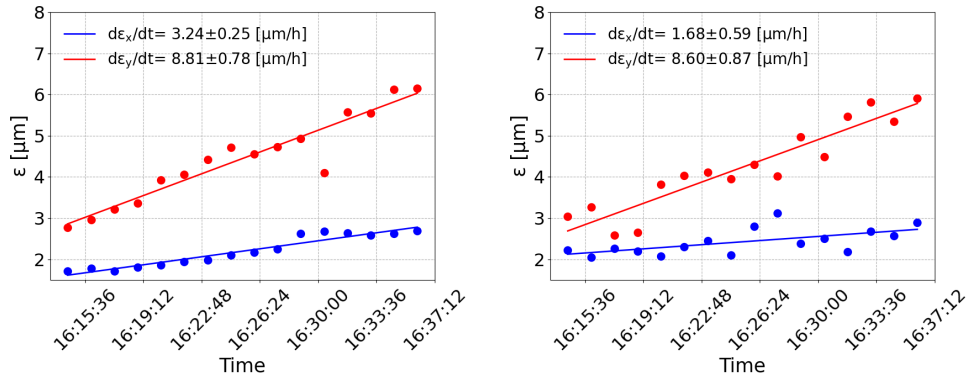(a) Emittance evolution from IN scan.   (b) Emittance evolution from OUT scan.

Figure E.2: Transverse beam profiles as obtained from SPS.BWS.51637.H during the CC experiment in the SPS in 2022. The data points from the IN (OUT) scan are shown with blue (orange) color.

E.2 Transverse emittance growth measurements

In this section, the individual emittance growth measurements for each coast from the SPS CC tests that were conduced in 2022 are presented.

E.2.1 Experiment II: sensitivity of emittance growth to amplitude-dependent tune shift
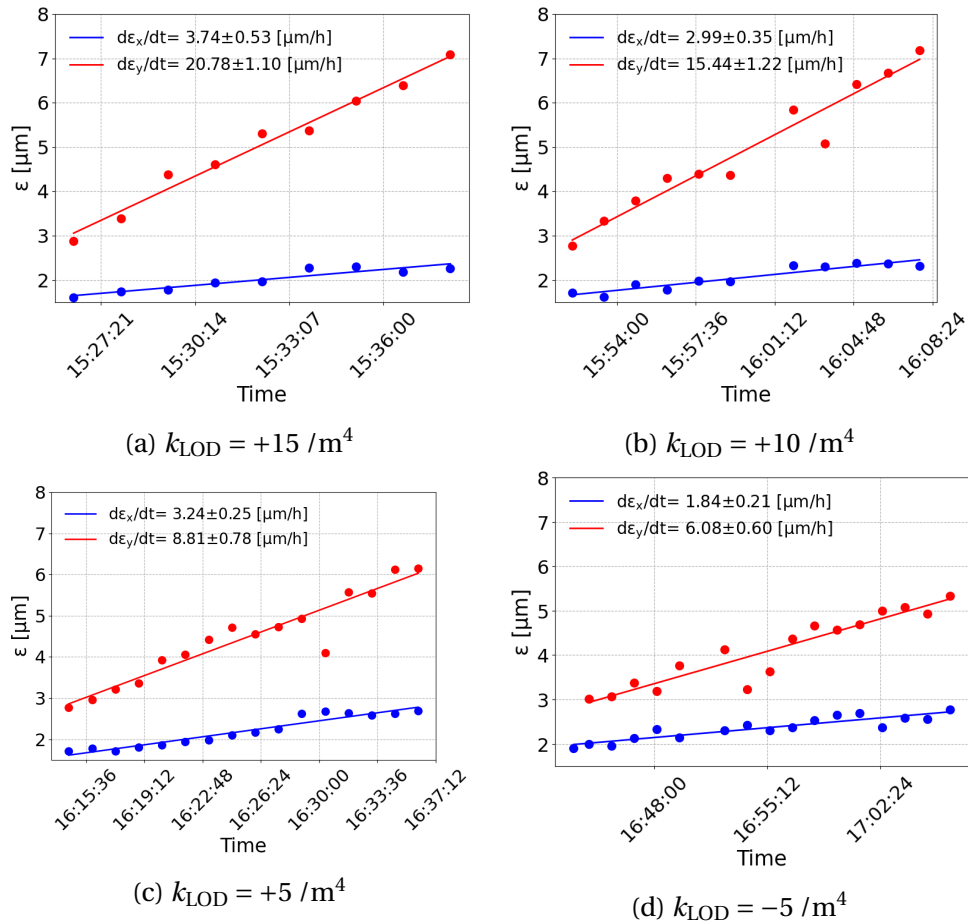
Figure E.3: Horizontal (blue) and vertical (red) emittance evolution of a single bunch during the CC experiment on 16 May, 2022 driven by phase noise of -104.7 dBc/Hz. The different octupole settings are displayed in the captions of each plot.

E.2.2 Experiment III: emittance growth measurements in the presence of strong octupoles

(a) $k_{\mathrm{LOD}} = -30/\mathrm{m}^4$

(b) $k_{\mathrm{LOD}} = -20/\mathrm{m}^4$

(c) $k_{\mathrm{LOD}} = -10/\mathrm{m}^4$

(d) $k_{\mathrm{LOD}} = +30/\mathrm{m}^4$

(e) $k_{\mathrm{LOD}} = +10/\mathrm{m}^4$
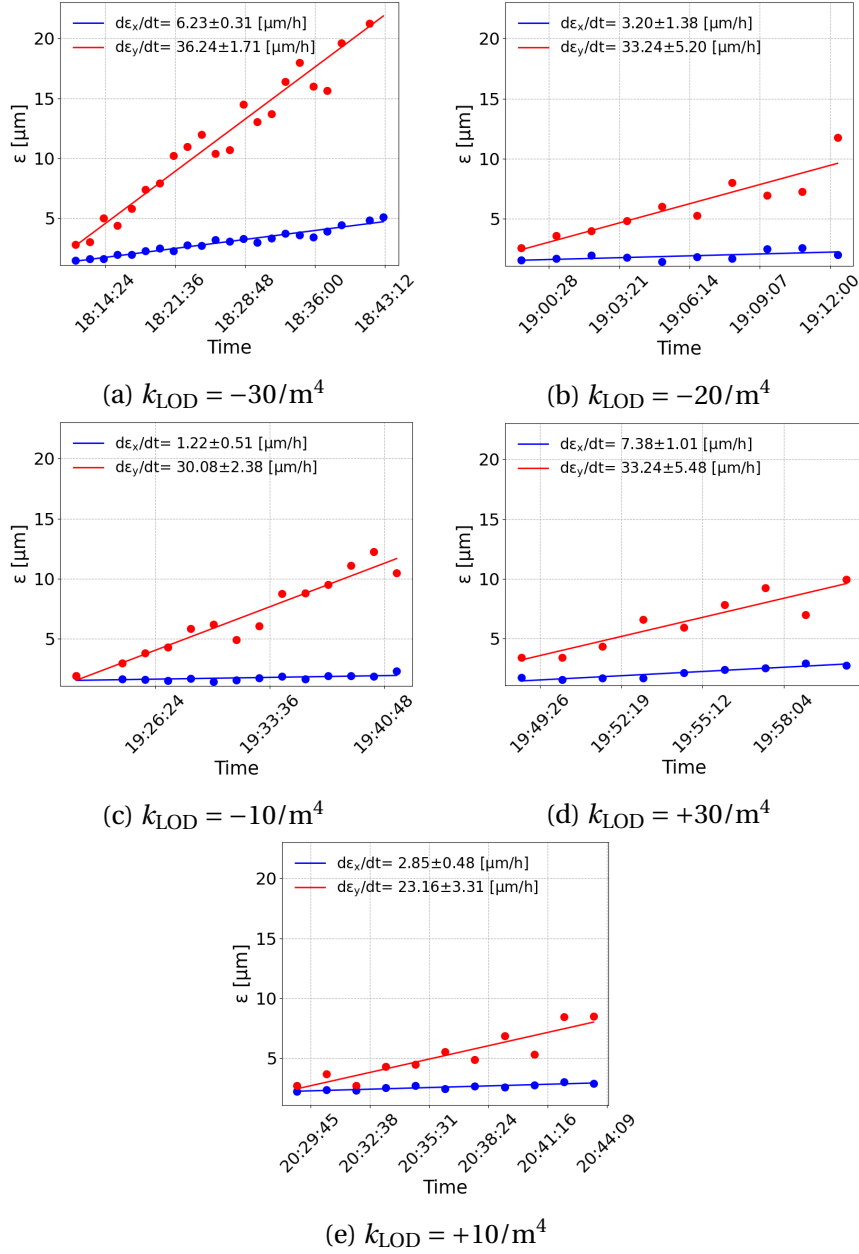
Figure E.4: Horizontal (blue) and vertical (red) emittance evolution of a single bunch during the experiment with dipole noise on September 12, 2022. The different octupole settings are displayed at the captions of each plot.

E.2.3 Experiment V: emittance growth driven by dipole noise
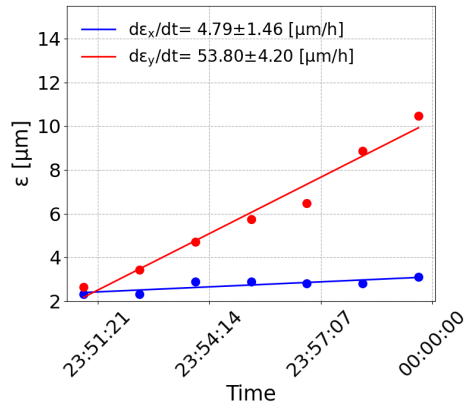
(a) $k_{LOD} = +15/\text{m}^4$
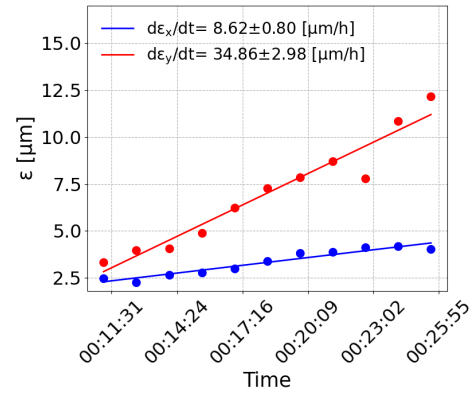
(b) $k_{LOD} = +10/\text{m}^4$
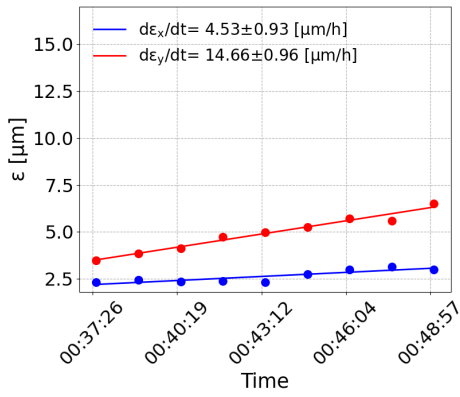
(c) $k_{LOD} = +5/\text{m}^4$
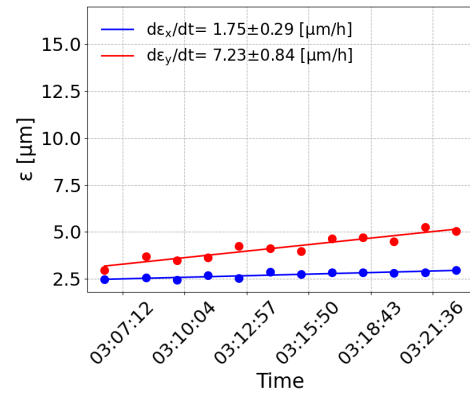
(d) $k_{LOD} = 0/\text{m}^4$
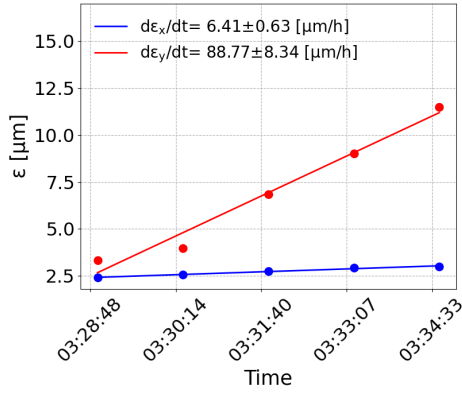
(e) $k_{\mathrm{LOD}} = -15/\mathrm{m}^4$
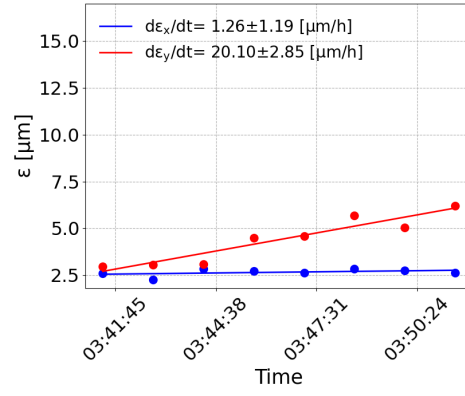
(f) $k_{\mathrm{LOD}} = -7.5/\mathrm{m}^4$
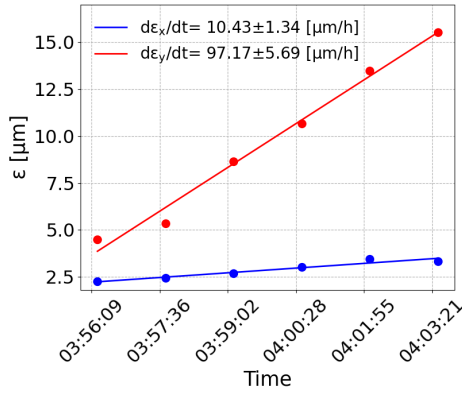
(g) $k_{\mathrm{LOD}} = +25/\mathrm{m}^4$

Figure E.5: Horizontal (blue) and vertical (red) emittance evolution of a single bunch during the experiment with dipole noise on May 16-17, 2022. The different octupole settings are displayed at the captions of each plot.

E.3 Bunch length measurements

The bunch length measurements presented in this section were performed with the Wall Current Monitor (WCM). The WCM acquires the longitudinal bunch profiles which are fitted with a Gaussian function in the post-processing for the evaluation of the bunch length. Each data point shown in the following plots corresponds to the average bunch length value obtained from 100 subsequent acquisitions, while the error bars indicate the standard deviation.

Further details on the WCM that are installed in the CERN Proton Synchrotron (PS) and Large Hadron Collider (LHC) can be found in [134, 135]. The device installed in the SPS follows the same working principle.

E.3.1 Experiment I: dependece of emittance growth on CC RF noise power
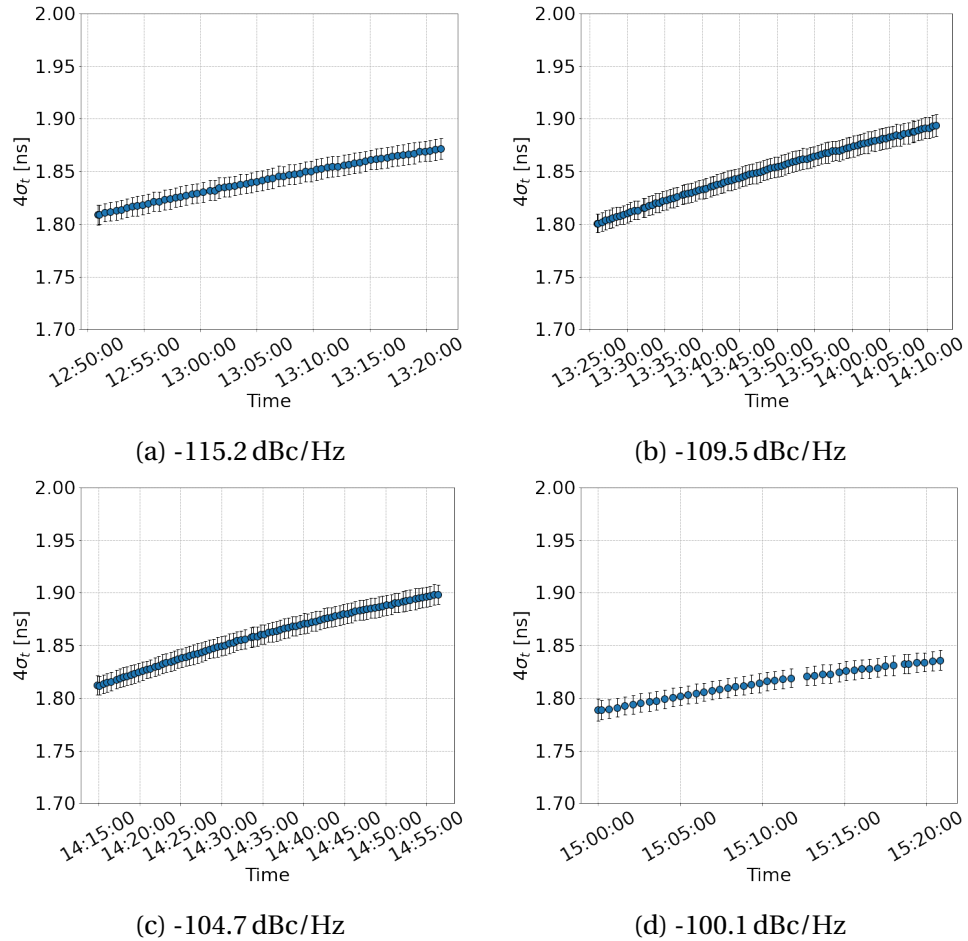
Figure E.6: Evolution of the bunch length during the CC Experiment I on May 16, 2022. The different phase noise levels injected in the RF system of CC1, are displayed at the captions of each plot.

E.3.2 Experiment II: sensitivity of emittance growth to amplitude-dependent tune shift

(a) $k_{\text{LOD}} = +15/\text{m}^4$

(b) $k_{\text{LOD}} = +10/\text{m}^4$

(c) $k_{\text{LOD}} = +5/\text{m}^4$

(d) $k_{\text{LOD}} = -5/\text{m}^4$

Figure E.7: Evolution of the bunch length during the CC Experiment II on May 16, 2022. The different octupole settings are displayed at the captions of each plot.

The average measured bunch length over all above coasts on May 16, 2022 (Experiments I and II) was found to be $4\sigma_t$=1.83 ns.

E.3.3 Experiment III: emittance growth measurements in the presence of strong octupoles

(a) $k_{\mathrm{LOD}} = -30/\mathrm{m}^4$

(b) $k_{\mathrm{LOD}} = -20/\mathrm{m}^4$

(c) $k_{\mathrm{LOD}} = -10/\mathrm{m}^4$

(d) $k_{\mathrm{LOD}} = +30/\mathrm{m}^4$

(e) $k_{\mathrm{LOD}} = +10/\mathrm{m}^4$
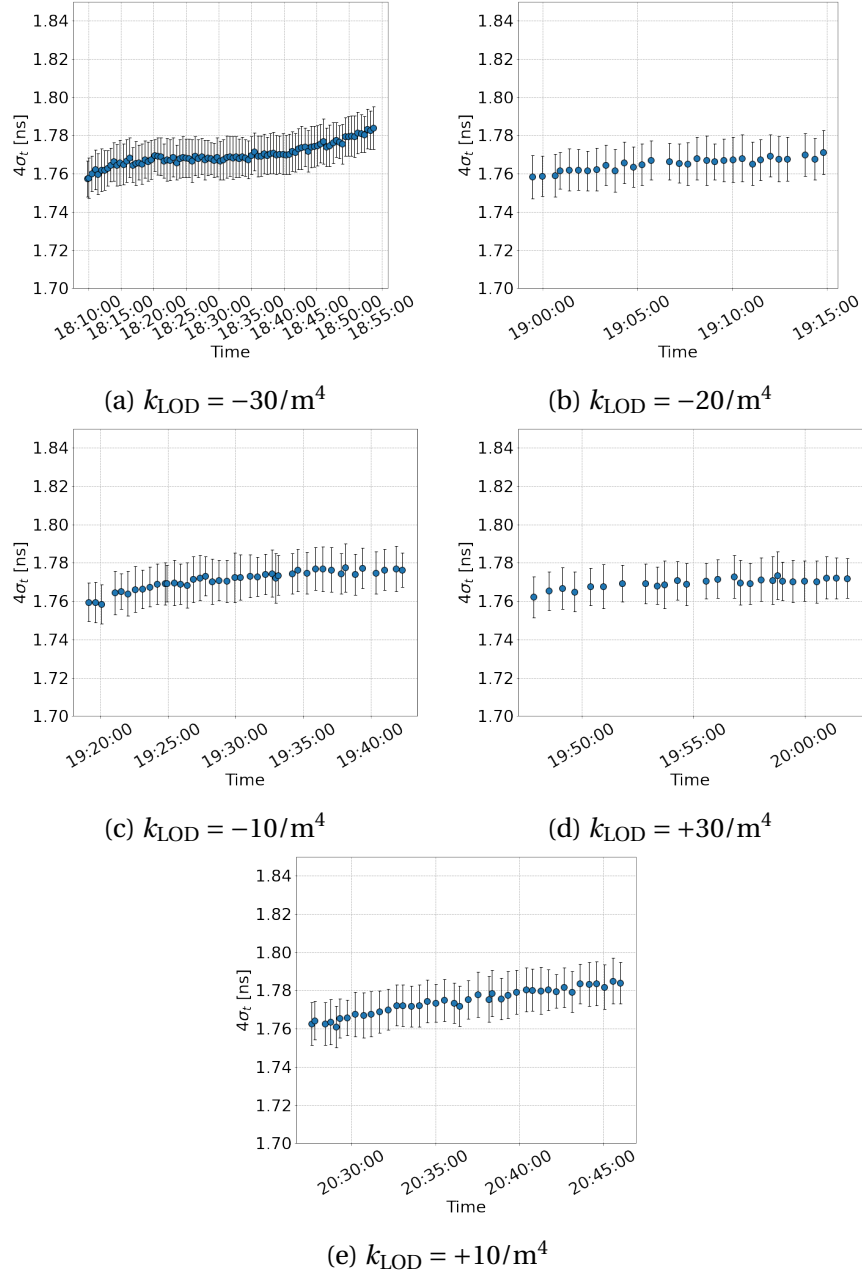
Figure E.8: Evolution of the bunch length during the CC Experiment III on September 12, 2022. The different octupole settings are displayed at the captions of each plot.

The average measured bunch length over all above coasts in 2022, was found to be $4\sigma_t$=1.77 ns.

E.3.4 Experiment IV: emittance growth measurements driven primarily by amplitude noise

§

Figure E.9: Evolution of the bunch length during the CC Experiment IV on September 12, 2022.

The average measured bunch length over the coast was found to be $4\sigma_t$=1.75 ns.

E.4 Intensity measurements

The intensity measurements presented in the section were acquired using the Beam Current Transformer (in particular with the device SPS.BCTDC.41435) which is installed in the SPS machine. The Beam Current Transformer measures the beam-induced current in its ferrite core and transforms it to the number of protons per beam. Further details on their working principle and operation can be found in [107, 108].

E.4.1 Experiment I: dependece of emittance growth on CC RF noise power

(a) -115.2 dBc/Hz

(b) -109.5 dBc/Hz

(c) -104.7 dBc/Hz

(d) -100.1 dBc/Hz
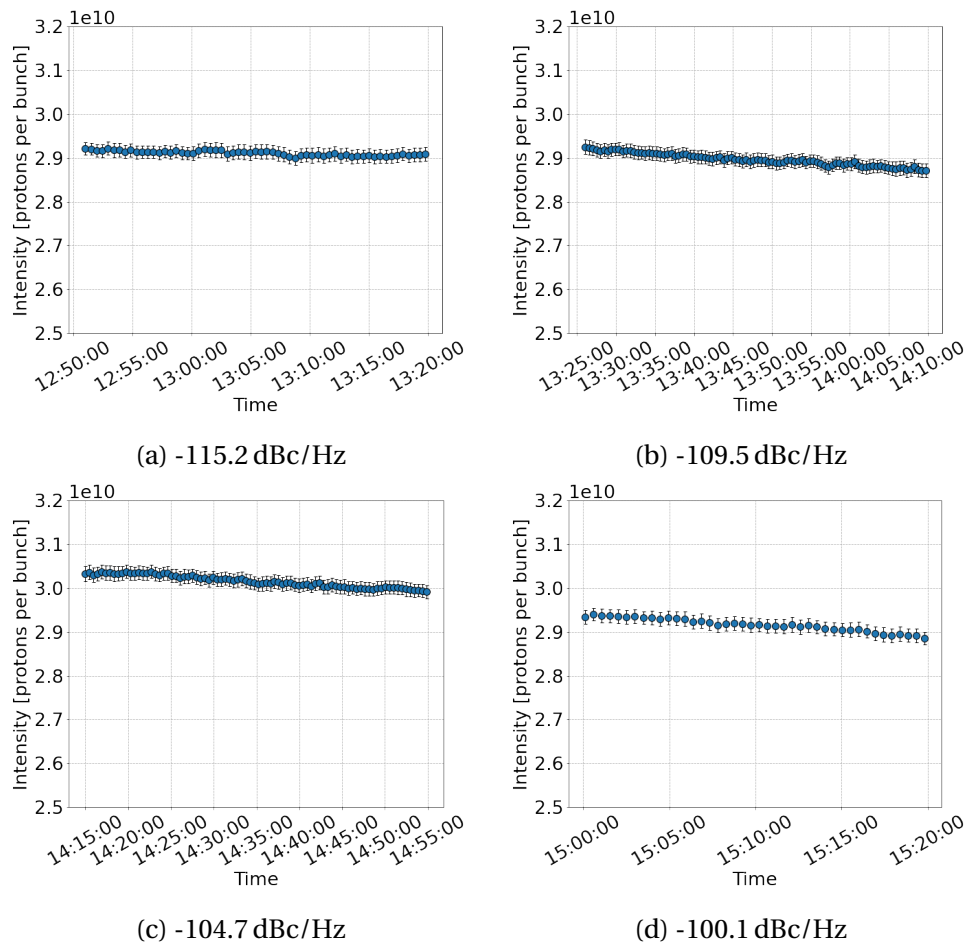
Figure E.10: Evolution of the intensity during the CC Experiment I on May 16, 2022. The different phase noise levels injected in the RF system of CC1, are displayed at the captions of each plot.

E.4.2 Experiment II: sensitivity of emittance growth to amplitude-dependent tune shift

(a) $k_{LOD} = +15/\text{m}^4$

(b) $k_{LOD} = +10/\text{m}^4$

(c) $k_{LOD} = +5/\text{m}^4$

(d) $k_{LOD} = -5/\text{m}^4$
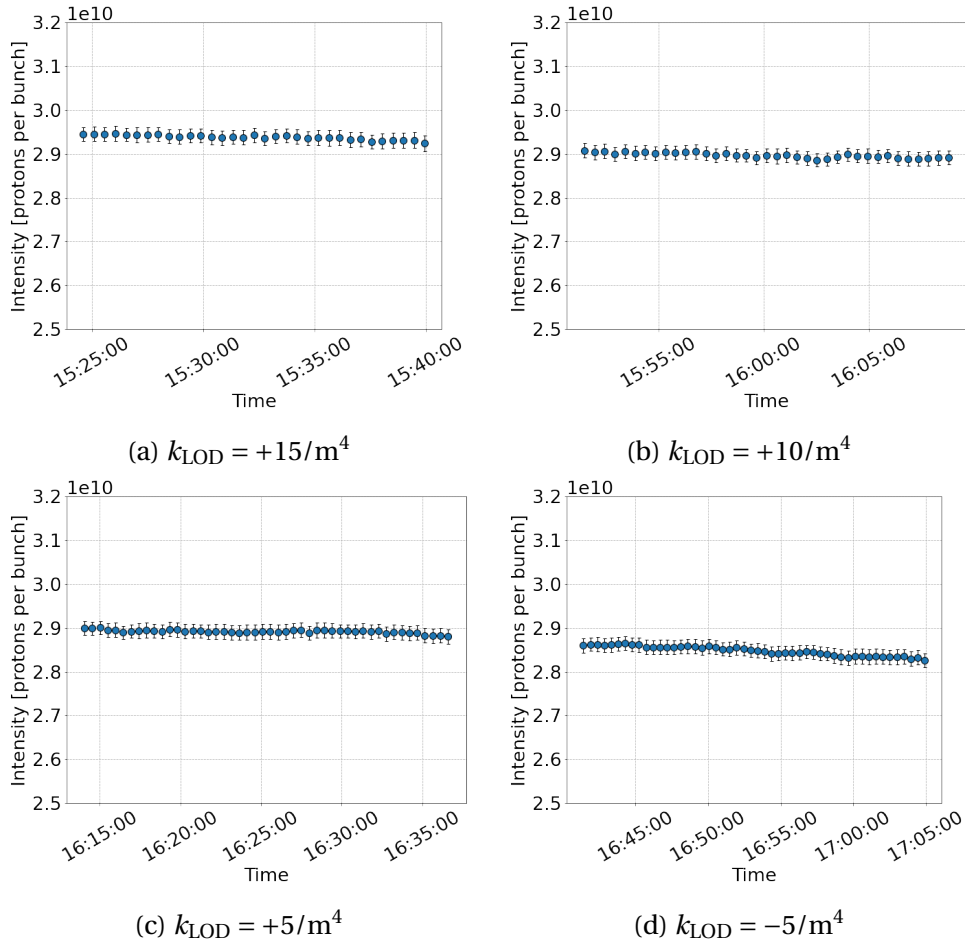
Figure E.11: Evolution of the intensity during the CC Experiment II on May 16, 2022. The different octupole settings are displayed at the captions of each plot.

The average measured intensity over all above coasts on May 16, 2022 (Experiment III) was found to be 2.9×10^{10} protons per bunch.

E.4.3 Experiment III: emittance growth measurements in the presence of strong octupoles

(a) $k_{\text{LOD}} = -30/\text{m}^4$

(b) $k_{\text{LOD}} = -20/\text{m}^4$

(c) $k_{\text{LOD}} = -10/\text{m}^4$

(d) $k_{\text{LOD}} = +30/\text{m}^4$

(e) $k_{\text{LOD}} = +10/\text{m}^4$
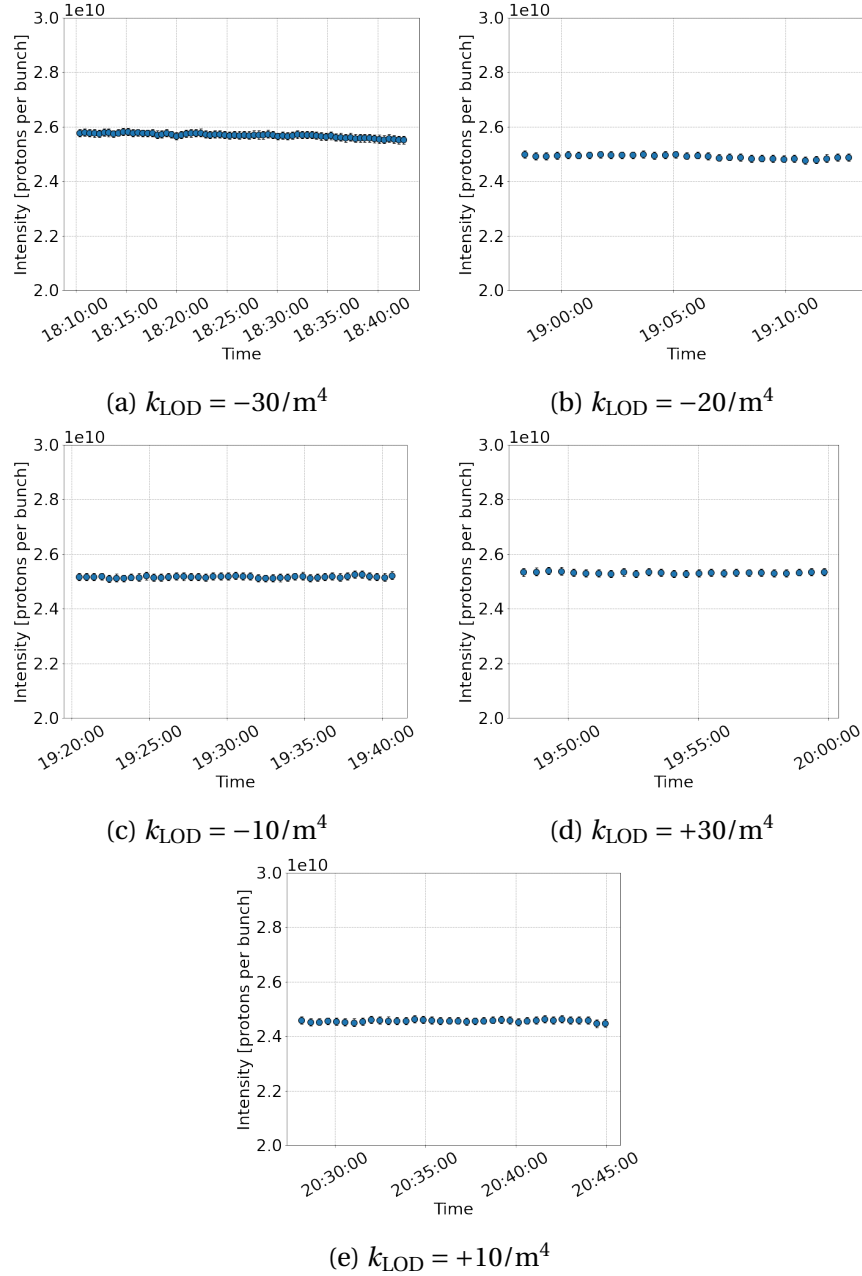
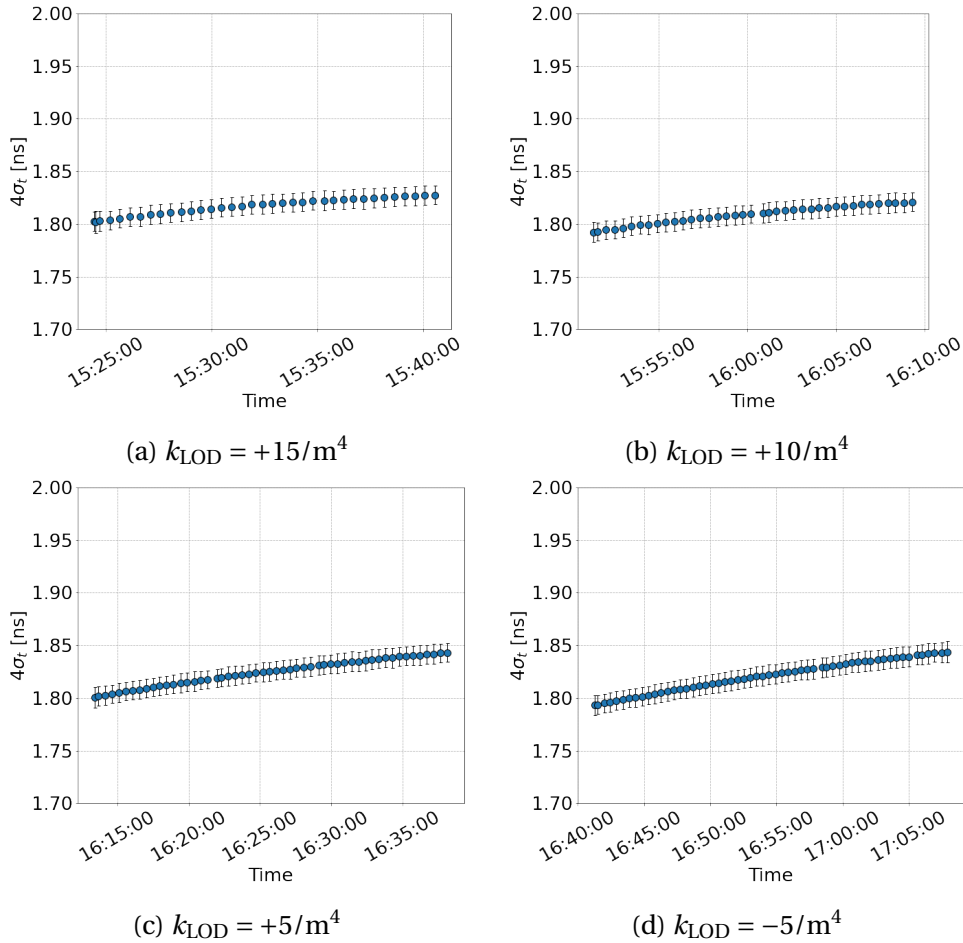Figure E.12: Evolution of the inensity during the CC Experiment III on September 12, 2022. The different octupole settings are displayed at the captions of each plot.

The average measured intensity over all above coasts on September 12, 2022 (Experiments III) was found to be 2.5×10^{10} protons per bunch.

E.4.4 Experiment IV: emittance growth measurements driven primarily by amplitude noise
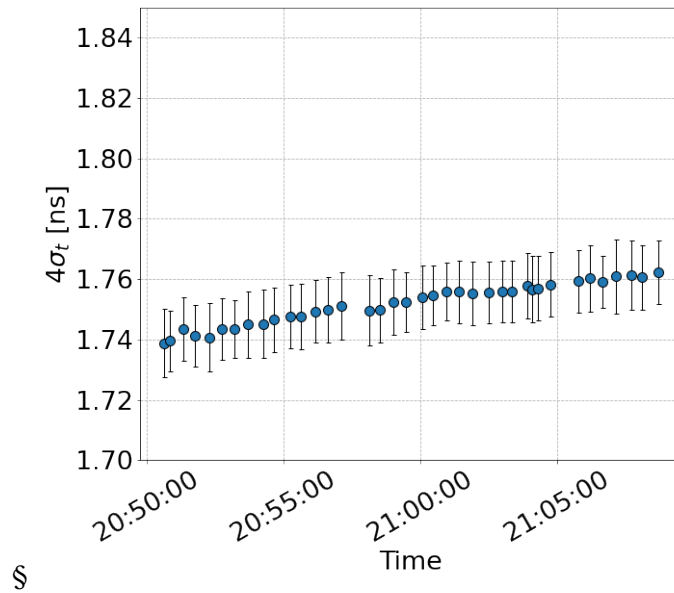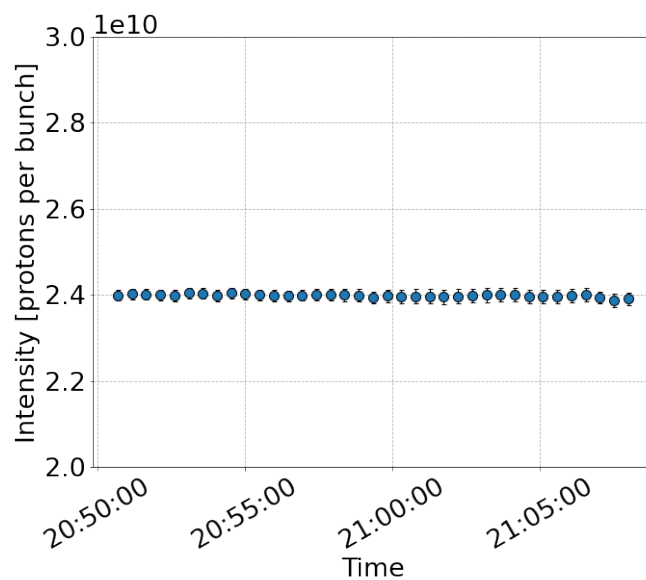

Figure E.13: Evolution of the intensity during the CC Experiment IV on September 12, 2022.

The average intensity over the coast was found to be 2.4×10^{10} protons per bunch.

Bibliography

[1]   Oliver Sim Brüning et al. *LHC Design Report*. CERN Yellow Reports: Monographs. Geneva: CERN, 2004. DOI: 10.5170/CERN-2004-003-V-1. URL: https://cds.cern.ch/record/782076.

[2]   G. Aad et al. "The ATLAS Experiment at the CERN Large Hadron Collider". In: *JINST* 3 (2008), S08003. DOI: 10.1088/1748-0221/3/08/S08003.

[3]   S. Chatrchyan et al. "The CMS Experiment at the CERN LHC". In: *JINST* 3 (2008), S08004. DOI: 10.1088/1748-0221/3/08/S08004.

[4]   K. Aamodt et al. "The ALICE experiment at the CERN LHC". In: *JINST* 3 (2008), S08002. DOI: 10.1088/1748-0221/3/08/S08002.

[5]   A Augusto Alves et al. "The LHCb Detector at the LHC". In: *JINST* 3 (2008). Also published by CERN Geneva in 2010, S08005. DOI: 10.1088/1748-0221/3/08/S08005. URL: https://cds.cern.ch/record/1129809.

[6]   ATLAS collaboration. "Observation of a new particle in the search for the Standard Model Higgs boson with the ATLAS detector at the LHC". In: *Physics Letters B* 716 (1) (2012), pp. 1–29. URL: https://www.sciencedirect.com/science/article/pii/S037026931200857X.

[7]   CMS collaboration. "Observation of a new boson at a mass of 125 GeV with the CMS experiment at the LHC". In: *Physics Letters B* 716 (1) (2012), pp. 30–61. URL: https://www.sciencedirect.com/science/article/pii/S0370269312008581.

[8]   Ewa Lopienska. "The CERN accelerator complex, layout in 2022. Complexe des accélérateurs du CERN en janvier 2022". In: (2022). General Photo. URL: https://cds.cern.ch/record/2800984.

[9]   CERN Yellow Reports: Monographs. *CERN Yellow Reports: Monographs, Vol. 10 (2020): High-Luminosity Large Hadron Collider (HL-LHC): Technical*

design report. en. 2020. DOI: 10 . 23731 / CYRM - 2020 - 0010. URL: https://e-publishing.cern.ch/index.php/CYRM/issue/view/127.

[10]   Oliver Brüning and Lucio Rossi. *The High Luminosity Large Hadron Collider.* WORLD SCIENTIFIC, Feb. 2015. DOI: 10.1142/9581. URL: https://doi.org/10. 1142/9581.

[11]   W. Herr. *"Particle Colliders and Concept of Luminosity".* at CERN Accelerator School. 2012. URL: https://cas.web.cern.ch/sites/default/files/lectures/ constanta-2018/l1.pdf.

[12]   O. Brüning and L. Rossi. *The High Luminosity Large Hadron Collider: the New Machine for Illuminating the Mysteries of Universe.* Vol. 24. World Scientic Publishing Company, 2015.

[13]   Rama Calaga. "Crab Cavities for the High-luminosity LHC". In: (2018), THXA03. 5 p. DOI: 10 . 18429 / JACoW - SRF2017 - THXA03. URL: https://cds.cern.ch/record/2673544.

[14]   Hans Peter Beck. *First Results from the Large Hadron Collider.* Accessed: 24-06-2022. URL: https://www.sps.ch/artikel/progresses/first-results-from-the-large-hadron-collider-24.

[15]   C. et al Zanoni. "Design of Dressed Crab Cavities for the HL-LHC Upgrade". In: (2015), THPB070. 5 p. DOI: 10.18429/JACoW-SRF2015-THPB070. URL: https://cds.cern.ch/record/2288282.

[16]   Subashini De Silva et al. "Electromagnetic Design of 400 MHz RF-Dipole Crabbing Cavity for LHC High Luminosity Upgrade". In: (2015), THPB053. 5 p. DOI: 10 . 18429 / JACoW - SRF2015 - THPB053. URL: https://cds.cern.ch/record/2288607.

[17]   Binping Xiao et al. "Design, prototyping and testing of a compact superconducting double quarter wave crab cavity". In: *Phys. Rev. Spec. Top. Accel. Beams* 18 (Feb. 2015), 041004. 10 p. DOI: 10 . 1103 / PhysRevSTAB . 18 . 041004. arXiv: 1502 . 04088. URL: https://cds.cern.ch/record/1992565.

[18]   S Verdú-Andrés et al. "Design and Prototyping of HL-LHC Double Quarter Wave Crab Cavities for SPS Test". In: (May 2015), 3 p. URL: https://cds.cern.ch/record/2113440.

[19]   N Toge. *KEK B-factory Design Report*. Tech. rep. Tsukuba: KEK, 1995. URL: https://cds.cern.ch/record/475260.

[20]   T. et al. Abe. "Beam operation with crab cavities at KEKB". In: *2007 IEEE Particle Accelerator Conference (PAC), Albuquerque, New Mexico, USA*. Vol. TUPAN045. 2007, pp. 1487–1489. DOI: 10.1109/PAC.2007.4440798.

[21]   Y. Funakoshi. "Operational experience with crab cavities at KEKB". In: (Oct. 2014). Comments: 10 pages, contribution to the ICFA Mini-Workshop on Beam-Beam Effects in Hadron Colliders, CERN, Geneva, Switzerland, 18-22 Mar 2013, 27–36. 10 p. DOI: 10.5170/CERN-2014-004.27. arXiv: 1410.4036. URL: https://cds.cern.ch/record/1955812.

[22]   K. Oide et al. "Compensation of the Crossing Angle with Crab Cavities at KEKB". In: *Proc. PAC'07* (Albuquerque, NM, USA, Jun. 2007). JACoW Publishing, Geneva, Switzerland, pp. 27–31. URL: https://jacow.org/p07/papers/MOZAKI01.pdf.

[23]   C. Zanoni et al. "The crab cavities cryomodule for SPS test". In: 874 (July 2017), p. 012092. DOI: 10.1088/1742-6596/874/1/012092. URL: https://doi.org/10.1088/1742-6596/874/1/012092.

[24]   Luis Eduardo Medina Medrano et al. *Effective pile-up density as a measure of the experimental data quality for High-Luminosity LHC operational scenarios*. Tech. rep. Geneva: CERN, Jan. 2018. URL: https://cds.cern.ch/record/2301928.

[25]   T. Mastoridis P. Baudrenghien. *Crab Cavity RF noise: Update 2*. Accessed: 27-06-2022. URL: https://indico.cern.ch/event/1044711/contributions/4389271/attachments/2264292/3861025/CC_Noise_Feedback_PB.pdf.

[26]   I. Ilias Efthymiopoulos. *Luminosity estimates including noise from crab cavities (without feedback*. Accessed: 27-06-2022. URL: https://indico.cern.ch/event/1044711/contributions/4389268/attachments/2264203/3844208/ie_WP2CCemitBU_14.06.2021.pdf.

[27] P. Baudrenghien and T. Mastoridis. "Transverse emittance growth due to rf noise in the high-luminosity LHC crab cavities". In: *Phys. Rev. ST Accel. Beams* 18 (10 Oct. 2015), p. 101001. DOI: 10.1103/PhysRevSTAB.18.101001. URL: https://link.aps.org/doi/10.1103/PhysRevSTAB.18.101001.

[28] Andrzej Wolski. *Beam Dynamics in High Energy Particle Accelerators.* Imperial College Press, 2014.

[29] Helmut Wiedemann. *Particle accelerator physics; 4th ed.* Berlin: Springer, 2015. DOI: 10.1007/978-3-319-18317-6. URL: https://link.springer.com/content/pdf/10.1007/978-3-319-18317-6.pdf.

[30] S Y Lee. *Accelerator physics; 3rd ed.* Singapore: World Scientific, 2012. URL: https://cds.cern.ch/record/1425444.

[31] Jean Buon. "Beam phase space and emittance". In: (Dec. 1990), 23 p. DOI: 10.5170/CERN-1991-004.30. URL: https://cds.cern.ch/record/216507.

[32] Bernhard Holzer. *Introduction to Accelerator Physics Beam Dynamics for Summer Students.* Accessed: 13-07-2021. URL: https://indico.cern.ch/event/91711/attachments/1096595/1564350/Summer_Stud_Holzer_2010.pdf.

[33] David Newton and Andy Wolski. *Design of Electron Storage and Damping Rings, Part 5: Coupling and Alignment.* Accessed: 13-07-2021. URL: https://uspas.fnal.gov/materials/13CSU/Lecture5.pdf.

[34] Linda Stoel et al. "Slow extraction loss reduction with octupoles at the CERN SPS". In: (2019), WEPMP033. 4 p. DOI: 10.18429/JACoW-IPAC2019-WEPMP033. URL: http://cds.cern.ch/record/2693915.

[35] G Rumolo. "Beam Instabilities". In: (2014). Comments: 21 pages, contribution to the CAS - CERN Accelerator School: Advanced Accelerator Physics Course, Trondheim, Norway, 18-29 Aug 2013, 21 p. DOI: 10.5170/CERN-2014-009.199. URL: https://cds.cern.ch/record/1982422.

[36]   W Herr. "Introduction to Landau Damping". In: (2014). Comments: 27 pages, contribution to the CAS - CERN Accelerator School: Advanced Accelerator Physics Course, Trondheim, Norway, 18-29 Aug 2013, 27 p. DOI: 10.5170/CERN-2014-009.377. URL: https://cds.cern.ch/record/1982428.

[37]   Jacques Gareyte, Jean-Pierre Koutchouk, and F Ruggiero. *Landau damping dynamic aperture and octupole in LHC.* Tech. rep. revised version number 1 submitted on 2003-08-21 14:12:02. Geneva: CERN, Feb. 1997. URL: https://cds.cern.ch/record/321824.

[38]   Frank Tecker. "Longitudinal Beam Dynamics - Recap". In: *CERN Yellow Rep. School Proc.* 5 (Dec. 2018). 17 pages, contribution to the CAS - CERN Accelerator School: Beam Instrumentation, 2-15 June 2018, Tuusula, Finland. arXiv admin note: substantial text overlap with arXiv:1601.04901, 31. 16 p. DOI: 10.23730/CYRSP-2018-005.31. arXiv: 2004.11908. URL: https://cds.cern.ch/record/2674860.

[39]   Frank Zimmermann. "Introduction to Collective Effects in Particle Accelerators". In: *ICFA Beam Dyn. Newsl.* 69 (2016), 8–17. 10 p. URL: https://cds.cern.ch/record/2264408.

[40]   Alexander Wu Chao. *Physics of collective beam instabilities in high energy accelerators.* New York, NY: Wiley, 1993. URL: http://cds.cern.ch/record/246480.

[41]   Giovanni Rumolo and Kevin Li. *Instabilities Part II: Longitudinal wake fields - impact on machine elements and beam dynamics.* Accessed: 20-07-2022. URL: https://indico.cern.ch/event/509762/contributions/2450946/attachments/1515079/2373718/London2_Longitudinal_v04a.pdf.

[42]   Benoit Salvant. *Building the impedance model of a real machine.* Accessed: 20-07-2022. URL: https://accelconf.web.cern.ch/ipac2019/talks/weypls1_talk.pdf.

[43]   Michael Schenk. "A novel approach to Landau damping of transverse collective instabilities in future hadron colliders". Presented 05 Feb 2019. 2019. URL: https://cds.cern.ch/record/2665819.

Bibliography

[44] A Vlasov. "On the kinetic theory of an assembly of particles with collective interaction". In: *Russ. Phys. J.* 9 (1945), pp. 25–40. URL: http://cds.cern.ch/record/426186.

[45] Frank James Sacherer. *Methods for computing bunched-beam instabilities.* Tech. rep. Geneva: CERN, Sept. 1972. URL: https://cds.cern.ch/record/322545.

[46] F J Sacherer. "Transverse bunched beam instabilities - Theory". In: (Apr. 1974), 5 p. URL: https://cds.cern.ch/record/322645.

[47] N. Biancacci, E. Métral, and M. Migliorati. "Fast-slow mode coupling instability for coasting beams in the presence of detuning impedance". In: *Phys. Rev. Accel. Beams* 23 (12 Dec. 2020), p. 124402. DOI: 10 . 1103 / PhysRevAccelBeams . 23 . 124402. URL: https://link.aps.org/doi/10.1103/PhysRevAccelBeams.23.124402.

[48] Laurent Deniau (editor). *MAD-X: Methodical Accelerator Design.* Accessed: 20-07-2022. URL: https://mad.web.cern.ch/madx/.

[49] *Official optics repository of the CERN accelerators.* Accessed: 20-07-2022. URL: https://gitlab.cern.ch/acc-models.

[50] *Official optics repository of the CERN Super Proton Synchrotron (official name SPS).* Accessed: 16-2-2022. URL: https://gitlab.cern.ch/acc-models/acc-models-sps/-/tree/2021/.

[51] *PyHEADTAIL code repository.* Accessed: 19-6-2022. URL: https://github.com/PyCOMPLETE/.

[52] Adrian Oeftiger. *An overview of PyHEADTAIL.* Accessed: 05-06-2022. URL: https://cds.cern.ch/record/2672381/files/CERN-ACC-NOTE-2019-0013.pdf.

[53] Michael Schenk. *Beam dynamics simulations with the PyHEADTAIL and PyECLOUD macroparticle codes.* Accessed: 05-06-2022. URL: https://www2.kek.jp/accl/legacy/seminar/file/PyHEADTAIL_PyECLOUD_2.pdf.

[54]   Benoit Salvant. "Impedance model of the CERN SPS and aspects of LHC single-bunch stability". Presented on 04 Mar 2010. 2010. DOI: 10.5075/epfl-thesis-4585. URL: https://cds.cern.ch/record/1274254.

[55]   *Sixtracklib code repository*. Accessed: 20-07-2022. URL: https://github.com/SixTrack/sixtracklib.

[56]   Martin Schwinzerl et al. *Introducing Sixtracklib*. Accessed: 20-07-2022. URL: https://indico.cern.ch/event/833895/contributions/3577803/attachments/1927226/3190636/intro_sixtracklib.pdf.

[57]   Martin Schwinzerl et al. "Optimising and Extending A Single-Particle Tracking Library For High Parallel Performance. OPTIMISING AND EXTENDING A SINGLE-PARTICLE TRACKING LIBRARY FOR HIGH PARALLEL PERFORMANCE". In: (Sept. 2021). DOI: 10.18429/JACoW-IPAC2021-THPAB190. URL: https://cds.cern.ch/record/2781835.

[58]   V Lebedev et al. "Emittance growth due to noise and its suppression with the feedback system in large hadron colliders". In: *Part. Accel.* 44 (Mar. 1993), 147–164. 28 p. URL: https://cds.cern.ch/record/248620.

[59]   V Lebedev. "Computer simulation of the emittance growth due to noise in large hadron colliders". In: *Part. Accel.* 44 (Mar. 1993), 165–199. 57 p. URL: https://cds.cern.ch/record/248622.

[60]   K. Ohmi et al. "Response of colliding beam-beam system to harmonic excitation due to crab-cavity rf phase modulation". In: *Phys. Rev. ST Accel. Beams* 14 (11 Nov. 2011), p. 111003. DOI: 10.1103/PhysRevSTAB.14.111003. URL: https://link.aps.org/doi/10.1103/PhysRevSTAB.14.111003.

[61]   Rama Calaga, Ofelia Capatina, and Giovanna Vandoni. "The SPS Tests of the HL-LHC Crab Cavities". In: (2018), TUPAF057. 4 p. DOI: 10.18429/JACoW-IPAC2018-TUPAF057. URL: https://cds.cern.ch/record/2649807.

[62]   Carver Lee. *First proton beam dynamics results with crab cavities*. Accessed: 10-11-2021. URL: https://indico.cern.ch/event/800428/attachments/1804664/2945632/CrabCavity_BE_Seminar.pdf.

[63]   Philippe Baudrenghien. *SPS Crab Cavity test RF Test Program.* Accessed: 11-11-2021. URL: https://indico.cern.ch/event/718127/contributions/2951305/attachments/1645650/2629988/SPSCCtestv3.pdf.

[64]   R Calaga et al. "Proton-beam emittance growth in SPS coasts". In: *Conf. Proc.* C1205201 (May 2012), THPPP007. 3 p. URL: https://cds.cern.ch/record/1451286.

[65]   A Alekou et al. *Emittance growth in coast in the SPS.* Accessed: 26-11-2021. URL:
https://indico.cern.ch/event/609486/contributions/2457542/attachments/1433340/2318716/EmittanceEvolutionCoastSPS_2017_April.pdf.

[66]   Fanouria Antoniou et al. "Emittance Growth in Coast in the SPS at CERN". In: *J. Phys.: Conf. Ser.* 1067 (2018), MOPMF061. 7 p. DOI: 10.18429/JACoW-IPAC2018-MOPMF061. URL: https://cds.cern.ch/record/2649815.

[67]   Michele Carlà et al. "Studies of a New Optics With Intermediate Transition Energy as Alternative for High Intensity LHC Beams in the CERN SPS". In: (2018), TUPAF022. 4 p. DOI: 10.18429/JACoW-IPAC2018-TUPAF022. URL: https://cds.cern.ch/record/2664976.

[68]   Androula Alekou et al. "SPS Long Term Stability Studies in the Presence of Crab Cavities and High Order Multipoles". In: (2018), WEP2PO008. 3 p. DOI: 10.18429/JACoW-HB2018-WEP2PO008. URL: https://cds.cern.ch/record/2640326.

[69]   K. Gheen. *Phase Noise Measurement Methods and Techniques.* Accessed November 5, 2020. Agilent Technologies. URL: https://studylib.net/doc/18034081/phase-noise-measurements.

[70]   "IEEE Standard Definitions of Physical Quantities for Fundamental Frequency and Time Metrology—Random Instabilities". In: *IEEE Std Std 1139-2008* (2009), pp. c1–35. DOI: 10.1109/IEEESTD.2008.4797525.

[71]   Kevin Shing Bruce Li. *SPS Head-Tail Monitor.* Accessed: 27-09-2022. URL: https://indico.cern.ch/event/931117/contributions/3913554/attachments/2096199/3523367/014_HeadtailMonitor.pdf.

[72] Tom Levens. *Head-Tail Monitor for CC Diagnostics.* Accessed: 11-04-2022. URL: https : / / indico . cern . ch / event / 826475 / contributions / 3457525 / attachments/1872464/3081710/2019-07-02_HL_WP2_tlevens.pdf.

[73] N. Triantafyllou et al. *Investigating the discrepancy between measured and expected emittance growth in SPS Crab Cavity tests.* Accessed: 27-09-2022. URL: https : / / indico . cern . ch / event / 965718 / contributions / 4064170 / attachments/2135267/3596606/WP4_3November_CCnoiseStudies.pdf.

[74] J. Bosser et al. "Transverse emittance measurement with a rapid wire scanner at the CERN SPS". In: *Nuclear Instruments and Methods in Physics Research Section A: Accelerators, Spectrometers, Detectors and Associated Equipment* 235.3 (1985), pp. 475–480. ISSN: 0168-9002. DOI: https : / / doi . org / 10 . 1016 / 0168 - 9002(85) 90096 - 8. URL: https : / / www . sciencedirect . com / science / article/pii/0168900285900968.

[75] OE Berrig et al. *CERN-SPS Wire Scanner Impedance and Wire Heating Studies.* Tech. rep. Geneva: CERN, Sept. 2014. URL: https://cds.cern.ch/record/1972478.

[76] Federico Roncarolo. "Accuracy of the Transverse Emittance Measurements of the CERN Large Hadron Collider". Presented 2005. 2005. URL: https://cds.cern.ch/record/1481835.

[77] *H. Bartosik personal communication, March, 2022.*

[78] Rogelio Tomas et al. "Improved algorithms to determine the non-linear optics model of the SPS from non-linear chromaticity". In: July 2007, pp. 4231–4233. ISBN: 978-1-4244-0916-7. DOI: 10.1109/PAC.2007.4439986.

[79] Department of Physics University of Pennsylvania and Lab manual astronomy. *Managin errors and uncertainties.* Accessed: 18-03-2022. URL: https : / / www . physics . upenn . edu / sites / default / files / Managing%20Errors%20and%20Uncertainty.pdf.

[80] Philippe Baudrenghien. *LLRF experience for SPS & HL-LHC Outlook.* Accessed: 11-11-2021. URL: https : / / indico . cern . ch / event / 787363 / contributions/3367294/attachments/1865644/3067685/HL-LHC19v6.pdf.

[81] F. Follin G. Papotti. *Online bunch length measurement for SPS OP*. Accessed: 26-11-2021. URL: https://indico.cern.ch/event/774525/contributions/3218683/attachments/1756129/2847423/20181120_LIUSPSBD.pdf.

[82] G. Papotti. "A Beam Quality Monitor for LHC Beams in the SPS". In: (Sept. 2008), 4 p. URL: https://cds.cern.ch/record/1124099.

[83] T. Argyropoulos. *Private communication, Nov 2020*.

[84] *T. Mastoridis and P. Baudrenghien, personal communication, November 25, 2020*.

[85] Alexander Wu Chao et al. *Handbook of accelerator physics and engineering; 2nd ed.* Singapore: World Scientific, 2013. DOI: 10.1142/8543. URL: https://cds.cern.ch/record/1490001.

[86] *Repository of SPS impedance model*. Accessed: 3-6-2022. URL: https://gitlab.cern.ch/IRIS/SPS_IW_model.

[87] Carlo Zannini. "Electromagnetic Simulation of CERN accelerator Components and Experimental Applications". Presented 15 Apr 2013. Mar. 2013. URL: https://cds.cern.ch/record/1561199.

[88] B Salvant et al. "Update of the SPS Impedance Model". In: (June 2010), 3 p. URL: https://cds.cern.ch/record/1271349.

[89] Carlo Zannini et al. "Benchmarking the CERN-SPS Transverse Impedance Model with Measured Headtail Growth Rates". In: (2015), MOPJE049. 4 p. URL: https://cds.cern.ch/record/2141779.

[90] J. Laskar. "The chaotic motion of the solar system: A numerical estimate of the size of the chaotic zones". In: *Icarus* 88.2 (1990), pp. 266–291. ISSN: 0019-1035. DOI: https://doi.org/10.1016/0019-1035(90)90084-M. URL: https://www.sciencedirect.com/science/article/pii/001910359090084M.

[91] Sofia Kostoglou et al. "Development of Computational Tools for Noise Studies in the LHC". In: (2017), THPAB044. 4 p. DOI: 10.18429/JACoW-IPAC2017-THPAB044. URL: https://cds.cern.ch/record/2289645.

[92] *NAFFlib code repository*. Accessed: 05-08-2022. URL: https://github.com/
      PyCOMPLETE/NAFFlib.

[93] Mario Beck. "Numerical and experimental studies to model and reduce the
      impedance in the CERN Super Proton Synchrotron (SPS). Numerische und
      experimentelle Studien zur Modellierung und Reduzierung der
      Strahlimpedanz im Super Proton Synchrotron (SPS)
      Teilchenbeschleuniger". Presented 08 Feb 2019. Dec. 2018. URL:
      http://cds.cern.ch/record/2683038.

[94] H Bartosik et al. "TMCI thresholds for LHC single bunches in the CERN SPS
      and comparison with simulations". In: (June 2016), 4 p. URL: https://cds.
      cern.ch/record/1742183.

[95] Carlo Zannini et al. *SPS impedance-induced observables pre and post LS2*.
      Accessed: 06-08-2022.   URL:
      https://indico.cern.ch/event/919160/contributions/3863191/attachments/
      2040319/3417759/SPS_pre_and_postLS2_HSC.pdf.

[96] *Updated SPS wakefields model repository*. Accessed: 12-08-2022. URL: https:
      //github.com/natriant/exploring_SPS/tree/master/updated_wakefields_
      model.

[97] Yu I Alexahin. "On the Landau Damping and Decoherence of Transverse
      Dipole Oscillations in Colliding Beams". In: *Part. Accel.* 59 (Aug. 1996),
      43–74. 19 p. URL: https://cds.cern.ch/record/314169.

[98] Yu I Alexahin. "A study of the Coherent Beam-Beam Effect in the Framework
      of the Vlasov Perturbation Theory". In: *Nucl. Instrum. Methods Phys. Res., A*
      480 (2002), 253–88. 33 p. DOI: 10.1016/S0168-9002(01)01219-0. URL: https:
      //cds.cern.ch/record/485304.

[99] J. Qiang et al. "Simulation of beam–beam interaction with crab cavities for
      LHC upgrade". In: *Nuclear Instruments and Methods in Physics Research
      Section A: Accelerators, Spectrometers, Detectors and Associated Equipment*
      900   (2018),   pp.   53–59.   ISSN: 0168-9002.   DOI:
      https://doi.org/10.1016/j.nima.2018.05.055. URL:
      https://www.sciencedirect.com/science/article/pii/S0168900218306740.

Bibliography

[100] X. Buffat et al. "Modeling of the emittance growth due to decoherence in collision at the Large Hadron Collider". In: *Phys. Rev. Accel. Beams* 23 (2 Feb. 2020), p. 021002. DOI: 10.1103/PhysRevAccelBeams.23.021002. URL: https://link.aps.org/doi/10.1103/PhysRevAccelBeams.23.021002.

[101] Sondre Vik Furuseth et al. "Emittance growth suppression with a multibunch feedback in high-energy hadron colliders: Numerical optimization of the gain and bandwidth". In: *Phys. Rev. Accel. Beams* 24 (1 Jan. 2021), p. 011003. DOI: 10.1103/PhysRevAccelBeams.24.011003. URL: https://link.aps.org/doi/10.1103/PhysRevAccelBeams.24.011003.

[102] Yu I Alexahin et al. "Coherent Beam-Beam Effects in the LHC". In: (Apr. 2001), 10 p. URL: https://cds.cern.ch/record/497415.

[103] Werner Herr and M P Zorzano-Mier. *Coherent Dipole Modes for Multiple Interaction Regions.* Tech. rep. Geneva: CERN, Feb. 2001. URL: https://cds.cern.ch/record/486007.

[104] W. Herr and T. Pieloni. "Beam-Beam Effects". In: (Jan. 2016). 29 pages, contribution to the CAS - CERN Accelerator School: Advanced Accelerator Physics Course, Trondheim, Norway, 18-29 Aug 2013, 431–459. 29 p. DOI: 10.5170/CERN-2014-009.431. arXiv: 1601.05235. URL: https://cds.cern.ch/record/1982430.

[105] Xavier Buffat. "Suppression of Emittance Growth by a Collective Force: Van Kampen Approach". In: *JACoW* IPAC2022 (2022), WEPOTK059. DOI: 10.18429/JACoW-IPAC2022-WEPOTK059.

[106] X. Buffat. *Crab Cavity experiments and underlying theory.* Accessed: 07-09-2022. URL: https://indico.cern.ch/event/1170242/contributions/4915101/attachments/2476586/4250387/2022-07-07_crabMD-expanded.pdf.

[107] R Jones et al. "Introduction to beam instrumentation and diagnostics". In: (2014). Comments: 38 pages, contribution to the CAS - CERN Accelerator School: Advanced Accelerator Physics Course, Trondheim, Norway, 18-29 Aug 2013, 38 p. DOI: 10.5170/CERN-2014-009.23. URL: https://cds.cern.ch/record/1982418.

[108] H Jakob et al. "A 40 MHz Bunch by Bunch Intensity Measurement for the CERN SPS and LHC". In: (2003), 4 p. URL: https://cds.cern.ch/record/624188.

[109] Friedhelm Caspers. "Schottky signals for longitudinal and transverse bunched-beam diagnostics". In: (2009). DOI: 10.5170/CERN-2009-005.407. URL: https://cds.cern.ch/record/1213284.

[110] M P Zorzano-Mier and Frank Zimmermann. "Simulations of coherent beam-beam modes at the Large Hadron Collider". In: *Phys. Rev. Spec. Top. Accel. Beams* 3 (2000), p. 044401. DOI: 10.1103/PhysRevSTAB.3.044401. URL: https://cds.cern.ch/record/446334.

[111] Elena Shaposhnikova et al. "LHC Injectors Upgrade (LIU) Project at CERN". In: *7th International Particle Accelerator Conference.* 2016, MOPOY059. DOI: 10.18429/JACoW-IPAC2016-MOPOY059.

[112] A Boccardi et al. *The FPGA-based Continious FFT Tune Measurement System for the LHC and its test at the CERN SPS.* Tech. rep. Geneva: CERN, 2007. URL: https://cds.cern.ch/record/1055568.

[113] K. Li. *Collective effects, Part IV: Coherent beam instabilities.* Accessed: 05-09-2022. URL: https://cas.web.cern.ch/sites/default/files/lectures/-27%20March%202022/Chavannes4_Instabilities.pdf.

[114] Tatiana Pieloni. "A study of beam-beam effects in hadron colliders with a large number of bunches". Presented on 4 Dec 2008. 2008. URL: https://cds.cern.ch/record/1259906.

[115] X Buffat et al. "Modeling of the emittance growth due to decoherence in collision at the Large Hadron Collider". In: *Phys. Rev. Accel. Beams* 23 (2020), 021002. 9 p. DOI: 10.1103/PhysRevAccelBeams.23.021002. URL: https://cds.cern.ch/record/2712068.

[116] D. Valuch. *The LHC transverse damper: a multi-purpose system.* Accessed: 13-09-2022. URL: https://indico.cern.ch/event/775147/contributions/3366413/attachments/1913791/3164486/MCBI2019_-_LHC_transverse_feedback_a_multi_purpose_system.pdf.

[117]   P. Baudrenghien. *Crab Cavity RF Noise: Update 2*. Accessed: 13-09-2022. URL: https : / / indico . cern . ch / event / 1044711 / contributions / 4389271 / attachments/2264292/3861025/CC_Noise_Feedback_PB.pdf.

[118]   Philippe   Baudrenghien,   Themistoklis   Mastoridis,   and Benjamin Nicholas Miller. "Crab Cavity RF Noise Feedback and Transverse Damper Interaction". In: (2019). URL: https://cds.cern.ch/record/2665950.

[119]   E. Metral. *Run 4 operational scenario and status of optics v1.6*. Accessed: 13-09-2022.   URL: https   : / / indico . cern . ch / event / 1197424 / contributions / 5035904 / attachments / 2507124 / 4308131 / HLLHCCollaborationMeeting _ Uppsala _ 19 - 09 - 2022_EM.pdf.

[120]   R. J. Barlow. *Statistics. A Guide to the Use of Statistical Methods in the Physical Sciences*. Manchester Physics Series. Wiley, 2013. ISBN: 9781118723234. URL: https://liverpool.idm.oclc.org/login?url=https://search.ebscohost.com/ login.aspx?direct=true&db=cat00003a&AN=lvp.b3130057&site=eds-live& scope=site.

[121]   K. K. Gan. *Chi Square Distribution (χ^2) and Least Squares fitting*. Accessed: 03-03-2022.   URL: https://www.asc.ohio-state.edu/gan.1/teaching/spring04/Chapter6.pdf.

[122]   *SciPy API Documentation*. Accessed: 16-2-2022. URL: https://docs.scipy.org/ doc/scipy/reference/generated/scipy.optimize.curve_fit.html.

[123]   William H. Press et al. *Numerical Recipes: The Art of Scientific Computing*. 3rd ed. USA: Cambridge University Press, 2007. ISBN: 0521880688. URL: http: //www.e-maxx-ru.1gb.ru/bookz/files/numerical_recipes.pdf.

[124]   A. Papoulis. *Probability, Random Variables, and Stochastic Processes*. Communications and Signal Processing. McGraw-Hill, 1991. ISBN: 9780070484771. URL: https://books.google.ch/books?id=4IwQAQAAIAAJ.

[125]   R. Bracewel. *The Fourier Transform and its Applications*. 2nd ed. McGraw-Hill, 1986.

[126] NumPy Project and Community. *NumPy API Documentation*. Accessed November 5, 2020. URL: https://numpy.org/doc/stable/reference/routines.fft.html.

[127] Hannes Bartosik et al. "Improved Methods for the Measurement and Simulation of the CERN SPS Non-linear Optics". In: (2016), THPMR036. 4 p. DOI: 10 . 18429 / JACoW - IPAC2016 - THPMR036. URL: https://cds.cern.ch/record/2207443.

[128] G. Kruk et al. *LHC SOFTWARE ARCHITECTURE [LSA] – EVOLUTION TOWARD LHC BEAM COMMISSIONING*.

[129] Lee Carver et al. "First machine development results with HL-LHC crab cavities in the SPS. First machine developments result with HL-LHC crab cavities in the SPS". In: (2019), MOPGW094. 4 p. DOI: 10 . 18429 / JACoW - IPAC2019 - MOPGW094. URL: https://cds.cern.ch/record/2696108.

[130] R. Jones and H. Schmickler. "The measurement of Q' and Q" in the CERN-SPS by head-tail phase shift analysis". In: *PACS2001. Proceedings of the 2001 Particle Accelerator Conference (Cat. No.01CH37268)*. Vol. 1. 2001, 531–533 vol.1. DOI: 10.1109/PAC.2001.987561.

[131] Thomas Levens, Kacper Łasocha, and Thibaut Lefèvre. "Recent Developments for Instability Monitoring at the LHC". In: (2017), THAL02. 4 p. DOI: 10 . 18429 / JACoW - IBIC2016 - THAL02. URL: https://cds.cern.ch/record/2313358.

[132] T. E. Levens et al. "Automatic detection of transverse beam instabilities in the Large Hadron Collider". In: *Phys. Rev. Accel. Beams* 22 (11 Nov. 2019), p. 112803. DOI: 10.1103/PhysRevAccelBeams.22.112803. URL: https://link.aps.org/doi/10.1103/PhysRevAccelBeams.22.112803.

[133] Tom Levens. *Beam instrumentation with SPS Crabs*. Accessed: 11-11-2021. URL: https : / / indico . cern . ch / event / 718127 / contributions / 2951309 / attachments/1646050/2630808/BI_SPS_Crabs.pdf.

Bibliography

[134] Jeroen Belleman, William Andreazza, and Andriy Nosych. "A New Wall Current Monitor for the CERN Proton Synchrotron". In: (2017), MOPG41. 4 p. DOI: 10 . 18429 / JACoW - IBIC2016 - MOPG41. URL: https://cds.cern.ch/record/2313362.

[135] T Argyropoulos. "Longitudinal beam quality monitoring". In: (2020), 6 p. DOI: 10 . 23732 / CYRCP - 2020 - 009 . 156. URL: https://cds.cern.ch/record/2752314.